RF Coil Design, Imaging Methods and Measurement of Ventilation with ^{19}F C$_3$F$_8$ MRI

Adam Mitchell Maunder

A thesis submitted in partial fulfilment of the requirements for the degree of
Doctor of Philosophy

The University of Sheffield
Academic Unit of Radiology
Department of Infection, Immunity and Cardiovascular Disease

Submission Date:

Supervisors: Professor Jim Wild

2nd Madhwesha Rao

3rd Professor Fraser Robb

i

Abstract

This thesis attempts to address the challenge of low signal in fluorinated gas ventilation imaging and optimize imaging methods considering the particular MR parameters of C_3F_8 by the following approaches:

(i) Exploration of coil designs capable of imaging both proton (^1H – 63.8 MHz at 1.5T) and fluorine (^{19}F – 60.1 MHz at 1.5T) nuclei involved:

1. The novel use of microelectromechanical systems to switch a single transceive vest coil between the two nuclei was compared to hard-wired or PIN diode switching.

2. The design of an 8 element transceive array with an additional 6 receive only coils for ^{19}F imaging. MEMs was utilized for broadband transmit-receive switching.

3. The amalgamation of a ladder resonator coil with a 6-element transceive array to reduce SAR and improve transmit homogeneity when compared to standard vest coil designs.

(ii) Development of imaging methods involved:

1. The optimization and comparison of steady-state free precession and spoiled gradient ^{19}F imaging with C_3F_8 at 1.5T and 3T. Simulation of the optimal SNR was verified through comprehensive phantom and in-vivo imaging experiments.

2. The investigation of compressed sensing via incoherent sparse k-space sampling to maximize the resolution in ^{19}F ventilation imaging under the constraint of low SNR. Retrospective simulation with hyperpolarized gas images were corroborated by prospective ^{19}F imaging of a 3D printed lung phantom and in-vivo measurements of the lungs.

(iii) In-vivo ventilation metrics obtained by ^{19}F ventilation imaging were explored by:

1. The in-vivo mapping of T_1 at 1.5T and 3T and mapping of FV and T_2^* at 3 T. The apparent diffusion coefficient (1.5T) and the evaluation of ventilated volume (1.5T and 3T) was also compared to imaging performed with ^{129}Xe (1.5T).

2. The optimization of imaging for the evaluation of percent ventilated volume with ^{19}F at 3T with a commercial birdcage coil.

iii

Table of Contents

List of Figures

List of Tables

Glossary of Terms

ADC	Apparent diffusion coefficient
AF	Acceleration factor
BW	Bandwidth
CF	Cystic fibrosis
COPD	Chronic obstructive pulmonary disease
CoV	Coefficient of Variation
D_0	Free diffusion coefficient
FA	Flip angle
FEV_1	Forced expiratory volume in one second
FOV	Field of view
FVC	Forced vital capacity
GRAPPA	Generalized autocalibrating partially parallel acquisition
HP	Hyperpolarised
IST	Iterative soft thresholding
iSNR	Intrinsic SNR
MEMS	Microelectromechanical system
NLCG	Non-linear conjugate gradient descent algorithm
NMR	Nuclear magnetic resonance
%VV	Percent ventilated volume
PCB	Printed circuit board
PDF	Probability distribution function
PFP	Perfluoropropane
PSF	Point spread function
RMSE	Root mean square error
RF	Radio frequency
Rx	Receive
RV	Residual volume
SAR	Specific absorption rate
SENSE	Sensitivity encoding
SEOP	Spin exchange optical pumping
SMASH	Simultaneous acquisition of spatial harmonics
SNR	Signal to noise ratio

SPGR	Spoiled gradient echo
SPIRiT	Self-consistent parallel imaging reconstruction
SSFP	Steady state free precession
S/V	Surface to volume ratio
T_{aq}	Acquisition Time
TP	Thermally polarized
Tx	Transmit
T_1	Longitudinal relaxation time
T_2	Transverse relaxation time
T_{2^*}	Reduced transverse relaxation time
TE	Echo time
TLC	Total lung capacity
TP	Thermally polarized
TR	Repetition time
TV	Total variation
UTE	Ultrashort echo time
ZTE	Zero echo time

Chapter 1 Introduction

1.1 Motivation

The objectives of this thesis are to improve the state-of-the art with regards to ^{19}F fluorinated gas pulmonary ventilation imaging in the following three ways: (i) to develop effective, novel and optimized radio-frequency coils for excitation and reception of magnetic resonance signal with both ^{19}F and ^{1}H nuclei; (ii) to optimize the imaging sequences used and image acceleration techniques, e.g. compressed sensing, for imaging C_3F_8; and (iii) to investigate the potential application of fluorinated gas imaging against ventilation imaging with hyperpolarized gas imaging.

1.2 Thesis Outline

Chapter 2 provides an introduction of basic MRI methods and theory including signal detection, image formation and compressed sensing. Following that, an overview of previous research and various applications of inert gas MR imaging of lungs and the current state-of-the-art is detailed. The application of thermodynamic equilibrium fluorinated gas imaging vs. hyperpolarized gas imaging is then compared, and finally the theoretical and experimental methods of RF coil design and previously employed methods of dual-tuning coils is reviewed.

Chapter 3 is the first chapter of original work, and described within is the design, simulation and measurement of a vest coil for imaging both fluorinated gas and proton. MEMS switches are used to switch the coil resonance between the Larmor frequency of the two nuclei and MEMS switching is compared to hard-wired switching or switching with the use of PIN diodes. Key coil performance measurements between the different switching methods are provided.

Chapter 4 presents an improved vest coil design for imaging ^{19}F and ^{1}H using an 8-element transceiver array for improved SNR and additional 6 receive-only coils. MEMS are employed for transmit-receive detuning with the 8-elements and performance is compared to the use of PIN diodes in terms of switching speed and isolation. SNR improvement over a single transceive element is simulated and measured and experimental comparison to the theoretically obtainable maximum SNR is investigated.

Chapter 5 demonstrates a novel vest coil design utilizing a mixed-mode excitation of a ladder resonator structure. Through improved approximation of the current patterns of a quadrature-driven birdcage coil, reduced SAR and improved transmit homogeneity are demonstrated, and derivation of the tuning for mixed-mode excitation is provided. The transmit/receive performance is compared to the previously detailed coil array.

1

Chapter 6 contains simulated and experimentally validated improvement of SNR in 3D ventilation imaging with C_3F_8 utilizing a steady-state free precession (SSFP) sequence. The use of SSFP compared to the normally used spoiled gradient echo (SPGR) sequences is compared in phantom measurements at both 1.5 T and 3 T and in vivo measurements at 1.5 T. The MR relaxation parameters of C_3F_8 are shown to be particularly suited for SSFP when compared to other fluorinated gas compounds.

Chapter 7 investigates the potential application of compressed sensing, via reconstructing incoherently undersampled MR data, for maintaining SNR, while improving effective resolution of fluorinated gas imaging. Retrospective optimization via simulation using two different reconstruction methods using a dataset of ^{3}He 3D lung imaging is validated by measurement with ^{19}F imaging of 3D printed lungs. The optimized compressed sensing parameters takes into account the expected lower SNR of ^{19}F imaging and is demonstrated with in vivo imaging.

Chapter 8 demonstrates the application of improved C_3F_8 image quality provided by the constructed 14-element receive array, SSFP imaging image resolution optimization to the voxel wise measurement of physiological related MR parameters such as ventilated volume, T_1, T_2^*, apparent diffusion coefficient and fractional ventilation. The acquisition of images and parametric maps with suitable SNR and higher resolution than previously obtained at 1.5 T are demonstrated and compared to data acquired at 3 T. Additionally, comparison to similar ventilation imaging carried out with ^{129}Xe is shown for relative assessment of ventilated volume and apparent diffusion coefficient with the two inhaled gases.

Chapter 9 summarizes the optimization of imaging parameters for protocol development and the registration/segmentation methods for measurement of ventilated volume at 3 T. Additionally, the results of analysing a cohort of healthy volunteers is presented.

Chapter 10 summarizes the findings presented in each of the thesis chapters and the challenges and future directions for future coil design and the application of ^{19}F MR imaging and its limitations based on the work presented here.

Chapter 2 Background

2.1 Introduction

The principles of nuclear magnetic resonance (NMR) were first described by Bloch and Purcell (1, 2). Their experiments quantified the behaviour of nuclear spins precessing in a static magnetic field, thereby opening up the field of NMR research. The later developments of Lauterbur and Mansfield (3, 4) provided a practical and robust method of using magnetic field gradients to encode image information that laid the foundation for the field of magnetic resonance imaging (MRI).

MRI has proven to be valuable clinical, diagnostic and research imaging modality that does not require ionizing radiation, and provides better contrast for soft-tissues (grey matter, fibrous connective tissue, muscular tissue, etc.) than other imaging modalities, such as computed tomography (CT) (5, 6) or ultrasound. Conventional MR imaging targets the ^{1}H nucleus to provide structural and physiological information about the human body, while MRI of other nuclei, such as ^{3}He, ^{13}C, ^{129}Xe, ^{19}F, ^{23}Na, ^{31}P, provides a multitude of additional information. This chapter provides an overview of the basics of MRI and the application of lung imaging with MRI.

2.2 Principle of NMR

The basics of the phenomenon of nuclear magnetic resonance and nuclear spin are based on models presented and developed in quantum physics and are described in detail in references (7-10). The most pertinent details are described as follows.

Neutrons and protons on their own have a property known as spin angular momentum. In atoms, protons and neutrons pair up with opposite spin partners in non-degenerate states. If there are an odd number of protons or neutrons the atomic nucleus has a non-zero spin angular momentum given by:

$$S = \hbar I \tag{2-1}$$

where $\hbar$ is Planck's constant, S is the spin singular momentum and I is the spin operator. For a spin ½ nuclei the Pauli matrix representation of I is expressed as:

$$I = \frac{\sigma}{2}, \sigma_x = \begin{pmatrix} 0 & 1 \\ 1 & 0 \end{pmatrix}, \sigma_y = \begin{pmatrix} 0 & -i \\ i & 0 \end{pmatrix}, \sigma_z = \begin{pmatrix} 1 & 0 \\ 0 & -1 \end{pmatrix} \tag{2-2}$$

where σ are the Pauli matrices, which shows the potential values that the spin may take in a chosen Cartesian coordinate system. The spin angular momentum results in a magnetic dipole moment given by:

$$\boldsymbol{\mu} = \gamma\boldsymbol{S} \tag{2-3}$$

where γ is the gyromagnetic ratio, which is a constant for every nuclei. The gyromagnetic ratio may be expressed as:

$$\gamma = \frac{g_n\mu_N}{\hbar} \tag{2-4}$$

where g_n is the nuclear g-factor of the particle/atomic nucleus and μ_N is the nuclear magneton. The magneton expresses the relation for the classical result for the magnetic moment of a charged particle moving in a circle with an effective angular momentum of $\hbar$, given as:

$$\mu_B = \frac{e\hbar}{2m} \tag{2-5}$$

where e is the charge (1.602×10^{-19} C for proton and electron) and m is the mass of the particle, respectively (11). In classical physics there is no analogy explaining the presence of the magnetic moment for the neutron, while in quantum mechanics the expected spin g-factor of a spin ½ point particle such as the electron may be derived as approximately 2. On the other hand, for free nucleons, the experimental spin g-factor is far from the expected value for point particles: it is 5.586 for the proton (expected value 2) and -3.826 for the neutron (expected value zero) (11). This was one of the first lines of evidence that the nucleons are not point particles, and in fact are each made up of three quarks (one up, two down for the neutron and two up, one down for proton), and adding the magnetic moments of the quarks gives rise the magnetic moment of each nucleon.

In atoms, nucleons typically pair up (neutrons with neutrons and protons with protons) and align in opposite spin states, so that only unpaired nucleons contribute to the overall angular momentum and magnetic moment. Therefore, it could be expected that magnetic quantum number, $m_I=[-\boldsymbol{I}, -\boldsymbol{I} + \boldsymbol{1}, \dots, \boldsymbol{I}]$, would only have values that are $m_I = [-\frac{1}{2}, \frac{1}{2}]$ for an unpaired neutron or proton (such as ^{1}H), or $m_I = [-1, 0, 1]$ for an atom with both an unpaired neutron and proton (such as ^{2}H). Generally, the case that the g-factor is negative or positive will come from whether the contribution to the angular momentum is from unpaired neutrons or protons, respectively.
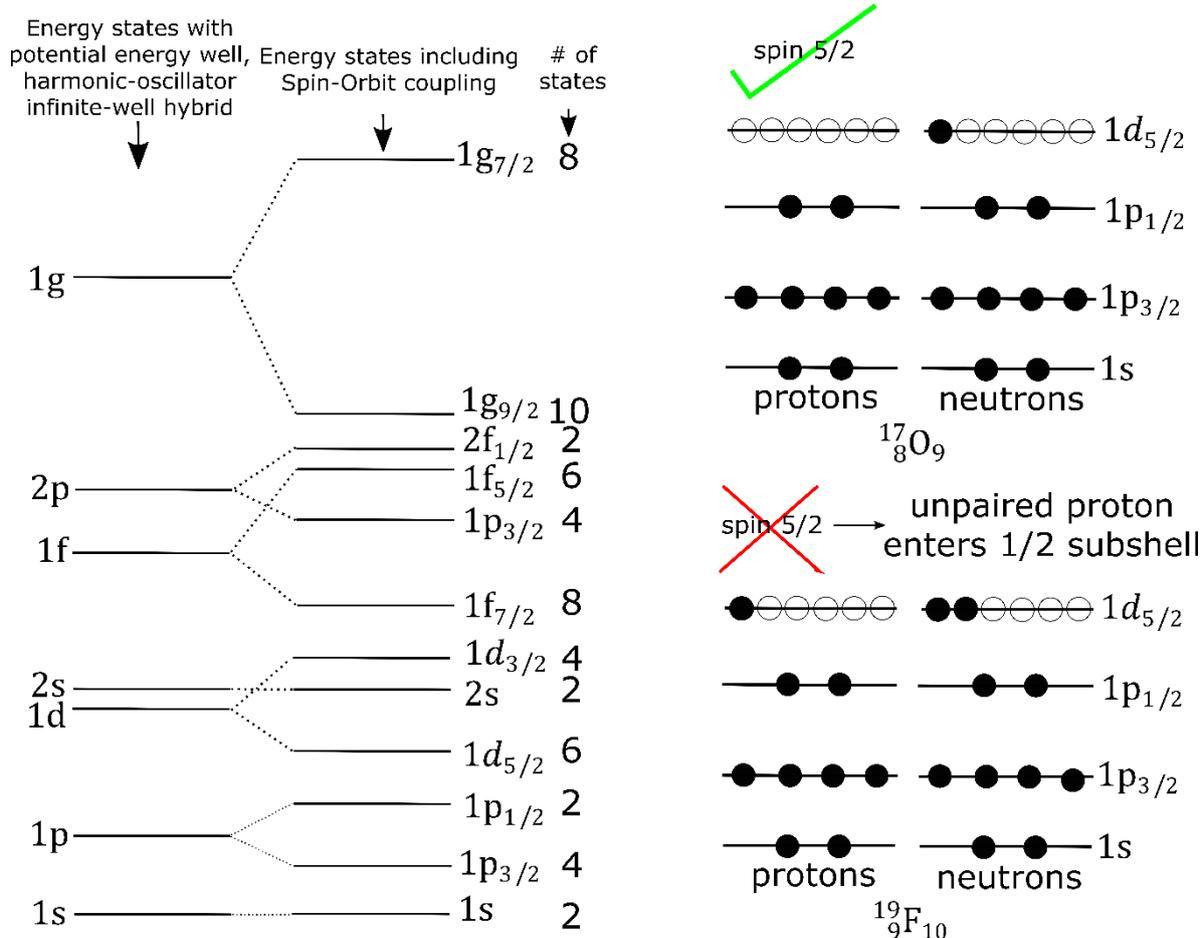
Figure 2-1: **a:** energy state diagram of "orbitals" in the nuclear shell model and **b:** example test cases for energy state filling by nucleons for ^{17}O and ^{19}F, where it is demonstrated that the model does not absolutely predict the spin states for ^{19}F.

For more complicated nuclei the internal structure of the nucleus and the interaction between nucleons must be considered. The nuclear shell model is analogous to the atomic shell model and helps to explain the presence of higher values spin states. In this model nucleons occupy independent energy states that are analogous to orbits and an associated energy difference is required to transition between states, which is generally much larger than the energy associated with collisions between nucleons in lower energy states. With inclusion of a spin-orbit potential the introduction of sub-shells predicts the presence of spin>1 nuclei, and for the majority of odd nucleon isotopes the model also predicts the correct value. However, there are many exceptions found, as based in the shell filling diagram in Figure 2-1b ^{19}F should have spin 5/2, but is in fact is spin 1/2. The difference can be somewhat accounted for by recognizing that the nucleus of ^{19}F is not spherical (12), leading to different splitting of the energy for the different sub-shells. This is the case for many other nuclei, such as many of the different isotopes of Na (13). The atomic shell model helps to explain the different g-factors of nuclei, where the predicted g-factor depends on the contribution from all the nucleons in the valence shell and

the angular momentum from both the spin and the orbital angular momentum. For the remainder of this thesis it will only be necessary to review the behaviour of spin ½ nuclei for the application of MRI. The relevant MR characteristics of common isotopes are listed in Table 2-1, demonstrating the large range of gyromagnetic ratio among common MR sensitive isotopes. MRI is most often performed using ^{1}H, because of its abundance in the human body and high gyromagnetic ratio leading to high obtainable signal relative to other nuclei. However, the other isotopes listed are also relevant and can provide information about biochemical and physiological changes that occur within the body. The focus of this thesis is imaging using inhaled inert gases, which here involves the ^{19}F, ^{129}Xe, or ^{3}He nuclei.

Table 2-1: The relative abundance and gyromagnetic ratios of common Isotopes used for in vivo MRI (14).

Isotope	Spin	Abundance (%)	Gyromagnetic ratio $\frac{\gamma}{10^7} (\frac{rad}{sT})$	Larmor Frequency at 1.5T (MHz)
^{1}H	1/2	99.9885	26.752 2128	63.9
^{3}He	1/2	0.000137	-20.380 1587	48.7
^{13}C	1/2	1.07	6.728 284	16.1
^{19}F	1/2	100	25.181 48	60.2
^{23}Na	3/2	100	7.080 8493	16.9
^{31}P	1/2	100	10.8394	25.9
^{129}Xe	1/2	26.44	-7.3997	17.7

The Zeeman effect refers to the splitting of energy levels in the presence of a static magnetic field ($\boldsymbol{B}$). The Hamiltonian describing the interaction of the magnetic moment with $\boldsymbol{B}$ is:

$$\widehat{H} = \widehat{H}_0 - \boldsymbol{\mu} \cdot \boldsymbol{B} \tag{2-6}$$

where $\widehat{H}_0$ describes the Hamiltonian of the nuclear system in the absence of Zeeman splitting due to kinetic and potential energies and $-\boldsymbol{\mu} \cdot \boldsymbol{B}$ is the spin contribution to the Hamiltonian, $\widehat{H}_{spin}$. $\widehat{H}_0$ is assumed to commute with the Hamiltonian describing the spin operators and therefore may be treated separately. It is customary to choose the coordinate system so that the static magnetic field is oriented with $\hat{\boldsymbol{z}}$, so $\boldsymbol{B} = B_0\hat{\boldsymbol{z}}.$ The potential energy of the nuclear magnetic moment is therefore described by:

$$\boldsymbol{E} = -\boldsymbol{\mu} \cdot B_0\hat{\boldsymbol{z}} = -\boldsymbol{\mu}_z B_0\hat{\boldsymbol{z}} \tag{2-7}$$

where $B_0\hat{z}$ is the static magnetic field. Since the spin operator has multiple values, as shown in equation (2-2) for a spin ½ system, this leads to non-degenerate energy states for the nuclear spin. For example, for a spin ½ nuclei like $^1H, ^{19}F, ^{129}Xe$ or ^3He, $m_z = \pm\frac{1}{2}$ and the energy difference between the parallel and anti-parallel states is given by:

$$\Delta E = \gamma\hbar B_0 \tag{2-8}$$

The Zeeman energy diagram of this energy difference is shown in Figure 2-2.
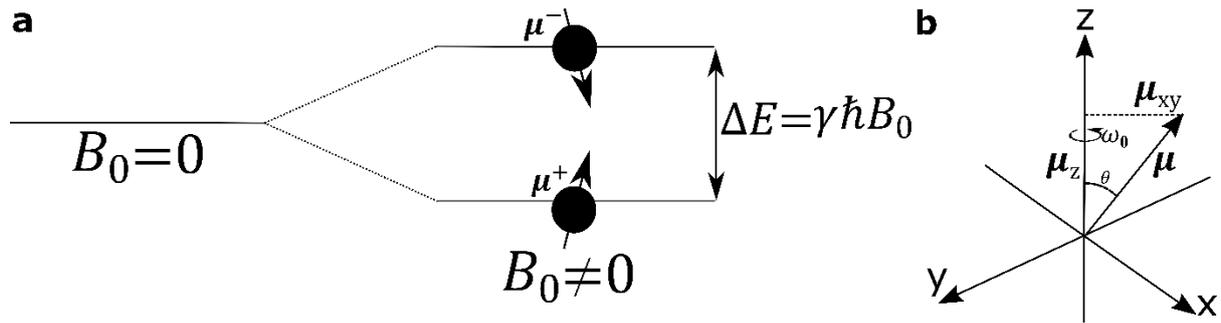
Figure 2-2: a: Zeeman energy levels for a spin ½ nucleus and b: orientation of magnetic moment of spin ½ nucleus that is parallel to the static magnetic field.

Following the principles of statistical physics this results in two populations of nuclei; those in the parallel ($n_\uparrow$) and those in the anti-parallel ($n_\downarrow$) state (15). The population ratio of the two states is given by:

$$\frac{n_\downarrow}{n_\uparrow} = e^{-\Delta E/k_bT} \tag{2-9}$$

where k_b is the Boltzmann constant and T is the temperature. The net resulting magnetization is given by:

$$M_0 = \frac{N\gamma^2\hbar^2 I(I+1)B_0}{3k_bT} \tag{2-10}$$

Since there is no energy difference for the orientation of magnetic moment in the transverse plane the angle of the magnetic moment is random, but the absolute value of the magnetic moment is given by:

$$|\boldsymbol{\mu_{xy}}| = \gamma\hbar\sqrt{I(I+1) - I^2} \tag{2-11}$$

Therefore, the orientation of the magnetic moment in the static magnetic field may be represented as in Figure 2-2b. The state of the spin system with time, $|\psi(t)\rangle$, is described by the unitary time-evolution operator (10):

$$|\psi(t)\rangle = \hat{U}(t)|\psi(0)\rangle = e^{-\frac{i\hat{H}_{spin}t}{\hbar}}|\psi(0)\rangle = e^{-\gamma I \cdot Bt}|\psi(0)\rangle \tag{2-12}$$

7

As a demonstrative example, if the system is originally in the eigenstate given by:

$$|\psi_{x+}\rangle = \frac{1}{\sqrt{2}}\begin{pmatrix}1\\1\end{pmatrix}, |\psi_{y+}\rangle = \frac{1}{\sqrt{2}}\begin{pmatrix}1\\i\end{pmatrix}, |\psi_z\rangle = \begin{pmatrix}1\\0\end{pmatrix} \tag{2-13}$$

the time progression of the state is then given by:

$$|\psi_{x+}(t)\rangle = \frac{1}{\sqrt{2}}\begin{pmatrix}e^{-i\gamma B_0 t}\\e^{i\gamma B_0 t}\end{pmatrix}, |\psi_{y+}(t)\rangle = \frac{1}{\sqrt{2}}\begin{pmatrix}e^{-i\gamma B_0 t}\\ie^{i\gamma B_0 t}\end{pmatrix}, |\psi_z(t)\rangle = \begin{pmatrix}e^{-i\gamma B_0 t}\\0\end{pmatrix} \tag{2-14}$$

The expectation values with time of the spins in this initial state are then determined by:

$$\langle \mathbf{S}\rangle = \langle\psi_{x+}|S_x|\psi_{x+}\rangle\hat{x} + \langle\psi_{y+}|S_y|\psi_{y+}\rangle\hat{y} + \langle\psi_z|S_z|\psi_z\rangle\hat{z} \tag{2-15}$$

This is expanded as:

$$\langle \mathbf{S}\rangle = \frac{\hbar}{4}[e^{i\gamma B_0 t/2} \quad e^{-i\gamma B_0 t/2}]\begin{bmatrix}0 & 1\\1 & 0\end{bmatrix}\begin{bmatrix}e^{-i\gamma B_0 t/2}\\e^{i\gamma B_0 t/2}\end{bmatrix}\hat{x} + \tag{2-16}$$

$$\frac{\hbar}{4}[e^{i\gamma B_0 t} \quad e^{-i\gamma B_0 t/2}]\begin{bmatrix}0 & -i\\i & 0\end{bmatrix}\begin{bmatrix}e^{-i\gamma B_0 t/2}\\ie^{i\gamma B_0 t/2}\end{bmatrix}\hat{y} +$$

$$\frac{\hbar}{2}[e^{i\gamma B_0 t/2} \quad 0]\begin{bmatrix}1 & 0\\0 & -1\end{bmatrix}\begin{bmatrix}e^{-i\gamma B_0 t/2}\\0\end{bmatrix}\hat{z}$$

with the result that:

$$\langle \mathbf{S}\rangle = \frac{\hbar}{4}\left(e^{i\gamma B_0 t} + e^{-i\gamma B_0 t}\right)\hat{x} + \frac{\hbar}{4i}\left(e^{i\gamma B_0 t} - e^{-i\gamma B_0 t}\right)\hat{y} + \frac{\hbar}{2}\hat{z} \tag{2-17}$$

$$= \frac{\hbar}{2}\cos(\omega_0 t)\hat{x} + \frac{\hbar}{2}\sin(\omega_0 t)\hat{y} + \frac{\hbar}{2}\hat{z}$$

so the expectation value of the spin precesses about the static magnetic field with angular frequency ω_0, designated by the Larmor frequency given by $\omega_0 = \gamma B_0$.

In the semi-classical sense, it can be stated that the rate of change in angular momentum (torque) induced by a static magnetic field is given by:

$$\frac{\partial \mathbf{J}\hbar}{\partial t} = \frac{1}{\gamma}\frac{\partial \boldsymbol{\mu}}{\partial t} = \boldsymbol{\mu} \times \mathbf{B} \tag{2-18}$$

Assuming an initial transverse magnetization, and the magnetic moment is aligned with the static field $B_0\hat{z}$, the resulting change in the magnetic moment is then given by:

$$\frac{\partial \boldsymbol{\mu}}{\partial t} = \omega_0\left(\mu_y\hat{x} - \mu_x\hat{y}\right) \tag{2-19}$$

Therefore, taking the y-axis as the imaginary component of the transverse magnetization so that $\mu_{xy}=\mu_x + i\mu_y$, the transverse component of the magnetic moment is given by:

$$\mu_{xy}(t) = e^{i\omega_0 t}\mu_{xy}(0) \tag{2-20}$$

which again represents a precession about the static magnetic field with angular frequency ω_0. It is interesting to note that the result obtained in equation (2-17) makes no explicit use of the

torque produced by a static field on a magnetic moment, but results in the same solution for the time progression of the magnetic moment vector as the semi-classical approach.

2.3 Excitation of Transverse Magnetization

In the presence of a time varying transverse magnetic field $\boldsymbol{B_1}$, with angular frequency ω, the Hamiltonian in equation (2-6) is modified to:

$$\widehat{H} = \widehat{H}_0 - \boldsymbol{\mu} \cdot (\boldsymbol{B_1} + B_0 \hat{\boldsymbol{z}}) \tag{2-21}$$

The resulting change in the expectation value of the magnetic moment vector can be most easily described in the rotating reference frame where:

$$\boldsymbol{x}' = \cos(\omega t)\,\hat{\boldsymbol{x}} - \sin(\omega t)\,\hat{\boldsymbol{y}} \tag{2-22}$$
$$\boldsymbol{y}' = \sin(\omega t)\,\hat{\boldsymbol{x}} - \cos(\omega t)\,\hat{\boldsymbol{y}}$$
$$\boldsymbol{z}' = \hat{\boldsymbol{z}}$$

In the rotating reference frame an effective ("fictitious") field $\boldsymbol{B_r}$ is produced given by $\boldsymbol{B_r} = \frac{-\omega}{\gamma}\hat{\boldsymbol{z}}$. The new modified spin Hamiltonian $\widehat{H}_{spin} = -\boldsymbol{\mu} \cdot (\boldsymbol{B_1} + B_0\hat{\boldsymbol{z}})$ in the rotating reference frame is then:

$$\widehat{H}_{spin} = -\boldsymbol{\mu} \cdot (\boldsymbol{B_1} + B_0\hat{\boldsymbol{z}} + \boldsymbol{B_r}) = -\boldsymbol{\mu} \cdot \left(\boldsymbol{B_1} + \left(B_0 - \frac{\omega}{\gamma}\right)\hat{\boldsymbol{z}}\right) \tag{2-23}$$

If $\omega=\omega_0$ the spins are at rest in the rotating reference frame and $\widehat{H}_{spin} = -\boldsymbol{\mu} \cdot \boldsymbol{B_1}$. The transverse magnetic field $\boldsymbol{B_1}$ can be decomposed into two counter-rotating components (16, 17):

$$\boldsymbol{B_1} = \boldsymbol{B_1^+} + \boldsymbol{B_1^-} \tag{2-24}$$

$$\boldsymbol{B_1^+} = \frac{(B_{1x}\cos(\omega t) + B_{1y}\sin(\omega t))/2\,\hat{\boldsymbol{x}}}{(-B_{1x}\sin(\omega t) + B_{1y}\cos(\omega t))/2\,\hat{\boldsymbol{y}}}$$

$$\boldsymbol{B_1^-} = \frac{(B_{1x}\cos(\omega t) - B_{1y}\sin(\omega t))/2\,\hat{\boldsymbol{x}}}{(B_{1x}\sin(\omega t) + B_{1y}\cos(\omega t))/2\,\hat{\boldsymbol{y}}}$$

where $\boldsymbol{B_1^+}$ and $\boldsymbol{B_1^-}$ are the right and left circularly polarized components of $\boldsymbol{B_1}$. The left circularly polarized component has an effective negative frequency of rotation, $-\boldsymbol{\omega}$, and over time does not interact with the precessing magnetization so that the spin Hamiltonian can instead be more usefully written as $\widehat{H}_{spin} = -\boldsymbol{\mu} \cdot \boldsymbol{B_1^+}$. This is already in the form given in equation (2-6), for which the evolution of the magnetic moment was solved both quantum mechanically and semi-classically. Therefore, in the rotating reference frame we can instead comfortably apply the equation for change in angular momentum presented in equation (2-18)

to the thermal equilibrium bulk magnetization. The change in the magnetization with the application of $\boldsymbol{B_1^+}$ is thus described as:

$$\frac{\partial \boldsymbol{M}}{\partial t} = \gamma \boldsymbol{M} \times \boldsymbol{B_1^+} \tag{2-25}$$

Similar to equation (2-20), the magnetization with time during the application of the $\boldsymbol{B_1^+}$ field is then given by:

$$\boldsymbol{M} = M_0(\cos(\alpha)\boldsymbol{z'} + \sin(\alpha)\boldsymbol{y'}) \tag{2-26}$$

where the flip angle, α, is:

$$\alpha = \gamma \int_0^\tau \boldsymbol{B_1^+} \, dt. \tag{2-27}$$

This demonstrates the process by which a transverse magnetization is excited, which then precesses about the direction of the static magnetic field according to equation (2-38) after the perturbing field $\boldsymbol{B_1^+}$ is removed.

2.4 Relaxation Processes

In an unperturbed and isolated system there would be no process to induce transitions between spin states, so that the expectation value of a spin system would be described effectively by the result in equation (2-17). Thus, to be able to model the relaxation processes that leads to the thermal equilibrium magnetization of equation (2-10) it is necessary to introduce a perturbation into equation (2-6). A mechanism/model of perturbation that has a strong physical basis and can been used to describe relaxation in a quantifiable way for many practical cases is the dipole-dipole interaction between magnetic moments. In the case of a system of two spins/dipoles the Hamiltonian is modified to (18):

$$\widehat{H} = \widehat{H}_0 - \boldsymbol{\mu_i} \cdot \boldsymbol{B} - \boldsymbol{\mu_j} \cdot \boldsymbol{B} + \widehat{H}' \tag{2-28}$$

$$\widehat{H}' = -\left(\frac{\hbar^2 \gamma_i \gamma_j}{|r|^3}\right)\left(3(\boldsymbol{I_i} \cdot \boldsymbol{r})(\boldsymbol{I_j} \cdot \boldsymbol{r}) - \boldsymbol{I_i} \cdot \boldsymbol{I_j}\right)$$

Using the coordinate system shown in Figure 2-3a $\widehat{H}'$ can be expanded as:

$$\widehat{H}' = \begin{bmatrix} I_{zi}I_{zj}F_0 \\ +[(I_{xi} - iI_{yi})(I_{xj} + iI_{yj}) + (I_{xi} + iI_{yi})(I_{xj} - iI_{yj})]F_0 \\ +[(I_{xi} + iI_{yi})I_{zj} + (I_{xj} + iI_{yj})I_{zi}]F_1 \\ +[(I_{xi} + iI_{yi})(I_{xj} + iI_{yj}) + (I_{xi} - iI_{yi})(I_{xj} - iI_{yj})]F_2 \end{bmatrix} \tag{2-29}$$

Where the geometric functions F_0, F_1 and F_2 are given by:

$$F_0 = k(1 - 3\cos^2\theta(t)) \tag{2-30}$$

$$F_1 = -\frac{3}{2} k \sin \theta(t) \cos \theta(t) \, e^{i\phi(t)}$$

$$F_2 = -\frac{3}{4} k \sin^2 \theta(t) \, e^{i2\phi(t)}$$

$$k = \hbar^2 \gamma_i \gamma_j / |r|^3$$

The change of spin states can therefore be seen to arise from the orientation of the dipoles fluctuating relative to each other.

The transition probabilities per unit time are denoted w_{ij} and u_{ij} for the longitudinal and transverse components of the spin, respectively. An energy state diagram is shown in Figure 2-3b showing the transitions for the longitudinal spin states. The transition probability per unit time between longitudinal states (ψ_j) is given by:

$$w_{ij} = \frac{1}{t\hbar^2} \left| \int_0^t \langle \psi_j | \hat{H}' | \psi_i \rangle \, e^{-i(E_j - E_i)t/\hbar} dt \right|^2 \tag{2-31}$$

and the transition probabilities for the transverse states can be defined similarly. As the functions in (2-28) are randomly fluctuating with time they have associated autocorrelation functions, $G_n(\tau)$, defined by:

$$G_n(\tau) = \langle F_n(t) F_n(t + \tau) \rangle \tag{2-32}$$

where the autocorrelation function has been established as having an exponential form given by:

$$G_n(\tau) = G_n(0) e^{-(t/\tau_c)} \tag{2-33}$$

Consequently, it can be seen from equation (2-29) that the transition probabilities take the form of Fourier transforms of the autocorrelation function (designated the spectral density function). For the sake of brevity only the explicit form of w_{13} is stated here as:

$$w_{13} = \frac{1}{t\hbar^2} \left| \int_0^t \frac{1}{4} G_0(t) \, e^{-i(\omega_i - \omega_j)t} dt \right|^2 = \frac{\tau_c}{8\hbar^2} \langle F_0(0)^2 \rangle \left(\frac{1}{1 + (\omega_i - \omega_j)^2 \tau_c^2} \right) \tag{2-34}$$

The additional transition probability per unit time can be found in a similar manner. With the transition probabilities established it is possible to define the rate of change of the longitudinal and transverse parts of the spin (assuming like spins with the same gyromagnetic ratios) as:

$$\frac{d(I_{iz} + I_{jz})}{dt} = -2(w_{12} + w_{13})\left(I_{iz} - I_{iz0} + I_{jz} - I_{jz0}\right) \tag{2-35}$$

$$\frac{d(I_{ix} + I_{jx})}{dt} = -2(u_{12} + u_{13})\left(I_{ix} - I_{ix0} + I_{jx} - I_{jx0}\right)$$

thus, this is a differential equation resulting in a simple exponential decay with relaxation times given by:

$$\frac{1}{T_1} = 2(w_{12} + w_{13}) = \frac{3}{10}\frac{\hbar^2\gamma^4}{b^6}\left[\frac{\tau_c}{1 + \omega^2\tau_c{}^2} + \frac{4\tau_c}{1 + 4\omega^2\tau_c{}^2}\right] \tag{2-36}$$

$$\frac{1}{T_2} = 2(u_{12} + u_{13}) = \frac{3}{20}\frac{\hbar^2\gamma^4}{b^6}\left[3\tau_c + \frac{5\tau_c}{1 + \omega^2\tau_c{}^2} + \frac{2\tau_c}{1 + 4\omega^2\tau_c{}^2}\right]$$

T_1 is the spin-lattice relaxation time and characterizes the return of the magnetization to the thermal equilibrium of its surroundings (the lattice). T_2 is the spin-spin relaxation time and characterizes the decay of the transverse magnetization by phase decoherence through interaction with local magnetic field inhomogeneity due to molecular interactions/processes, such as the dipole-dipole interaction described here. T_2 is always lower or equal to T_1 since any process that induces spin-lattice relaxation also induces spin-spin relaxation. Processes that only induces spin-spin relaxation are called secular contributions to the relaxation. The secular interactions are independent of the Larmor frequency and depend only on the correlation time (related to molecular motion), as shown for the first bracketed for $1/T_2$ in equation (2-36). This means that for solids or very viscous fluids, where correlation times are extremely long, the T_2 becomes extremely short (right of the minimum in Figure 2-3).

As water is a highly abundant in the body it provides an interesting example for evaluating the applicability of equation (2-36). If the distance between ^{1}H nuclei in the molecule is taken as 1.58×10^{-8}m then the variation of the relaxation parameters with correlation time is as shown in Figure 2-3. The correlation time of water is known to vary greatly with the viscosity (19) and for typical solutions can encompass much of the range shown. In different tissues within the human body the T_1 has a typical range of 200-4000 ms, while the T_2 has a typical range of 1-2000 ms at 1.5 T. The approximation shown in Figure 2-3 matches experiment to with an order of magnitude, but more accurate theoretical predictions require: including the effect of neighbouring molecules, the presence of dissolved gases and the potential presence of paramagnetic ions.

In the case that one of the spins has a much larger gyromagnetic ratio, such as the spin of a paramagnetic ion, there is no significant perturbation on the state of the ion's electronic spin induced by the nuclear spin. Furthermore, in such a paramagnetic solution typically the relaxation is close to the extreme narrow case (left of minimum in Figure 2-3) where $T_1 = T_2$. As such, the decay constants for the nuclear spin system are simply given by:

$$\frac{1}{T_1} = \frac{1}{T_2} = \frac{\hbar^2\gamma_{Ii}^2\gamma_{Ij}^2}{b^6}\tau_c \tag{2-37}$$

Although only the dipole-dipole relaxation was detailed explicitly there are other mechanisms that induce relaxation that are a result of fluctuating magnetic field either caused by microscopic atomic interactions, or from macroscopic variations in the field.

In gases, such as ^{129}Xe and ^{19}F, the correlation time becomes largely related to the kinetic collision time (20). For the case of inhaled ^{129}Xe gas the presence of paramagnetic oxygen becomes the determining factor for T_1/T_2, and therefore T_1/T_2 changes from hours when isolated to <20 s in the lungs. In fluorinated gases the rotational and intermolecular dipole-dipole interactions are predominant and T_1/T_2 is nearly identical and very short (<20 ms for C_3F_8). Consequently, the T_1/T_2 becomes dependent on the partial pressure, due to the direct relation with mean collision time. Therefore, the presence of oxygen has a similar effect as with ^{129}Xe of lowering the T_1/T_2, but in contrast the mechanism is by increasing the free diffusion coefficient of the gas mixture (T_1/T_2 reduced to <8 ms when C_3F_8 is mixed with >95% O_2).
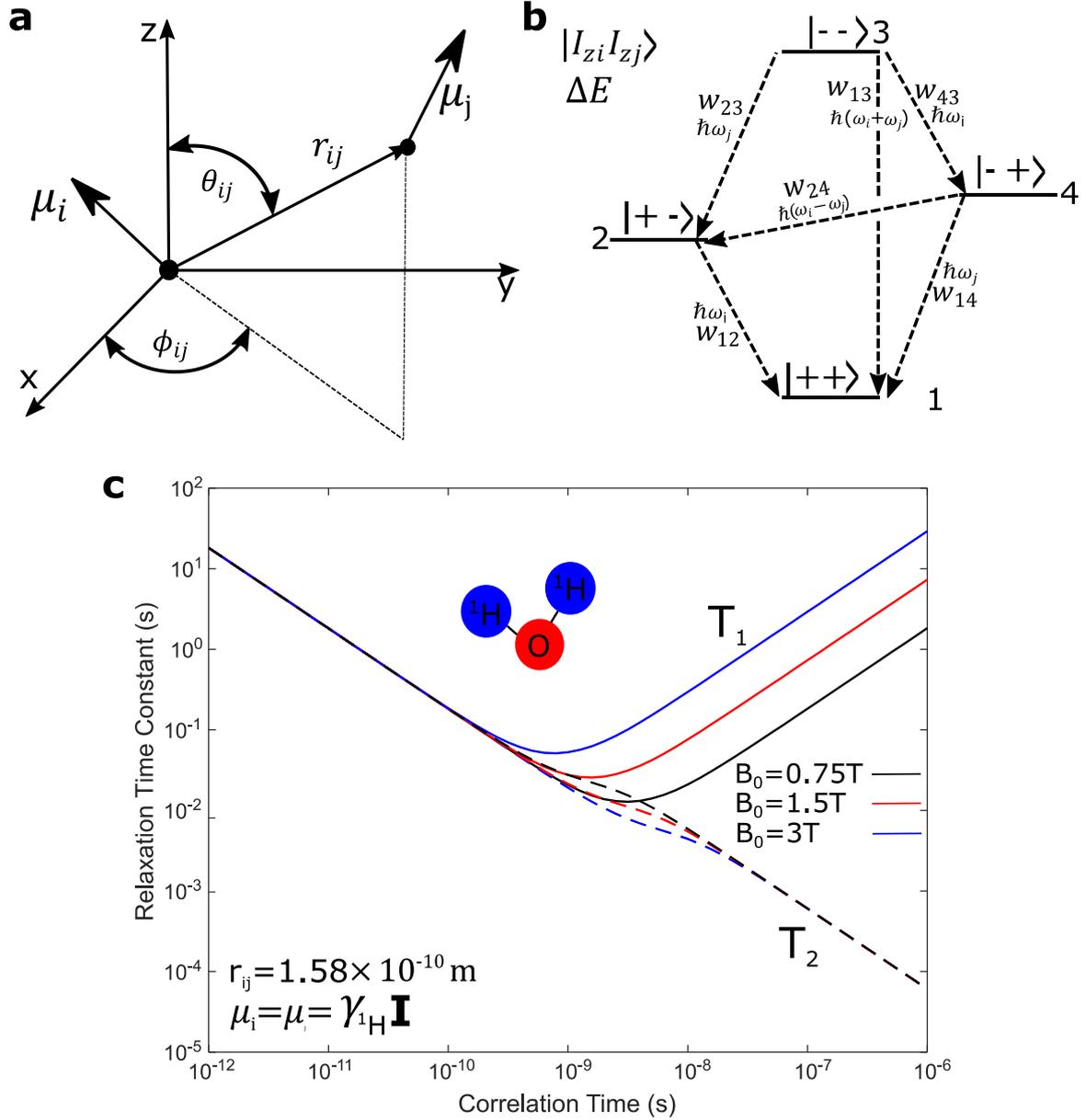
Figure 2-3: **a:** Spatial orientation diagram of dipole-dipole coupling interaction, **b**: energy state diagram for coupled dipole-dipole system and **c**: predicted relaxation times based on only intramolecular dipole-dipole coupling between ^{1}H atoms in a water molecule.

2.5 The Spin Echo and Free Induction Decay

Based on the theoretical background provided in sections 2.2-2.4 the behaviour of the magnetization during NMR can now be described effectively. In the rotating reference frame the equations of motion for the bulk magnetization are defined by the Bloch equations (8), given as:

$$\frac{\partial(\boldsymbol{M})}{\partial t} = \gamma \boldsymbol{M} \times \left(\boldsymbol{B_0} + \frac{\boldsymbol{\omega}}{\gamma} + \boldsymbol{B_1^+} \right) - \frac{\boldsymbol{M_{xy}}}{T_2} - \frac{M_z(t) - M_0}{T_1}\hat{\boldsymbol{z}} \qquad (2\text{-}38)$$

where M_{xy} is the transverse component of the magnetization and M_z is the longitudinal component of the magnetization. Inhomogeneity in the static magnetic field reduces the T_2 to the effective time constant T_2^*, given by:

$$\frac{1}{T_2^*} = \frac{1}{T_2} + \frac{1}{T_2'} \tag{2-39}$$

where T_2' depends on factors such as magnet design and regions of high variation in tissue susceptibility.
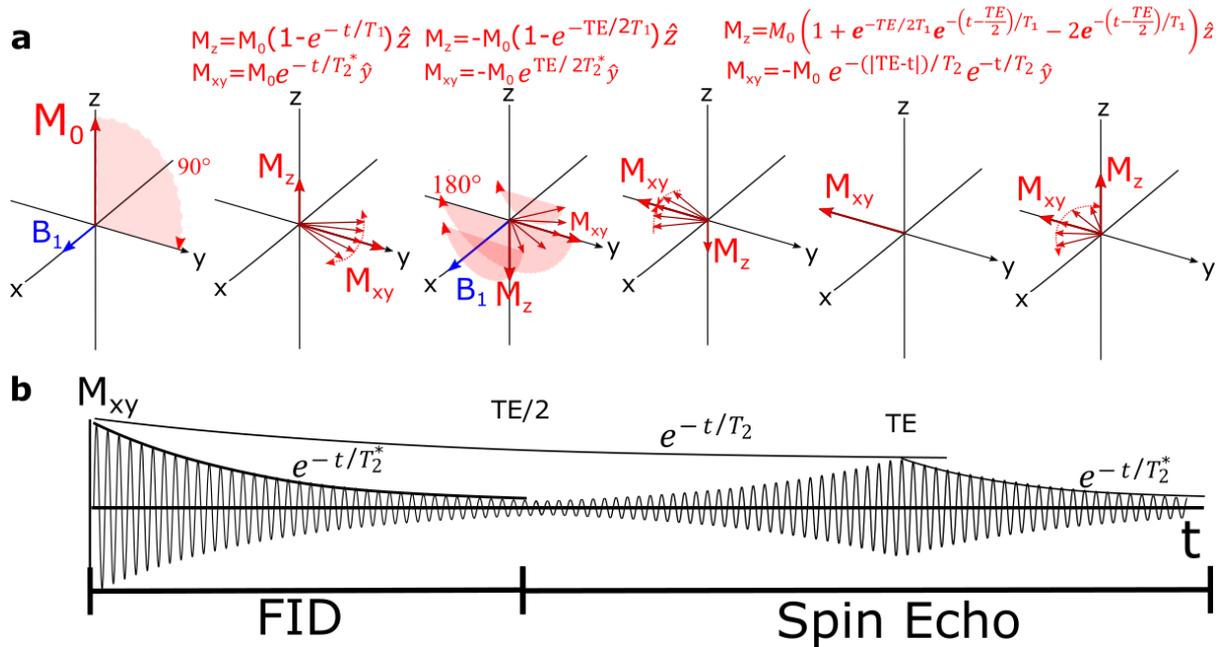
Figure 2-4: **a:** Spin diagrams demonstrating the state of the magnetization during the FID/Spin-echo NMR sequence in the rotating reference frame. As an illustration, the transverse magnetization is split into multiple vectors representing groups of spins with greater and lower frequencies of precessional rotation that contribute to phase decoherence resulting in the decay of the transverse magnetization. **b:** An illustration of the time dependence of the transverse magnetization during the spin-echo.

According to the defined equations of motion the behaviour of the bulk magnetization in a typical NMR spin-echo experiment is shown in Figure 2-4. In this example, following a brief application of the $\boldsymbol{B_1^+}$ RF field (an RF pulse) the bulk magnetization is tipped in to the transverse plane by a 90° angle, as described by equation (2-27), and the transverse magnetization decays according to:

$$\boldsymbol{M_{xy}} = M_0 e^{-t/T_2^*} \boldsymbol{y'} \tag{2-40}$$

After a time *TE/2* a 180° RF pulse is applied. As demonstrated in Figure 2-4, spins that are precessing at slower/faster rate than the central Larmor frequency due to ΔB_0 begin to return to phase coherence, and the transverse magnetization is described by:

$$\boldsymbol{M_{xy}} = -M_0 e^{-|TE-t|/T_2^*} e^{-t/T_2} \boldsymbol{y'} \tag{2-41}$$

Thus an echo is formed at $t = TE$ and the magnetization at this time point is dependent on the decay constant T_2 (any decay due to ΔB_0 is reversed after the application of the $180°$ pulse). During this time the longitudinal magnetization has also been returning to its thermal equilibrium according to the relaxation time constant T_1 according to:

$$M_z = \begin{array}{l} M_0\left(1 - e^{-t/T_1}\right)\hat{z}, 0 < t < TE/2 \\ M_0\left(1 + e^{-TE/2T_1}e^{-\left(t-\frac{TE}{2}\right)/T_1} - 2e^{-\left(t-\frac{TE}{2}\right)/T_1}\right)\hat{z}, \frac{TE}{2} < t \end{array} \tag{2-42}$$

The example of the spin-echo reveals the basic time-evolution of the magnetization vectors in NMR, assuming short RF pulses relative to the relaxation and a homogeneous sample. In practice, the finite length the RF pulse and spatial dependence of the parameters can be included with more comprehensive simulation with equation (2-38).

2.6 Receive Signal

From the principle of reciprocity, the open-circuit voltage induced on a coil (or any analogous electromagnetically reactive detecting device) by a time varying magnetic field is directly proportional to the magnetic field produced by the coil, $\widehat{\boldsymbol{B}}_r$, where the 'hat' symbol indicates that it is the field produced per-unit-current. The induced voltage is given by (21):

$$V(t) = -\frac{\partial}{\partial t}\int \widehat{\boldsymbol{B}}_r \cdot \boldsymbol{M}(\boldsymbol{r}, t)dr \tag{2-43}$$

It can be shown that only the left circularly polarized component of the magnetic field is sensitive to the MR signal, so the resulting induced voltage is more accurately given as (8, 22):

$$V(t) = e^{\frac{i\pi}{2}}\int \omega(\boldsymbol{r})\widehat{\boldsymbol{B}}_1^- \boldsymbol{M}_{xy}(\boldsymbol{r}, t)e^{-i\omega(\boldsymbol{r})t}dr \tag{2-44}$$

By mixing the resulting time domain voltage waveform with the carrier signal $\boldsymbol{e}^{i\omega(\boldsymbol{r})t}$ the resulting signal equation is:

$$S(t) = e^{\frac{i\pi}{2}}\int \omega(\boldsymbol{r})\widehat{\boldsymbol{B}}_1^- \boldsymbol{M}_{xy}(\boldsymbol{r}, t)dr \tag{2-45}$$

2.7 Spatial Encoding of the Signal

The use of gradient magnetic fields to encode image information was one of the most fundamental technological advances in the formation of the field of MRI. For image formation, linear variations in the static magnetic field, $\boldsymbol{B}_0$, are introduced by three different gradient coils. The full imaging system is shown in Figure 2-5a, with a diagram of the windings of a gradient coil in Figure 2-5b. Gradients create a linear variation in the precession frequency which cause

a change in the phase and frequency encoding information in the spatial-frequency domain, which is quantified with:

$$k(t) = -\frac{\gamma}{2\pi} \int_0^t G_r \, d\tau \tag{2-46}$$

where G_r is the gradient vector applied, in units of T/m, and $k(t)$ represents the position in "k-space".

Assuming that the gradients applied are the only modifying term to the precession frequency in a volume, $\omega(r) = k(t) \cdot r$, the application of the gradients modifies the signal voltage in equation (2-45) to:

$$S(t) = e^{\frac{i\pi}{2}} \omega_0 \int \widehat{B}_1^- M_{xy}(r, t) e^{-i2\pi k(t) \cdot r} dr \tag{2-47}$$

Obtaining an image from the acquired time domain signal requires performing the inverse Fourier transform, resulting in:

$$\omega_0 \widehat{B}_1^- M_{xy}(r, t) = e^{\frac{-i\pi}{2}} \int S(t) \, e^{i2\pi k(t) \cdot r} dk \tag{2-48}$$

This shows that the image obtained in MRI is in fact a spatial measurement of the factor $\omega_0 \widehat{B}_1^- M_{xy}(r, t)$. In practice data is acquired at discrete time points and the integral is replaced with the discrete Fourier transform. The resulting image is explicitly dependent on the receive sensitivity $\widehat{B}_1^-$, while $M_{xy}(r, t)$ has a spatial and time dependence that depends on the relaxation parameters (2-38) and applied RF magnetic fields $B_1^+(r, t)$.
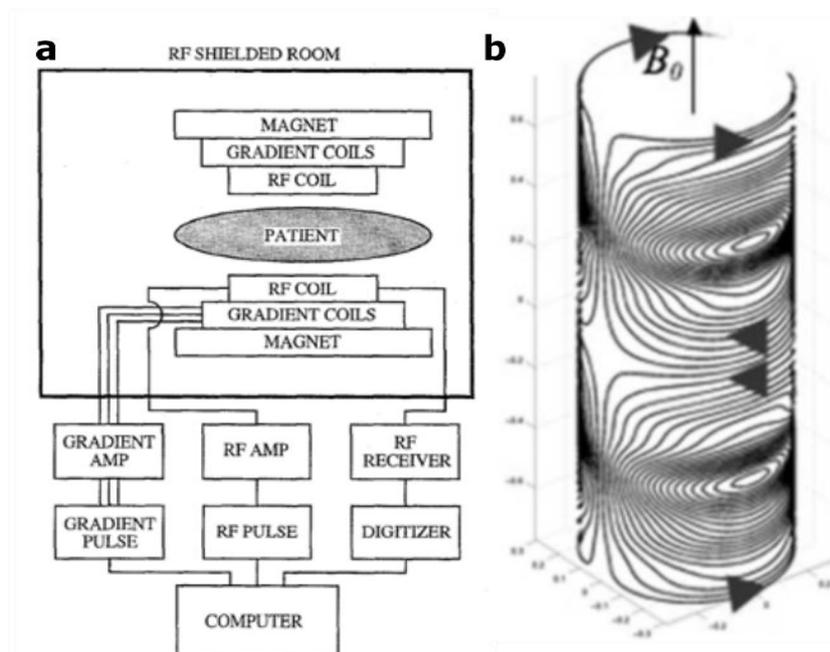
Figure 2-5 a: MRI system diagram (reproduced with permission from (23)) © 1998 IEEE and b: schematic of the windings for a G_y gradient coil (reproduced with permission from (24)).

2.8 Imaging Sequences and Methods

2.8.1 2D and 3D Imaging

In 2D imaging the $\boldsymbol{B_1^+}$ RF pulse is applied with frequency ω_0, while $\boldsymbol{G_r}$ is applied perpendicular to the slice direction during the RF pulse (timings shown in Figure 2-6a). The RF pulse amplitude is modified with a carrier function $sinc(2\pi BW_{RF}t)$ so that a resulting slab is excited with thickness Δs equal to:

$$\Delta s = \frac{2\pi BW_{RF}}{\gamma G_r} \tag{2-49}$$

In practice, the RF pulse shape is different than a *sinc* pulse since it must be limited in duration and the pulse waveform is designed for minimal duration, while maximizing selectivity and linearity (25). This same slab is excited for each variation of the phase encoding direction, while the gradient in the frequency encoding/readout direction is applied each time to obtain lines of k-space in a Cartesian sampling pattern. In 3D imaging a homogeneous excitation pulse without applied gradient may be employed, with phase encoding also applied in what constitutes the slice selection direction of 2D imaging. For 2D imaging a 2D Fourier transform is applied on the k-space data acquired for each slice/slab, while for 3D imaging a 3D Fourier transform is applied to the acquired k-space data.
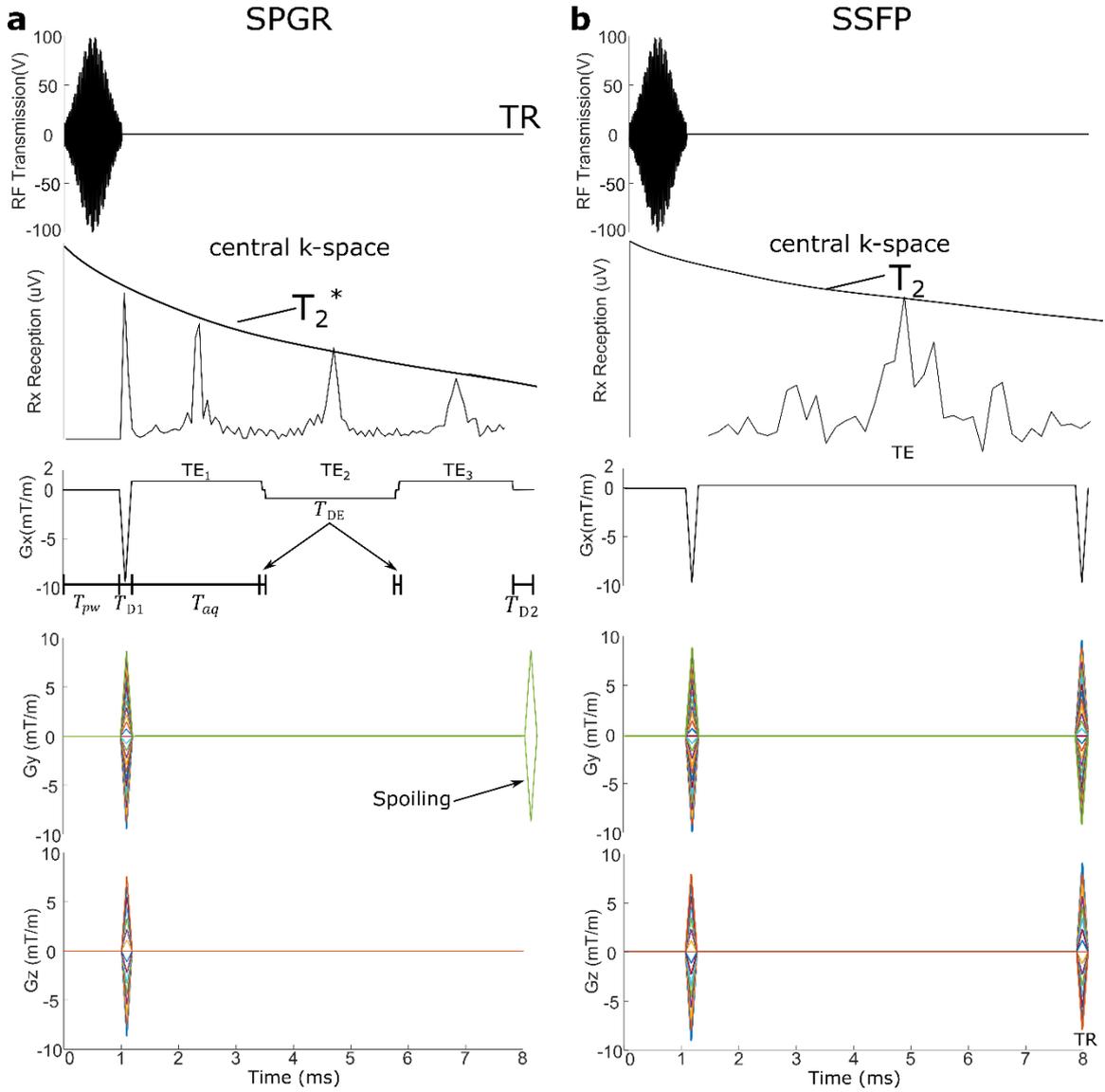
Figure 2-6: Imaging sequence diagrams for gradient echo imaging included the a: spoiled gradient echo sequence (with three gradient recalled echoes) and b: balanced steady-state free precession sequence

2.8.2 Spoiled Gradient Echo

In the sequence shown in Figure 2-6a a spoiling gradient is applied after every readout gradient that de-phases the transverse magnetization and spoils the precessing signal. In addition, phase shifts can be applied to each RF pulse to prevent refocussing of any residual transverse magnetization. The resulting steady state transverse magnetization at time $t=TE$ (at the centre of k-space) in this sequence therefore is T_2 independent, relying on T_1 and the T_2^* decay after each excitation, and is given by (26-28):

$$M_{xy}(r, TE) = M_0 \frac{e^{-\frac{TE}{T_2^*}}\left(1 - e^{-\frac{TR}{T_1}}\right)\sin(\alpha)}{1 - e^{-\frac{TR}{T_1}}\cos\alpha} \tag{2-50}$$

19

Using the Ernst angle, $\alpha = \cos^{-1}(e^{-\frac{TR}{T_1}})$, that maximizes the steady state magnetization (29), the steady state magnetization is given by:

$$\boldsymbol{M_{xy}}(\boldsymbol{r}, TE) = M_0 \frac{e^{-TE/T_2^*}(1 - e^{-TR/T_1})}{\sqrt{1 - e^{-2TR/T_1}}} \tag{2-51}$$

Though not explicitly stated, the parameters T_1, T_2^* and M_0 are spatially dependent.

The resulting image SNR is related to the transverse magnetization by (28):

$$SNR \; \alpha \; \frac{M_{xy}}{M_0} \Delta V \sqrt{\frac{N_{avg}}{BW}} = \frac{M_{xy}}{M_0} \Delta V \sqrt{\frac{T_s}{N_p}} \sqrt{\frac{T_{aq}}{TR}} \tag{2-52}$$

where BW is the bandwidth per-pixel, N_{avg} is the number of averages, ΔV is the voxel size, N_p is the number of phase-encode steps, T_{aq} is the readout gradient acquisition time ($1/BW$) and T_s is the total imaging time. The factor T_{aq}/TR represents the efficiency of the sequence in terms of maximizing the fraction of the TR devoted to sampling the signal. The expected optimal T_{aq} with SPGR is close to $T_{aq} \approx T_2^*$ (305).

Imaging timing parameters that impact upon TE and T_{aq} include the following: the RF pulse width (T_{pw}) and imaging gradient encoding/refocusing delays before (T_{D1}) and after (T_{D2}) frequency encoding. Therefore, TE$=\frac{T_{pw}}{2} + T_{D1} + \frac{T_{aq}}{2}$ and $T_{aq} = TR - T_{pw} - T_{D1} - T_{D2}$. These variables are labelled in Figure 2-6.

Images reconstructed from multiple echoes may be combined by the sum of squares of each of each individual echo, so that the image SNR is given by:

$$SNR \propto \frac{(1 - e^{-TR/T_1})}{\sqrt{1 - e^{-2TR/T_1}}} \sqrt{T_{aq}} e^{-T_{D1}/T_2^*} \sqrt{\sum_{n=0:(m-1)} e^{-(2n(T_{aq}+T_{DE})-T_{aq})/T_2^*}} \tag{2-53}$$

where T_{DE} is the delay between readout of multiple echos. For a rapid 3D SPGR imaging sequence and for most tissues for ^{1}H imaging, $TR \ll T_1$, so $\frac{(1-e^{-TR/T_1})}{\sqrt{1-e^{-2TR/T_1}}} = 1$.

2.8.3 Steady State Free Precession

The balanced steady state free precession (b-SSFP) sequence shown in Figure 2-6 uses additional gradients that wind back the dephasing caused during phase and frequency encoding each k-space acquisition repetition. This results in a steady state magnetization that depends on the propagation of transverse coherence from the previous excitations. The derivation of the transverse magnetization during each pulse is detailed in reference (30) as follows.

During each TR, the nutation of the magnetization caused by the RF pulse is given by:

$$R_\alpha = \begin{bmatrix} 1 & 0 & 0 \\ 0 & \cos\alpha & \sin\alpha \\ 0 & -\sin\alpha & \cos\alpha \end{bmatrix}$$

(2-54)

while the free precession over a time τ is given by:

$$P(\tau) = \begin{bmatrix} \cos(2\pi\Delta f\tau) & \sin(2\pi\Delta f\tau) & 0 \\ -\sin(2\pi\Delta f\tau) & \cos(2\pi\Delta f\tau) & 0 \\ 0 & 0 & 1 \end{bmatrix}$$

(2-55)

where Δf is the off-resonance frequency (the difference between RF excitation frequency and transverse magnetization precession frequency). If the relaxation matrix is given by:

$$C(\tau) = \begin{bmatrix} e^{\frac{-\tau}{T_2}} & 0 & 0 \\ 0 & e^{\frac{-\tau}{T_2}} & 0 \\ 0 & 0 & e^{\frac{-\tau}{T_1}} \end{bmatrix}$$

(2-56)

then the relaxation over the time τ due to T_2 and T_1 is given by:

$$D(\tau) = (I - C(\tau)) \begin{bmatrix} 0 \\ 0 \\ M_0 \end{bmatrix}$$

(2-57)

So the resulting magnetization after each RF pulse (at time TE) is related to the magnetization after the previous RF excitation by:

$$M(r, t + \tau) = P(TE)C(TE)R_\alpha P(TR - TE)C(TR - TE)M(r, t)$$
$$+ P(TE)C(TE)R_\alpha D(TR - TE) + D(TE)$$

(2-58)

Dependence on $T_2{}^*$ does not appear explicitly in this equations, which is a reasonable approximation as it is expected that the transverse magnetization will refocus at time *TE~TR/2* (31). However, similar to the spin-echo sequence it is expected that from this time-point there is an additional $T_2{}^*$ component that causes signal decay away from the centre.

Equation (2-58) describes the transient behaviour of the SSFP sequence, while the steady-state magnetization of the SSFP sequence can be shown to be (32):

$$M_{xy}(r) = M_0 \frac{\sqrt{e^{-\frac{TR}{T_2}}\left(1 - e^{-\frac{TR}{T_1}}\right)}\sin(\alpha)}{1 - \left(e^{-\frac{TR}{T_1}} - e^{-\frac{TR}{T_2}}\right)\cos\alpha - e^{-\frac{TR}{T_2}}e^{-\frac{TR}{T_1}}}$$

(2-59)

However, this equation is only valid for the case that the RF pulse is on-resonance (alternating by 180° each pulse). The effects of off-resonance excitation frequency is shown in Figure 2-6. The SSFP sequence can result in higher signal than SPGR, and allow signal to be weighted by T_2 and T_1 rather than $T_2{}^*$, but off-resonance artefacts, like the banding in Figure

2-6, are prevalent. In addition to inhomogeneities in B_0 resulting in banding, inhomogeneities in FA can result in similar nulls.
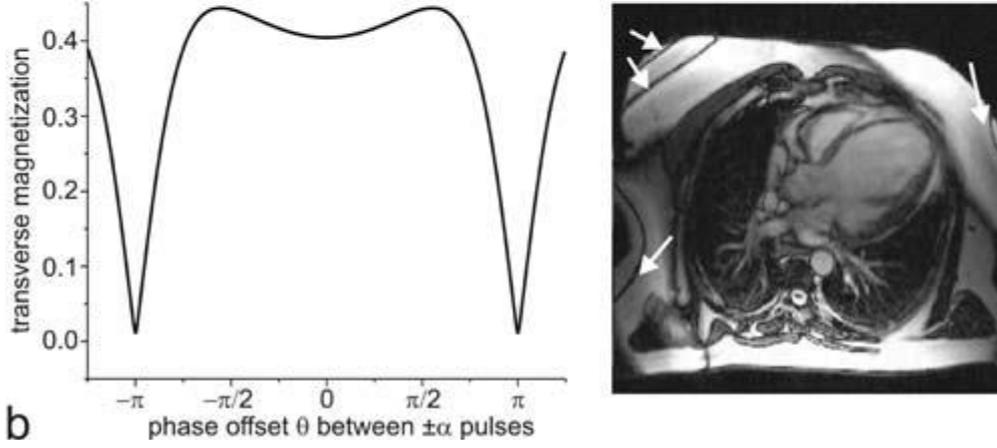
Figure 2-7: Steady state magnetization as a function of RF offset between pulses and image including banding artifacts as a result of regions with offset center frequencies (reproduced with permission from reference (32))

2.8.4 Signal in Hyperpolarized Gas Imaging

The natural thermodynamic (Boltzmann) equilibrium longitudinal magnetization density of TP nuclei is given by equation (2-10) (15). However, HP gases have an artificially enhanced magnetization density of (132):

$$M_i = NP \frac{\gamma \hbar}{2} \tag{2-60}$$

here M_i is the initial longitudinal magnetization of the HP sample at the start of imaging, P is the polarization percent (typically 10-40%) and N is the density. The signal dynamics of HP MRI differs from conventional TP MRI since the non-renewable longitudinal magnetization is depleted with the application of RF excitations and due to T_1 decay as the longitudinal magnetization returns to its TP equilibrium. For SPGR imaging, instead of equation (2-50), the dynamics of HP magnetization are described by (33)

$$\boldsymbol{M_{xy}}(\boldsymbol{r}, n, TE) = M_i e^{-\frac{TE}{T_2^*}} e^{-\frac{(n-1)TR}{T_1}} \sin(\alpha) \cos(\alpha)^{n-1}. \tag{2-61}$$

The signal strength is mainly determined by the magnitude of signal at the centre of k-space. Therefore, for typical sequential Cartesian sampling, the angle that maximizes the signal at the centre of k-space (α_{opt}) is given by

$$\alpha_{opt} = \tan^{-1}(\frac{1}{\sqrt{N_p/2 - 1}}) \tag{2-62}$$

22

where N_p is the number of phase encodes (equivalent to the number of RF pulses). Contrary to acquiring k-space in a sequential manner, acquiring the central k-space lines first will result in the highest signal, but result in blurring of the image (discussed in section 2.8.6). In this case equation (2-51) may still be applied as an approximation of the optimal FA.

For SSFP imaging with HP the non-renewable longitudinal magnetization also results in different signal dynamics then in TP imaging (34). Thus, equations (2-54)-(2-58) are modified such that there is an initial starting magnetization $M_z(\boldsymbol{r}, 0) = M_i$ that is much greater than the thermal equilibrium magnetization M_0. Consequently, the $\boldsymbol{P}(TE)\boldsymbol{C}(TE)\boldsymbol{R}_\alpha\boldsymbol{D}(TR - TE) + \boldsymbol{D}(TE)$ terms can typically be neglected as $M_i \gg M_0$.

For ^{129}Xe HP gas imaging it has been shown that, in the optimal case, the longitudinal magnetization at the centre of k-space $(M_z(\boldsymbol{r}, N_pTR/2))$ will be approximately 50% of M_i, with a FA~10°, such that $M_{xy}(\boldsymbol{r}, N_pTR/2)\sim0.5M_i\sin(10°)$(35). Thus a factor 2-4 improvement in SNR is expected compared to SPGR imaging with comparable optimized imaging parameters (36). However, this case cannot be generalized for all HP imaging since the results is highly dependent on the particular relaxation parameters of ^{129}Xe in-vivo.

2.8.5 Diffusion Weighted Imaging

One parameter that is typically measured by MRI to characterize lung function is the apparent diffusion coefficient (ADC), which is a measure of the magnitude of diffusion. There are a number of different sequences that can be used to measure diffusion, such as the diffusion weighted spin echo sequence (37). The most relevant sequence for measuring the ADC in the study of inert gas MRI, as presented in this thesis, is shown in Figure 2-8, where the diffusion is measured in the $\hat{y}$ direction. The ADC is measured by applying opposite polarity gradients in succession during imaging and relating the effect of restricted diffusion due to the lungs on the expected loss of signal due to dephasing from the gradients with and without free movement of the molecules (38) as will be detailed further in section 2.10.2.
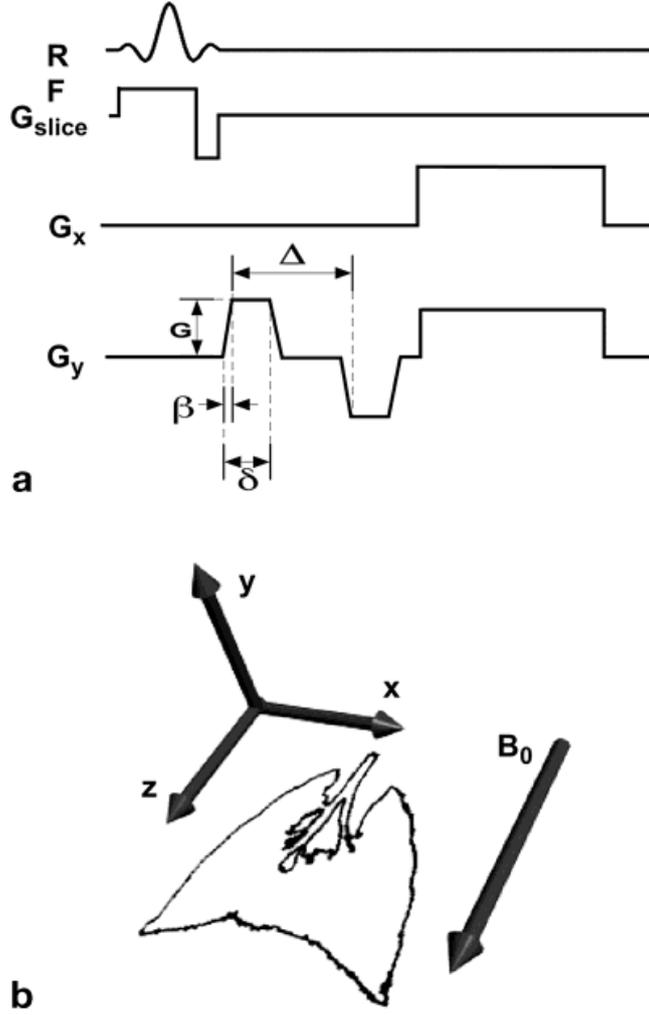
Figure 2-8: A typical sequence used for ADC measurement. (reproduced with permission from (39))

2.8.6 K-space Filtering and Point Spread Function

Although the steady state signal for SPGR and b-SSFP may be described effectively by equation (2-50) and equation (2-59), k-space filtering due to transient behaviour during a sequence, and the transverse magnetization decay during the gradient echo, are additional factors affecting image formation. The impact of k-space filtering may be characterized by the point-spread function (40, 41). If the ideal image is taken from equation (2-48) to be directly proportional to $M_{xy}(r, TE)$, then the filtered image, I_{filt}, is given by:

$$I_{filt} \propto M_{xy}(r, TE) \otimes PSF(r) \tag{2-63}$$

where $PSF(r)$ is the point spread function. Since data in MRI is acquired in the k-space domain the optical transfer function $OTF(k) = \mathcal{F}(PSF(r))$ may be used to describes the k-space filtering according to:

$$\mathcal{F}(I_{filt}) \propto \mathcal{F}\left(M_{xy}(r, TE)\right) OTF(k) \tag{2-64}$$

where $\mathcal{F}$ is the Fourier transform operator. In the case of filtering along the readout direction (typically designated k_x filtering) the decay of transverse magnetization (T$_2$* decay) results in an altered point spread function leading to blurring. For gradient echo imaging, filtering in the phase encoding directions occurs partially due to the transient oscillation in the magnetization prior to reaching the steady state condition. Figure 2-9a shows the expected signal decay curves for k_y and k_x points acquired in a 2D SPGR sequence assuming a Cartesian sampling pattern and uniform relaxation parameters as labelled in the figure. In reality, the tissue parameters vary significantly between tissues and the decay will affect the resolution of different tissues separately. However, as a demonstrative example the affect these decay curves would have on a hypothetical 2D brain image with all tissues having the same relaxation parameters is shown in Figure 2-9b.
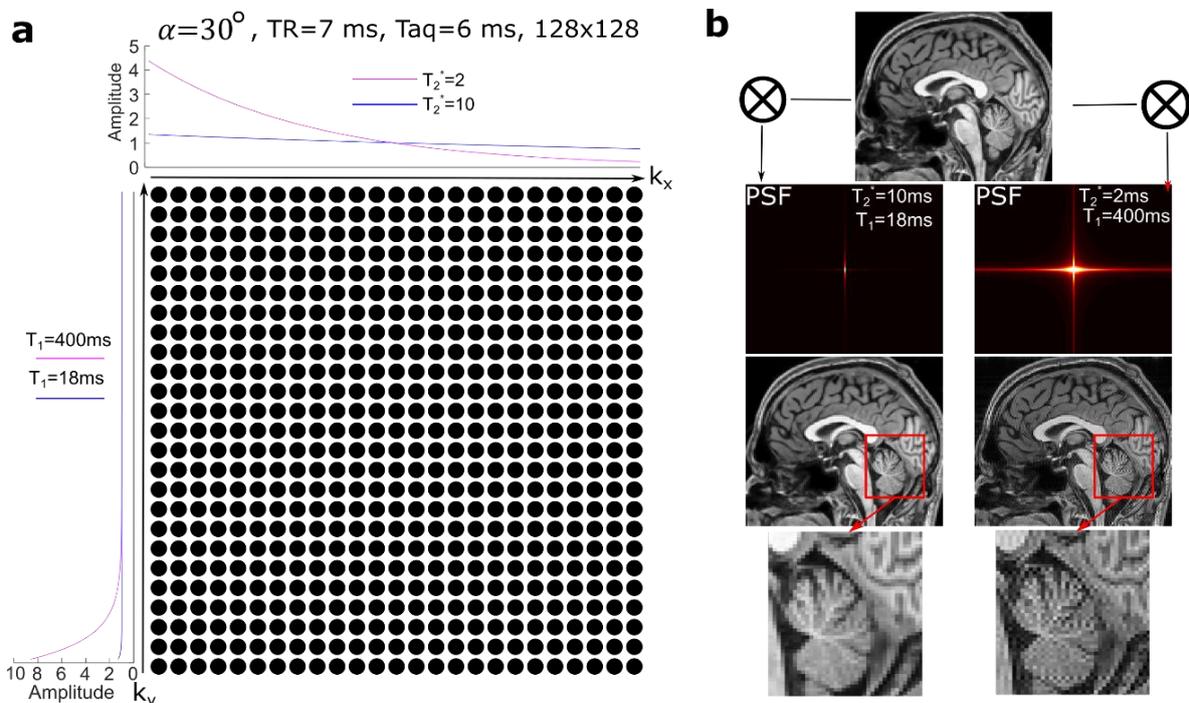
Figure 2-9: **a:** k_x and k_y filtering curves for a 2D SPGR sequence with given sequence parameters and MR relaxation parameters and **b:** corresponding PSFs and resulting filtered images given an ideal 2D brain image.

2.8.7 Compressed Sensing and Parallel Imaging

To perform the discrete Fourier transform required by equation (2-48) for image formation full Nyquist sampling of k-space is required. This places a fundamental limit on the acquisition time possible in MRI. Compressed sensing and parallel imaging are related methods of undersampling k-space, whilst obtaining an artefact free image resulting in reduced acquisition time. The acceleration factor (AF) is the ratio of sampled points to the amount required for full

Nyquist sampling, and characterizes the degree of undersampling. Parallel imaging generally uses the additional information provided by the different sensitivity profiles of the coil elements in receive arrays. Two classes of parallel imaging methods exist: image domain based methods like sensitivity encoding (SENSE) (42) and k-space based methods like SiMultaneous Acquisition of Spatial Harmonics (SMASH) (43). Both these methods involve skipping phase-encoding lines of k-space as shown in Figure 2-10, which results in the folding-in of the image domain data, but the methods of recovering the fully sampled image are different.
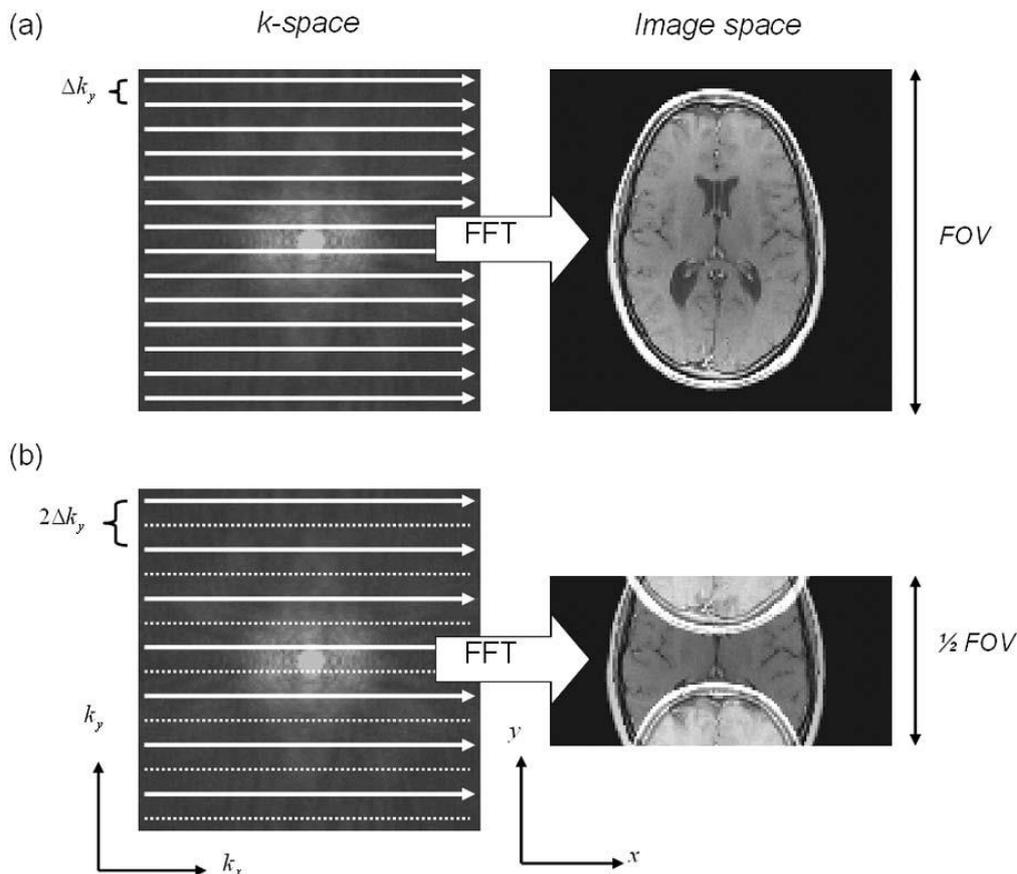
Figure 2-10: Demonstration of parallel imaging where compared to a: fully sampled k-space and resulting image b: skipping k-space lines results in a folded-in image (image reproduced with permission from (44)). Parallel imaging involves the reconstruction of the unfolded image with the partially sample k-space.

In SENSE (42) the fully sampled image is reconstructed for a set of superimposed pixels of number n_ρ less than the number of separate receive channels n_I. For each pixel in the folded-in image (ex. location of folded-in pixel I_{1-4} in Figure 2-11) the complex coil sensitivities at each of the unfolded fully sampled image pixel positions (ex. ρ_{1-4} in Figure 2-11) are contained in the $n_I \times n_\rho$ coil sensitivity matrix, $\boldsymbol{C}$:

$$\boldsymbol{C}_{I,\rho} = s_I(\boldsymbol{r}_\rho) \tag{2-65}$$

With the sensitivity matrix, the unfolding matrix is calculated as:

$$U = (C^{\mathcal{H}}\Psi^{-1}C)C^{\mathcal{H}}\Psi^{-1} \qquad (2\text{-}66)$$

and for each folded in pixel the vector containing values from the multiple elements, I, is used to reconstructed the unfolded pixel values with:

$$\rho = UI \qquad (2\text{-}67)$$

The elements of the noise covariance matrix, Ψ, are found as

$$\Psi_{ij} = \frac{1}{2N}\sum_{k=1}^{N} n_{ik}\, n_{jk}^{*} \qquad (2\text{-}68)$$

where N is the number of sampled points of a reconstructed fully sampled noise image (image acquired without RF excitation) used to determine the noise statistics and n_{ik} and n_{jk} are the measurements by receiver i and j, respectively, for point k.

The SNR using SENSE is given by:

$$SNR_{recon} = \frac{SNR_{full}}{g\sqrt{R}} \qquad (2\text{-}69)$$

where the g-factor g represents the loss in SNR due to the inability of the coil sensitivity profiles to fully encode the missing information due to undersampling and is given by:

$$g = \sqrt{(C^{\mathcal{H}}\Psi^{-1}C)^{-1}{}_{\rho,\rho}(C^{\mathcal{H}}\Psi^{-1}C)_{\rho,\rho}} \qquad (2\text{-}70)$$
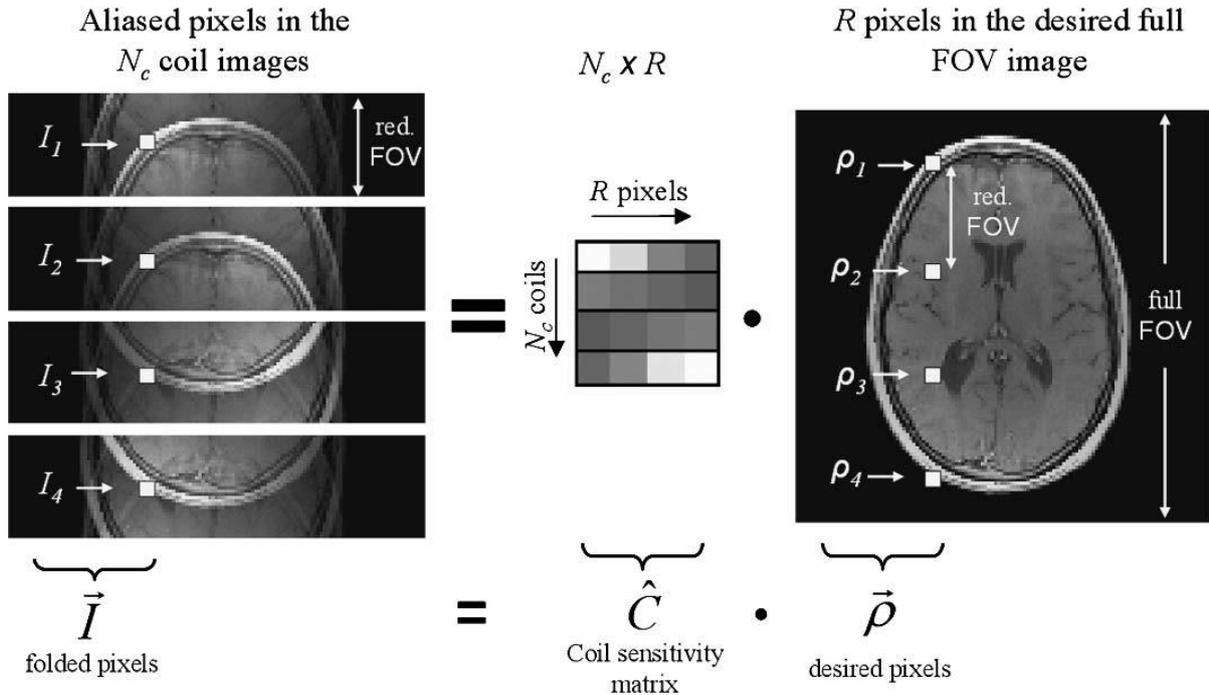
Figure 2-11: Illustration of the basic SENSE relation using(Figure reproduced with permission from (44)).

Generalized Autocalibrating Partially Parallel Acquisition (GRAPPA) (45) is a similar but generally more robust method than SMASH where missing/unsampled points in k-space are obtained by weighting surrounding sampled k-space points according to (46):

$$S_j(k_x, k_y + m\Delta k_y) \tag{2-71}$$

$$= \sum_{l=1}^{N} \sum_{a=-a_{max}}^{a_{max}} \sum_{b=-b_{max}}^{b_{max}} n(j,a,b,l,m) S_l(k_x + a\Delta k_x, k_y + (br+1)\Delta k_y)$$

where S_j is the k-space measurement for coil j, **N** is the number of coils and the values of a_{max} and b_{max} determine the number of k-space point in the k_x and k_y direction used for the interpolation. The weighting parameters $n(j,a,b,l,m)$ are calculated from the central k-space lines acquired for calibration, where S_j is a vector containing the target k-space points to be reconstructed and S_l is a vector containing the surrounding known/measured k-space points. Similar to SENSE, GRAPPA also has an associated g-factor, (47) which is similar in pattern when calculated for equivalent coil geometries and images, but is also typically larger. However, GRAPPA is a self-calibrating method that does not require acquisition of an additional sensitivity map, that may be mismatched in position or of insufficient quality to perform accurate SENSE reconstruction.
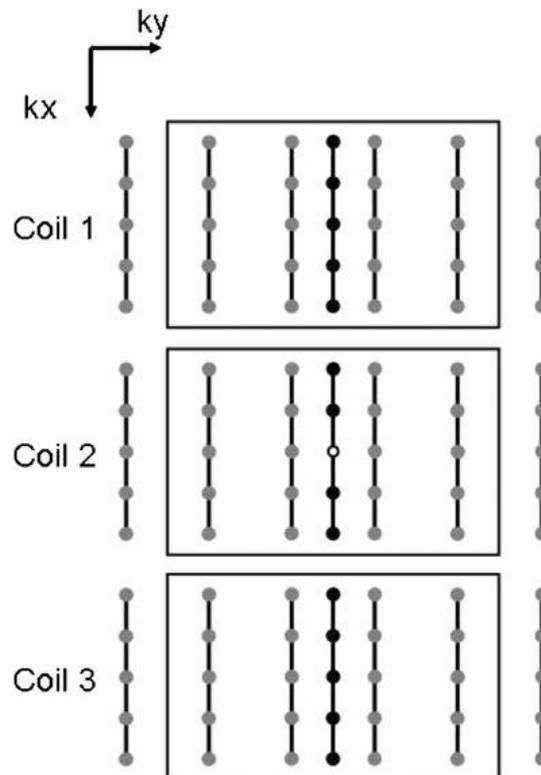
Figure 2-12: Reconstruction kernel with three coils. Points in gray correspond to acquired data, auto calibration lines are shown in black. To estimate the signal at unsampled points, the weights are determined from the auto calibration lines. (Figure reproduced with permission from (46))

2.8.8 **Compressed Sensing**

The parallel imaging methods described thus far skip lines of phase encoding in a regular pattern resulting in folding-in of the image. Another method of undersampling termed sparse sampling involved sampling the central part of k-space and then under sampling in a random or incoherent manner for k-space points outside the central region as shown in Figure 2-13. Rather than folding in, undersampling results in incoherent noise/aliasing in the image domain. Therefore, the method of reconstruction of k-space sampled in this way is different to that with parallel imaging and requires the removal of the incoherent noise based on known properties of the reconstructed image. Namely, the property that MR images are sparse in some domain, and/or that the aliasing caused by the undersampling behaves in a way that can be reproduced and removed based on the reconstructed image.

One method of correcting for the incoherent noise is to use the non-linear conjugate gradient descent (NLCG) algorithm to modify the data to enforce the sparsity of the data (48). In the NLCG method the conjugate-gradient descent algorithm is used to minimize the function (48):

$$f(x) = \|\mathcal{F}_u x - y\|_2^2 + \lambda_{Xfm}\|\psi_{Xfm}x\|_1 + \lambda_{TV}\|\psi_{TV}x\|_1 \tag{2-72}$$

where $\mathcal{F}_u$ is the undersampled Fourier transform, y is undersampled k-space, x is the reconstructed undersampled image and ψ_{Xfm} is the sparsifying domain transform. The operator ψ_{TV} is a total variation (TV) transformation that quantifies the spatial variation of x and is typically included as an extra regularization term to maintain image quality. The weighting terms λ_{Xfm}, λ_{TV} determine the trade-off between sparsifying and maintain original k-space data consistency.

Equation (2-72) is minimized by the iterative modification of the undersampled image by:

$$x_{i+1} = x_i - t(\nabla f(x_{i+1}) + \frac{\|\Delta f(x_{i+1})\|_2^2}{\|\Delta f(x_i)\|_2^2}\nabla x_i \tag{2-73}$$

where $\Delta f(x)$ and ∇x_i are the gradients of $f(x)$ and x_i and the constant parameter t($<$1) determines the rate at which the algorithm minimizes (2-72) with each iteration. The gradient in $f(x)$ for each iteration of (2-73) is given by:

$$\Delta f(x) = 2\mathcal{F}_u^*(\mathcal{F}_u x - y) + \lambda_{Xfm}\frac{\psi_{Xfm}x}{\sqrt{|\psi_{Xfm}x|}} + \lambda_{TV}\frac{\psi_{TV}x}{\sqrt{|\psi_{TV}x|}} \tag{2-74}$$

One benefit of this method over parallel imaging is that multiple receive channels are not required. However, the reduction in SNR is difficult to quantify in sparse sampling, and there is no equivalent g-factor since the error introduced is not a geometric variable. This also means error is not introduced from the mismatch of the sensitivity profile acquisition.

A more recent advance in reconstruction is the iterative self-consistent parallel imaging reconstruction (SPIRiT) method which includes information from multiple channels to reconstruct sparsely sampled data with arbitrary sampling patterns (49). SPIRiT is similar to GRAPPA in that it reconstructs the data within the k-space domain, but the kernel changes with each reconstructed points and uses the info from other reconstructed k-space points. SPIRiT is still largely a parallel imaging method, but the modified version ℓ1-SPIRiT (50) includes the general algorithm of SPIRiT with the additional modification that the reconstruction of the missing k-space data satisfies an equation similar to equation (2-72).

With the evolving state of parallel and compressed sensing methods there is no clearly superior method of accelerated MRI. SENSE and similar image based methods require an accurate sensitivity map, which is not possible to obtain in many applications and can be highly affected by motion and SNR. GRAPPA requires self-calibration lines for k-space, which reduces the level of AF possible for lower resolution imaging. Even though GRAPPA is more robust, in the ideal case it typically results in a higher SNR penalty. However, the method of ℓ1-SPIRiT and other related hybrid techniques may prove to be better reconstruction and sampling methods.
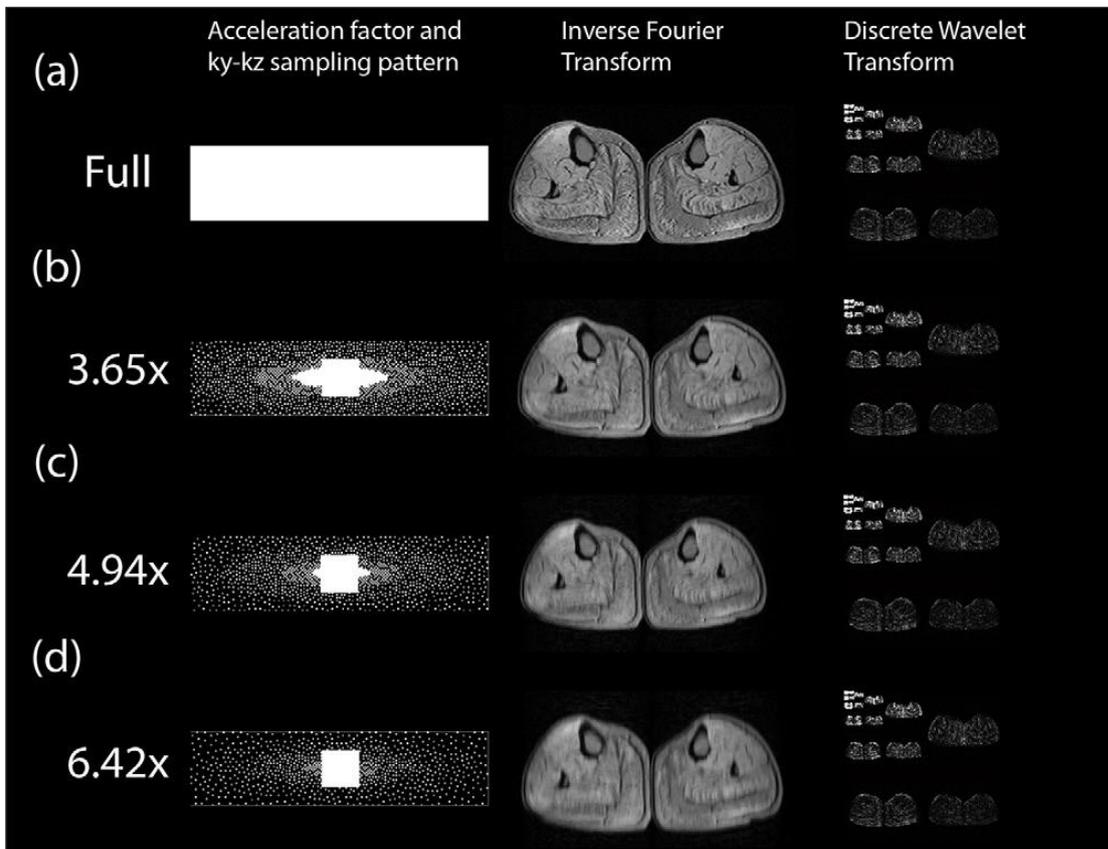
Figure 2-13: Examples of variable density undersampling patterns with different accelerations. (reproduced with permission from (51))

2.9 Inert Gas MRI for Lung Imaging of Diseases

2.9.1 Lung Physiology and function

Each of the lungs are contained within a double-layered membrane called the pleura that forms the pleural cavities. The trachea is the largest airway and connects the triple-lobed left lung and the double-lobed right lung. In each lung the trachea splits into the primary bronchi, which further divides for approximately 23 generations of binary branches. The major airways conduct gas to the respiratory zone, which consists of the peripheral airways with bronchioles and alveolar sacs at the end, where oxygen diffuses into the blood by gas exchange between alveoli and the blood in capillaries. In healthy lungs the alveolar-capillary wall is thin and the distribution of inhaled gas to the alveolar sacs is rapid and mostly homogenous, with some natural heterogeneity due to gravitational (52) and other effects (53). Lung diseases affect the delivery of oxygen to the blood by different pathophysiological mechanisms resulting in a less efficient gas exchange. MRI is used in a number of ways to monitor and characterize the mechanisms of lung disease, providing detailed and regional information not obtainable by other modalities of lung function testing.

2.9.2 Pulmonary Function Tests

There are various tests used in diagnosing and treating lung disease to determine the severity of obstruction(54). Some of these include the following, which will be detailed further: lung volume tests, diffusion and gas exchange tests and the measurement of forced expiratory volume in one second (FEV1) compared to the forced vital capacity (FVC).

Figure 2-14a shows the different lung volume sub-divisions corresponding to different levels of lung inflation. To measure lung volume a test subject/patient may be placed in a special sealed box and the volume of the different lung capacities can be measured by changes in pressure in the box. In restrictive lung conditions lungs cannot expand fully because lungs have lost elasticity.

The diffusing capacity for carbon monoxide is a measure of the ability of gas to transfer from the alveoli to the red blood cells. The alveolar volume, regional variation in ventilation and thickness of the blood-gas barrier affect the indirect measurement of perfusion. After patients breath in some carbon monoxide, hold their breath for some time (about 10s), then exhale, the amount of exhaled carbon monoxide is compared to the predicted value based on age and ethnicity.

Finally, the measurement of FEV1/FVC is performed by have the test subject/patient forcefully exhale from total lung capacity into a spirometer (the device that is used in measuring lung function) and then comparing the total volume of air exhaled in one second to the total than can be exhaled. The normal range of FEV1/FVC is 0.75-0.85, and a value lower than 0.7 is indicative of obstructed lung function, while restrictive lung diseases often produce a FEV1/FVC ratio that may be normal or high. A representative example of volume flow for a normal or obstructed forced expiratory lung function test is shown in Figure 2-14b.
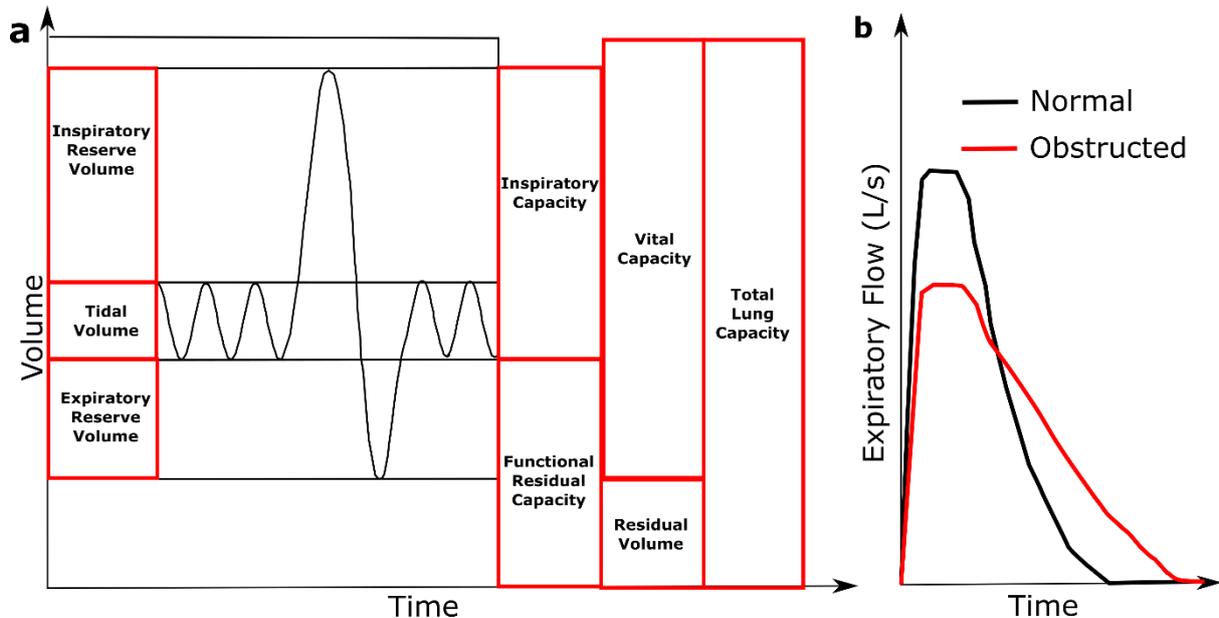
Figure 2-14: **a**: A volume-time graph representing lung inflation level during a typical breathing pattern. **b:** Representative diagrams of forced expiratory flow with for the case of healthy and obstructed lungs. Lungs with obstructed flow are typically characterized by reduced flow with expiration.

2.9.3 Lung Imaging

In lung diseases airflow and ventilation are regionally impaired, so alveoli are not supplied with enough oxygen. A perhaps more direct method of assessing lung function than the pulmonary lung function test described previously is imaging with MRI through ventilation imaging of inhaled inert gases during breath-hold (55, 56). Performing ventilation imaging of the inhaled gas is an approximate measure of the density throughout the lungs. In conjunction with anatomical imaging of the surrounding tissue through ^{1}H imaging, the assessment of total lung volume, percent ventilated volume (%VV), and ventilation heterogeneity (57) can be obtained. The %VV is found as the fraction of the lung cavity that is ventilated, defined by the boundaries of the anatomical image, that contains a concentration of inert gas after inhalation discernible in ventilation imaging. The measurement of fractional ventilation (FV) is a related method where imaging is performed over multiple breaths and the increase/decrease in gas

concentration is determined for each pixel during wash-in/wash-out of the tracer gas (58, 59). Compared to ventilation imaging, fractional ventilation can provide more specific regional lung information and may correlate better with overall lung function (58).

Further to ventilation and diffusion imaging, there are methods of measuring the ventilation/perfusion ratio (V/Q) (60-62). For example, by imaging the dissolved phase of a tracer gas (^{129}Xe) alongside ventilation imaging (62). In healthy lungs the amount of gas that dissolves into the blood should be approximately proportional to the gas that is distributed to the alveoli. In diseased lungs, inflammation, disruption of blood flow and/or damaged lung tissue may lead to mismatch between ventilation and perfusion. In many such cases there may be normal or unimpaired ventilation, but abnormal perfusion.

2.9.4 Different Lung Diseases

Lung diseases cause disability, reduced economic productivity, suffering and death for millions. Furthermore, 6 million hospital admissions a year and one in eight of all deaths each year are due to respiratory illnesses and lung conditions (63). As such, lung diseases have a huge cost to hospital care and treatments, as well as a huge associated economic burden due to the loss of productivity for people that also may die early because of them. Estimations of the total direct and indirect costs to the lung disease to the European Union alone exceed £380 billion each year (64). Therefore, improved methods of diagnosis and monitoring have large potential value for the treatment of the following described conditions.

Asthma is a condition where airways are hyper-responsive to different stimuli, such as histamines or exercise, resulting in bronchoconstriction and chronic or acute inflammation. Patients with asthma have obstructed lung function and will have abnormal FEV1/FVC, but typically normal FVC. Asthma begins in the peripheral airways and results in remodelling of the airways from chronic inflammation process can result in permanent obstruction and chronic mucus plugging. Therefore, early detection with ventilation imaging can help improve patient outcomes.

Cystic fibrosis (CF) is a genetic disease where the regulation of the production and elimination of mucus and digestive fluids is affected. This leads to blockages and inflammation in the lungs. In CF changes occur peripherally in the small airways (65) and by the time a change in global lung function by methods such as spirometry is detected major damage may already be caused (66). Patients with CF may have both restricted and obstructed lung function.

Chronic obstructive pulmonary disease (COPD) is used as an umbrella term to describe irreversible airflow obstruction in specific diseases such as chronic bronchitis and emphysema, partially characterized by narrowing of the airways because of chronic inflammation. A major cause of COPD is smoking (67). Late diagnosis and under-treatment contribute to the high mortality of COPD, so early detection to treat and prevent the losses of lung function is crucial (68).

2.9.5 Hyperpolarized Gas MRI for Lung Imaging

Hyperpolarisation is a process of drastically increasing the ratio of nuclear spins parallel to the static magnetic field high above the thermal equilibrium ratio (69). The foundation for hyperpolarization was introduced in the 1950s (70), with the extension to MRI/NMR occurring in the early 1990s .

Hyperpolarization of noble gases for MRI studies was introduced in 1994 (71), and first demonstrated for use in humans soon after (72). For Xenon, there are three stages in the method of hyperpolarization by spin exchange optical pumping (SEOP) using alkali-metal atoms (specifically Rubidium). Rubidium gas is vaporized in the polarisation glass chamber due to the vapour pressure of a small heated sample.

i. In the first stage the electron orbital spin of the Rubidium gas is excited into the +1/2 spin state of the 794.7 nm D1 transition ($S_{1/2} - P_{1/2}$) using optical pumping with a circularly polarized laser (73).

ii. In the second stage a van der Waals molecules is formed between a Rubidium molecule, Xenon and typically Nitrogen. The nuclear spin lost by the rubidium atom in this molecule is transferred to the nuclear spin of Xenon and the rotational motion of the molecule.

iii. In the last stage the molecule is broken up by collision with another particle (74). At high pressures binary collisions becomes the dominant source of spin transfer rather than the complicated van der Waals interactions (75, 76).

In addition to its function in the van der Waal molecule formation Nitrogen also acts as a buffer to prevent the radiative emission of the excited Rubidium state photons (77), while the use of helium in the mix broadens the D1 transition linewidth through collisional broadening (78). The statistical physics relations of the polarization of rubidium and its dependence on a multitude of factors is detailed further in (79). The relation of the nuclear polarization of xenon by rubidium spin transfer is related to these statistical factors, as well as on others relating to

its gas density, surface effects and temperature as shown in (80). The different optimizations for high density (80, 81) vs. low density (82) hyperpolarization have been detailed, with the result that although higher polarization may be achieved with lower density it requires a higher power and more expensive laser, while requiring a longer time, or larger glass cell, to collect as a large a sample by cryogenic freeze-out of the ^{129}Xe.

^{3}He hyperpolarization can be done using SEOP, or via metastable optical pumping (MEOP) on the electron orbital spins of Helium itself. In this case the $2^3S \rightarrow 2^3P$ state is excited with lasers of 1083 nm wavelength and the excitation of ground state ^{3}He atoms to the +1/2 nuclear spin state then occurs by collision with the 2^3P excited Helium atoms (83). The use of enriched ^{3}He and ^{129}Xe (natural abundance of 1.37×10^{-4}% and 26.4% respectively) for pulmonary ventilation imaging is expensive. Xenon is cheaper than helium and it is also feasible to use naturally abundant xenon (26% ^{129}Xe) as demonstrated in (84).

For the clinical diagnosis and monitoring of the diseases such as late stage cystic fibrosis, wherein the morphological and physiological changes may be significant, current state-of-art proton MR imaging of the lungs may be clinically useful. However, in disorders like early stage cystic fibrosis or emphysema structural changes are less obvious and the low tissue density of the lungs makes imaging a challenge (56). Hyperpolarized gas MRI allows the direct imaging of the lung's microstructure and ventilation with high signal-to-noise (71), which enable detection of impaired function in diseased lungs as illustrated in Figure 2-15.
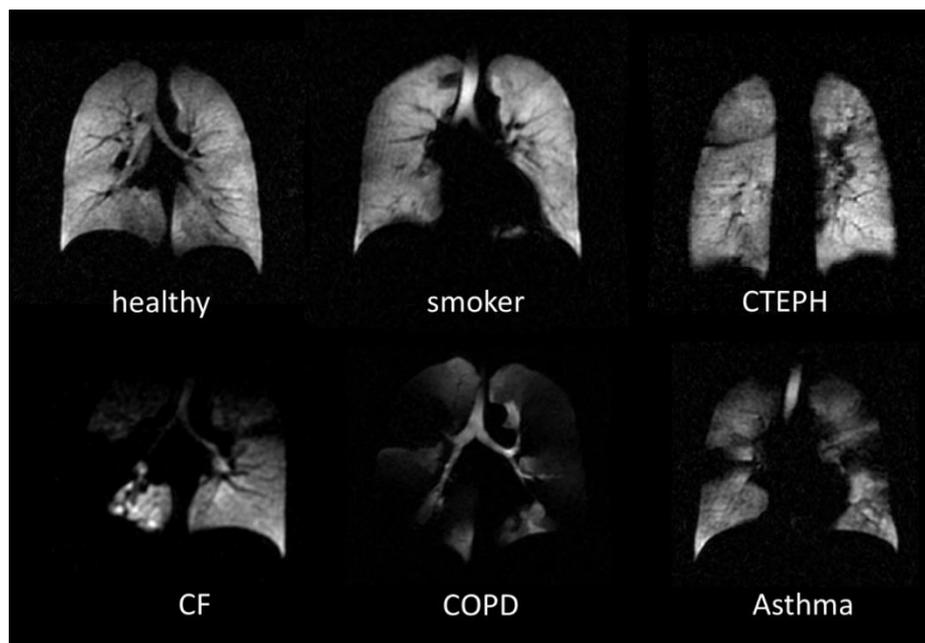
Figure 2-15: Hyperpolarised ^{3}He MR human lung images for various lung diseases: smoker, Chronic Thromboembolic Pulmonary Hypertension (CTEPH), Cystic Fibrosis (CF), Chronic Obstructive Pulmonary Disease (COPD) and Asthma. © University of Sheffield.

The measurement of diffusion (85, 86), ventilation (87, 88) and the estimation of perfusion by imaging dissolved phase ^{129}Xe (62, 89, 90) has been demonstrated and validated with HP gases. In addition, longitudinal studies have been performed showing the validity and use of important biomarkers only measureable by HP gas imaging. For example, the signal from red blood cells diminishes relative to the tissue/plasma signal as idiopathic pulmonary fibrosis progresses (91), %VV and ventilation heterogeneity correlates with spirometry measures of lung function in cystic fibrosis (92), measurement of collateral ventilation can reveal regions where normal paths for air flow are obstructed (93) and treatment response mapping in imaging subjects with asthma before and after use of a bronchodilation agent correlates with lung function. However, there are complicating factors in the assessment of the sensitivity of HP gas imaging. For example, it is known that lung volume has an effect on the quantitative measures of lung ventilation (%VV and ventilation heterogeneity shown in reference (94)), with differences in diffusion demonstrated previously as well (95). However, HP gas imaging has still proven to be a sensitive technique for evaluating and studying lung physiology.

2.9.6 **Fluorinated Gas Imaging**

^{19}F is a naturally 100% abundant isotope, has a higher Larmor frequency than ^{129}Xe and ^{3}He, and is available in gaseous compounds with higher spin density for a standard pressure than ^{129}Xe or ^{3}He due to the presence of multiple nuclei per each molecule, thus they need not be hyperpolarized. The outline of ^{19}F imaging by Holland et al. (96) noted some of the potential benefits of ^{19}F MRI: there are no background endogenous biological signals when a ^{19}F tracer is introduced, the Larmor frequency is close to proton so the same RF equipment may be used and many fluorocarbons compounds are biologically inert. Most importantly, the longitudinal relaxation time T_1 is small ($\approx$20 ms for C_3F_8 alone (97), and $\approx$12 ms when in the lungs and mixed with 20% oxygen (98)), meaning that many averages can be performed in a short time in order to compensate for the low density of gases (2.37×10^{19} atoms /cm^3(99)).

The chemical structure and molecular weight of a number of fluorinated gases used in previous MRI studies (100) are shown in Table 2-2. Of the chemical species used CF_4 (tetrafluoromethane) has four chemically equivalent ^{19}F atoms within a molecule, while C_2F_6 (perfluoroethane), SF_6 (sulfurhaxafluoride) and C_3F_8 (perfluoropropane) all have six and C_4F_8 (cyclo-octafluorobutane) has eight. C_3F_8 has two additional ^{19}F atoms with a 48ppm chemical shift in Larmor frequency. C_4F_8 has been shown to cause convulsions, while SF_6 has a low level of anaesthetic potency. On the other hand, CF_4, C_2F_6 and C_3F_8 are insoluble in blood and non-

toxic. Of the three only C_3F_8 has been commonly used because of its established precedent shown for safe inhalation in human subjects. Therefore, C_3F_8 is generally considered the most relevant in-vivo fluorinated gas imaging agent.

Table 2-2: Chemical structures and molecular weights of perfluorinated gases used in MRI.

Molecule	Molecular Weight (g/mol)	Chemical Structure
CF_4	88.01	F—C(F)(F)—F (F up, F down, F left, F right)
C_2F_6	138.02	CF_3———CF_3
Cyclo-C_4F_8	200.04	CF_2———CF_2 / CF_2———CF_2
SF_6	146.06	F–S–F with F at all six positions
C_3F_8	188.02	CF_3———CF_2———CF_3
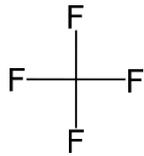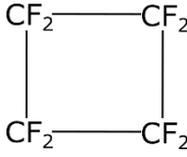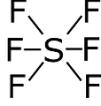
The concept of lung imaging with ^{19}F fluorocarbons was first introduced, by liquid breathing of oxygenated fluorocarbon liquids, which was realized later (101, 102). However, the first in-vivo imaging of a fluorinated gas compound were performed using CF_4 (103). For a relatively long period after ^{19}F imaging was primarily focussed on the use of chemical tracers (as an approximation a concentration of 0.1 M was determined as the detection level at 0.15T (104)). The use of fluorinated gas imaging was first found to be usable for the evaluation of solid materials (ceramics) imbued with a fluorinated gas, in which it was noted that surface adsorption and the small features cause changes in the spin density T_1 and the diffusion (105). Consequently, the change in diffusion and T_1 was hypothesized as a potential way to characterize differences in the local surface-to-volume ratios, which would have future implications for lung-imaging.

The first comprehensive studies with in-vivo fluorinated gas MRI (within a rat model (106)) used C_2F_6 mixed with oxygen. The choice of C_2F_6 has a number of advantages over CF_4 and

SF_6, which have shorter T_2^* (107). However, from 2000-2004 publications on ^{19}F lung-imaging (within porcine (88, 108) or rat models (109, 110)) were dominated with the use of SF_6: partially because it was approved for human use, and had been used for many years in the multiple inert gas elimination technique. At this time, the concept of measuring the ventilation-to-perfusion ratio with fluorinated gases by MRI imaging was introduced. In this method it is expected that inert insoluble gases become concentrated where ventilation-to-perfusion ratio is low (111), and in obstructed alveoli soluble gases comes to equilibrium with blood. Thus, the difference in signal intensity when breathing a high vs. low O_2-fluorinated gas concentration is weighted by the ventilation-perfusion.

The measurement of fluorinated gas diffusion within the lungs was then developed with methods that had similarly been employed in hyperpolarized gas imaging (39, 112, 113). Diffusion imaging was performed in rat lungs (114), showing that diffusion was restricted within airways and also has a measurable dependence on the pressure and composition of the gas mixture (115). Imaging C_2F_6 (97) further expanded the theoretical basis for diffusion imaging with fluorinated gases, showing that the diffusion was restricted by the lung microstructure and was higher in emphysematous lungs. Correspondingly, the variation of T_1 with different properties, such as partial pressure, field strength and temperature, was theoretically and experimentally described for a number for fluorinated gas compounds (116, 117). This would prove to allow for more accurate optimization of imaging parameters and the mapping of T_1 to relate to physiological parameters such as the perfusion-ventilation ration, rather than the previous signal based technique (60, 118).

All the ^{19}F imaging performed up to this point required imaging times far above that of a single breath-hold, which would have greatly restricted the clinical application of ^{19}F gas imaging. Wolf et al. (119) demonstrated that imaging with longer than previously employed TR, and the use of C_2F_6 gas instead of SF_6, could allow rapid fluorinated gas image acquisition. As such, with this advancement and appropriate regulatory hurdles overcome, the ability to image human lungs for the first time was demonstrated with SF_6 by Wolf et al. (120). A modest SNR of 9 for full lung projection human lung imaging was obtained. The main challenge to achieving high SNR in ^{19}F imaging in humans is the short T_2^* relaxation time (for SF_6 a T_2^* of 1.2ms in the lungs, and approximately equal T_1 reported in (114)).

In subsequent developments for human in-vivo fluorinated gas imaging Perfluoropropane (C_3F_8) was employed, which has largely proven to be a better imaging agent due to its even longer T_2^* compared to C_2F_6 and SF_6 (98, 121). The use of ultra-short echo time (UTE) sequences for imaging C_3F_8 was investigated (98), but overall images obtained with this

method appeared more blurred than those obtained with conventional SPGR imaging methods (121). Future measurements in rat lungs (with C_3F_8 and SF_6) produced higher-quality images than use of UTE with an "X-centric" sequence (partial Fourier echo with measurement of missing data with additional TR). With the culmination of previous improvements, ^{19}F imaging was demonstrated to be applicable in mapping ventilation in healthy volunteers, with comparable measured values of %VV and lung volumes as with HP ^3He imaging (122). Probably one of the main potential advantages of fluorinated gas imaging was demonstrated in a rat model with SF_6 and x-centric imaging: the mapping of fractional ventilation (FV) during washout (58). Fractional ventilation requires dynamic imaging over multiple breath holds and provides functional information on gas trapping, which is not as easily performed with HP gas imaging.

The state of ^{19}F imaging has now advanced to the point that clinical research studies with large cohorts of healthy volunteers and patients are being performed. Most recently, imaging of C_3F_8 to evaluation ventilation and FV has been performed in a cohort of healthy volunteers and those with COPD (123). Additionally, the use of ^{19}F washout imaging has been compared with the use of Fourier decomposition MRI to evaluate FV in COPD patients, with significant correlation indicating that a combination of ^{19}F and ^1H imaging may be used concurrently for functional lung imaging. For additional information, there are a number review articles that further describe the past progress of fluorinated gas imaging (124-127), but the published results are largely contained in what has been described thus far and the following results of this thesis.
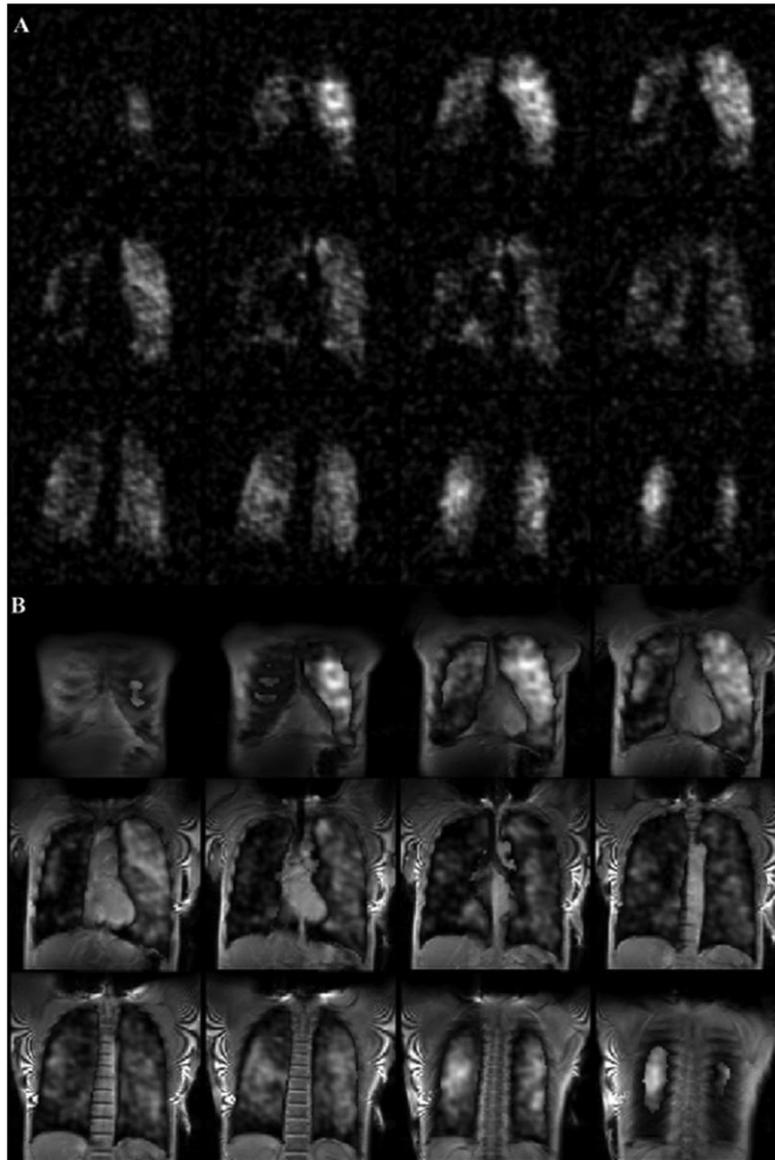
Figure 2-16: a: UTE lung ventilation images mixture of 79% PFP and 21% O2 inhaled by a patient with emphysema and b: the same ventilation images registered to ^{1}H anatomical images and overlaid in greyscale (Reproduced with permission from (126))

2.10 **Hyperpolarized vs. Fluorinated Gas Imaging**

There is a fundamental SNR advantage to hyperpolarized gas imaging compared to fluorinated gas imaging. In Figure 2-16 images taken with inhaled perfluorocarbon are shown from Ref. (126). These images can be compared to those taken with hyperpolarized ^{3}He (red), and ^{129}Xe in Figure 2-17. The images in Figure 2-17 are clearly less blurred with better resolution then the images of Figure 2-16, but the localization of the gas in the lungs is still clear and show the defects in ventilation with emphysema.
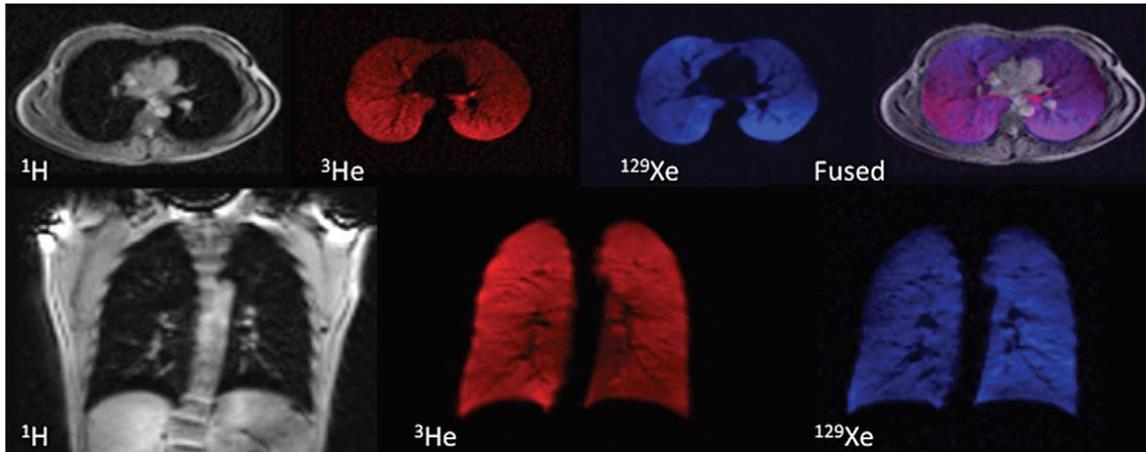
Figure 2-17: Images taken of the lungs with ^{1}H (left), ^{3}He (red), and ^{129}Xe (blue). Images for all three were taken in the same breath-hold. (reproduced with permission from (128))

The relevant parameters for a number of common fluorinated compounds and the two most important hyperpolarized gas imaging agents, ^{129}Xe and ^{3}He, are shown in Table 2-3. As noted earlier, of the potential fluorinated compounds C_3F_8 is one of the most promising because of its biological inertness, high number of nuclei per atom, potential for diffusion studies and cost.

Table 2-3: Summary of fluorinated compounds and hyperpolarized gas relaxation parameters and diffusion coefficients

Gas	T_1 (ms)	T_2 (ms)	T_2^* (ms)	D_0 (cm$^2\cdot$s^{-1})	ADC (cm$^2\cdot$s^{-1})	Density (mg/cm^3)	Gyromagnetic ratio (MHz/T)
^{129}Xe	32000 (126)	20000 (113)	20 (129)	0.062 (39)	0.021 (39)	0.575 (125)	-11.77
^{3}He	20000 (99)	310 (112)	18.5 (130)	2.05 (39)	0.016 (39)	1.34 (125)	-32.434
SF$_6$	1.2 (126)	4.23 (114)	1 (131)	0.033 (126)	0.022 (114)	6.51 (125)	40.052
C$_2$F$_6$	5.9 (106)	5.9 [84]		0.033 (97)	0.018 (97)	6.16 (125)	40.052
C$_3$F$_8$	12.4 (98)	18 (117)	2.2 (98)	0.028 (117)	0.022 (86)		40.052

2.10.1 SNR difference in HP gas and TP Fluorinated Gas MRI

The SNR that may be expected with TP fluorinated gas MRI when compared to the more established experimental evidence base of HP gas imaging experiments is detailed here as a theoretical starting point. The received signal is proportional to the transverse magnetization, which is dependent on the imaging sequence parameters by some proportionality factor α_{0xy}, as:

$$M_{xy} = \alpha_{0xy}M_0 \qquad (2\text{-}75)$$

Here, the proportionality factor α_{0xy} describes the relationship between the longitudinal magnetization (this is taken as the magnetization at the beginning of imaging, to draw equivalence between TP and HP imaging) and the steady state transverse magnetization (taken as approximately the magnetization at the point of encoding the central line of k-space). The factors affecting the proportionality factor are T_1, T_2 and T_2^* relaxation, FA and sequence parameters, which are detailed for TP SPGR imaging in section 2.8.2, for TP SSFP imaging in section 2.8.3, and for HP SPGR and SSFP imaging in section 2.8.4. Specifically, for TP imaging equation (2-51) details the relation for SPGR imaging, equation (2-59) details the relation for SSFP imaging and for HP imaging equation (2-61) details the relation for SPGR imaging. For HP SSFP imaging more detailed simulations are required, rather than closed form expressions.

For an RF coil with loading that is body-dominated the EMF induced by the transverse magnetization is proportional to $(\gamma B_0)^2$, whilst the standard deviation of the thermally generated Johnson noise voltage is proportional to (γB_0) (9). Therefore, when comparing the SNR in imaging different nuclei with different gyromagnetic ratios, assuming that the imaging coils have equivalent geometries, we have:

$$SNR \propto \gamma \alpha_{0xy} M_0 \tag{2-76}$$

Finally, assuming equal imaging resolutions, bandwidths and imaging time a comparison between the SNR of TP and HP imaging can be drawn as follows. Using the expressions for the longitudinal magnetization at the beginning of imaging, equation (2-10) for TP and equation (2-60) for HP, the ratio of SNR ($SNR_{T/H}$) in a ventilation image obtained via a TP sample compared to a HP sample at the same B_0 is given by:

$$SNR_{T/H} = \frac{P_T N_T}{P_H N_H} \frac{\alpha_{0xyT}}{\alpha_{0xyH}} \frac{\gamma_T^2}{\gamma_H^2}. \tag{2-77}$$

The subscripts T and H denote that the variable is associated with the TP or HP sample, respectively. The polarization percent for the TP sample ($P_T N_T$) is isolated from equation (2-10) as:

$$P_T = \frac{B_0 \hbar \gamma_T}{2 k_b T}. \tag{2-78}$$

As a demonstrative example relevant to the motivation and results of this thesis the relevant parameters for equation (2-77) comparing the SNR of C_3F_8 and ^{129}Xe MRI for ventilation imaging are summarized in Table 2-4. The density of gas in the lungs is approximated by the

ideal gas law, but there are additional approximations for the density of the two gases in the lungs during imaging. For C$_3$F$_8$, there are 6 chemically equivalent ^{19}F nuclei for each gas atom and the lungs approximately reach full saturation of the gas, while mixed with 20% oxygen: $N_T = N(0.8 \times 6)$. For isotopically enriched (86%) HP ^{129}Xe a typical inhalation dose is 500mL→1L, which is mixed within a lung volume of ~5L: $N_H = N(0.86 \times (0.5L \to 1L)/5L)$.

For the demonstrated case of optimizing 3D steady SSFP for HP ^{129}Xe imaging (35) a flip angle of α_{opt}=10° and imaging bandwidth of ±8 kHz coincides with a steady state longitudinal magnetization at the centre of k-space ($M_z(N_p/2)$) that is approximately 50% the initial longitudinal magnetization (M_i). Likewise, the steady state transverse magnetization for perfluoropropane will be ~50% the thermal equilibrium longitudinal magnetization using a fully optimized SSFP sequence, considering that T$_1$=T$_2$ (133).

Table 2-4: Summary of relevant properties of HP ^{129}Xe and TP C$_3$F$_8$ gases at 1.5T for comparison of expected difference in relative SNR. The values shown are for a hypothetical imaging resolution of 4x4x10mm^3, matrix size=100×82×24 ($N_p = 82 \times 24$), TR=5 ms and relaxation parameters matching those in Table 2-3.

Gas	N * $(10^{24}/m^3)$	γ $(10^6 \frac{rad}{Ts})$	α_{0xy} SPGR	α_{0xy} SSFP	P
^{129}Xe	$2.11 - 4.21$	-74.0	$e^{-\frac{TE}{T_2^*}}e^{-\frac{(N_p-1)TR}{2T_1}}\sin(\alpha)\cos(\alpha)^{\frac{(N_p-1)}{2}}$-Eq. (2-61)** **0.017**	$\frac{M_z(N_p/2)}{M_i}\sin(\alpha_{opt})$*** **0.088**-Ref. (35, 134)	**0.1-0.4**
C$_3$F$_8$	117	251.7	$\frac{e^{-TE/T_2^*}(1-e^{-TR/T_1})}{\sqrt{1-e^{-2TR/T_1}}}$-Eq. (2-51) **0.14**	$e^{-TE/T_2}/2$-Eq. (2-59) **0.43**-Ref. (32)(135)	$\frac{B_0\hbar\gamma_T}{2k_bT}$-Eq. (2-78) **$9.6\times 10^{-6}$**

*based on ideal gas law at 1 atm and 300K, $N = 24.7 \times 10^{24}/m^3$

**$\alpha_{opt} = tan^{-1}(1/\sqrt{N_p/2 - 1})$-Eq. (2-62)

***$M_z(N_p/2)$ refers to the longitudinal magnetization at the central k-space encoding line, $\alpha_{opt} = 10°$ for $\frac{M_z(N_p/2)}{M_i} \sim 0.5$ in Ref (35)

Therefore, using the parameters detailed in Table 2-4 in (2-77) under optimum conditions for imaging both nuclei the SNR ratio for in-vivo SPGR imaging may be approximated as:

$$SNR_{T/H}(SPGR) = \frac{1}{3.8} \to \frac{1}{30} \tag{2-79}$$

Likewise, for optimal SSFP imaging the SNR ratio can be approximated as,

$$SNR_{T/H}(SSFP) = \frac{1}{5.8} \to \frac{1}{46} \tag{2-80}$$

In summary, if two equal resolution ventilation images are acquired within the same acquisition time (for example, a single breath-hold), one with TP fluorinated gas (C$_3$F$_8$) and one with HP ^{129}Xe gas, the SNR of the ^{19}F image can be expected to be smaller than the HP ^{129}Xe image by the appreciable range given in (2-80) for SSFP imaging.

2.10.2 Apparent Diffusion Coefficient Measurement with Hyperpolarized and Fluorinated Gas

In healthy lungs the ADC is largely homogeneous and in the peripheral sections of the lungs diffusion is restricted and therefore lower compared to the larger airways (86). A simple model for the diffusion of lung acinar airways is a cylinder covered with an alveolar sleeve (136). Based on this model, the MRI signal from a voxel is given by:

$$S_b = S_0 e^{-bD_T} \left(\frac{\pi}{4b(D_L - D_T)} \right)^{\frac{1}{2}} \Phi\left[(b(D_L - D_T))^{1/2} \right] \tag{2-81}$$

where $\Phi(x)$ is the error function, D_L is the diffusion coefficient in the longitudinal direction and D_T is diffusion coefficient in the transverse direction (38). For an applied trapezoidal bipolar gradient the b-value is obtained from (137):

$$b = \gamma^2 G^2 \left[\delta^2 \left(\Delta - \frac{\delta}{3} \right) + \tau \left(\delta^2 - 2\Delta\delta + \Delta\tau - \frac{7}{6}\Delta\tau + \frac{8}{15}\tau^2 \right) \right] \tag{2-82}$$

where γ is the gyromagnetic ratio, G is the gradient strength, δ is the gradient duration, Δ is the temporal separation between the leading edges of the diffusion-sensitizing gradient pulses and τ is the ramp up time. The variable $t = \Delta - \frac{\delta}{3}$ may be defined as the diffusion time, which is related to the characteristic free-diffusion length (L_{diff}) by:

$$L_{diff} = (4D_0 t)^{1/2} \tag{2-83}$$

where D_0 is the free diffusion coefficient. The free-diffusion length characterizes the mean distance travelled by a gas atom for a given time when unrestricted. For the typical diffusion times used in inert gas experiments (<10 ms), the mean free path of C_3F_8 is approximately 0.35 mm, which is comparable with the ~0.2 mm diameter of the alveoli (136). Equations (2-82)-(2-81) establish that the signal decay in diffusion imaging is highly dependent on the geometrically dependent parameters of the lung airways. Thus, the use of imaging with multiple interleaved b-values has been used to characterize the effective geometric parameters, or diffusion length scales, of this and other models (such as the stretched exponential model(138)) with ^{3}He (38, 85) and ^{129}Xe (139), demonstrating how lung morphometry is altered with disease.

An alternate expression may be obtained analogous to diffusion in porous media, with (140):

$$\frac{ADC}{D_0} \approx 1 - \left(\frac{2}{9\sqrt{\pi}} \right) \frac{S}{V} L_{diff} \tag{2-84}$$

where S/V is the physiologically related surface-to-volume ratio, and (2-81) may be simplified to:

$$S_b = S_0 e^{-bADC} \qquad (2\text{-}85)$$

where ADC is the apparent diffusion coefficient. For $S/V \, L_{diff} < 1$ equation (2-85) is an accurate approximation to equation (2-81), with $D_T = ADC$. This may be termed the linear regime, or edge restricted, based on the expression in (2-84). In this case, the ability to probe the lung microstructure with multiple b-value imaging is limited, but still allows the probing of the S/V of the lung structure. Due to the low diffusivity of C_3F_8, as well as the low T_2^* and inherently low signal relative to HP gas imaging, it is not feasible to perform in-vivo diffusion weighted imaging with b-values that would place the ADC outside the linear regime.

In diseased lungs fibrosis changes the dimensions of the alveolar sac resulting from alveolar wall breakdown. Therefore, in patients with emphysema there is a substantial increase in ADC levels compared to healthy volunteers as represented by the diagram in Figure 2-18. In addition, the distribution of ADC and effective mean diffusion length scale (L_{m_d}) measured through multiple b-value imaging have been shown to be heterogeneous in diseased lungs (141).

Through multiple studies it has been established that in progressive stages of emphysema and COPD the measured ADC can increase by a factor of 2-4 compared to healthy lungs. To determine differences in healthy lungs (S/V$\approx 250 cm^{-1}$) and emphysematous lungs (S/V$\approx 50 cm^{-1}$) L_{diff} should be chosen to result in a measurable change in equation (2-84). Studies with both HP ^{3}He and ^{129}Xe imaging have shown that comparable results are obtained through diffusion imaging with both gases (142).

Healthy Lungs   Emphysematous Lungs
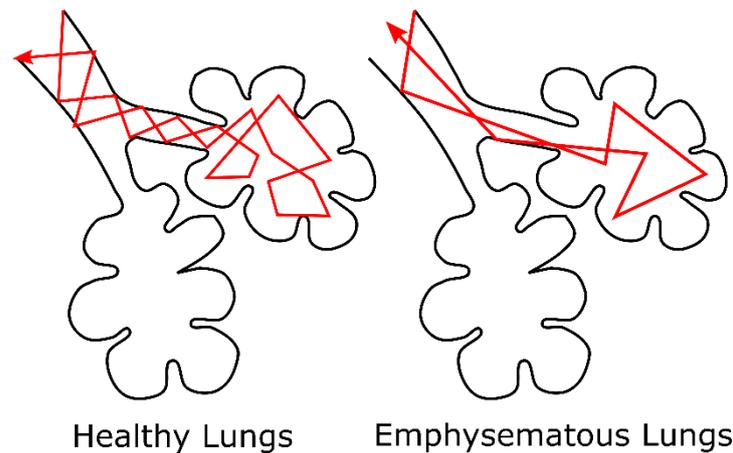
Figure 2-18: Representative diagram of typical path of gas atoms in healthy or emphysematous lungs. In healthy lungs atoms are more restricted leading to lower ADC, while in emphysema gas atoms are less restricted leading to a larger mean free path and larger ADC.

Hyperpolarized ^{129}Xe and ^{3}He have a more favourable ADC (39, 86, 99, 130) compared to fluorinated compounds as shown in Table 2-3. The low diffusion constant of fluorinated gases mean that only with high RF power and very fast gradients can useful information be obtained

(115). However, because of the longer T_2 and T_1 it has be shown that when imaging C_2F_6 in excised human lungs it is possible to measure the ADC and show a significant difference between normal and emphysematous lungs using imaging sequences in a reasonable breath-hold timescale (10s) (97). ADC maps taken using perfluoropropane is shown in Figure 2-19(b), which accurately reveals increased ADC resulting from emphysema (86). However, the maximum ADC is much reduced (only 0.022 cm^2/s for C_3F_8 (86)) compared to ^{3}He indicating inferior potential sensitivity. This is particularly detrimental to evaluating the functioning of structures such as alveoli and acinar airways. ADC maps with ^{3}He measured in healthy lungs vs. lungs of patients with emphysema is shown in Figure 2-19(a), where a significant difference in emphysematic lungs is apparent.
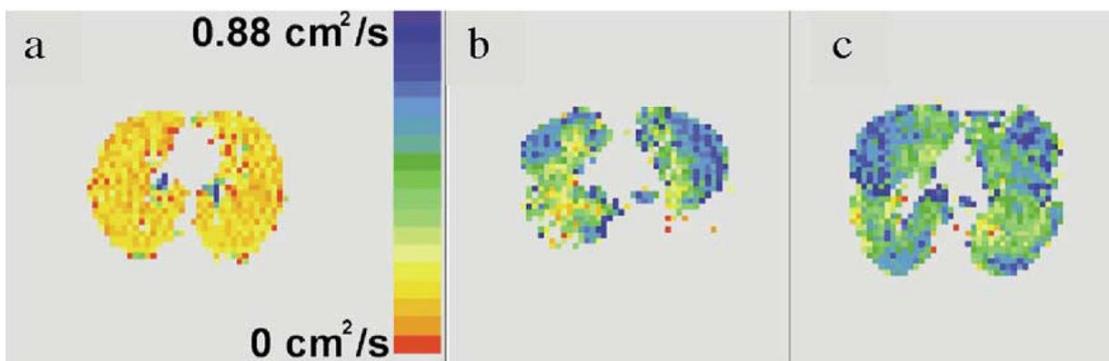
(a)
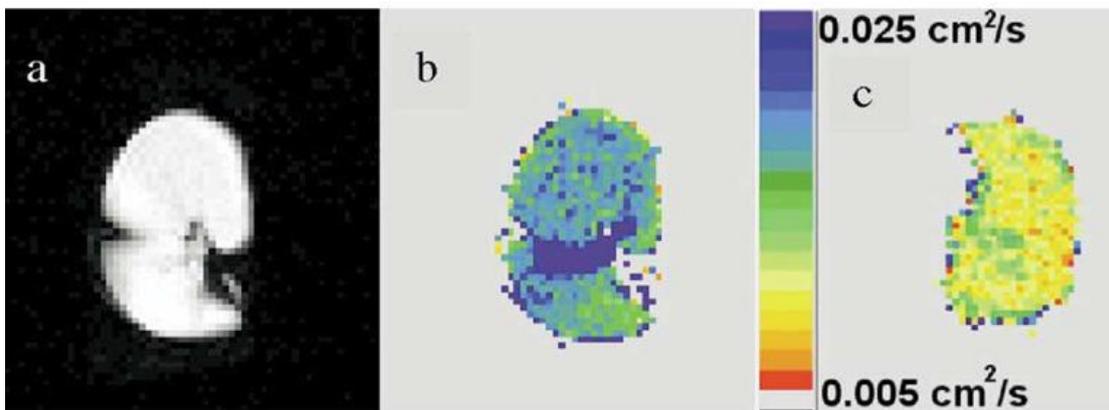
(b)

Figure 2-19: ^{3}He ADC maps in a volunteer (left) and patients with emphysema, (two right). The maximum is the free diffusivity without obstruction. The ADC is much higher in emphysematic lungs than in healthy lungs. ^{3}He ADC maps can be compared to those using C_3F_8 gas, perfluoropropane, in (b). ADC from a lung of patient with emphysema shown on right and from an excised normal lung on the right. (reproduced with permission from (86)).

There are also changes in diffusion parameters that occur naturally due to affects such as posture and the physiological makeup of healthy lungs. For example, in healthy volunteers a 22% decrease in the mean ADC with ^{129}Xe imaging was found moving from the anterior to posterior of the lungs in healthy volunteers, which was not observed in volunteers with COPD

(81). Furthermore, a decrease of 24% in the superior-inferior direction was also found, which was potentially attributed to regional differences in ^{129}Xe concentration, since the partial pressure of gases greatly affects the diffusivity, and in a single breath the inhaled ^{129}Xe gas may not fully mix in the lungs. In previous works a similar gradient in ADC has been observed in the anterior/posterior direction as well as the craniocaudal direction (although <15% in the superior inferior direction) (143, 144), which changes depending on the posture during imaging. Also, regions of the lung next to the heart experience compression (145), which result in regional changes in ADC that can be observed in HP gas diffusion imaging. Furthermore, lung inflation has a similar effect on mean ADC values, while at TLC the anterior-posterior gradient is no longer observable (95). The changes in ADC observed with posture are smaller than those observed with disease. Therefore, by replicating the results of previous studies measuring the dependence of ADC on lung inflation and physiological distribution in healthy volunteers with ^{19}F C_3F_8 imaging the feasibility of detecting changes in diseased lungs may be extrapolated.

2.11 Theoretical Description of the Radio-Frequency System

The signal-to-noise-ratio (SNR) and spatial homogeneity of the MR image is highly dependent on the RF coil design. Thus depending on the volume coverage and sensitivity, two different classes of coils are typically used: transmit volume coils such as a birdcage which produce a homogeneous magnetic field in the field-of-view (FOV) and the receive coil arrays, which have higher sensitivity due to their close proximity to the ROI. In theory the transmit and receive networks are part of the same RF system as shown in Figure 2-20a, but in practice they are usually detuned to a high degree from each other during the separate transmit and receive phases of MRI and can be treated separately as decoupled receivers.

2.11.1 Transmit System Characterization

For the transmit system there are three relevant figures of merit. First, the mean transmit efficiency (μ_T) given by:

$$\mu_T = \frac{1}{V} \int \frac{B_1^+}{\sqrt{P_{in}}} dV \tag{2-86}$$

where P_{in} is the input power and B_1^+ is the perturbing RF magnetic field in equation (2-27) that results in the tipping of the magnetization into the transverse plane. Second, the homogeneity represented by the standard deviation of the transmit efficiency (σ_T) given by:

$$\sigma_T = \frac{1}{V}\sqrt{\int \left(\frac{B_1^+}{\sqrt{P_{in}}} - \mu_T\right)^2 dV} \tag{2-87}$$

where the volume V encompasses the desired imaging FOV or ROI. Finally, there is the specific absorption rate (SAR), typically averaged over 10g volumes for MRI (146):

$$SAR_{10g}(\boldsymbol{r}) = \frac{1}{V}\int_{10g\ sample} \frac{\sigma(\boldsymbol{r})\mathbf{E}\cdot\mathbf{E}^*}{\rho(r)} dV \tag{2-88}$$

where $\boldsymbol{r}$ is at the centre of the 10g volume, $\rho(r)$ is the sample density, and the electric field $\mathbf{E}$ is for a given input power. SAR is therefore given in units of W/kg, but the value must be related to an associated input power or mean transmit efficiency. The level of SAR that can be deposited into the human body is strictly regulated and often restricts the imaging parameters that can be used in MRI imaging sequences (146, 147).

The fidelity of the transmit signal is another important criterion for performance, but the passive portion of the RF transmit system (the coil and matching network) should not affect this. The receive part of the network is arguably more complicated as described in the next section.

2.11.2 Network Theory Description of Signal and Noise in Receive Arrays

The theory of the coil array for MRI was formalized by Roemer et al. (148), but many of the theoretical concepts and design principles of coil arrays are shared by multiple input- multiple-output (MIMO) antennas, which is a field that has been in development since the 1960s (149). Early in the development of coil arrays there were attempts to develop a coherent and complete network description of the receive system (26, 150-155), however it has only been relatively recently all aspects have been able to be combined effectively.

From equations (2-43) and (2-45) the open circuit EMF induced on a network of receivers $(\widehat{\boldsymbol{v}_s}(\boldsymbol{r}))$ by the magnetization at position $\boldsymbol{r}$, with small voxel volume ΔV, can be approximated as:

$$\widehat{\boldsymbol{v}_s}(\boldsymbol{r}) = \begin{bmatrix} \widehat{\boldsymbol{B}}_1^-(1,\boldsymbol{r}) \\ \vdots \\ \widehat{\boldsymbol{B}}_1^-(N,\boldsymbol{r}) \end{bmatrix} \Delta V \omega(\boldsymbol{r}) M_{xy}(\boldsymbol{r}) \tag{2-89}$$

In equation (2-89), $\widehat{\boldsymbol{B}}_1^-(n,\boldsymbol{r})$ is the receiver dependent component of the signal and is often used interchangeably with the term "coil sensitivity". The voltage is induced in series with the windings of the receive coils and its propagation through the receive chain is determined by the network that makes up the receive chain as diagrammed in Figure 2-20a.

The analysis of preamplifier noise in multiport systems have been developed using S-Parameters in the field of MIMO antennas (156-159), and also with a Z-Parameter representation of the including matching networks (160), based the on noise theory of passive networks and preamplifiers (161, 162).
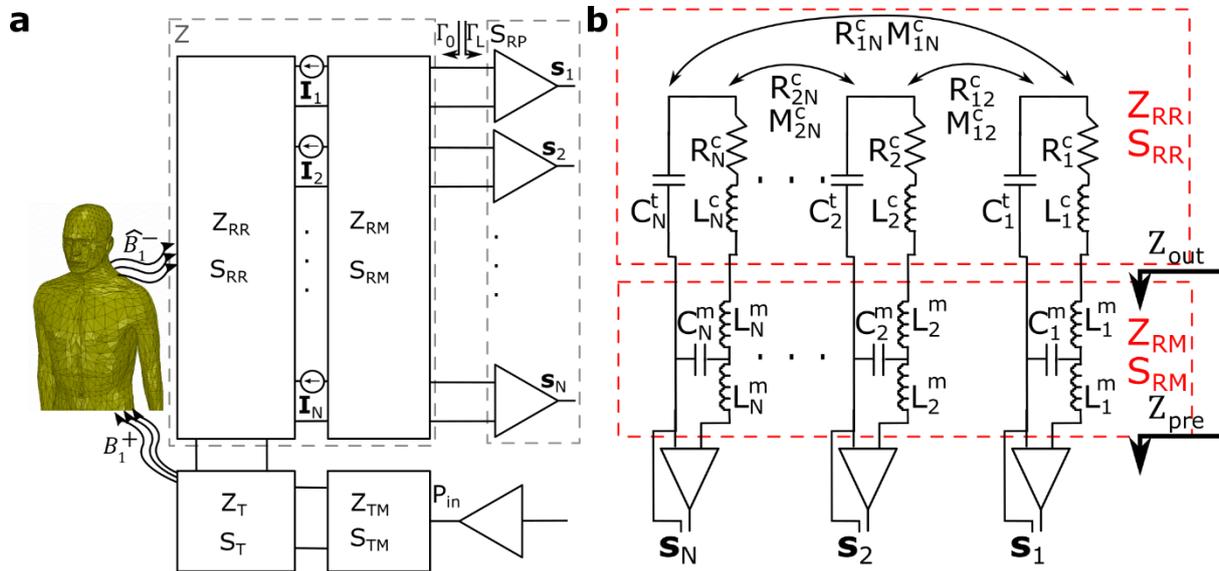
Figure 2-20: **a:** Diagram of the RF system network in MRI with receive coil -port network (Z_{RR}/S_{RR}) connected directly to the N-port matching network (Z_{RM}/S_{RM}) with N individual preamplifiers (S_{RP}) for each receiver. The transmit coil network (Z_T/S_T) can be modelled as coupled to the receive coil network with its own individual matching (Z_{TM}/S_{TM}) **b:** A general circuit schematic of simple multi-coil receive-array with individual LC t-matching networks for each coil. Coupling between coils is described by mutual resistance (R_{nm}) and mutual inductance (M_{nm}) between m and n elements.

Using network theory, the voltage covariance and the signal voltage (functionally equivalent to the sensitivity matrix) at the output of the network is given by:

$$s = QG_0\widehat{v_s} \tag{2-90}$$

$$\Psi = Q(\Psi_p)Q^{\mathcal{H}}$$

where Ψ_p is the voltage covariance at the preamplifier input terminals, G_0 is transformation of $\widehat{v_s}$ to the voltage at the preamplifier input, while Q relates the voltages at the preamplifier input to output and they are given by:

$$Q = \sqrt{Z_0}(I + \Gamma_L)\left[(I - \Gamma_0 S_{A11})(S_{A21}^{-1})(I - \Gamma_L S_{A22}) - \Gamma_0 S_{A11}\Gamma_L\right]^{-1} \tag{2-91}$$

$$G_0 = \frac{1}{2\sqrt{Z_0}}S_{21}(I - S_{RR}S_{11})^{-1}(I - S_{RR})$$

S_{RR}, S_{mn} and S_{Amn} are the N-port scattering parameters of the array, matching network, and preamplifier network as shown in Figure 2-20a and Figure 2-20b. The full scattering parameter matrices for the preamplifiers and matching networks are related to S_{mn} and S_{Amn} by the block matrix description of:

$$S_{RM} = \begin{bmatrix} S_{11} & S_{12} \\ S_{21} & S_{22} \end{bmatrix} \tag{2-92}$$

$$S_{RP} = \begin{bmatrix} S_{A11} & S_{A12} \\ S_{A21} & S_{A22} \end{bmatrix}$$

The covariance matrix at the preamplifier input ($\boldsymbol{\Psi_p}$) is given by:

$$\boldsymbol{\Psi_p} = BW k_b \left(T_\alpha \boldsymbol{I} + T_\beta \boldsymbol{\Gamma_0} \boldsymbol{\Gamma_0}^{\mathcal{H}} - T_\gamma^* \boldsymbol{\Gamma_0}^{\mathcal{H}} - T_\gamma \boldsymbol{\Gamma_0} + \boldsymbol{I} - \boldsymbol{\Gamma_0} \boldsymbol{\Gamma_0}^{\mathcal{H}} \right) \tag{2-93}$$

where BW is the bandwidth and T_α, T_β and T_γ are the amplifier noise wave temperature parameters (here assuming identical preamplifiers). $\boldsymbol{\Gamma_0}$ is the combined scattering matrix of the matching and coil networks given by:

$$\boldsymbol{\Gamma_0} = \boldsymbol{S_{22}} + \boldsymbol{S_{21}} (\boldsymbol{I} - \boldsymbol{S_{RR}} \boldsymbol{S_{11}})^{-1} \boldsymbol{S_{RR}} \boldsymbol{S_{12}} \tag{2-94}$$

The noise figure for an individual preamplifier is often described by (163):

$$F_{pre} = \frac{SNR_{in}}{SNR_{out}} = F_{min} + \frac{R_N}{G_S} |Y_S - Y_{opt}|^2 \tag{2-95}$$

where Y_S is the source admittance presented to the amplifier, Y_{opt} is the optimal source admittance, R_N is the equivalent noise resistance of an amplifier, G_S is the real part of the source admittance and F_{min} is the minimum noise figure of the transistor. $Y_{opt}, R_N\ F_{min}$ are the oft-quoted preamplifier noise parameters and are directly related to the amplifier noise wave temperature parameters as detailed in reference (164). Thus the introduction of noise in equation (2-93) can be seen to come from the noise from the amplifier and from the real part of $\boldsymbol{\Gamma_0}$, which is related to the resistive Johnson noise contributed by the coils and matching networks.

The noise figure of a cascaded system is given by (163):

$$F_{cas} = F_1 + \frac{F_2 - 1}{G_1} + \frac{F_3 - 1}{G_1 G_2} + \cdots \tag{2-96}$$

where F_n and G_n are the noise figure and gain of the n_{th} stages respectively. Consequently, after the preamplifier stage the noise contribution from subsequent stages are minimized by the ideally large gain of the preamplifier stage. Thus, excluding the minor effect of subsequent stages equations (2-89)-(2-94) can accurately describe the signal and noise of the MR front-end RF receive system, as well as any similar array of receivers. In addition, the description is put in terms of measurable and/or simulatable parameters: S-parameters and noise parameters of active devices.

In most cases, there are a number of simplifications that can be made to reduce the complexity of analysing the system:

- noise from the output side of preamplifiers is not coupled back into the system, so $T_\beta = 0, T_\gamma = 0$. This is typically valid for low frequencies where feedback by parasitic capacitance is minimized.

- in equation (2-95) the noise figure of the preamplifiers is close to the minimum noise figure (F_{min}), which is equivalent to $\frac{G_S}{R_N} \gg |Y_S - Y_{opt}|^2$.

- the matching networks have no loss associated with them

If the preamplifiers are assumed to add noise individually to each channel. based on the individual noise figure of each amplifier, the final noise covariance at the preamplifier output is then given by:

$$\Psi = Q(\Psi_p)Q^{\mathcal{H}} + \text{diag}(Q(\Psi_p)Q^{\mathcal{H}})(F_{pre} - I) \tag{2-97}$$

where F_{pre} is a diagonal matrix containing the noise factors of the preamplifiers.

The noise contribution to only individual channels proves to be good approximation under certain conditions, since noise introduced by the FET of a preamplifier is largely from the thermal generated channel noise on the output side of the preamplifier (164), that has marginal coupling back to the input side of the preamplifier. Therefore, the approximation that the preamplifier noise only affects the diagonal of the covariance matrix has been used in the past (165). It has been shown previously that, excluding active devices, the optimally combined signal from an array of receivers is identical with or without the removal of coupling (166). In theory, the active impedance of a multiport array can be noise matched to the preamplifier optimal input impedance as in a single receiver case, implying that there is no penalty to noise figure from mutual coupling (157). Nonetheless, The matching of array antennas can often be done in such way that coupling does not reduce the SNR (160).

A commonly employed method in the field MRI RF coil design the use of preamplifier decoupling. The concept of preamplifier decoupling can be explored by looking at the input impedance of a single receiver in Figure 2-20. If the value of the LC elements of the matching networks are defined by $\omega_0 = \frac{1}{\sqrt{C_n^m L_n^m}}$ the active input impedance at the coil input for receiver one is given by:

$$Z_{in}(1) = (Z_{RR} + Z_{out} - Z_{out}(1,1))^{-1} \begin{bmatrix} (L_1^m \omega_0)^2 \\ 0 \\ \vdots \end{bmatrix} \tag{2-98}$$

where Z_{out} is the output impedance observed at the coil ports given as:

$$Z_{out}(m,n) = \begin{cases} \dfrac{(L_n^m \omega_0)^2}{Z_{pre}}, & m = n \\ 0, & m \neq n \end{cases} \tag{2-99}$$

and Z_{pre} is a diagonal matrix containing the values of the preamplifier input impedances. In the case that the preamplifier input impedances are very small (2-98) can be approximated as:

$$Z_{in}(1) = \left(Z_{RR}(1,1) + \sum_{n=2}^{N} \frac{Z_{1n} Z_{n1}}{Z_{nn} + Z_{out}(n,n)} \right)^{-1} (L_1^m \omega_0)^2, \quad Z_{pre} \ll L_n^m \omega_0 \tag{2-100}$$

Consequently, for $Z_{out}(n,n) \gg Z_{1n} Z_{n1}$ the active impedance is the same as the impedance of the isolated coil $(L_1^m \omega_0)^2/(R_1^c + L_1^c + C_1^t)$, where R_1^c is the lumped coil resistance, L_1^c is the lumped coil inductance and C_1^t the lumped tuning capacitance shown in Figure 2-20b. Thus preamplifier decoupling removes the additional complication of coupling between elements of the receive array when matching and the associated coupling of noise and signal.

However, preamplifier decoupling places more constraints on preamplifier and matching design, and the use of highly reflective preamplifiers lessens stability. Instability in the preamplifier results in oscillations that may be many orders of magnitude higher than the MRI signal, which will appears as noise and image artefacts. Therefore, there is the case to be made that the MRI arrays can be built without preamp decoupling and achieve the same sensitivity (167).

As a final note on the network theory treatment of arrays, the intrinsic signal and noise covariance of the array can be stated for the case that the matching networks and preamplifiers have unity available gain and add no noise, so that $G_0 = I$ and $Q = I$, so:

$$s = \widehat{v_s} \tag{2-101}$$

$$\Psi = 4k_b T \mathbb{R}(Z)$$

where Z is the impedance matrix for the set of receivers. The use of equation (2-101) to evaluate the sensitivity of a coil array provides the intrinsic SNR (iSNR) (168, 169).

In MRI at high frequencies, the resistance of coils/receivers is usually dominated by the loss induced by the imaging sample due to random thermal motion and the resulting eddy currents, the level of which is directly proportional to the electric fields produced by the receiver per-unit-current. Therefore, in the case of body dominated noise there is a proportional increase in noise with frequency for a coil of the same geometry (22, 154, 170), while if the loss is dominated by loss in the windings the increase in resistance is instead related to the skin depth effect (163). Based on this fact a naïve approach to improving coil performance at low frequencies might be to use higher conductivity materials for coil development, however ultra-

pure copper has only a 5% higher conductivity than normal annealed copper (resulting in only a 2.5% decrease in resistance due to skin effect), which is negligible for the exorbitant increase in cost. A better strategy at low frequencies is therefore double winding the same coil, leading to square increase in the body loaded loss compared to a proportional increase in coil loss. In addition, for low frequencies where coil loss is dominant over loss from the body cooling coils to the temperature of liquid nitrogen (77K) can result in a factor of 2.8 improvement in SNR (171), however the coils must then be contained in airtight and insulated containers.

2.11.3 SNR Combination

The following formalism for pixelwise image reconstruction by multiple receivers follows that presented in reference (172). The combined signal from a set of independent receivers is given by:

$$\rho = \boldsymbol{w}^{\mathcal{H}} \boldsymbol{d} \tag{2-102}$$

where ρ is the resulting signal (pixel value in image combination), $\boldsymbol{w}$ is a vector containing the weighting coefficients and $\boldsymbol{d}$ is a vector of the signal from each independent receiver. The resulting SNR is given by:

$$SNR = \frac{\boldsymbol{w}^{\mathcal{H}} \boldsymbol{d}}{\sqrt{\boldsymbol{w}^{\mathcal{H}} \boldsymbol{\Psi} \boldsymbol{w}}} \tag{2-103}$$

where $\boldsymbol{\Psi}$ is the covariance matrix (153). For optimal combination (highest SNR) the weighting coefficients are given by:

$$\boldsymbol{w} = \boldsymbol{\Psi}^{-1} \boldsymbol{s} \tag{2-104}$$

where $\boldsymbol{s}$ is given by equation (2-90). Using equation (2-101) the intrinsic SNR (iSNR) for a receive array can therefore be stated as:

$$iSNR \propto \sqrt{\boldsymbol{s}^{\mathcal{H}} \mathbb{R}(\boldsymbol{Z})^{-1} \boldsymbol{s}} \tag{2-105}$$

2.11.4 Electromagnetic Simulation by the Finite Element Method

Analytical solutions for the fields produced and impedance parameters exist for specific and simple coil and load geometries (173). However, for the multitude of different coil designs and geometrically complex imaging regions numerical methods must be used to determine the relevant coil related RF parameters (174, 175). Electromagnetic simulation methods fall into two categories: time and frequency domain. In time domain methods the propagation and decay of electromagnetic fields/waves from a source is found with increments in time that are small

enough for a stable solution. In frequency domain methods, the steady-state solution is found assuming a sinusoidally varying source at a specific frequency. The objective of electromagnetic simulation is to determine the electric ($\mathbf{E}$) and magnetic ($\mathbf{H} = \boldsymbol{B}/\mu$) fields produced when the coil is excited by a source, where here μ refers to the magnetic susceptibility here, rather than a magnetic moment as earlier.

In this work the finite-element method (FEM) solver HFSS is used, so a brief overview of the methods of FEM is provided as follows. The first step in this method is discretizing the geometry into volume elements, by creating a mesh on the surface of the contained objects of different electromagnetic properties and then extending the mesh inside the different objects (178). The use of tetrahedronal elements is generally preferred due to their versatility (179) and the simplicity of converting a surface into triangular elements (180). Finally, to limit the size of the geometry terminating boundaries must be introduced, these can include perfectly matched layers, perfectly radiating and perfectly reflecting (magnetic or conductive walls) surrounding the solution volume (181). Due to the complexity and intricacies involved in forming the FEM mesh, and accurately solving and applying the field equations in FEM space, commercial software is typically used. This includes a number of different products: COMSOL, ANSYS (HFSS), CST, SIM4LIFE FEKO, etc. The main purpose in using numerical methods for coil design is to obtain the variables $\widehat{\boldsymbol{B}}_1^-, \boldsymbol{B}_1^+$ for a given input voltage/power, and $\mathbf{Z}$ so the analysis presented in equations (2-86)-(2-105) can be performed. Also, the simulated $\boldsymbol{E}$-field is used to calculated SAR according to equation (2-88).

2.11.5 Ultimate SNR

From equation (2-103) it is not clear that if there is any limit on the SNR obtainable by increasing the number of receivers, or by improvements in the receive design. However, it has been shown that there are theoretical constraints on the maximum SNR based on electromagnetic principles, termed the ultimate SNR (uSNR). The calculation of the SNR provides a basis for objectively comparing the performance of a receive array for imaging a particular region of interest. Therefore, methods for calculating the uSNR have been developed for simple geometries such as a cylinder or box (22, 182), a sphere (165, 183) and even in realistic models of the human head (184).

The theory of the ultimate SNR can be understood by looking at the general integral equations for the resistance, inductance and capacitance for an element in an array (163):

$$R_{ij} = \frac{1}{I_i I_j} \int_V \sigma(\mathbf{r}) \mathbf{E} \cdot \mathbf{E}^* \, dr \tag{2-106}$$

$$L_{ij} = \frac{1}{I_i I_j} \int_V \mu(\mathbf{r}) \mathbf{H} \cdot \mathbf{H}^* \, dr$$

where $I_{i/j}$ is the unit current for element i/j and the position dependent variables μ and σ refer to the permeability and conductivity, while **E** and **H** are the electric and magnetic fields produced per unit current. For MR frequencies and small coils the parallel/stray capacitance can be excluded from analysis. Since the magnetic and electric fields are coupled, and in general MRI involves imaging a lossy body (generally for imaging in the >10MHz range loss is body dominated), it can be seen that there is a resistance associated with the RF magnetic field produced by a coil, that by the principle of reciprocity results in Johnson noise being picked up by a receiver element.

To calculate the uSNR a set of infinite basis functions can be constructed that are solutions to Maxwell's equation for the particular imaging geometry:

$$E(\mathbf{r}) = \sum_i^\infty w_i E_i(\mathbf{r}) \tag{2-107}$$

$$H(\mathbf{r}) = \sum_i^\infty w_i H_i(\mathbf{r})$$

where w is equivalent to the weights in equation (2-103), with optimal values obtained by equation (2-104) with the covariance matrix found by determining the resistance matrix by integrating the electrical field of each basis-field (E_i) in equation (2-107) and applying equation (2-105). For example, in the interior of a source free homogeneous medium an infinite linear combination of plane waves may be used given by (22):

$$E_i(\mathbf{r}) = E_{i0} e^{-j[k_i \cdot r]} e^{j\omega t} \tag{2-108}$$

$$H_i(\mathbf{r}) = H_{i0} e^{-j[k_i \cdot r]} e^{j\omega t}$$

The set of equations to derive H_{i0} and E_{i0} are given by (22, 185):

$$H_{i0} = \frac{1}{j\omega\mu_0} k_i \times E_{i0} \tag{2-109}$$

$$k_i \cdot k_i = -j\omega\mu_0[\sigma + j\omega\varepsilon]$$

$$E_{i0} \cdot k_i = 0$$

$$k_i = \overline{k_i}\sqrt{-j\omega\mu_0[\sigma + j\omega\varepsilon]}$$

where $\overline{\boldsymbol{k}_i}$ is a unit vector. For an elliptical cylinder there is an analytical solution for the mutual and self-resistances of the plane waves given by:

$$\mathbf{R}_{ij} = \sigma E_{i0}{}^* E_{j0}{}^* \frac{2\sin\left((k_{jz} - k_{iz}{}^*)l\right)}{(k_{jz} - k_{iz}{}^*)} \frac{2}{k}\sqrt{\frac{\pi}{2}} r_c J_1(k' r_c), \tag{2-110}$$

where $k' = \left[c^2(k_{jx} - k_{ix}{}^*)^2 + (k_{jy} - k_{iy}{}^*)^2\right]^{1/2}$, J_1 is the first-order ordinary Bessel function, $r_c = \sqrt{\frac{x^2}{c^2} + y^2}$, l is half the cylinder length and x/y are the minor/major axis radii. With these sets of equations the ultimate SNR at position $\mathbf{r}$ can be determined defining the "sensitivity" of each plane wave at $\mathbf{r}$ as:

$$\widehat{B}_1^- = \mu_0 \frac{H_{ix}(\mathbf{r}) - jH_{iy}(\mathbf{r})}{2} \tag{2-111}$$

Therefore, given a sufficient number of the plane waves the uSNR can be calculated to a sufficient degree of accuracy and compared to the intrinsic SNR of a receive array with simulated values of the sensitivity for each element $\widehat{B}_1^-$ and resistance matrix $\mathbb{R}(\boldsymbol{Z})$.

2.12 Practical Radio-Frequency Coil Design

With the electromagnetic and network theory description of RF in MRI provided thus-far the practical design of RF coils are now provided.

2.12.1 Volume Coils

To produce a uniform magnetic field within a cylinder a current density that is sinusoidally distributed about the cylinder's surface is required; a birdcage coil is made of a set of conducting legs spaced equally around a cylinder that approximates this current distribution (186, 187). A diagram of the birdcage coil with discrete legs and rungs is shown in Figure 2-21(a) with the capacitors used to tune the birdcage coil visible. The optimum current distribution for an elliptical surface has also been derived, which maximizes the usage of space in the MRI bore (188). Asymmetrical designs also increases the flexibility of design, which is useful for multi-nuclear MRI where the birdcage coil must fit in the available space in the bore of the MRI scanner and be as large as possible for high performance and patient comfort (189, 190).
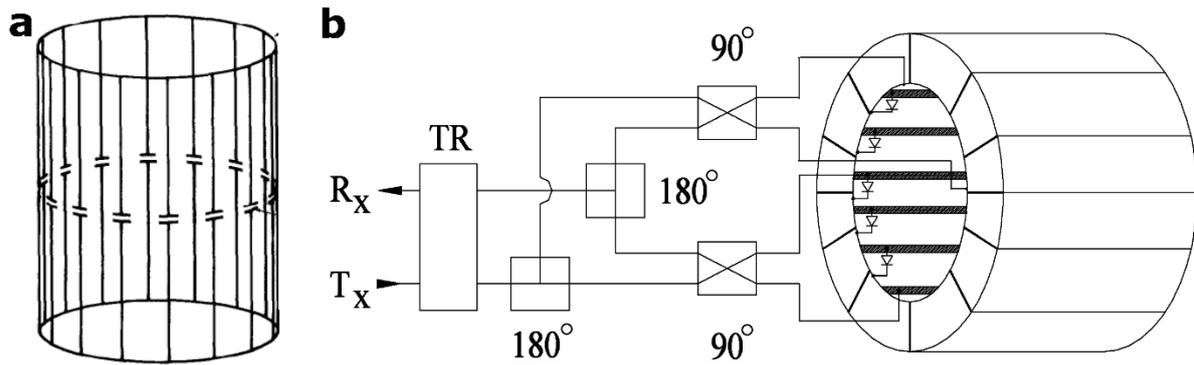
Figure 2-21: The homogeneous resonator birdcage coil is shown in (a), while the TEM coil is shown in (b). ((a) is reprinted permission from (191) and (b) is reprinted from (192))

Transverse electromagnetic (TEM) coils approximate the same sinusoidal distribution, but individual elements, equivalent to the legs of the birdcage, are excited individually and the return path of the current is provided by a surrounding ground plane vs. the end rings of the birdcage coil (193). TEM coils are especially suited for higher frequency (>3T) MRI (194). The phase and amplitude of excitation to the elements can be varied to optimize the homogeneity of excitation (195). The elements may also be excited with fixed phase and amplitude as shown in Figure 2-21(b), where although there are 16 elements only four are fed and the remaining are excited through inductive coupling (192). At higher field strengths (7T) the TEM coil has better homogeneity, SAR (196) and SNR compared to birdcage coils (197). At ultra-high field arrays of elements placed around the ROI, with a geometry similar to TEM coils, are often used with independently controlled phase and amplitude to optimize homogeneity. Generally, for frequencies >64 MHz these transmit arrays may have better performance, but at 64 MHz result in a significantly larger SAR (196).

2.12.2 Receive Arrays

Receiver coil arrays were introduced early in the history of MRI as a method of extending the SNR benefits of small surface coils to larger fields of view (198, 199). Signal is received from multiple coils and optimally combined as outlined by Roemer et al. (148). Additionally, the localized sensitivity profiles of the coils can be employed to reduce the acquired k-space data for accelerated imaging (42, 45). Three of the most common surface coil elements in arrays are shown in Figure 2-22. The microstrip coil (geometry optimization presented in (168)) consisting of a long conductor and ground plane return path along with the loop coil (optimization of size for region presented in (155)) is shown in in Figure 2-22(a). The loop coil

is also shown Figure 2-22(b) combined with a butterfly (figure of 8) coil, whose geometry is optimized for quadrature combination with a loop coil in (200).
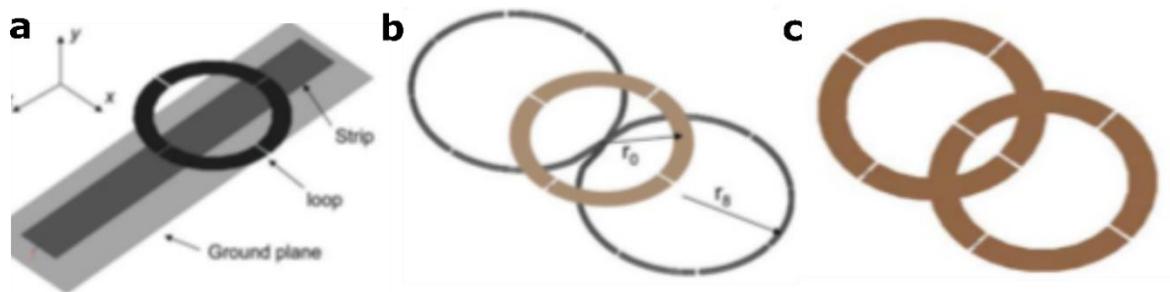
Figure 2-22: Commonly used coil in quadrature combination with loop coils. In (a) a microstrip coil is shown with a loop coil, in (b) a butterfly coil is shown with a loop coil and in (c) two loops coils are joined together. (reproduced with permission from (200))

Examples of array geometries typically employed are shown in Figure 2-23. Arrays like those in Figure 2-23(a) are useful for reducing the acquired k-space data in the direction of the coils by parallel imaging as described earlier (42). The array in Figure 2-23(c) provides the same advantage for a FOV with cylindrical geometry. Figure 2-23(b) and (e-l) are variations on these designs, while (d) is a demonstration of using orthogonal coils that are naturally decoupled to image over the same region. Generally, for best MRI imaging performance high-density coil arrays are used for receive in combination with volume coils for transmit (190).
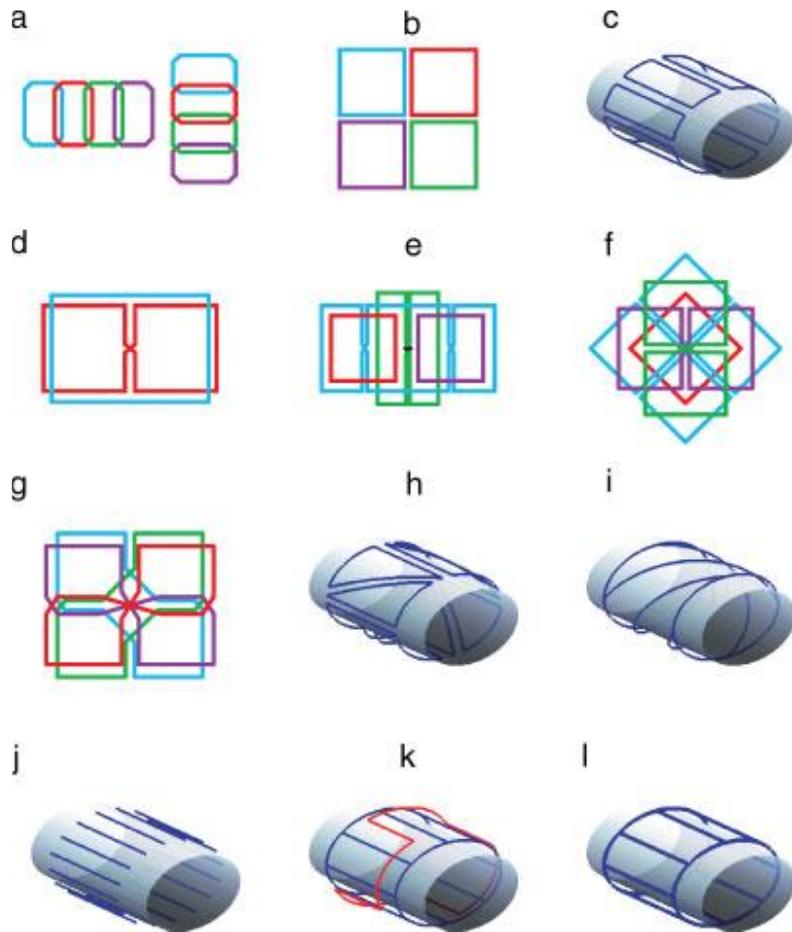
Figure 2-23: Variations of coil array designs for high sensitivity and parallel imaging performance (reproduced from permission from (201))

2.12.3 Coil Design for Multi-Nuclear Imaging

Many of the principles for multinuclear coil design are exemplified in reference (202); an early study in the history of MRI that uses modern imaging methods. Firstly, the RF coils used for different nuclei need to be isolated from each other. As shown in Figure 2-24 the coils for ^{1}H and ^{23}Na are naturally orthogonal due to their geometry. Common designs of nested/overlaid coils separately used for imaging different nuclei are shown in (203), where coils are either naturally orthogonal or isolated by the use of resonant "traps" on the coils. Secondly, different amplifiers and hardware are switched between before transmission and reception of each nuclei because of the different resonance frequencies (17 MHz for ^{23}Na and 64 MHz for ^{1}H at 1.5T). In this case, the different T_1 values (≈ 50 μs in ^{23}Na and ≈ 1s (204) for ^{1}H) are taken advantage of by performing interleaved imaging on the nuclei.
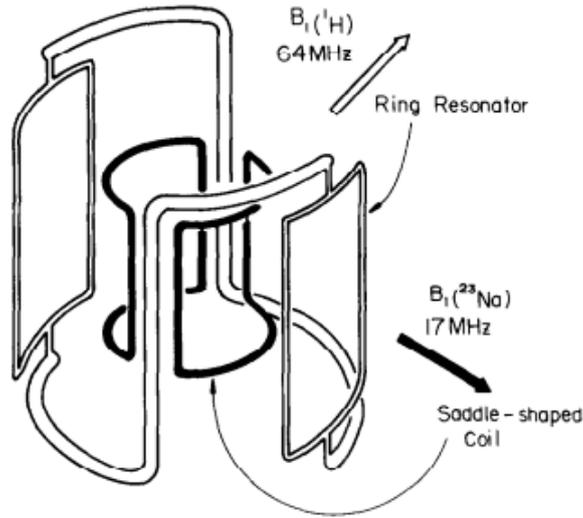
Figure 2-24: Example of orthogonal coils used to image different nuclei (^{1}H and [23]Na) in the same FOV. (reproduced with permission from (202))

Other methods can include the design of dual-resonant coils that operate at the resonance frequencies of both nuclei. One specific design is a resonant ladder network (205) tuned to both ^{31}P and ^{1}H using parallel inductor/capacitor components termed "traps" (206). To be used in conjunction with transmit coils receive coils are decoupled through the use of diode controlled high impedance "traps" (Figure 2-25a). Without these traps large currents would be induced on the receive coils that would distort the transmit field; the required blocking impedance provided by the traps to limit the distortion is a function of the receive coil area (207).

For dual ^{19}F and ^{1}H imaging a coil design employing a split resonance frequency from strong mutual coupling was implemented in (208), allowing matching at both frequencies so that simultaneous imaging could be performed on both nuclei with nearly identical coil sensitivity (209). This design is especially suited to [19]F (60.0 MHz) and [1]H (63.8 MHz) imaging because of their close resonance frequencies, but for [129]Xe and ^{1}H/[3]He dual tuned coils a common method is use of "trap" circuits that allow a coil to be resonant at different frequencies (210).

2.12.4 Dual-Tuned Coils

Figure 2-25 shows two circuits used for the implementation of multi-tuned coils. The input impedance (Z_{in}) of the coil in Figure 2-25 is given as:

$$Z_{in} = \frac{(Z_p)(R_{coil} + j\omega L_{coil} + \frac{1}{j\omega C_t} + Z_p)}{(Z_p + R_{coil} + j\omega L_{coil} + \frac{1}{j\omega C_t} + Z_p)} \tag{2-112}$$

60

where R_{coil} is the series resistance of the coil and L_{coil} is the coil inductance. For a multi-tuned coil the reactive elements Z_p and Z_s are designed so the matching condition $Z_{in} = Z_0 = 50\ \Omega$ is met at multiple frequencies.
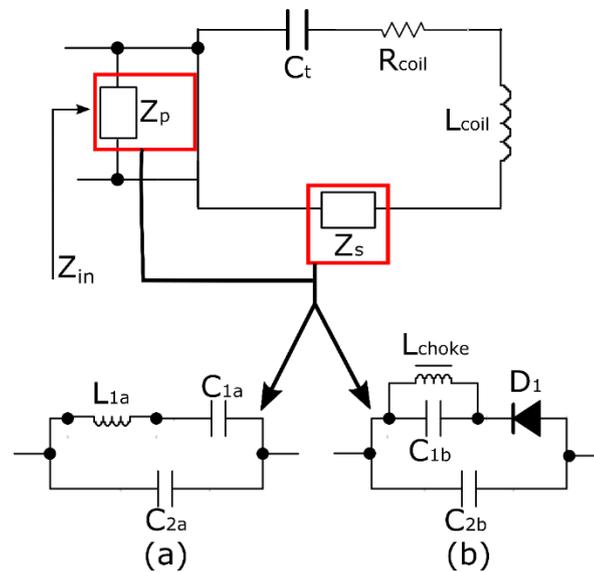
Figure 2-25: Various circuits used for multi-tuned coils: the coil with tuning/matching elements used to multi-tune coils identified in red boxes (1) a generalized passive trap circuit (b) an actively switched capacitor-diode circuit.

Figure 2-25(a) shows a generalized tank circuit (211), which typically only employs the L_{1a} and C_{2a} elements (212-214). The equivalent series resistance (ESR) of a parallel LC circuit is higher than the ESR of the inductor alone, while the ESR of the LCC network shown is lower (215). The operation of passive tank circuits (used for example for ^{23}Na, ^{31}P, and ^{1}H (216)), in either matching or tuning circuitry (217), may result in coils which are comparable to single tuned counterparts in terms of efficiency and homogeneity (218). For example, the efficiency with trap circuits can be as high as 98% at the nuclei with lower frequency (219). In addition, reference (218) reports an operating efficiency of 80-90% and 40-50% for the lower (^{23}Na) and higher (^{1}H) frequency nuclei compared to single tuned counterparts, respectively. This also indicates the large impact loss in trap circuits can have on coil performance.

Another method employing this trap circuit topography, with C_{1a} excluded, tunes the parallel LC circuit L_{1a} and C_{2a} to the Larmor frequency of a nuclei. The large blocking impedance greatly reduces induced current on the coil so separate coils tuned to different nuclei may be used concurrently. The combination of many such trap circuits can theoretically be used for many multiple resonance frequencies, but a significant increase in overall loss would occur as described in reference (212) where a tank circuit used to block currents on a coil tuned to ^{1}H (63.8 MHz) at the ^{3}He frequency (48.7 MHz), which utilized a 30 pF capacitor (C_{2a}) and 360 nH inductor (L_{1a}). For a Q_L of 150 and Q_C of 1500 this would correspond to a series resistance

of 2.3 Ω at 63.8 MHz. Because of the increased resistance from trap circuits using either method the configuration in Figure 2-25(b) may be preferred, despite the added complexity of introducing DC biasing.

For the case of the diode switched capacitor shown, when forward biased the tuning capacitors of the coil C_{2b} and C_{1b} combine in parallel, and when reverse biased only C_{2b} is functional. The ESR of a forward biased diode (0.2 Ω in (214)) can be considerably less than low quality factor inductors (eg. $Q \sim 120$ at 128 MHz in (220)). Therefore, a diode switched circuit such as that shown in (b) will result in lower loss when compared to tank circuits. Also, the implementation of many diode switches in parallel can be used to create a wide range of switchable frequencies of operation, without any additional loss when compared to a single switch (221). However, in high power transmission the RF pulse may unintentionally reverse bias the diodes and change the tuning with pulse transmission power. The next section introduces the use of MEMS as an alternative to diodes in the network of Figure 2-15(b).

2.12.5 Application of Microelectromechanical Systems to Switching coils

Microelectromechanical systems (MEMs) are a fundamentally different technology from solid-state devices because they involve moving (mechanical) parts. To be used in multi-tuned coils MEMs replace the use of diodes in circuit topologies employing the strategy presented in Figure 2-25(b). The basic element of a common MEMs switch is shown in Figure 2-26, where the beam that makes up the working element of the switch is activated by an applied voltage potential with the gate. To introduce/implement MEMs in MRI RF coil circuitry they must first be evaluated against the current state-of-the art solid-state devices such as PIN diodes and FETs. The figures of merit that can be used to compare typical solid state devices (diodes, FET switches) include isolation, insertion loss, switching speed, reliability, power handling, signal distortion, power loss, cost and implementation complexities necessitate MR system hardware changes. These quantities are highly dependent on the frequency of operation and at high frequencies MEMS have proven to be better than solid state devices (222), hence their use in many high frequency satellite and phone antenna applications.
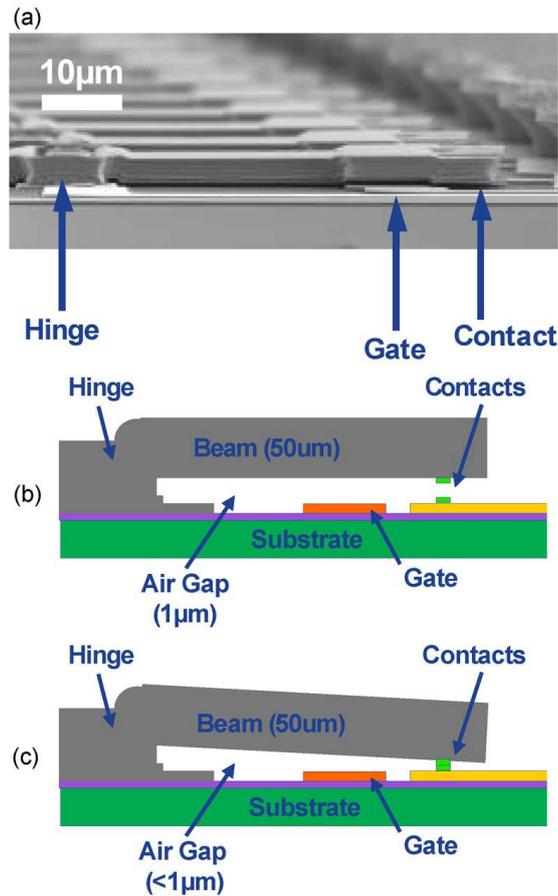
Figure 2-26: (a) Side-view of MEMs switch. An array of these switches reduces the effective resistance. When actuated (gate voltage high) the contacts connect and when open (gate voltage low) a high isolation is present (reproduced with permission from (224) © 2012 IEEE)

There is little room for improvement at low frequencies for the listed figures of merit of solid state devices (222). MEMs still provide some benefits, such as very low power consumption and high isolation, but their power handling, reliability and insertion loss is typically worse at low frequencies. Recent improvements in the technology involving the use of a large array of MEMs, improved driver circuitry allowing improved switching speed and reduced arcing has effectively eliminated these downsides (224). MEMs switches typically require higher DC voltages ($\geq 30V$) than PIN diodes. Also, MEMs are particularly susceptible to failure due to electrostatic discharge, which can fuse the moving parts in place, and to stiction, or cracking from mechanical impact (225). Typically, solid-state devices are more mechanically and electrically stable and therefore more reliable (226). However, MEMS have the benefit that they cannot be reverse biased with high transmission power and have a similar ESR to high-performance PIN diodes.

2.13 **Summary and Conclusion**

In this chapter, the essential basics of MRI and state-of-the art in the fields of inert gas lung MRI and multi-nuclear RF coil design was established. The background provided should allow the reader to understand the motivation and results of the research presented in the following chapters of original research in this thesis.

Chapter 3: Comparison of MEMS switches and PIN diodes for switched dual tuned RF coils[1]

3.1 Overview

Purpose: To evaluate the performance of micro-electromechanical systems (MEMS) switches against PIN diodes for switching a dual-tuned radio-frequency (RF) coil between ^{19}F and ^{1}H resonant frequencies for multi-nuclear lung imaging at 1.5 T.

Methods: A four-element fixed-phase and amplitude transmit-receive RF coil was constructed to provide homogeneous excitation across the lungs, and to serve as a test system for various switching methods. The MR imaging and RF performance of the coil when switched between the ^{19}F (60.0 MHz) and ^{1}H (63.8 MHz) frequencies using MEMS switches, PIN diodes and hardwired configurations were compared.

Results: The performance of the coil with MEMS switching was comparable to the coils performance with PIN diode switching in terms of RF measurements, transmit efficiency and image SNR on both ^{19}F and ^{1}H nuclei. When the coil was not switched to the resonance frequency of the respective nucleus being imaged, reductions in the transmit efficiency were observed of 32% at the ^{19}F frequency and 12% at the ^{1}H frequency. The coil provides transmit field homogeneity of ±12.9 % at the ^{1}H frequency and ±14.4 % at the ^{19}F frequency in phantoms representing the thorax with the air space of the lungs filled with perfluoropropane gas.

Conclusion: MEMS and PIN diode were found to provide comparable performance in on-state configuration, while MEMS were demonstrated to be more suitable in off-state high-powered operation (>1 kW) with higher isolation and necessitating a lower DC switching voltage than reverse biasing of PIN diode. Additionally, the benefits of switching the lung T-R coil between the ^{19}F and ^{1}H resonances was demonstrated, despite the proximity of their respective Larmor frequencies.

---

[1] The work presented in the chapter has been published in the journal Magnetic Resonance in Medicine: A. Maunder, M. Rao, F. Robb, and J. M. Wild, "Comparison of MEMS switches and PIN diodes for switched dual tuned RF coils," *Magn Reson Med,* 2018;80(4):1746-53. Experiments, simulations and analysis on data were carried and described in the written manuscript by AMM. Manuscript revisions performed with MR, JMW, FR

3.2 **Introduction**

In non-proton MRI applications, it is desirable to be able to acquire ^{1}H structural imaging that is co-registered to the complementary functional imaging provided by the other nucleus, as demonstrated previously with hyperpolarized gas lung MRI (128). The motivation for this work was development of switched dual-tuned radio-frequency (RF) coil designs to allow detection of inhaled C_3F_8 gas and ^{1}H signals from the lungs at 1.5T in the same scan session.

In previous human lung imaging studies with perfluorinated ^{19}F gases, the ^{1}H body coil has typically been used with an actively decoupled ^{19}F vest coil (131). The use of a coil for both ^{1}H and ^{19}F nuclei without dual-tuning has been implemented previously (227), but the detection sensitivity and homogeneity was only optimized at the ^{19}F frequency. Trap circuits are commonly employed to tune the coil resonance to multiple frequencies (210) using inductive and capacitive elements in parallel. However, for ^{19}F (60.06 MHz at 1.5 T) and ^{1}H (63.8 MHz at 1.5 T) the bandwidth of passive traps with the typical Q-factors of commercially available components is comparable to the frequency separation, limiting their use, as discussed previously (212). Another approach is to actively switch-in capacitors parallel to the existing tuning capacitors using PIN diodes, and more recently the use of field effect transistors (228) and micro-electromechanical systems (MEMS) (223, 229, 230) have also been reported. The equivalent series resistance (ESR) of these three devices are reported to be insignificant when compared to the quality factor (Q) of trap circuit inductors (eg. $Q \sim 120$ at 128 MHz in (220)), which results in negligible additional loss. For example, when comparing a dual-tuned coil design to single tuned counterparts, SNR losses of 25% and 50% were reported for ^{19}F and ^{1}H, respectively (231), while the switching employed in (232) resulted in more equivalent performance for imaging both ^{19}F and ^{1}H when compared to respective single tuned coils. Therefore, due to the close frequencies of ^{19}F and ^{1}H at 1.5T the use of switching is favoured.

Recent improvements in the technology for MEMS switches and associated driver circuitry has allowed increased switching speed, better power handling and reduced insertion loss (224), so that MEMS switches have been successfully demonstrated for coil decoupling (233) and reconfigurable RF coils (226) in MRI. A summary of typical performance parameters for FETs, MEMS or PIN diodes is presented in Table 3-1, with the specific values for the PIN diodes and MEMS components used in this study. Notably, the switching speed has been found to be limited by the driver circuitry rather than the devices themselves (228). It would therefore be beneficial to use low DC power MEMS or FETs for switching, but for FETs the breakdown voltage is lower than often present for high power transmission pulses, which restricts their use.

In this Chapter two methods for switching the matching network tuning are compared: MEMS and PIN diodes, and these are compared to a hard-wired configuration. The switching comparison is exemplified

using a four element fixed phase/amplitude transmit-receive RF coil designed for lung imaging of ^{1}H and ^{19}F perfluorinated gases at 1.5 T.

Table 3-1: Performance parameters of common switching devices: Pin diodes, MEMS and FETs.

Device	Isolation Impedance	Switching Speed (µs)	Current (mA)	Cost	Size	Control Voltage	Peak Current	Stand-off Voltage	R_{on} Ω
PIN Diode MA4P7435F-1091T	< 3 pF	0.35-35 (228, 234, 235)	> 100	low	small	~5V	10 A	Peak Reverse 1100V	< 0.3
GaAs FETs	3.1-7.1 pF (228)	Similar to diode (228)	< 0.001	medium	medium	~5V	2-6.3 A (228)	Vds breakdown ~100 V (228)	0.28-0.6 (228)
MEMS MM7100	< 2 pF	~4	< 0.001	high	large	82 V	5 A	500 V	~0.4

3.3 Methods

3.3.1 Component evaluation - Power Handling of PIN Diode and MEMS

The mechanism of actuating MEMS switches is fundamentally different to that of PIN diodes. The MEMS used here consist of an array of beam type structures that operate as relays actuated electrostatically by a DC voltage applied between the beam and gate (233). A representative side view of the MEMS structure is shown in Figure 3-1a displaying the method of operation, as the switch is actuated the beams make contact with the central conductor providing a connection between RF_a and RF_b in the circuit schematic model. More details on the device structure are provided in reference (224). To compare the large signal behaviour of both PIN diode and MEMS under the higher RF transmit power conditions experienced in whole-body MRI, a bench-top test was set up. A pulse-modulated signal of 60 MHz with pulse duration of 0.2 ms (duty cycle 0.02%) was generated by a WS8352-Taber waveform generator. A 335953-Picker linear pulse amplifier was used to generate peak output powers from 7.3 – 2380 W. The output time-domain voltage waveform was measured on a high-speed oscilloscope (DSO 104A-Keysight) after 30 dB attenuation. Transmission to the attenuator was through MEMS switch or PIN diode placed in series, and DC bias isolated by choke inductors. The MEMS switch configuration was evaluated with the switch in open or closed position, and the PIN diode configuration was evaluated with varying reverse bias voltages and forward bias currents.
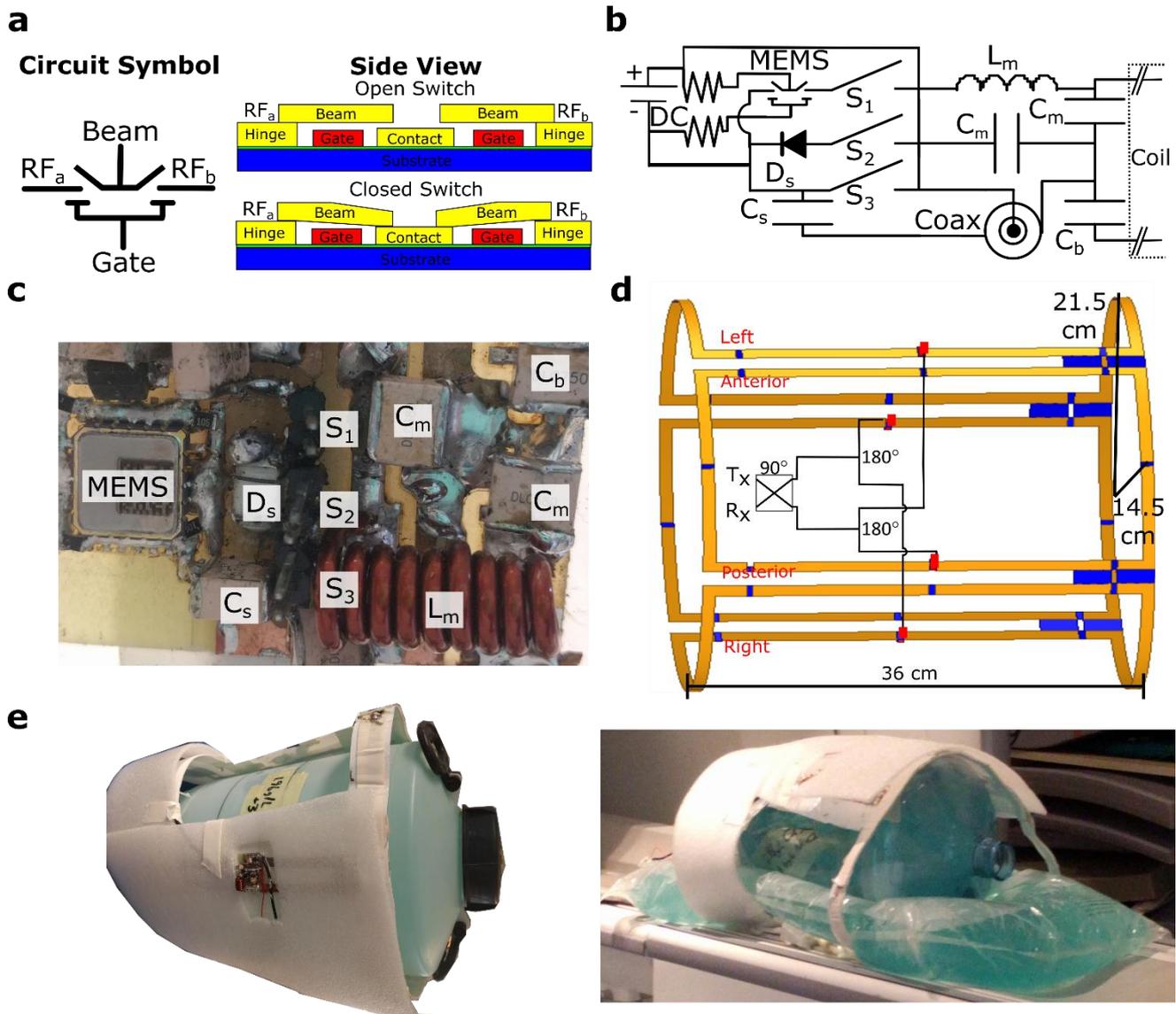
Figure 3-1: a: Circuit schematic of MEMS switch used here and wafer level representative diagrams of the devices employed b: A circuit schematic of the matching network design employing the various switching methods. c: The constructed matching network on anterior coil. d: Schematic of transmit-receive coil for 19F and 1H imaging at 1.5T with dimensions labelled. Included in the driving circuitry is a 90° hybrid, a pair of 180° splitters/combiners, and a T/R switch. e: The coil prototype with cylindrical and bag phantom used to emulate body loading.

3.3.2 Coil Design for Switching Application

To test the switching performance, a four element fixed phased transmit-receive coil was designed for dual tuned use for imaging ^{19}F (60.06 MHz) and ^{1}H (63.8 MHz) at 1.5T on a GE Signa HDx system equipped with a 4kW broadband RF amplifier. A circularly polarized B_1^+ excitation was achieved using a combination of 90º and 180º hybrid circuits that were custom built for both the ^{1}H and ^{19}F frequencies. The circuit schematic and constructed splitter for the 180° combiner is shown in Figure 2-5. The 90° hybrid has a similar design layout, but modified for the different lumped impedance equivalent (163).
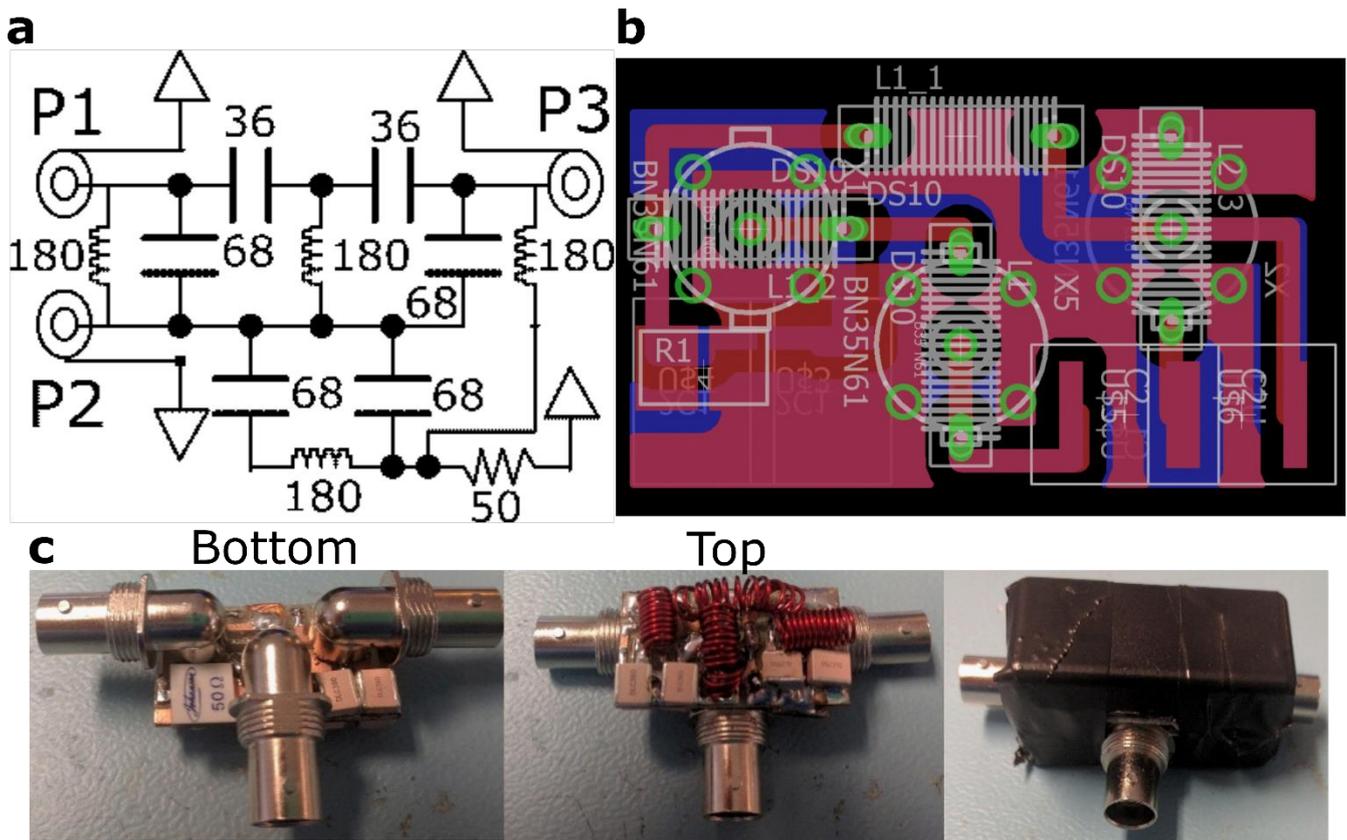
Figure 3-2: **a:** Circuit schematic for lumped element rat-race (branch-line) 3 dB power splitter. Inductance is in nH and capacitor values are in pF, **b**: the PCB outline and **c:** top and bottom views of the splitter, and placed inside the protective box.

In the matching network topography shown in Figure 3-1b, the capacitor C_s was switched-in to change the matching tuning (resonance) of the coil from the Larmor frequency of ^{1}H to ^{19}F by three possible mechanisms:

(i)   MEMS (MM7100**,** MenloMicro, Irvine, CA, USA) switched on by application of 82 V DC,

(ii)   PIN diode (MA4P7435F-1091T, MACOM, MA, USA) forward biased with 100 mA DC current,

(iii)   Hard-wired configuration for either nucleus.

The matching capacitance (10C package, Dali Capacitors, Dalian, China) and inductance values were; $C_m = 68$ pF and $L_m = 92\ nH$ for the left and right coils and C_m =56 pF and L_m =111 nH for the anterior and posterior coils, as annotated in Figure 3-1c. The capacitor was C_s=75 pF for all four coil elements. The manufactured matching networks are shown in Figure 3-1c. RF scattering parameters were measured on the bench using an Agilent E5061A Network Analyzer (Keysights, Santa Clara, CA). To characterize the loss of the matching networks, the scattering parameters of the matching network were measured without the coil connected and the power loss ratio, P_{LR}, was calculated (163).

Decoupling between adjacent coil elements was achieved using capacitive decoupling networks (236). The axial cross section of the modelled RF coil follows the conformation of an ellipse and the topology and dimensions of the coil (Figure 3-1d) were designed to provide a receive sensitivity and transmit field profile that covered the lungs of a large adult male, with homogeneity within the region of interest

comparable to a body coil. The widths were 25.5 cm for the anterior/posterior and 30 cm for the right/left elements coils. The coils were constructed from 11 mm wide and 72 µm thick self-adhesive copper tape mounted on a flexible Polytetrafluoroethylene substrate. There were five capacitor break-points in each coil. For ^1H imaging and RF measurements a cylindrical phantom was used consisting of 3.6 g/L NaCl and 1.96 g/L $CuSO_4 \cdot 5H_2O$ salt solution (237) to represent a human load. For ^{19}F imaging two glass canisters (2 L volume) were filled with C_3F_8 gas mixed with 21% O_2 at 1.5 bar pressure, which emulates the air-space in the human thorax. The glass phantoms were placed in a cylindrical shell and surrounded with a 12L bag containing the saline solution and placed over another equal volume bag for suitable loading. The phantoms and coil are shown in Figure 3-1e.

3.3.3 Simulation

The finite-element method solver software HFSS (ANSYS, Canonsburg, PA) was used for full-wave electromagnetic simulation of the impedance parameters, right circularly polarized transmit field B_1^+ and the left circularly polarized field per-unit-current $\widehat{B_1}^-$ (using current sources in place of lumped ports) for each receive element. Coils are tuned, decoupled and matched using EM simulation. The reported B_1^+ was normalized for a 1 kW RMS input power.

3.3.4 Imaging tests

Measurement of T_1 of both ^1H and ^{19}F was performed in homogeneous phantoms by 2D spoiled gradient echo (SPGR) imaging. First, the flip angle (FA) was fit against image intensity with varying input power with TR $\gg T_1$ (TR 600 ms for ^1H phantom experiments and TR 80 ms for ^{19}F in C_3F_8/O_2 phantom). Next, T_1 was fit against the image intensity with varying FA, according to equation (2-50), but with TR$<T_1$ (TR 8 ms for ^1H phantom experiments and TR 7.5 ms for ^{19}F in C_3F_8/O_2 phantom).

To normalize the data to SNR units the signal was first divided by the standard deviation of noise in images was measured in a signal-free region of greater than 100 pixels as described in (239). To compare the effect of the respective switched tuning methods on transmit efficiency, the FAs were measured for ^1H and ^{19}F SPGR imaging by varying input power and fitting FA according to equation (2-50) with the phantom measured T_1's for ^1H and ^{19}F (reported in results section) when the coil tuning was set to both ^{19}F and ^1H respectively. The corresponding transmit efficiency with known input power and pulse width was subsequently calculated.

3.3.5 In-vivo imaging

In vivo lung imaging evaluation was performed with inhaled C_3F_8 mixed with 21% O_2 with a healthy adult male volunteer (28 y) following informed consent and a protocol approved by UK National research

ethics committee. Three-breaths of the gas were inhaled and then 3D ^{19}F SPGR imaging was performed within a single breath-hold (37 s scan time). In addition, ^{1}H 3D SPGR anatomical imaging was performed during a separate breath-hold (13 s) of air with the lungs at the same inflation level. Both images were localized to cover the same geometry. MEMS were used to switch between the two tuning states during in-vivo imaging. A summary of all sequence and acquisition parameters used for the imaging experiments are provided in Table 3-2.

Table 3-2: Imaging parameters for coil performance evaluation

Measurement	Sequence	TE (ms)	TR (ms)	BW (± kHz)	Matrix size	FOV (cm^3)	Mean FA (°)	Avg.
^{1}H – T$_1$	2D Axial SPGR	4.6	FA fit - 600 T$_1$ fit - 8	14.76	128× 128 × 1	40× 40 × 1	varied	1
^{19}F – T$_1$	2D Axial SPGR	3.4	FA fit - 80 T$_1$ fit - 7.5	8.06	30× 25 × 1	30× 24 × 10	-	20
^{1}H – Tx efficiency	3D Coronal SPGR	3.1	8 ms	31.25	128× 96 × 30	44 × 33 × 30	-	1
^{19}F – Tx efficiency	3D Coronal SPGR	2.1	5.1	6.94	50 × 42 × 10	30× 24 × 20	-	10
^{1}H – In-Vivo	3D Coronal SPGR	3.7	9.1	8.06	100× 100 × 28	42× 42 × 28	35	1
^{19}F – In-Vivo	3D Coronal SPGR	0.9	4.3	10	50 × 42 × 14 (75% kx)	42× 34 × 28	27	15

3.4 **Results**

3.4.1 **Coil Bench Testing**

Both the MEMS when switched closed, and PIN diode when forward biased, remained operational up to the maximum powers tested (2380 W, or approximately 6.9 A peak current), in accordance with the maximum values specified in Table 3-1. However, as demonstrated in Figure 3-4b the reverse biased PIN diode began to conduct RF power when the reverse bias DC voltage was lower than the peak RF voltage, which was not the case with the MEMS switch in the open position. However, at the maximum power (equivalent to a peak voltage of 690 Vpp as delivered to 50 Ω load), the MEMS switch in the open position suffered critical failure. Figure 3-4d displays measured pulse waveforms with increasing RF power and reverse bias of PIN diode demonstrating conduction was primarily coming from undesired injection of carriers in the intrinsic region on the negative voltage swing. Additionally, with high power there was an observed droop in the voltage over the pulse length when the diode was insufficiently reverse biased. This was related to rapid heating of the PIN diode during the RF pulse resulting in increased impedance. The waveform observed when the pulse length and power was increased (Vpp = 648V) shows the effect

became more pronounced and also led to device destruction. The same droop was not observed in any configuration other than with PIN diode insufficiently reverse biased, as the waveform obtained using the same power and 3 pF capacitor in place of the PIN diode corroborates. The MEMS switch used here was found to have a marginally higher isolation (19.4 dB) when compared to the diode (18 dB) when a sufficiently high reverse bias voltage was applied. The power levels tested on the bench were higher than those expected in the scanner and with the maximum 2kW RMS input pulse there was no observed unintentional reverse biasing of the forward-biased PIN diode or failure of the MEMS switch.
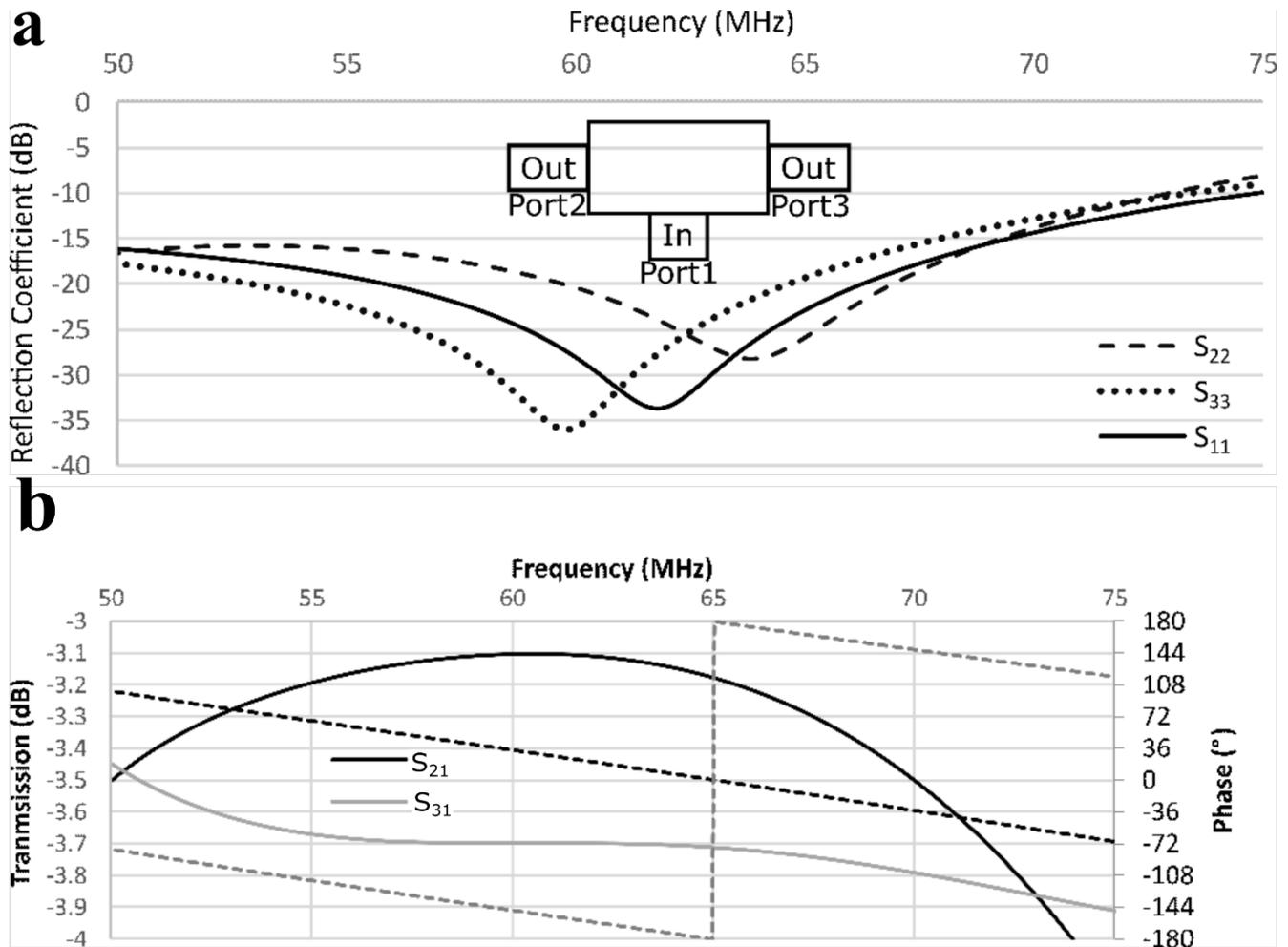
Figure 3-3: **a**: Measured reflection coefficients for three ports of 180° hybrid combiner and **b**: transmission from input port (port 1) and output ports (port 2 and port 3) with relative phase.

The measured unloaded and loaded quality factors of coils were 165 and 14.4 for anterior/posterior coils and 195 and 14.3 for right/left coils, respectively. The measured coil resistance when loaded with a cylindrical phantom was $\sim$24 Ω for the anterior/posterior coils and $\sim$26 Ω for left/right coils (Figure 3-1e). The reflection coefficient of one of the coil elements (right) when switched between the ^{19}F and ^{1}H frequencies via each of the three methods is shown in Figure 3-4a. The reflection coefficients of all of the elements were found to be less than -20 dB at the frequencies of interest (60.06 MHz for ^{19}F and 63.8 MHz for ^{1}H). The 90° hybrid and 180° power dividers used had a reflection coefficient less than -15 dB

for both frequencies with insertion loss of <0.5 dB as shown in Figure 2-10 for the 180° combiner. The decoupling between nearest neighbour coils (e.g. anterior and right) was optimized for the ^{19}F frequency, where isolation was greater than 15 dB for quadrature channels. P_{LR} was 12 ± 2 % for the matching network for MEMS, PIN diode and hard-wired configurations of the coil, which was verified with three repeated measurements.
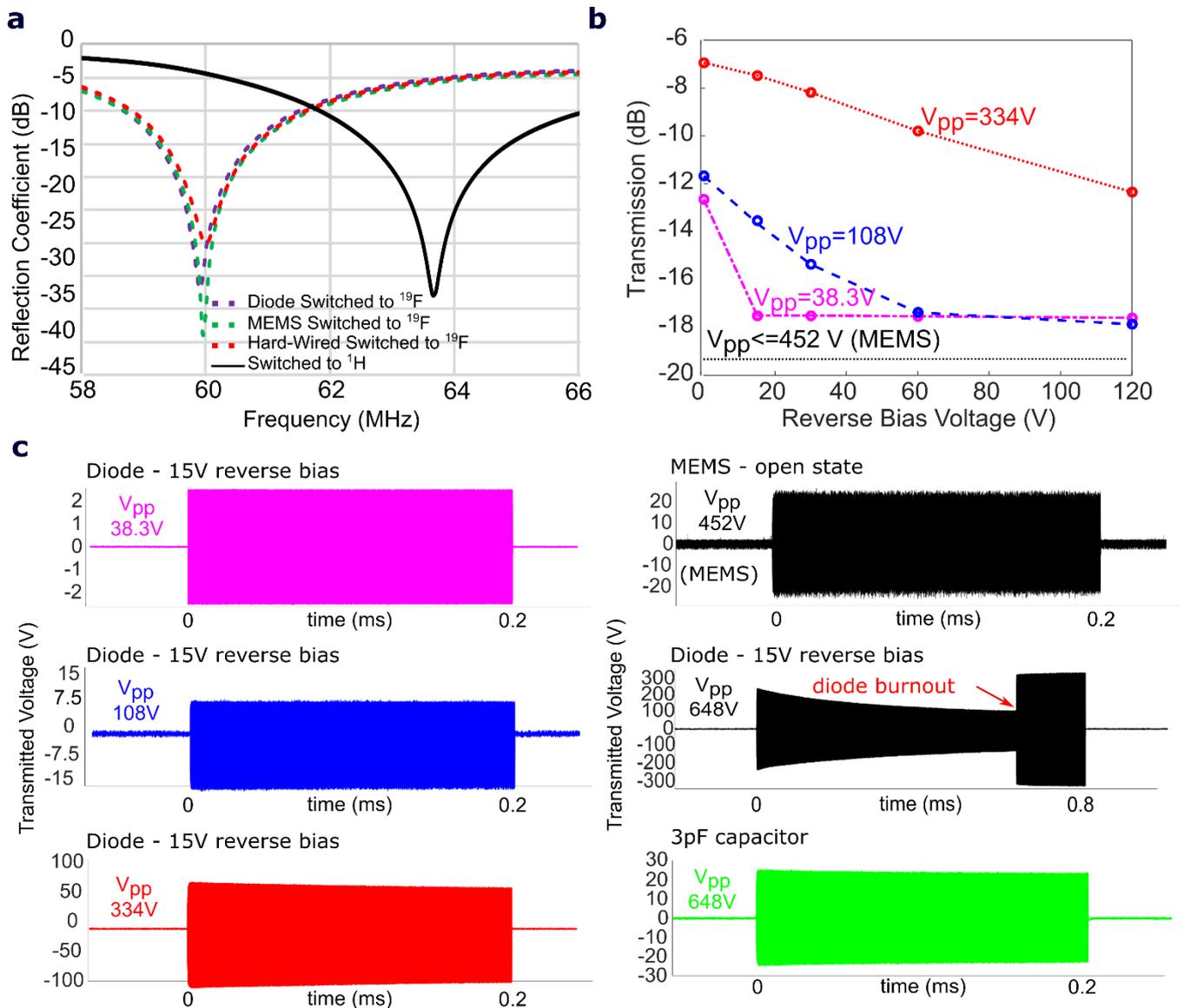
Figure 3-4: a: Measured right coil reflection coefficient when coils are tuned to ^{1}H or switched to ^{19}F tuning by the three methods: Diodes, MEMS and hard-wired. b: Transmission relative to operation in the conducting state for MEMS and PIN diode with different reverse bias voltages c: Measurement waveforms with increasing RF power when PIN diode is reverse biased by 15V and with MEMS in open-state. The waveform during an extended high-power pulse with PIN diode leading to device destruction, as well as transmission with a series 3 pF capacitor replacing switches are also displayed. The Vpp labelled next to waveforms is the voltage measured in the forward conducting state with 100 mA bias current.

3.4.2 Transmit Uniformity and Efficiency with Switching

The measured T_1 of ^{1}H in the salt solution phantom was 39.5 ms, while the T_1 of ^{19}F in the C_3F_8/O_2 mixture was 16.6 ms. Using the flip angle mapping method described, the measured transmit efficiency

within a cylindrical phantom at 63.8 MHz is shown in Figure 3-5a and Figure 3-5b, when the coil is hard-wired tuned to ^{1}H and ^{19}F respectively. A measured reduction of ~12% in the mean transmit efficiency and a ~21% increase in the B_1 inhomogeneity (standard deviation) was observed when the resonance of coil was set to the ^{19}F frequency, whilst transmitting and receiving at the ^{1}H frequency. Similarly, for ^{19}F, the mean transmit efficiency decreased by 32% and the B_1 inhomogeneity (standard deviation) increased by 67% when the resonance of coil was set to ^{1}H.
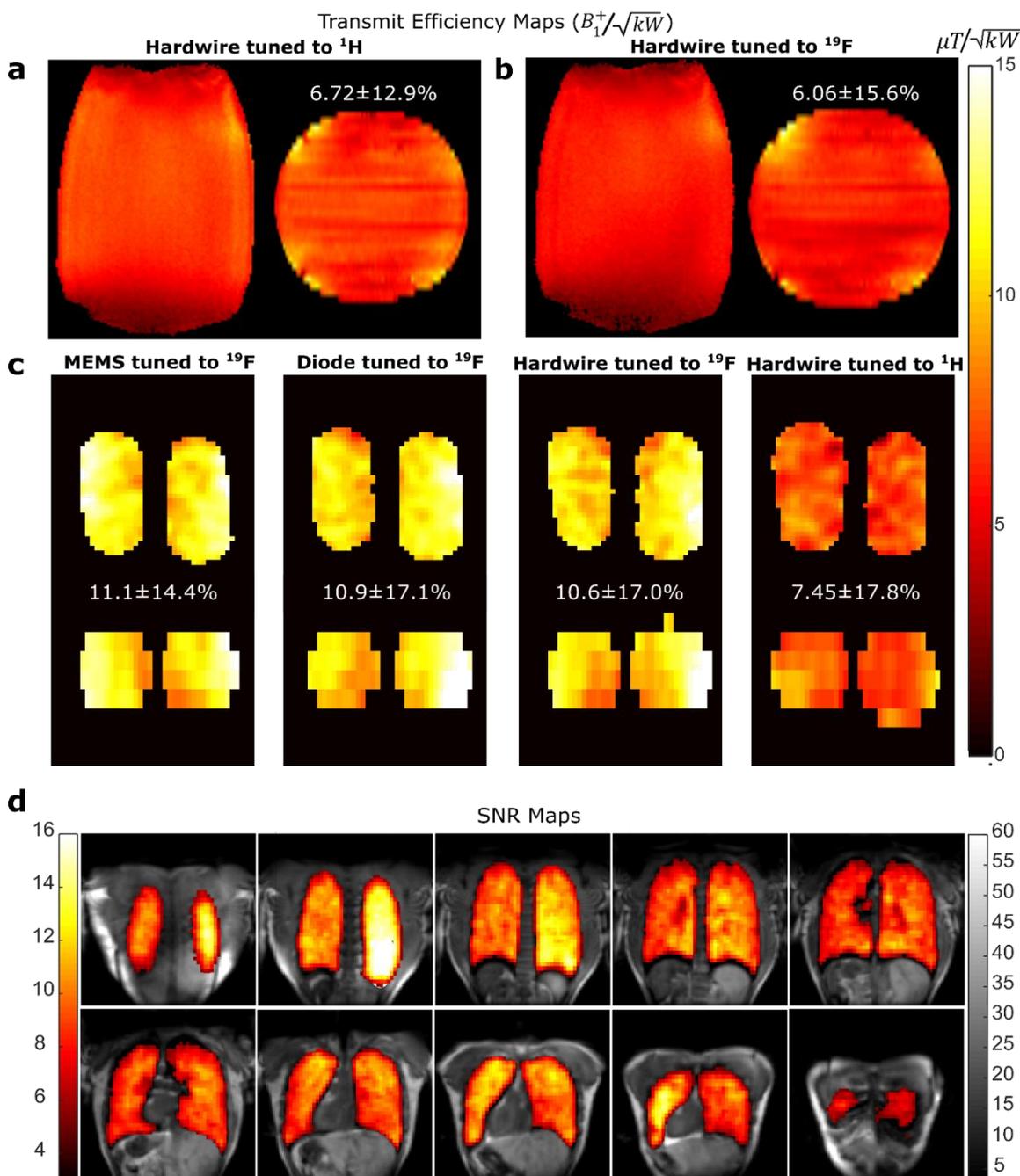
Figure 3-5: Measured transmit efficiency at 63.8 MHz within a cylindrical phantom in central axial and coronal slices. In measurement the coil is either tuned to a: ^{1}H or b: ^{19}F frequency. The mean transmit efficiency shown above axial slices is calculated within the volume of the circled region. c: Measured transmit efficiency within multi-nuclear phantom tuned to ^{19}F frequency using the three methods: MEMS switch, PIN diode, hard-wired connection and additionally the coil tuned to ^{1}H frequency. d: Coronal ^{19}F ventilation images overlaid upon ^{1}H images from a healthy volunteer (male, 28 years old) utilizing MEMS to switch the coil resonance.

The measured transmit efficiency for the three switching methods are presented in Figure 3-5c. The mean and standard deviation of the transmit efficiency calculated from the fitted FA from equation (2-50) is displayed above the axial images. The SNR expected with fully recovered magnetization and 90° excitation, fitted from equation (2-50), within the ^{19}F phantom was 43.6±17.8% with MEMS, 43.4±23.1% with PIN diode, 48.7±28.1% with hard-wired ^{19}F tuning and 44.6±28.6% with hard-wired ^{1}H tuning. The mean SNR changed marginally when tuning was switched from ^{19}F to ^{1}H, but the standard deviation increases demonstrating a reduction in homogeneity of the transmit and receive sensitivity profiles. Results of transmit efficiency and SAR simulation (146) for a cylindrical phantom and realistic human body model with HFSS® (ANSYS, Canonsburg, PA) and Sim4Life® (duke model (240)) (ZMT, Zurich Switzerland) shown in Figure 3-6, which substantiate the measured results.
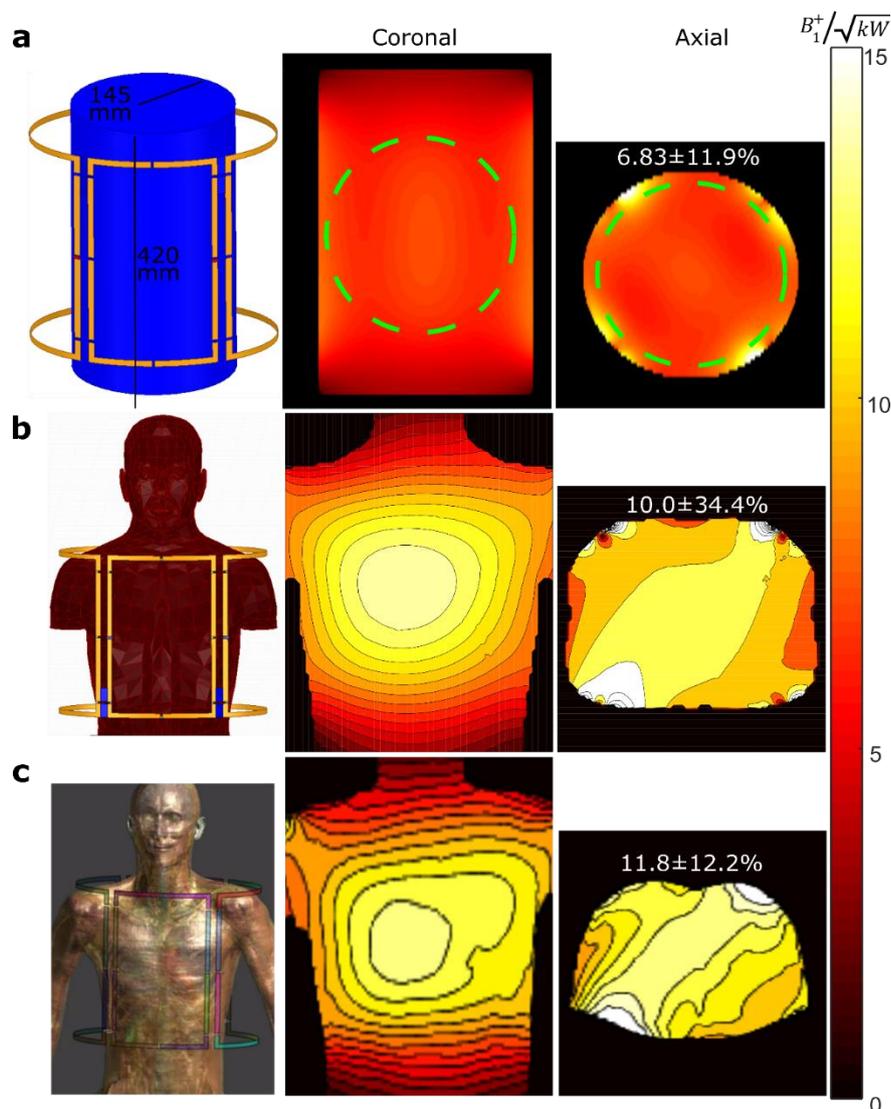
Figure 3-6: a: Simulated transmit efficiency at 63.8 MHz within a cylindrical phantom in central axial and coronal slices. Simulated transmit efficiency ($\mu T/\sqrt{kW}$) with 1 kW RMS input power at 60 MHz using b: HFSS or c: SIM4LIFE using realistic human body models. The mean transmit efficiency ± standard deviation shown above axial slices is calculated within the volume of the circled region with phantom and over the displayed region in human body models. Greater inhomogeneity is observed in HFSS human model due to the larger size, thereby having regions much closer to conducing elements of coil. However, Local 10g averaged SAR for the same input power calculated by HFSS or SIM4LIFE with the body models at 60MHz were close at 121 W/kg and 125 W/kg, respectively.

3.4.3 **In-vivo imaging**

Eight central slices of ^{19}F in-vivo lung ventilation images overlaid on ^{1}H images are shown in Figure 3-5c. The resulting inhaled ^{19}F C_3F_8 lung ventilation MRI display similar SNR homogeneity to those performed with the phantom. SNR was found to be high enough ($\sim$12) with the given imaging parameters for single breath-hold lung ventilation images to be obtained and co-registered with proton structural images.

3.5 **Discussion**

In this study there was no measurable difference in the power loss introduced by MEMS or PIN diode switching (P_{LR}) when compared to a hard-wired connection, as would be expected from their relatively low nominal ESR (Table 3-1). The loss in the matching networks is less than the insertion loss incurred across the power-dividers used to feed power to the coil elements (0.3-0.5 dB loss for each stage) and primarily comes from the use of inductors, which have physically limited Q factors. There was only a 4.5 % difference (10.6-11.1 $\mu T/\sqrt{kW}$) in the mean transmit efficiency measured with the three switching configurations, which is likely in part due to the variation in re-positioning the phantom. This is in accordance with other studies, which showed similar imaging performance with switched dual-tuned coils when compared to single-tuned counterparts (214, 232). Therefore, we believe the choice of switching method is primarily one of practicality and we summarize below the salient considerations.

From a component perspective, MEMS typically have a higher cost and occupy a larger circuit footprint than PIN diodes. PIN diodes require high DC power consumption and biasing requires multiple inductive chokes to prevent RF currents induced on DC lines, rather than resistive networks. MEMS switches typically require higher DC voltages, since their operation is based on electrostatic actuation, which would require the scanner interface to be in accord with voltage directives for medical devices (241). However, to prevent unintentional forward biasing of PIN diodes in their off-state requires higher reverse bias voltage (235). Additionally, without sufficient reverse biasing the isolation the transmitted power is non-linear (242) and unsafe for device operation as it can lead to device destruction (243), as demonstrated here with high power pulse leading to diode burnout. The lower switching speed of MEMS switches when compared to PIN diodes is mentioned in Table 3-1, but previous research has demonstrated MEMS switches have adequate switching speed for most MR imaging methods (223, 244). The coil presented in this work was body loaded with low Q factor ($\sim$14) and switching was only applied in the matching network, so expected losses were minor with either method of switching.

In this study, matching the coil to the correct frequency reduced the reflection coefficient from $\sim$-5 dB to < -20 dB, which corresponds to an increased mean transmit efficiency and homogeneity at the ^{19}F and ^{1}H frequency. Therefore, a clear advantage of the use of dual-tuning was identified, despite the relatively

close frequencies. Nevertheless, in situations where the required scope of ^{1}H imaging is limited, e.g. for initial localizer imaging or low-resolution structural lung imaging in the same-breath, a coil optimized for ^{19}F frequency could be sufficient for ^{1}H imaging. The limitations of using the coil in this manner depends on the loaded quality factor of the coil, which primarily depends on the physical dimension of individual element/loop.

Although the primary theme of the work was the switching comparison, the ^{19}F perfluoropropane lung image quality obtained with the transceiver coil at 1.5T is encouraging, as 1.5T may have potential benefits over 3T for this application in terms of reduced SAR and longer T_2^* of the gases in vivo.

3.6 Conclusion

The losses introduced by switching a dual-tuned coil between ^{19}F and ^{1}H with either MEMS or PIN diode switches was found to be not measurably different to the losses experienced with hard-wired connections. Moreover, the MEMS switch did not fail during high RF power pulsing. Therefore, we believe MEMS switches are suitable for use in high power transmit coils and may be used in applications, which currently employ PIN diodes or in T-R switch networks for dual tuned MRI coils.

Chapter 4: An 8-element Tx/Rx Array Utilizing MEMS Detuning Combined with 6 Rx Loops for ^{19}F and ^{1}H Lung Imaging at 1.5 T[2]

4.1 Overview

Purpose: To improve the attainable image signal-to-noise (SNR) of ^{19}F and ^{1}H C$_3$F$_8$ lung imaging at 1.5T using an 8-element transmit/receive (Tx/Rx) array with a 6-element receive-only array.

Methods: An 8-channel TR RF coil array was designed utilizing MEMS switches for broadband isolation of Tx/Rx circuitry for ^{1}H and ^{19}F imaging at 1.5T. An additional 6 receive-only loops were added. Rx decoupling and switching performance was compared to the use of LC traps with diodes and tested in the MR scanner system. In a phantom, measured SNR with ^{1}H and ^{19}F imaging were compared with simulated receive sensitivity for: (i) the TR array operating with fixed phase transmission/reception, (ii) with the optimally combined signal of the TR array, and (iii) including the 6 receive-only loops. The transmit efficiency and homogeneity was measured/simulated for ^{1}H imaging in a cylindrical phantom and in-vivo ^{19}F/^{1}H imaging. Theoretical considerations of the SNR were investigated by comparison to the ultimate SNR.

Results: A measured MEMS switching speed of 12 µs and isolation between the 8 Rx on-coil ports and 4 superior/inferior coil pair Tx ports lower than -30 dB was found to be sufficient for Tx/Rx switching. For ^{1}H imaging the measured transmit efficiency/homogeneity ($6.82\mu T/\sqrt{kW} \pm 20\%$) was comparable to simulated ($7.57\mu T/\sqrt{kW} \pm 20\%$). The transmit field variation was measured as 17.5% for ^{19}F in-vivo lung imaging. The mean increase of the simulated receive sensitivity within the volume of typical human lungs was 2.6x for the 8-element array compared to operation as a single transceive element. The addition of 6 receive-only loops led to a further increase of 1.39x in simulation and 1.36x in measurement. Comparison of simulation and calculated ultimate SNR (uSNR) showed that a further mean increase of 6.57x throughout the lung region is theoretically possible with an increased number of receive elements, but in regions central to the body the 14-element array achieves >=75% of the uSNR.

Conclusion: The described coil array improved image resolution and/or SNR obtainable with ^{19}F ventilation imaging to a level that approaches the theoretical limits in the centre of the body.

4.2 **Introduction**

MRI of inert fluorinated gases is a developing method for pulmonary ventilation imaging, but image quality is constrained by low spin density ($\sim 2.37 \times 10^{19}$ atoms/cm^3 for gases (99) vs. $\sim 6.62 \times 10^{22}$ atoms/cm^3 for ^{1}H) and short T_2^* (< 3 ms (126)). Therefore, in-vivo image resolution attainable within a single breath-hold is limited.

Most commonly, ^{19}F lung imaging has been performed with the use of single-channel transmit-receive (TR) coils (131, 245). Receive arrays provide improved SNR, while maintaining a large field of view (FOV), by combining individually received signals from multiple isolated smaller RF coils (148). Therefore, the use of a receive array for ^{19}F lung imaging, as in reference (123), is critical to facilitating the acquisition of higher resolution ventilation images. Additionally, an emerging method of investigating lung function relates the change in ^{1}H signal with different inflation volumes (246), based on algorithmic analysis and Fourier decomposition methods (247) with registered images (248). Therefore, the improvement of ^{1}H imaging with the use of an array for both ^{19}F and ^{1}H nuclei would be beneficial for the combined investigation of complementary methods of lung imaging.

However, the commonly used combination of a birdcage coil and receive array has two potential disadvantages for the application of ^{19}F lung imaging:

i. The patients participating in ventilation imaging often have debilitating conditions, such as COPD or Asthma, so patient comfort and minimizing time spent in the MRI bore are high priorities. A body sized birdcage coil within the scanner bore is cumbersome because it restricts patient movement in the bore, reduces available space for a nested receive array and increases set-up/removal times.

ii. A large ^{19}F birdcage coil will couple strongly to the integrated system ^{1}H body coil and any ^{1}H/^{19}F receive arrays. The close proximity of the ^{19}F and ^{1}H resonance frequencies also mean that isolating the different coils at both frequencies with conventional strategies is challenging.(249)

For these reasons, in this work an 8-element array is designed as a TR array at 1.5 T; combining the receiver (Rx) elements in transmission (Tx) with a distributed transmit-receive switching network. Microelectromechanical systems (MEMS) have been proposed as a method for decoupling coils with a number of advantages (e.g. broadband operation, low DC power, fast switching (223, 226, 229)) over the strategy of utilizing tanks circuits enabled by pin diodes (233). Therefore, to protect the receive chain from coupling to transmit power the MEMS

switches were incorporated in the receive detuning network. The broadband nature of MEMS means that the coil can also be used for ^{1}H imaging without any additional circuit. With this method the issue of coupling between Tx and Rx coils for both frequencies of ^{19}F and ^{1}H is mitigated. Therefore, the 8-element array is operational for combined ^{19}F and ^{1}H lung function and structure examinations.

The proposed 8-element TR array is designed for reasonable transmit homogeneity, and thus has limited sensitivity in receive to central portions of the lungs, bordering the heart. A targeted receive-only array combined with a TR array has been shown to improve receive sensitivity, without interfering with the transmit performance (250). Consequently, here a 6-element receive-only array is added. Decoupling is provided by series active detuning using LC traps and PIN-diode switching for both ^{1}H and ^{19}F frequencies.

In addition to practical considerations, there are fundamental limits on the ultimate SNR (uSNR) obtainable through increasing the number of receive channels/coils (22, 182, 183). The uSNR at the center of an object is quickly approached by increasing the number of elements on the surface (169), as found for objects that resemble the head (165) (a sphere), or torso (182) (a cylinder). Therefore, the performance of the designed 14-element array was compared to uSNR from simulation to assess the performance by an objective reference and explore the potential for future improvement of ^{19}F lung imaging by more complex receive coil array design. Finally, 3D in-vivo fluorinated gas ventilation images and structural ^{1}H images were obtained, demonstrating the achievable image quality with an optimized image sequence (251) and the designed coil array.

4.3 Methods

4.3.1 Coil Array Design

The printed circuit board (PCB) design schematic for the flexible 8-element TR coil is provided in Figure 4-1a, with the labelled dimensions selected to be suitable for the majority of adult body sizes. Adjacent coils were decoupled by critical overlap, while capacitive decoupling (236) was used to decouple superior-inferior pairs. Additional decoupling in reception was provided by low input impedance preamplifiers (~1.5 Ω for WanTCom WMM series, with measured noise figure of ~1.5dB for both ^{1}H and ^{19}F frequencies) (252).
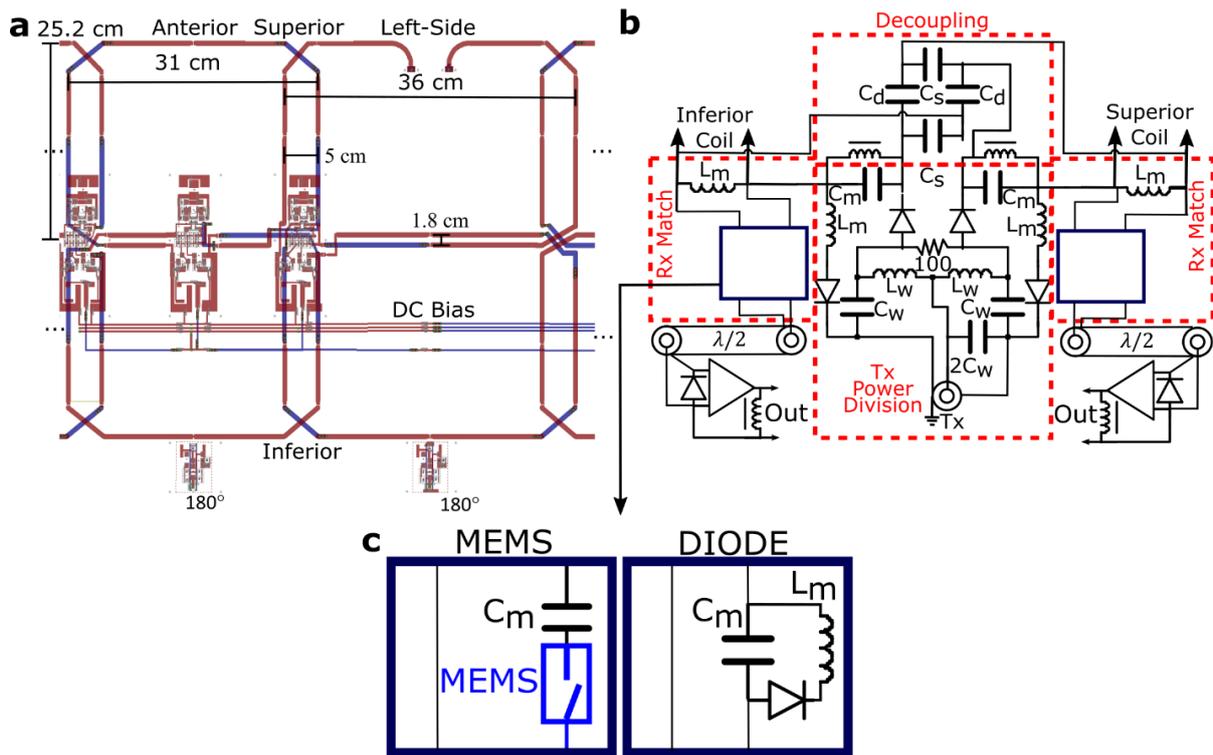
Figure 4-1: **a:** Layout schematic and dimensions of 8-element TR array with coils, 180⁰ couplers and DC bias lines labelled. **b:** A circuit schematic of the matching Tx power splitting and Tx-Rx decoupling circuitry used for superior-inferior coil pairs. Two methods of Isolating Rx circuitry are compared: **c:** MEMS with switches open, or with PIN diode forward biased producing a high impedance with the LC trap

The circuit diagram for matching and decoupling for superior-inferior pairs is provided in Figure 4-1b. Matching for both Tx and Rx was performed with lumped networks made up of the labelled C_m and L_m circuit components. Tx-Rx decoupling and transmit power division is also provided for superior-inferior pairs in the same network. There are two potential mechanisms that can be employed to provide detuning as shown in Figure 4-1c. For the Tx/Rx detuning that employs MEMS the MEMS is switched open during transmission and the intrinsic capacitance (~2 pF) provides a high blocking impedance. For the detuning method employing PIN diodes the diode in Figure 4-1c is forward biased introducing the L_m inductor into the circuit, which forms a high impedance with the capacitor C_m. In transmission the PIN diodes present Figure 4-1b are forward biased to enable operation of transmit circuitry and further protect the receive preamplifiers during Tx.

For the 8-element TR array the transmit power delivered to the four coil pairs was split equally using lumped element hybrid couplers, providing the phase necessary for circular polarization, as diagrammed on the HFSS simulation model for the combined 8-element TR array and 6-element receive array in Figure 4-2a. The geometric model of the 6-element array is shown in Figure 4-2b. The location of the lattice baluns used for matching and detuning LC traps switched during transmit (two tuned to 64 MHz and two tuned to 60 MHz included for

each coil) are labelled. The constructed 8-element TR array PCB is shown in Figure 4-2c while unfolded with a torso shaped phantom placed on top. Coupling between receiver coil cables and the coil itself during transmit is limited significantly by the cables running primarily along an axis of symmetry along the middle. Interaction with volunteers and cables are avoided with additional foam padding.
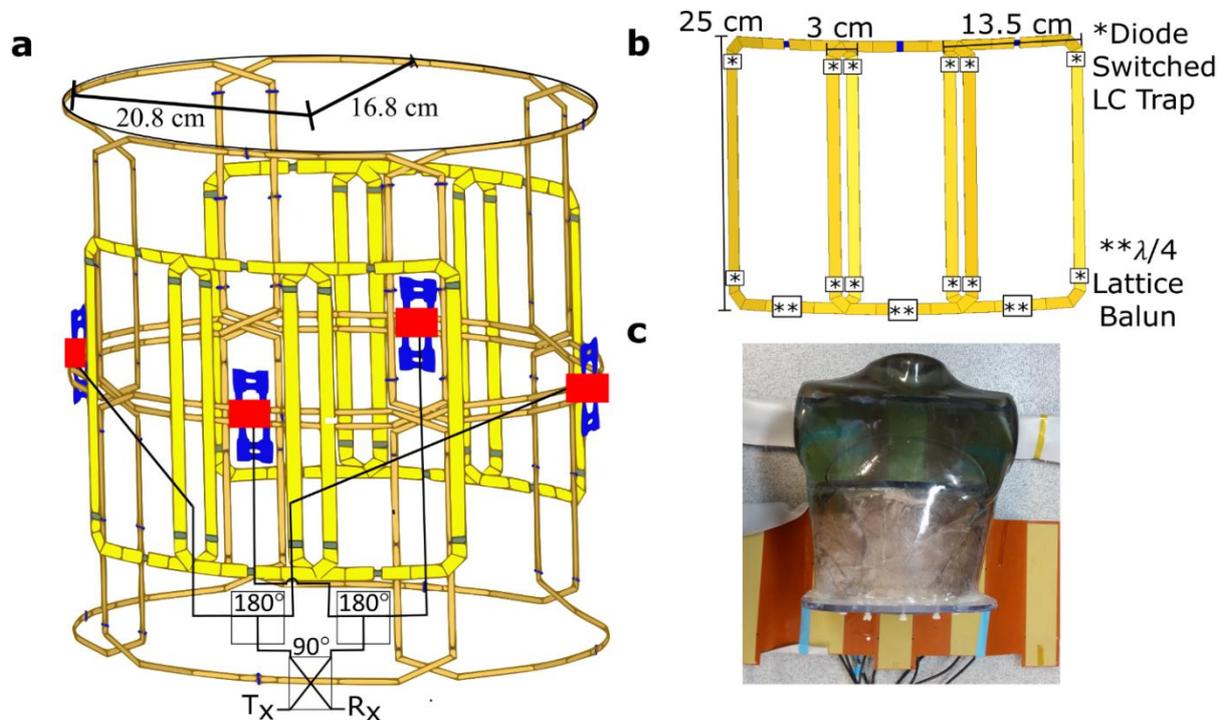
Figure 4-2: **a:** The simulation model of both 8-element TR (orange) and 6-element receive-only (yellow) array is displayed with locations of coil excitation labelled with power/phase division shown schematically. **b:** HFSS simulation model of 6-element receive only array with dimensions labelled and location of LC traps for Tx-Rx detuning and lattice balun for coil matching indicated. **c:** The constructed coil PCB is shown with a human torso sized phantom positioned on the coil.

Measurement of coil Rx and Tx matching and coupling between coils is performed when the coil is DC biased in the appropriate state with the preamplifier stage bypassed using an Agilent E5061A Network Analyzer (Keysights, Santa Clara, CA). A home-built cylindrical phantom (15.5 cm radius and 42 cm height) was used consisting of 3.6 g/L NaCl and 1.96 g/L $CuSO_4 \cdot 5H_2O$ salt solution (18) to represent a human load.

4.3.2 MEMS Switching Voltage Up-conversion

The particular MEMS switch employed requires 82 V between the beam and gate to transition between the "on" and "off" state. However, the GE HDx MRI scanner only provides a +5 V DC bias voltage on the signal line of the receive channels to control transmit-receive switching. To exploit the new MEMS paradigm of switching the MRI system electronics must be modified and high voltage switching functionality must be added.

The simplified circuit schematic shown in Figure 4-3 shows the PCB blueprint of the method devised for control voltage up-conversion from 5 V to 82 V. The constant 10 V source provided by the system is up-converted to 82 V using a FAN7085 switching voltage regulator, which constantly monitors the 82 V output voltage and switches a BSR92P BJT to regulate the voltage.
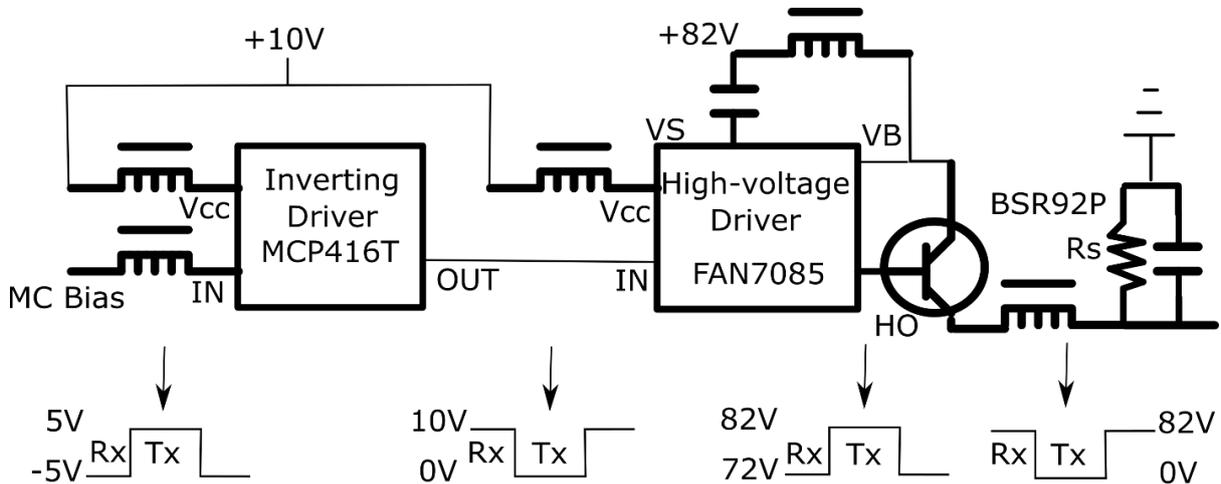
Figure 4-3: Simplified circuit schematic of voltage up conversion circuity to convert 5 V control voltage to 82V.

4.3.3 MEMS Performance Testing

The operational consistency of MEMS switching was demonstrated using a test circuit consisting of a bias signal emulating system default signals, the MEMS driver and a RF source. The bias signal and RF source (2 MHz voltage signal delivered to the RF pins of MEMS) were provided by a WS8352-Taber waveform generator, while a Keysight DSO 104a oscilloscope was used to measure the output. Further, MEMS switching was also measured while scanning (on the 1.5T GE HDx Signa system) to verify the switching operation. The transmission between the Tx and the Rx port of a single coil was measured to determine the isolation provided by the MEMS.

MEMS switching was also measured while scanning on the 1.5T GE HDx signa system to verify the operation. Testing in the MR system consisted of using the Keysight DSO 104a oscilloscope to measure the induced RF and DC voltages on the Rx input of a single coil, the Tx input to the 8-element array and on the MEMS DC bias line at the point of connection on the coil array.

This measurement was performed with the 50 Ω oscilloscope directly connected to the Rx port, so the expected voltage induced on the preamplifier ports is expected to be less with the low-input impedance and additional PIN diode forward biased in Tx mode by an amount approximately given by:

$$V_{pre} = V_{osc} \frac{Z_{pre}//R_{Don}}{Z_0} \frac{Z_0 + \frac{1}{j\omega C_{MEM}}}{Z_{pre}//R_{Don} + \frac{1}{j\omega C_{MEM}}} \qquad (4\text{-}1)$$

where R_{Don} is on the resistance of the forward biased pin diode included for safety (0.2 Ω), Z_{pre} is the input impedance of the preamplifier (1.5 Ω), V_{osc} is the voltage measured with the oscilloscope, C_{MEM} is the capacitance of the MEMS when switched open (2 pF) and V_{pre} is the expected voltage across the preamplifier input terminals. Equation (4-1) is valid as long as $\frac{1}{j\omega C_{MEM}} \gg Z_0$.

4.3.4 **Simulation**

Simulation is carried out for each element as described in section 3.3.3. Simulation of transmit efficiency was performed with ideal power division/excitation matching that in Figure 4-1b. Simulation of transmit efficiency is performed at 64 MHz and 60 MHz in a cylindrical phantom with dimensions and dielectric properties ($\varepsilon_r = 76$ and $\sigma = 0.8$S/m (54)) matching the measurement phantom. The simulated $\widehat{B_1}^-$ was used to calculate the intrinsic SNR (iSNR) with the coil either acting as a single TR coil or as receive array with the iSNR calculated usingEquation (2-105). To emulate a single coil the fields were combined with a fixed phase corresponding to the opposite circular polarization of that in transmission, while for a receive array the weights for optimum combination used as described by equation (2-104). The optimally combined iSNR of the array was compared to the ultimate SNR (uSNR) as calculated in section 2.11.5 within a phantom equal in size to that of the simulated cylindrical phantom. The fields from a plane-wave basis set with the first 400 plane-wave field modes was used to calculate the uSNR as detailed in Chapter 2 (22).

Noise introduced in the receive chain by lossy passive elements and the preamplifiers was approximated as described by equation (2-97). To more accurately match realistic MRI conditions a 1.5 dB noise figure was added to each individual channel in the array due to preamplifiers, and 2.5 dB for the single TR element for an additional 0.5 dB noise figure from each of the two additional stages of power dividing circuitry.

4.3.5 **Phantom Imaging**

Coil receive and transmit performance was evaluated with the designed coil operating as (i) a 14-element array, (ii) 8-element TR array, or (iii) with the receive cables and preamplifiers in Figure 4-1b removed so that the coil acted as a single TR element. For the purpose of this study the receive sensitivity and transmit efficiency in the phantom were compared at the ^{1}H frequency (64 MHz), which should be closely applicable at the ^{19}F frequency (60 MHz) due to

the relative proximity of the two Larmor frequencies. Mismatch at the ^{1}H frequency was expected to slightly reduce the transmit efficiency and homogeneity (255). However, for receive sensitivity the potential difference in the preamplifier noise figure due to mismatch was marginal (163). Flip angle (FA) maps from the cylindrical phantom were generated by imaging using a 3D spoiled gradient echo sequence (SPGR) with previously measured T_1 (39.5 ms), varying input power and fitting to the SPGR signal equation:

$$S_{SPGR} = \frac{\rho(1 - e^{-TR/T1}) \sin FA}{\sigma(1 - e^{-\frac{TR}{T1}} \cos FA)}$$
(4-2)

where ρ is a proportionality factor that depends upon system hardware and the TE, which was fixed (256, 257). The noise standard deviation, σ, is included to scale the signal to SNR units. The standard noise deviation of noise in images was measured in a signal-free region of greater than 100 pixels as described in (20). The factor ρ/σ represents the potential image SNR allowing for fully recovered longitudinal magnetization prior to excitation, and is therefore used to represent receive sensitivity.

The FA in the cylindrical phantom was related to the transmit efficiency by

$$\frac{FA}{\gamma \int V(t)dt}\left(\frac{316.2V}{\sqrt{kW}}\right) = \frac{B_1^{+}}{\sqrt{kW}}$$
(4-3)

where the voltage waveform V(t) input to the coil by the MR system was measured by oscilloscope, while adjusting for cable loss and an additional 60 dB attenuation used in measurement. Imaging sequence parameters for FA mapping and the later detailed imaging experiments are detailed in Table 3-2.

Images from the array were optimally reconstructed according to the method described in section 2.11.3.

4.3.6   In-Vivo Imaging

In vivo lung imaging with inhaled C_3F_8 mixed with 21% O_2 was performed in a healthy adult volunteer (29 years old) with the 8-element TR array combined with 6-element receive only array following informed consent and a protocol approved by UK National research ethics committee. Prior to breath-hold 4 deep inhalations were taken of the mixture to fully saturate the lungs. At 1.5T optimized SSFP imaging of C_3F_8 provides improved SNR over the commonly used SPGR sequences by a mean factor of ~1.7 with in-vivo imaging (see Chapter 6) (251), and is therefore employed here. Additionally, for a more accurate comparison a hamming filter was applied to k-space as in references (131, 258), so that SNR was higher and could be accurately measured throughout the lungs region. FA mapping was performed in-vivo

by acquiring three 3D SPGR sequences within the same breath-hold and nearly identical imaging parameters, but with varying RF pulse amplitude. The actual FA was subsequently calculated pixelwise according to equation (4-2) based on the different in image SNR obtained. Finally, using the TR array co-localized ^{1}H anatomical (15 second breath-hold) and ^{19}F ventilation imaging (the average of two 16 second breath-holds) was achieved.

Table 4-1: Imaging parameters for phantom and in-vivo SSFP and SPGR performance verification with C_3F_8

Measurement	Sequence	TE (ms)	TR (ms)	BW ($\pm$ kHz)	Matrix size (pixels^3)	FOV (cm^3)	Prescribed FA (°)	Avg.	T_{pw} (μs)
					1.5 T				
					Phantom Imaging				
^{1}H FA mapping phantom	3D SPGR	4.5	10	3.97	$64 \times 52 \times 36$	$48 \times 38.4 \times 36$	5-42	2	872
					In-Vivo Imaging				
FA mapping	3D SPGR	2.2	30	3.01	$32 \times 24 \times 10$	$40 \times 32 \times 30$	26/52/77.4	2	832
^{1}H anatomical	2D SPGR	1.8	130	42	$100 \times 100 \times 24$	$40 \times 40 \times 28$	30	1	800
^{19}F ventilation	3D SSFP	1.9	5	95	$40 \times 34 \times 24$	$40 \times 34 \times 24$	77.4	8	832

4.4 **Results**

For the matched and tuned 8-element array low reflection loss ($S_{11} < -15$ dB) and low coupling ($S_{21} < -15$ dB) between superior and inferior coils was measured, as shown in Figure 4-4a for a single superior-inferior coil pair. Anterior, posterior, left and right coil pairs all performed similarly. The reflection coefficient at the Tx port of the anterior coils is shown in in Figure 4-4b demonstrating very low reflection loss (< -25 dB). The isolation between preamplifier inputs and the Tx input of superior-inferior coils provided by Tx/Rx detuning is shown in Figure 4-4c. The baseline isolation is measured when the Tx diodes are forward biased, but no Rx detuning is employed. The isolation provided when the two methods of detuning are employed, MEMS or PIN diode, is compared. In Figure 4-4b an additional >20 dB isolation between the Tx input and Rx ports of one of the coils in the 8-element TR array is added by the MEMS to the inherent isolation of 12dB. It is observed that although MEMS provides more broadband isolation, the isolation provided by PIN diode detuning is higher at the ^{19}F Larmor frequency. There is an additional 6 dB of isolation expected to be provided by the additional two stages of power division. The impedance mismatch between the preamplifiers (1.5 Ω) and 50 Ω impedance of the vector network analyzer (VNA) further increases the isolation in practice. Furthermore, additional detuning from the switching of PIN diodes at the preamplifier input also protects preamplifiers. Therefore, the isolation provided by the MEMS detuning is

sufficient and there is no significant difference to be found in the performance when detuning is provided by MEMS or by PIN diode.
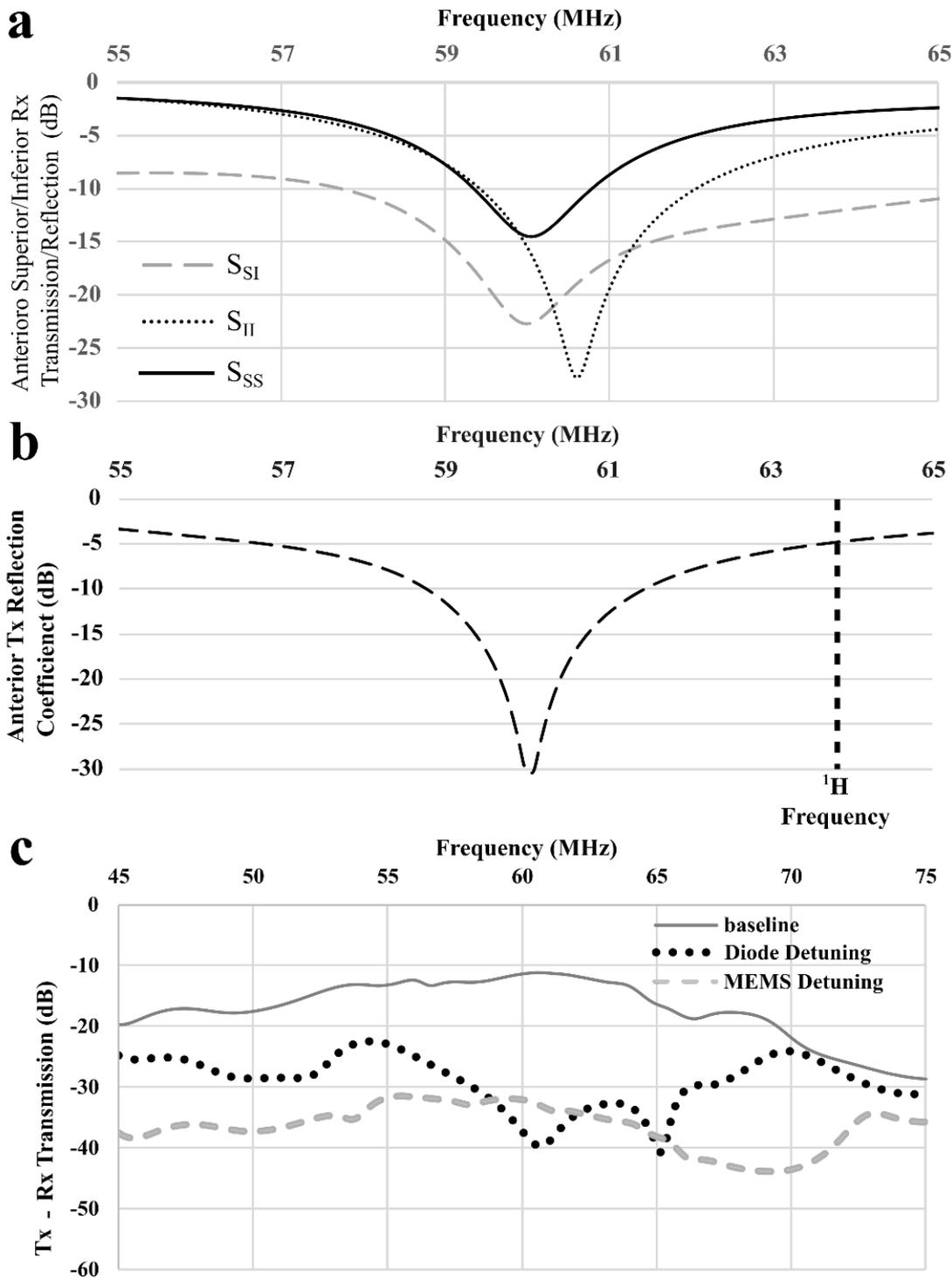
Figure 4-4: **a:** Scattering parameters measured at the preamplifier input ports of the anterior superior and inferior coils. S_{ss} is the reflection coefficient for the superior coil, S_{ss} is the reflection coefficient for the inferior coil and S_{SI} is the transmission coefficient for superior/inferior coils. **b:** Reflection coefficient at the anterior coils Tx port when Rx circuitry is decoupled. **c:** Transmission between Rx port of superior anterior coil, with preamplifier bypassed, and input of hybrid coupler feeding Tx ports of anterior coils with no detuning, or with detuning provided by MEMS or PIN diode detuning methods. Further isolation is provided by the low input impedance of the preamplifiers compared to the 50 Ω port impedance of the VNA used in measurement.

The performance of the MEMS driver and MEMS state switching is presented in Figure 4-5b. The MEMS showed a ~15 μs delay when switching into receive (low impedance) state and ~12 μs delay when switching to transmit (high impedance) state. In both cases approximately 4 μs of this period is attributable to the MEMS switching itself and the remaining delay to the driver circuitry.

During measurement of the MEMS biasing within the scanner (Figure 4-5c-e) it was observed that the delay between Tx pulse and start of signal receive is significantly longer ($>50\ \mu s$) than the MEMS driver switching delay. Furthermore, Figure 4-5b demonstrates the voltage induced on the MEMS DC bias line by the high power Tx pulse is small compared to the 82 V switching voltage. Also, the RF voltage induced on the Rx ports of the coils is low enough (<5 Vpp) to avoid damage with a given approximately 2 kW peak power pulse (voltage waveform shown in Figure 4-4e). This measurement was performed with the 50 Ω oscilloscope directly connected to the Rx port, so the actual expected voltage induced on the preamplifier ports is expected to be <20mVpp according to equation (4-1).
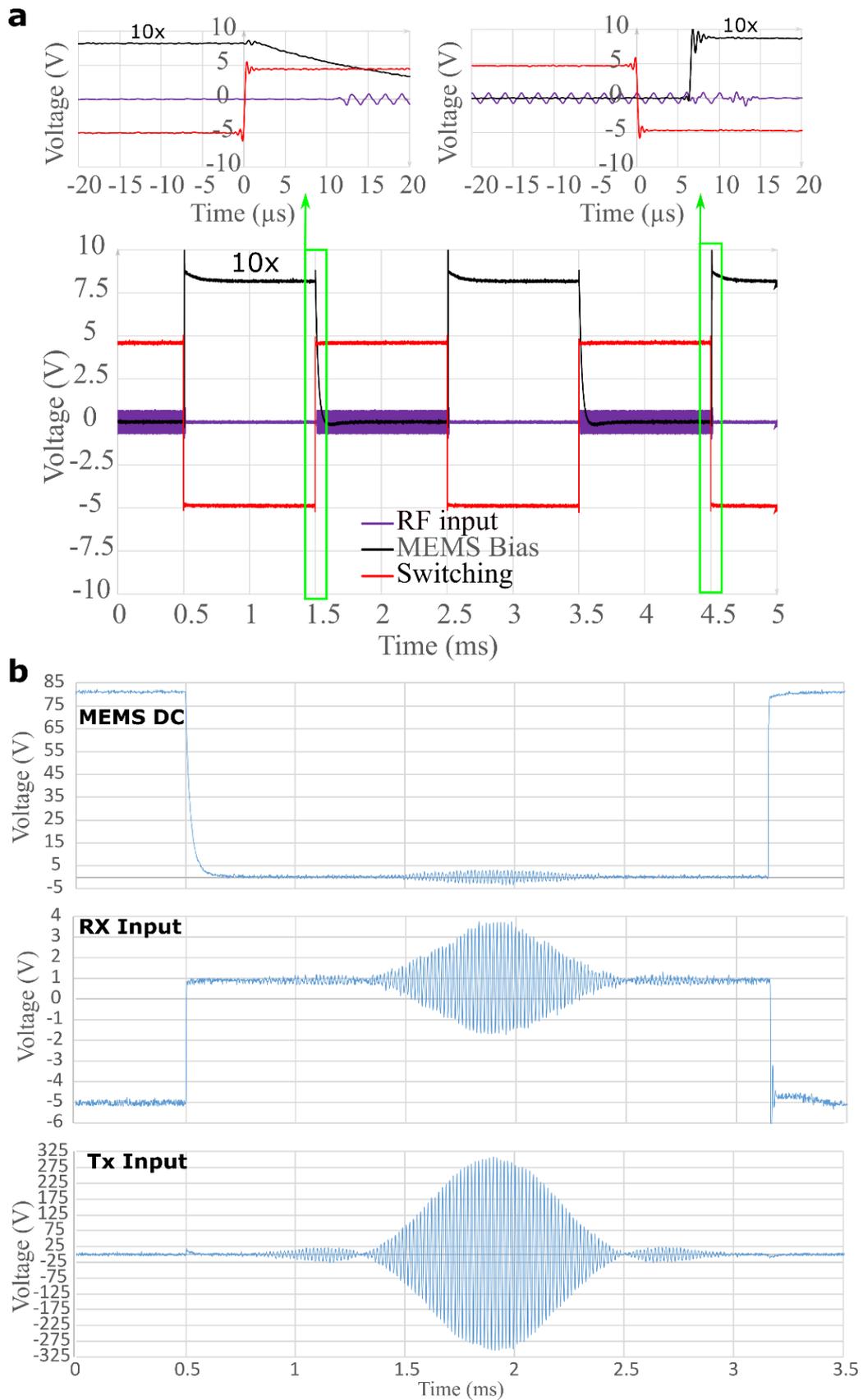
Figure 4-5: **a:** Driver circuitry used for converting coil Tx-Rx biasing voltage to regulate 82 V required for MEMS switching. **b:** The switching performance test of MEMS devices and driver circuitry together demonstrated with oscilloscope measurements of voltage waveforms across ports of MEMS. In-scanner measurement of MEMS bias switching, receive coil preamplifier port isolation and transmit input.
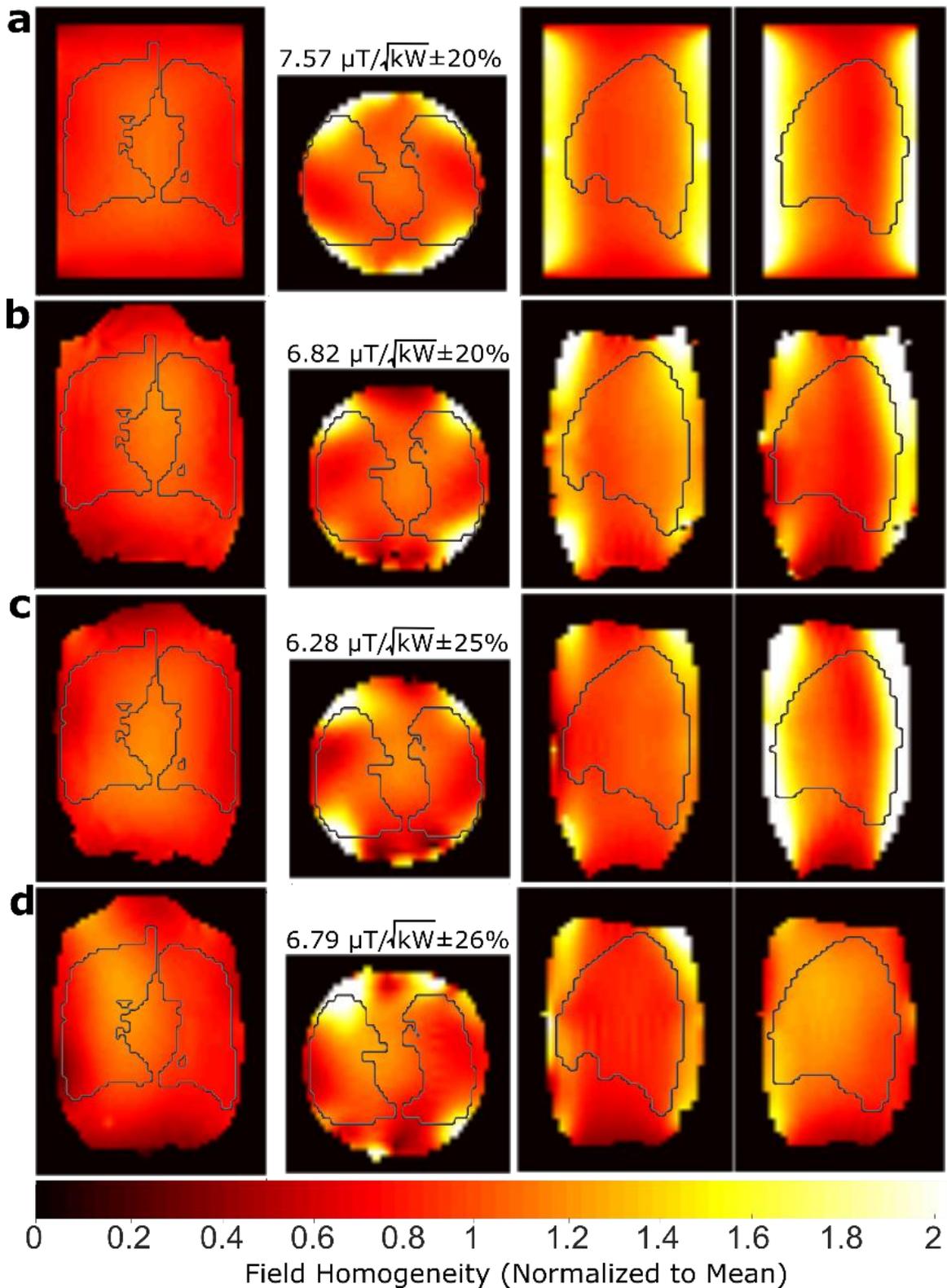
Figure 4-6: **a:** Simulated transmit homogeneity at the ^{1}H frequency in axial, coronal and sagittal slices within a cylindrical phantom. The mean and standard deviation of transmit efficiency is displayed above the axial slices. Also depicted is the measured transmit homogeneity in a cylindrical phantom for the coil acting as **b:** a single TR element **c:** an 8-element TR array, or **d:** as the TR array with additional 6-element receive only array included (total of 14-elements). Sagittal slices are taken through the center of each lung region that is outlined in transmit homogeneity maps. Line art is the location of a typical lung.

The simulated transmit homogeneity in central coronal, axial and sagittal slices are shown for the cylindrical phantom (Figure 4-6a). Measurement results in the cylindrical phantom are displayed: for case (i) when the coil is acting in single TR configuration (Figure 4-6b), for case (ii) with the 8-element TR array configuration (Figure 4-6c) and for case (iii) with the 6-element receive only array also included (14 elements in total) (Figure 4-6d). The simulated field maps are normalized to the mean transmit efficiency, measured as B_1^+ (µT), for a 1 kW RMS input power, found within the exemplified lung volume. Losses in the power dividers of ~0.5 dB were measured for each of the three power divider stages, resulting in the lower transmit efficiency in measurement for case (i), single TR configuration ($6.82\mu T/\sqrt{kW}\pm20\%$), when compared to simulation ($7.45\mu T/\sqrt{kW}\pm20\%$). The measured transmit efficiency was lower and less homogeneous in case (ii), the 8-element TR array configuration ($6.28\mu T/\sqrt{kW}\pm25\%$), and also slightly changed in case (iii), when the 6-element array was included ($6.79\mu T/\sqrt{kW}\pm26\%$), which indicates minor coupling/loss with the receive circuitry (cables, preamplifiers and MEMS detuning) and possible effects from changes in positioning between imaging sessions.

Coil sensitivity maps are presented in Figure 4-7a for the 14-channels. No significant coupling is evident between the coils as represented by the varied and largely non-overlapping regions of sensitivity, which is further corroborated by the low noise correlations (Figure 4-7b) (generally <0.25) between individual channels.
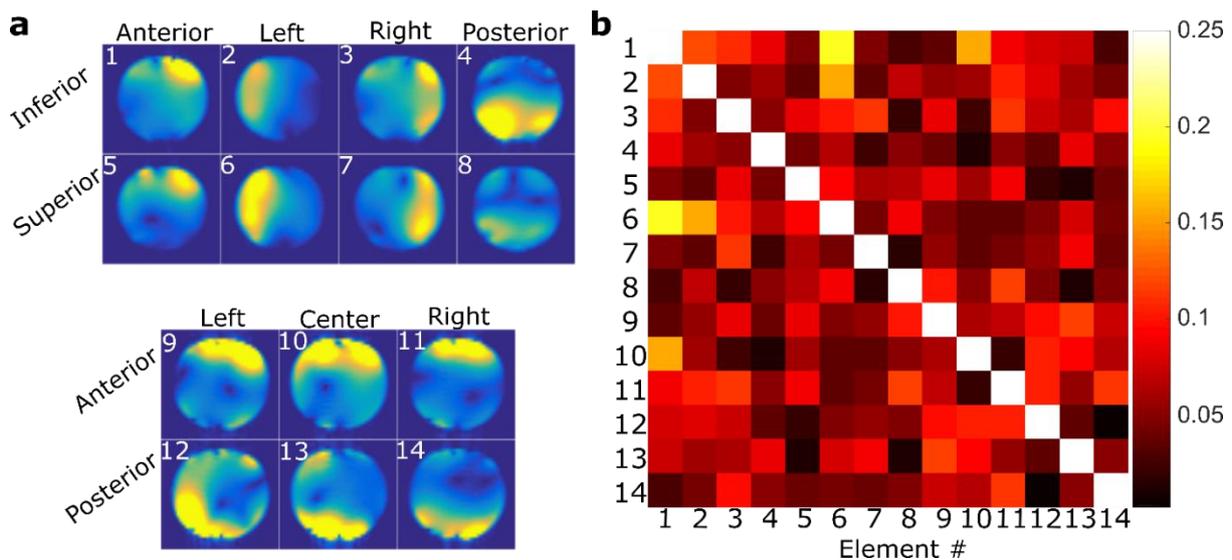
Figure 4-7: **a:** Individual sensitivity maps for coils shown as axial slices through the center of each coil with a cylindrical phantom and **b:** measured noise correlation matrix for the 14-element array

The measured receive performance in a central axial and coronal slice of the cylindrical phantom, (characterized by the ρ/σ in equation (4-2)), are shown for the single TR element, 8-element TR array configuration and with the additional 6-element receive only array included (14-receive elements) is shown in Figure 4-8a-c. Also, the simulated receive sensitivity, characterized by equation (2-50)) for the single TR element, 8-element array and 14-element array is presented in Figure 4-8d-f.
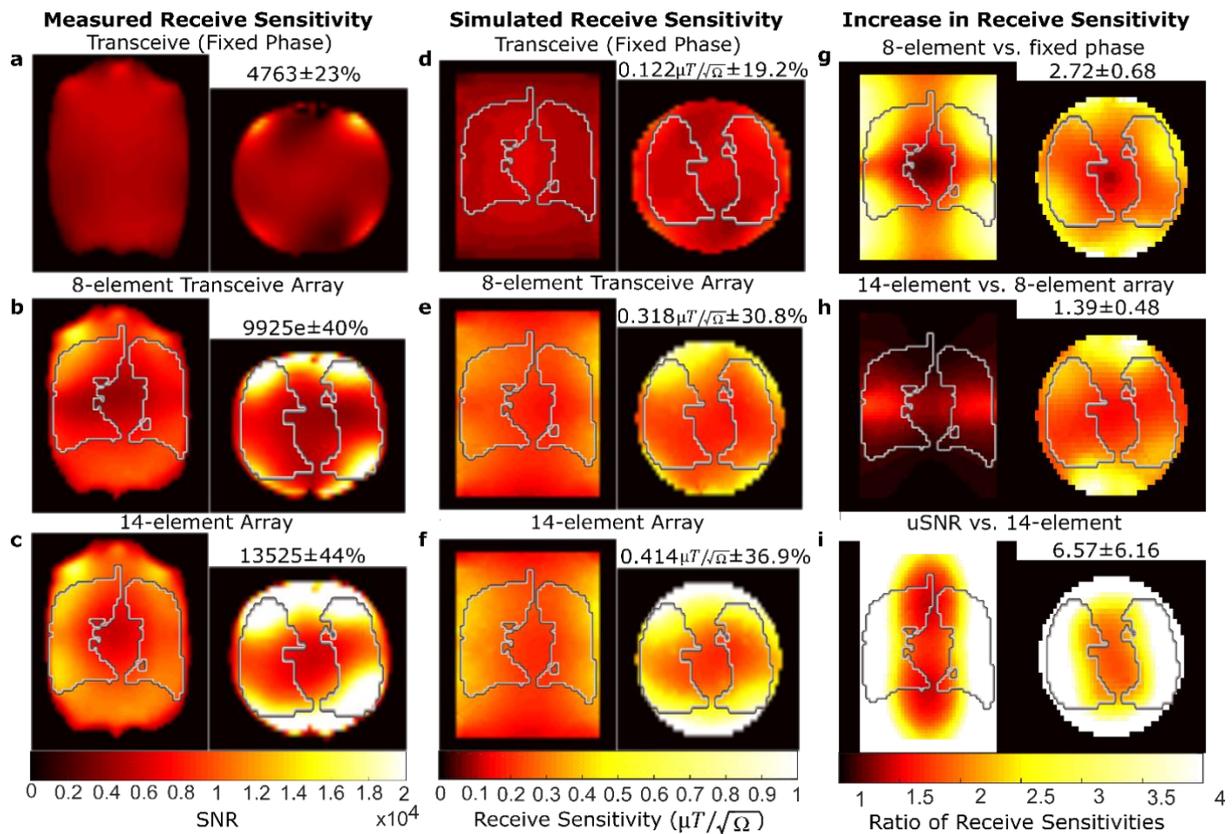
Figure 4-8: The measured receive sensitivity for three different coil configurations in a cylindrical phantom for axial and coronal slices are presented as follows: **a:** the coil operating as a single TR element, **b:** operating as an 8-element TR array, **c:** or with the 6 additional receive elements (total of 14 receive elements). The simulated receive sensitivities in a cylindrical phantom are also presented for the same three configurations in (**d-f**). The ratio of simulated increase in receive sensitivity is shown for **g:** the 8-element TR array compared to the TR array acting as a single transceiver element and **h:** 8-element TR array with additional receive 6-elements compared to the 8-element TR array alone. Additionally, **i:** the uSNR is compared to the combined 8-element TR array and 6 additional receive loops (total 14 receive elements). The mean and standard deviation of the presented maps, within the outlined lung volumes, are labelled above the axial slices.

The measured mean increase in SNR using the 14-element array over the coil single TR configuration within the outlined lung volume is significant (a factor of 2.8 increase); it was slightly larger in simulation (a factor of 3.4 increase), which may be a product of slightly different imaging conditions as the coil is changed between imaging sessions. Also, in simulation the 14-element array results in a further 1.39 factor increase that closely matches the measured increase of 1.36. A large increase is observed in the central area of the lungs

92

(Figure 4-8h), where the 8-element array has low sensitivity. The comparison of the optimally combined iSNR to uSNR in Figure 4-8i demonstrates that in central portions of the lung volume ~75% of the uSNR is achieved with the 14-element array. However, at the periphery significant increases in SNR may still be achieved with increased receiver element count.

In Figure 4-9a a lower FA is observed in the inferior region of the torso, since the coil was positioned more superior than in simulation with the volunteers arms raised above the head. However, the observed in-vivo FA homogeneity is still 17.5%, which is better than the 20% simulated within a cylindrical phantom (Figure 4-6a) due to the array conforming better to the shape of a human torso than that of a cylinder. The ability to obtain co-registered ^{1}H structural and ^{19}F ventilation images is demonstrated with the coronal ventilation slices in Figure 4-9b, and coronal anatomical slices in Figure 4-9c.

4.5 **Discussion**

The use of MEMS in MRI RF coil design is a relatively new development (223), and has required improvements over previous MEMS switches. Namely: higher stand-off voltage, simultaneous high beam reliability with high conductance, and non-magnetic design (224, 233). In subsequent applications the MEMS device has been employed for detuning in receive arrays (233), coil dual-tuning (257), reconfigurable coil arrays (229), wireless power transfer in the MR system (259) and coils for B_0 shimming (260). For the first time, this study demonstrates the use of MEMS in the Tx/Rx detuning of a transceive array. The 4 µs delay of the MEMS switch used here is minimal, but the driver circuitry employed adds an additional 11 µs. This delay is small when compared to the 50 µs reported in earlier performance testing of MEMS for MR applications (223), and is sufficiently short for the ultra-short TE (UTE) and zero TE (ZTE) sequences expected to be employed for imaging ^{19}F (98, 258, 261) and ^{1}H (262, 263) in the lungs. Further improvements in driver circuitry are therefore probably not necessary. Also, using individual transmit switching for each superior/inferior pair in the circuit topology eased constraints on the isolation required for each channel. Consequently, the method of using MEMS with the MR system established here introduces many new opportunities for multi-tuned coil design.
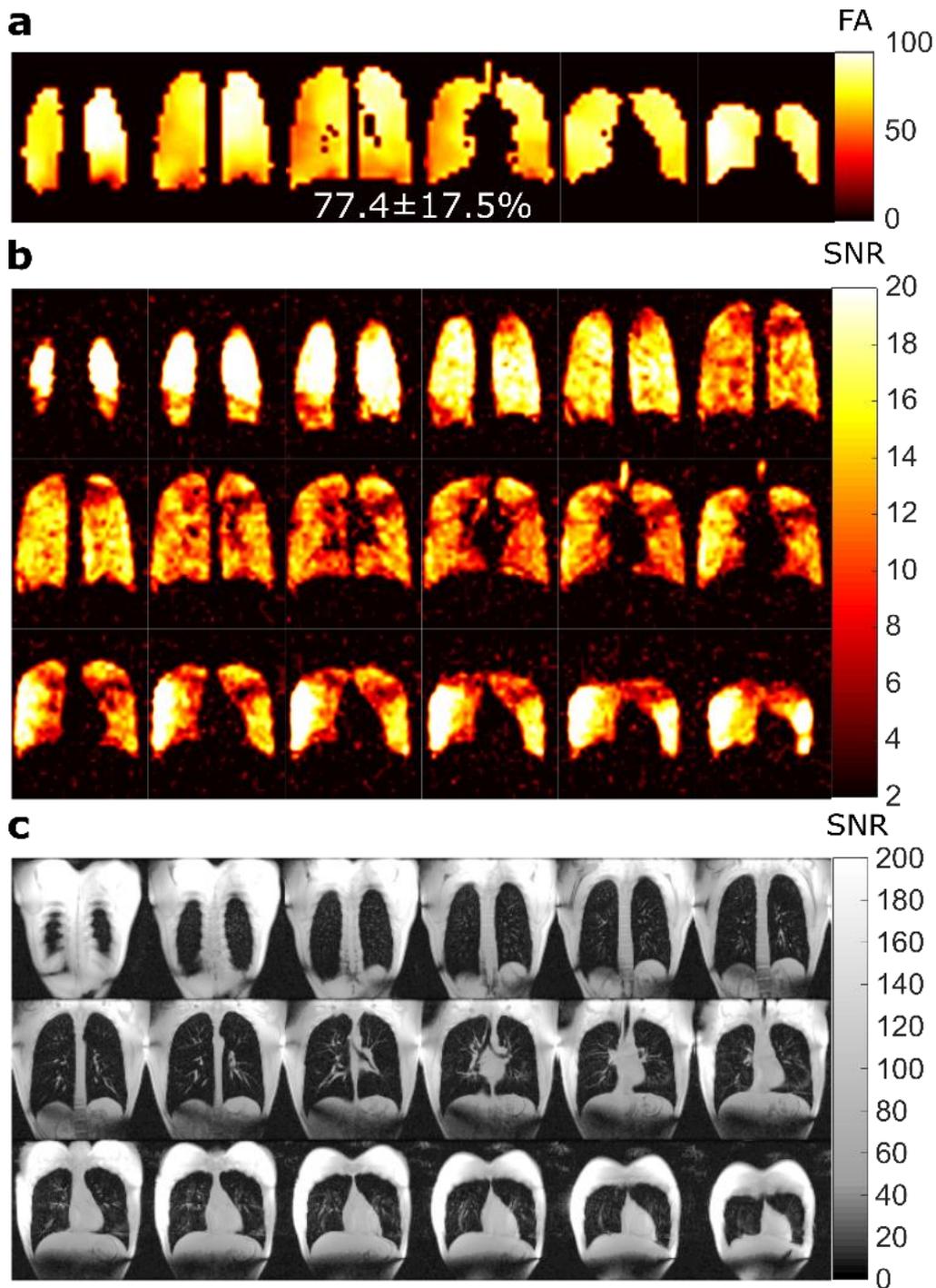
Figure 4-9: In-vivo ventilation and co-localized anatomical/structural data sets acquired in the same imaging session with the coil operating as a 14-element array are displayed as follows: **a:** ^{19}F FA maps, **b:** SNR maps of the ^{19}F C_3F_8 ventilation imaging using a 3D SSFP sequence acquired in two separate breath-holds and **c:** ^{1}H anatomical/structural images measured with a 2D SPGR sequence.

However, there are still a number of barriers to the routine use of MEMS in coil design. First, the MEMS employed here are still rare and expensive when compared to PIN diodes (>£200 compared to <£10 for the devices used in this Chapter). Furthermore, the activation voltage is still much larger than that easily provided by an MR system. We overcame this issue with a driver circuit that operated as a step-up voltage transformer. The MEMS employed here also

have higher ESR and slower switching speed than the PIN diodes, with a much larger board footprint, requiring additional resistors and coupling capacitors. Most importantly, although the MEMS employed functioned well during imaging and testing, a majority of them failed when left alone for a period of time or would transition between functioning and not functioning (>80%). From discussion with other groups researching the use of these MEMS (260, 264) the failure rate issue was found to be common. The reliability of MEMS is well-known issue, since there are many potential methods of failure, stiction, electrostatic discharge related breaking and failure from "hot-switching" (225). Since the reliability of MRI coils for clinical and research purposes is the often the most critical requirement the use of PIN diodes may be preferred. For this reason, the same coil design employed PIN diodes for Tx/Rx switching was employed in the subsequent imaging presented in the remainder of this thesis.

Previously, the use of a TR array with additional receive-only elements has been limited, and predominantly done at ultra-high field strengths (≥4.7 T), where TR arrays are commonly employed (250, 265-267). It has been demonstrated that although TR arrays designed for transmit homogeneity may not be optimal in receive configuration, the addition of receive only elements targeting regions of low sensitivity may be an equally good alternative, with less complexity, to designs with total separate transmit-only receive-only arrays. The geometry of the 8-element TR array in this study allows an efficient layout of cables and circuitry for equal power division to each element that doesn't impede patient/volunteer access or comfort while providing satisfactory transmit homogeneity. However, in the direct center of the imaging region and between coils the receive sensitivity was poor due to the double-row design (see Figure 4-8), motivating the addition of a receive-only array. The elements of the 6-element array placed between the rows on the anterior and posterior coils of the 8-element array have sensitivity profiles (Figure 4-7a) that are complementary and were found to greatly increase the sensitivity in these regions, also improving the homogeneity of the signal reception profile of the entire array. The receive sensitivity of the combined 14-elements array was therefore significantly improved compared to the single element equivalent configuration of the 8-element array (throughout the lungs a 2.8x increase in measurement and 3.4x increase in simulation). Therefore, the combination of a TR array with receive-only array is found to be beneficial when imaging at the relatively low frequencies used here, as they can address the need for coils to be close to the subject, while allowing for geometrical flexibility and avoiding the use of tight-fitting fixed-geometry coil housing.

A similar increase in SNR was obtained with in-vivo imaging as to simulation and phantom measurement with the array configurations performing better than a single element TR coil.

Here, the simulated imaging volume was cylindrical to match the measurement phantom, but simulation with an elliptical cylinder may more closely match the case of a human torso. Practically, the geometry of the receive coils are designed more favourably for a thinner sagittal dimension, and would therefore more closely approach the ultimate SNR in the center of an elliptical cylinder or torso shaped geometry.

The receive sensitivity of the 14-element array was found to be close to the uSNR in central portions of the lung volume (>=75%) bordering or near the heart. Therefore, the potential increase in SNR with greater element number is limited. Limited increases in SNR with increasing element counts has been demonstrated previously in ref. (165, 182), where the improvements found by doubling the number of elements from 8 to 16 results in marginal gains in central portions of the imaging volume. In fact, for imaging ^{3}He at 48 MHz reference (268) also found only a ~2x factor increase in the average SNR within the lungs using a 32-channel receive array when compared to a birdcage coil in TR mode. Additionally, SNR at the center of the lungs was markedly lower than at the periphery, which fits with the simulation results presented here.

Although transmit efficiency at the ^{1}H frequency may be reduced due to impedance mismatch, the overlaid images of ^{19}F and ^{1}H confirm that the coil array can successfully be used for obtaining co-registered images of both nuclei in the same exam without adjustment. The ability to image both ^{1}H and ^{19}F provides the SNR benefits of a receive array at both nuclei, while avoiding the cumbersome alternative of multiple transmit and receive coils for both nuclei.

The imaging resolution for diagnostic images are limited by the lowest SNR region obtained, since lung defects must be detected equally reliably throughout. Therefore, in the application of ^{19}F/^{1}H imaging further increases in array element count may provide no benefit considering the increase in background noise (253), the complexity in compensating for receive sensitivity inhomogeneity in images (269) and potential associated artefacts that can adversely affect quantitative image analysis (270). If additional receivers were desired, elements orthogonal to the loop coils (200, 220, 271) could be added with no detriment to the transmit efficiency or reception of the current design.

4.6 Conclusion

An 8-element transceiver array with additional 6-element receive only array was presented. Through simulation and experiment this array was shown to provide significantly higher SNR

than that of a single channel coil. Furthermore, the use of MEMS in the transmit receive was demonstrated, which allowed the array to be used for ^{19}F and ^{1}H MRI, with the only trade-off being reduced transmit efficiency at the ^{1}H frequency. The improvement in receive sensitivity measured experimentally was similar to the simulated. Additionally, simulation showed that in the central part of the lungs (bordering the heart) >75% of the uSNR is expected to be achieved. Therefore, the results presented here are close to the maximal C_3F_8/^{19}F ventilation image quality obtainable with optimized sequence (Chapter 6) and RF coil hardware design, as limited by the central lung region.

Chapter 5: Linear Ladder Resonators for Improved Transmit Efficiency of Individual Elements in Transceive Arrays: Application for a Thorax Transceive Array for ^{19}F and ^{1}H Lung MRI[3]

5.1 Abstract

In magnetic resonance imaging (MRI) of ventilation with inhaled inert gases, (^{3}He, ^{129}Xe, ^{19}F), wearable radiofrequency (RF) coils are often used, termed vest coils, to provide volunteer comfort and produce RF magnetic fields at the Larmor frequency of the gas nucleus that target the lung region. Conventional vest coil designs typically have less homogeneous excitation and higher SAR than rigid volume resonators (birdcage coils), while transceiver arrays can provide higher transmit efficiency, receive sensitivity and comfort. Here we introduce a hybrid vest coil design combining non-periodic ladder networks with a transceiver array. A network theory approach is derived for the calculation of tuning circuit components. Also, the novel concept of using asymmetric tuning capacitors values in a ladder resonator network to produce circularly polarized excitation with a single port is introduced. In simulation, different coil designs (a 7-mesh non-periodic array, 6-mesh hybrid ladder/transceiver array, 8-mesh elliptical birdcage coil and 8-element transceiver array) are compared in terms of transmit efficiency, SAR and receive sensitivity for ^{19}F lung imaging at 1.5 T. Construction and measurement of the transmit and receive performance of the hybrid ladder/transceiver array is demonstrated. Transmit homogeneity and SAR is improved relative to a transceiver array with similar dimensions and is shown to be comparable to that of a birdcage coil, albeit with homogeneity that is more sensitive to subject loading variation.

5.2 Introduction

At higher field strengths greater signal-to-noise (SNR) and contrast-to-noise is expected, but these benefits are often unobtainable due to restriction on imaging parameters imposed by the SAR constraints and magnetic field inhomogeneity. For example, for ^{19}F gas lung imaging with C_3F_8 it has been demonstrated that at 1.5T SAR constraints limits the pulse sequence optimization of a steady-state free precession sequence (SSFP) with the use of a common quadrature driven vest-coil design (251). Consequently, a continual research area of magnetic resonance (MR) radio-frequency (RF) coil engineering is to improve efficient and

---

[3] This chapter will be submitted to the journal IEEE Transactions on Medical Imaging. All experiments, simulations and analysis on data were carried and described in the witten manuscript by AMM. PH assisted in in-vivo scanning. Manuscript revisions performed with MR, JMW and AMM.

homogeneous generation of the circularly polarized field (B_1^+) for MR excitation in diverse applications.

Two classes of coils exist for the excitation of the MR signal: transmit arrays and volume resonators. Transmit arrays consist of a collection of distinct elements with separate RF excitations achieved by power and phase division from either a single power source (244, 272) or separate sources with adjustable phase (195, 273). In contrast, volume resonators have a single electrical structure connected physically or by strong electromagnetic coupling. The birdcage coil is the most commonly used volume ladder resonator in magnetic resonance imaging (MRI) (192, 274), and forms a periodic structure.

For ^{19}F ventilation imaging the use of a whole body birdcage coil may not be suitable because:

- The ease of use and volunteer/patient comfort is reduced because access to the scanner bore is compromised due to the reduced space.

- The proximity of a close coupled vest coil to the lung provides higher SNR

- Birdcage coils resonant at the [19]F Larmor frequency (60 MHz) will couple strongly to any [1]H (64 MHz) receive or transmit coils in the system, thereby increasing complexity of design

Therefore, it may be preferable to combine the receive and transmit coils as a single array to further reduce the complexity and improve the imaging subject's comfort.

Methods of combining the benefits of a birdcage coil in terms of homogeneity and a transceiver array for improved receive sensitivity have been explored previously. For example, the use of a birdcage coil tuned for degenerate mode excitation, with adjacent current meshes capacitively decoupled was demonstrated in (275). In this coil design the individual current mesh is fed by a Butler matrix network for circularly polarized excitation, and the individual meshes were also used as individual receive channels. In similar designs employing transmission arrays emulating the current pattern of a quadrature driven birdcage coil the local SAR has been shown to be reduced, and the reduction increases with a greater number of transmit elements (276).

In these examples the size of the array structure remains similar to that of a birdcage coil and the power feeding network remains complex and cumbersome. Alternatively, the half/open birdcage (208, 277-291) and two-dimensional ladder resonators (205) are non-periodic structures that allow for greater conformity to the structure being imaged, while having a single

feed point. These examples of ladder coils operate on the principle of exciting a resonant mode of the structure for linear excitation.

Here, we present a novel and efficient thoracic vest coil design for ^{19}F lung MRI that combines a number of coil design concepts (non-periodic ladder resonator, the degenerate birdcage and transceive arrays) to reduce SAR, while maximizing transmit efficiency and homogeneity and increasing receive sensitivity, while producing quadrature/circular polarization excitation.

A theoretical framework was developed linking the design of linear ladder resonators with network theory in a previously unexplored way. Also, using this framework an elliptical birdcage coil, linear ladder resonator and hybrid ladder/transceive array vest coil were designed and simulated. The theory developed for tuning is analogous to that presented for birdcage coils previously (186, 189, 292), but for the ladder/transceive array vest coil an asymmetric capacitor distribution on the rungs is shown to produce circularly polarized excitation. Through simulation with a realistic body model phantom and in-vivo imaging we demonstrate the potential benefits of the novel ladder resonator transceive coil design for combined ^{19}F and ^{1}H lung imaging in humans.

5.3 Theory

5.3.1 General Solution for N-element Linear Ladder Resonator

In the network analysis presented here the generalized one-dimensional ladder network is separated into N^l and N^r mesh elements to the left and right of a central mesh, respectively, as diagrammed in Figure 5-1. In the notation used throughout "l" (left) and "r" (right) are included and treated separately since in many cases excitation occurs at a single point with a symmetric structure to the left and right. Also, in the ladder coil design investigated here an electrical asymmetry is introduced about the central mesh, which is not easily expressed without separating "left" and "right" sections.

Adjacent meshes are joined by shared current paths as diagrammed in Figure 5-1. In the illustrative example shown the central mesh is excited at the port labelled V_0, while additional ports are labelled as $\boldsymbol{V}_n^r$ and $\boldsymbol{V}_n^l$, representing ports of meshes to the left and right of the central mesh, respectively. Tuning capacitors (C_n^r and C_n^l) and intermesh capacitors ($C_{(n-1)n}^r$ and $C_{(n-1)n}^l$) are distributed as shown in in the diagram of Figure 5-1.
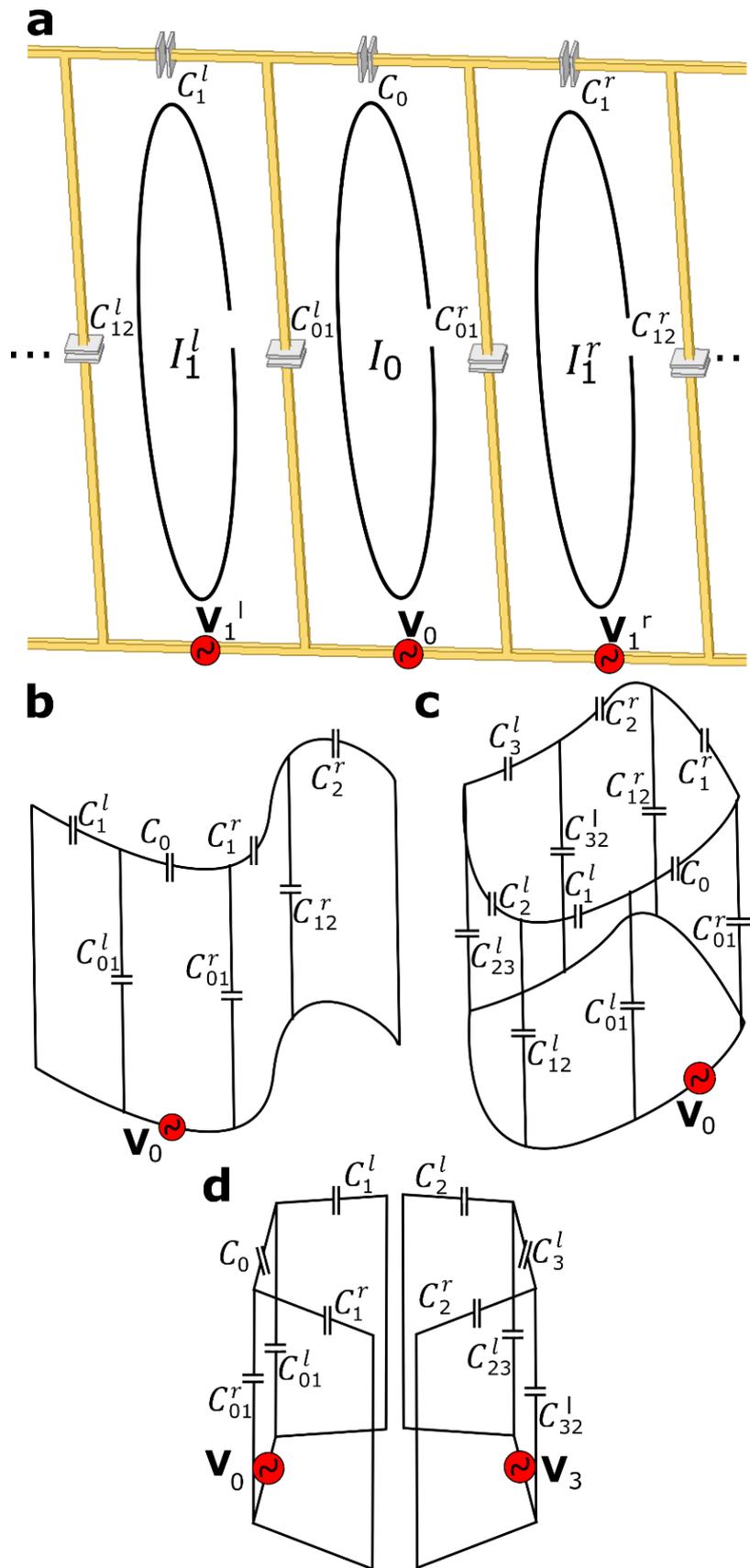
Figure 5-1: a: Conceptual diagram of a general linear ladder resonator with lumped capacitors, currents and port excitations labelled. Example diagrams of different one-dimensional ladder networks with arbitrary geometry are shown including: b: a non-periodic ladder network, c: a periodic ladder network and d: network consisting of two separate 3-mesh non-periodic ladder networks (ladder/transceiver-array hybrid).

Since the lumped capacitors could potentially consist of resistive or inductive components, or more complex LC networks, in the network formalism that follows the lumped impedances are represented by Z_n^{Hr} and Z_n^{Hl}, and $Z_{(n-1)n}^{Lr}$ and $Z_{(n-1)n}^{Ll}$. These are incorporated into the two vectors:

$$Z^L = \begin{bmatrix} Z_{(N^l-1)N^l}^{Ll} \\ \vdots \\ Z_{01}^{Ll} \\ Z_{01}^{Lr} \\ \vdots \\ Z_{(N^r-1)N^r}^{Lr} \\ Z_{N^lN^r}^{L} \end{bmatrix}, Z^H = \begin{bmatrix} Z_{N^l}^{Hl} \\ \vdots \\ Z_0^{Hlr} \\ \vdots \\ Z_{N^r}^{Hr} \end{bmatrix} \tag{5-1}$$

where the z^L vector contains the inter-mesh coupling impedances and the z^H vector contains the individual mesh tuning impedances.

For any network the relation between mesh currents and voltage excitation is expressed by:

$$ZI = V \tag{5-2}$$

where Z is the impedance parameter matrix, I is the mesh currents vector and V is the voltage vector. For the one-dimensional ladder network diagrammed in Figure 5-1a, Z can be separated into $Z = Z_G + Z_C + Z_T$, where Z_T is the lumped mesh tuning impedances matrix, Z_C is the lumped mesh coupling impedances matrix and Z_G is the geometrically dependent portion of the final impedance matrix. Therefore, for a one-dimensional ladder network (5-2) can be expressed as:

$$(Z_G + Z_C + Z_T)I = V \tag{5-3}$$

where the voltage vector (V) and current vector (I) are given by:

$$I = \begin{bmatrix} I_{N^l}^l \\ \vdots \\ I_0^t \\ \vdots \\ I_{N^r}^r \end{bmatrix}, V = \begin{bmatrix} V_{N^l}^l \\ \vdots \\ V_0^t \\ \vdots \\ V_{N^r}^r \end{bmatrix} \tag{5-4}$$

Previously, the elements of Z_G have been solved for with analytical equations for the mutual and self-inductance of meshes, or by numerical methods (188, 274, 292, 293). Here, electromagnetic simulation or measurement may be used to solve for Z with known $Z_C + Z_T$ to determine Z_G. The tuning matrix Z_T is unidiagonal, with elements along the diagonal equal to:

$$Z_{Tmn} = \begin{cases} Z_m^H, \text{for } m = n \\ 0, \text{otherwise} \end{cases} \tag{5-5}$$

while the coupling matrix Z_C is given by:

$$Z_C = \begin{bmatrix} \mathbf{Z}_1^L + \mathbf{Z}_{N^l+N^r}^L & -\mathbf{Z}_1^L & 0 & 0 & -\mathbf{Z}_{N^l+N^r}^L \\ -\mathbf{Z}_1^L & \mathbf{Z}_1^L + \mathbf{Z}_2^L & -\mathbf{Z}_2^L & \ddots & 0 \\ 0 & -\mathbf{Z}_2^L & \ddots & \ddots & 0 \\ 0 & \ddots & \ddots & \ddots & -\mathbf{Z}_{N^l+N^r-1}^L \\ -\mathbf{Z}_{N^l+N^r}^L & 0 & 0 & \mathbf{Z}_{N^l+N^r-1}^L & \mathbf{Z}_{N^l+N^r-1}^L + \mathbf{Z}_{N^l+N^r}^L \end{bmatrix}$$

(5-6)

For the case of a non-period ladder resonator, as diagrammed in Figure 5-1b, there are no intermesh capacitors between the outermost left and right meshes and $\mathbf{Z}_{N^l+N^r+1}^L = 0$. For a periodic ladder resonator, as diagrammed in Figure 5-1b, $\mathbf{Z}_{N^l+N^r+1}^L$ is the intermesh capacitor between outermost left and right meshes. As for the ladder network in Figure 5-1b, if there is an even number of meshes one more mesh is arbitrarily assigned to the group of left-side meshes than the right side.

Typically, the desired current distribution is known, while the lumped impedance parameters are solved for, so (5-3) is more naturally expressed as:

$$I_C Z^L + I_T Z^H + Z_G I = V \tag{5-7}$$

The matrix I_T is unidiagonal, with elements equal to:

$$I_{Tmn} = \begin{cases} I_m, \text{ for } m = n \\ 0, \text{ otherwise} \end{cases} \tag{5-8}$$

while I_C is given by:

$$I_C = \begin{bmatrix} I_1 - I_2 & 0 & \cdots & 0 & I_{N^l+N^r} - I_1 \\ I_2 - I_1 & I_2 - I_3 & \ddots & \ddots & 0 \\ 0 & I_3 - I_2 & \ddots & \ddots & \vdots \\ \vdots & \ddots & \ddots & \ddots & 0 \\ 0 & \cdots & 0 & I_{N^l+N^r-1} - I_{N^l+N^r} & I_{N^l+N^r} - I_{N^l+N^r-1} \end{bmatrix}$$

(5-9)

In order to obtain the desired relative current phase and magnitude difference between meshes it can be shown that it is necessary to solve the homogeneous form of (5-7), with $V = 0$ (294). Therefore, the equation:

$$I_C Z^L + I_T Z^H = -Z_G I \tag{5-10}$$

yields the required $\boldsymbol{Z^L}$ and $\boldsymbol{Z^H}$ that allows the network to hold the desired current distribution $\boldsymbol{I}$. In practice, to ensure that the correct current distribution is induced with multiple voltage/port excitations the specific solution must be solved unless the network has a known symmetry that enforces a symmetric voltage distribution as well. Equation (5-10) predicts that any arbitrary current distribution can be produced, however in practice this is limited by the impedance parameters and structure of the network. The use of resistive impedances is not desired and negative resistance is not applicable. In the most general case there are $2(N^l + N^r + 1)$ variables for the resulting $N^l + N^r + 1$ mesh equations; so the system is underdetermined.

5.3.2 Application to the Birdcage Coil

Following canonical birdcage coil theory the total number of meshes $(N^l + N^r + 1)/4$ must be an integer for quadrature excitation. Also, for quadrature excitation two current distribution modes must be supported by the network structure concurrently:

$$\text{mode 1: } \boldsymbol{I_m} = I_0 \cos\left(\frac{2\pi}{N^l+N^r+1}(m-1)\right) \tag{5-11}$$

$$\text{mode 2: } \boldsymbol{I_m} = I_0 \cos\left(\frac{2\pi}{N^l+N^r+1}(m-1+(N^l+N^r+1)/4)\right)$$

In this case there are $2(N^l + N^r + 1)$ equations to match the number of variables, but depending on the suitability of matrix $\boldsymbol{Z_G}$ to support these current modes a solution may not exist (292).

It is often assumed that resistive losses and resistive coupling between meshes of the birdcage coil are both negligible, such that the impedance/coupling matrices introduced are positive definite, therefore resulting in a real solution and requiring purely reactive tuning impedances (188, 292). However, further simplification at this point reduces the accuracy of the solution for different practical cases, such as large loading as by the human body. Also, asymmetric loading cannot be accounted for, where different meshes have different resistive self-impedances and resistive coupling between adjacent meshes.

Consequently, one method of determining the required tuning capacitors is to determine the elements of $\boldsymbol{Z^L}$ that satisfy the following minimization:

$$\begin{matrix} min|\mathbb{Re}(Z^H)|_1 \\ min|(Z_{m1}^H - Z_{m2}^H)|_1 \end{matrix} \left[\begin{bmatrix} Z_{m1}^H \\ Z_{m2}^H \end{bmatrix} = \begin{bmatrix} -\boldsymbol{I_T}^{-1}(\boldsymbol{Z_G} \boldsymbol{I} + \boldsymbol{I_C} \boldsymbol{Z^L}),\ mode1 \\ -\boldsymbol{I_T}^{-1}(\boldsymbol{Z_G} \boldsymbol{I} + \boldsymbol{I_C} \boldsymbol{Z^L}),\ mode2 \end{bmatrix} \right] \tag{5-12}$$

The minimization of $|\mathbb{R}(Z^H)|_1$ is the same as ensuring that the tuning impedances are reactive (capacitors or inductors). The minimization of $|(Z_{m1}^H - Z_{m2}^H)|_1$ ensures that the tuning impedances employed result in a network with two quadrature current modes. Consequently, strong resistive coupling and potential asymmetric loading that may disrupt the expected symmetry is

accounted for with (5-12), while not making assumptions on the geometry or structure of the network.

Similarly, the elements $\boldsymbol{Z^H}$ can be determined to satisfy the minimization:

$$\min_{\substack{min|\mathbb{R}(Z^H)|_1 \\ min|(Z^H_{m1}-Z^H_{m2})|_1}} \begin{bmatrix} Z^L_{m1} \\ Z^L_{m2} \end{bmatrix} = \begin{bmatrix} -I_C^{-1}(\boldsymbol{Z_G}\,\boldsymbol{I} + I_T\boldsymbol{Z^H}),\ mode1 \\ -I_C^{-1}(\boldsymbol{Z_G}\,\boldsymbol{I} + I_T\boldsymbol{Z^H}),\ mode2 \end{bmatrix} \tag{5-13}$$

Practically, the complexity of varying the intermesh impedances $\boldsymbol{Z^L}$ for (5-12), or $\boldsymbol{Z^H}$ for (5-13), is simplified for the case of birdcage coils due to geometric symmetry. For example, for the simplest case of a circular birdcage coil each rung capacitor is equal, so only the value of a single capacitor needs to be determined. Also, for an elliptical birdcage there is a mirror symmetry of tuning/coupling elements about the coronal and sagittal planes of the coil, resulting in $(N^l + N^r + 1)/4$ capacitor values to determine. Due to symmetry, in these cases there is typically not a single solution of $\boldsymbol{Z^H}$ and $\boldsymbol{Z^L}$.

For the case where either only inter-mesh impedances (low-pass) or individual mesh tuning impedances (high-pass) are employed, (5-10) can be rearranged as:

$$\boldsymbol{Z^L} = -I_C^{-1}(\boldsymbol{Z_G}\,\boldsymbol{I} + I_T\boldsymbol{Z^H}), \text{for } \boldsymbol{Z^H} = \boldsymbol{0}, or \tag{5-14}$$
$$\boldsymbol{Z^H} = -I_T^{-1}(\boldsymbol{Z_G}\,\boldsymbol{I} + I_C\boldsymbol{Z^H}), \text{for } \boldsymbol{Z^L} = \boldsymbol{0}$$

where it can be seen there is a single solution in either case.

5.3.3 Application to the Non-Periodic Linear Ladder Resonator

As discussed here, for a linear non-periodic ladder network as shown in Figure 5-1b to emulate the desired current pattern of a quadrature driven birdcage coil, or fixed phase/power transmit array, the magnitude of the current on each mesh is equal with a constant progression of phase between meshes. Stated formally this means that:

$$\boldsymbol{I} = I_0 \begin{bmatrix} e^{-i\phi_c N^l} \\ \vdots \\ 1 \\ \vdots \\ e^{+i\phi_c N^r} \end{bmatrix} \tag{5-15}$$

where ϕ_c is the phase progression.

Practically, this may be achieved by a similar method as that introduced for the birdcage coil, by determining the elements of $\boldsymbol{Z^L}$ or $\boldsymbol{Z^H}$ that results in the minimization of:

$$\min_{|\mathbb{R}e(Z^H)|_1}\left[\boldsymbol{Z^H} = -I_T^{-1}(\boldsymbol{Z_G}\,\boldsymbol{I} + I_C\boldsymbol{Z^L}), \text{or}\right. \tag{5-16}$$
$$\min_{|\mathbb{R}e(Z^L)|_1}\left[\boldsymbol{Z^L} = -I_C^{-1}(\boldsymbol{Z_G}\,\boldsymbol{I} + I_H\boldsymbol{Z^L})\right.$$

where I is given by (5-15). For a single port excitation, the value of the tuning capacitor on the feeding mesh does not change the relative phase or magnitude between other meshes. Therefore, for a non-periodic resonator there are a resulting $2(N^l + N^r)$ relevant variables in $\mathbf{Z^L}$ and $\mathbf{Z^H}$. The explicit set of equations to determine the tuning capacitors from equation (5-2), and applied for a 3-element non-periodic ladder resonator, is detailed in (295) and shown in the appendix.

There may be no solution resulting in purely reactive tuning impedances. Also, there are no simplifications that can be made based on geometric symmetry since the non-periodic ladder resonator with imposed current distribution of (5-15) is not electrically symmetric. In addition, to produce the desired phase shift the self-impedances of the meshes must have a resistive component, which differs from previous description of ladder resonators/networks (296).

5.3.4 Hybrid Linear Ladder Network and Transceiver Array

The extension of the network theory developed to arrays of non-periodic ladder networks is simple. As shown in Figure 5-1d separate ladder networks can be treated as together in the network equations (5-2) and (5-3), except with elements of the inter-mesh capacitors, $\mathbf{Z^L}$, set to zero or excluded. As an example, for the specific case of two three-mesh ladder networks in Figure 5-1d:

$$\mathbf{Z^L} = \begin{bmatrix} Z_{23}^{Ll} \\ 0 \\ Z_{01}^{Ll} \\ Z_{01}^{Lr} \\ 0 \\ Z_{32}^{Ll} \end{bmatrix}, \mathbf{Z^H} = \begin{bmatrix} Z_3^{Hl} \\ Z_2^{Hl} \\ Z_1^{Hl} \\ Z_0^{Hlr} \\ Z_1^{Hr} \\ Z_2^{Hr} \end{bmatrix} \tag{5-17}$$

Equation (5-16) can therefore be applied in the same way as for a single connected ladder network.

5.4 Methods

5.4.1 Simulation of Transmit/Receive Comparison Metrics

Simulation of transmit and receive performance was performed at 60 MHz as described in sections 3.3.3 and 4.3.4. To test the variation of transmit homogeneity with loading, the size of a phantom, with dielectric properties $\varepsilon_r = 76$ and $\sigma = 0.8$ S/m (54), was varied in size. The phantom was an elliptical cylinder with major radius 20% larger than the minor radius, simulated with sizes of 12 cm, 14 cm and 16 cm for the minor radius. The transmit efficiency

(B_1^+) for 1kW RMS input power, and SAR averaged for 10 g regions (146) were compared for each coil and the intrinsic SNR (iSNR) with the coil acting in receive mode with the iSNR calculated according to (2-105). To emulate a single coil for the elliptical birdcage coil the fields were combined with a fixed phase corresponding to the opposite circular polarization of that in transmission, while for the coils acting as receive arrays the weights for optimum combination used were obtain according to (2-104).

5.4.2 Simulation of 7-mesh Linear Ladder Resonator

A demonstrative example of a non-periodic ladder coil using asymmetric capacitor tuning for circular polarization was developed with dimensions as shown in Figure 5-2a. The 7-mesh coil is excited from a central port and the conductor is split on the opposing side with capacitive decoupling employed (236) ($C_{ds} = 12\ pF, C_d = 60\ pF$) to isolate the two outer-most meshes. The desired current distribution from (5-15) is:

$$I = I_0 \begin{bmatrix} e^{-i\frac{6\pi}{7}} \\ e^{-i\frac{4\pi}{7}} \\ e^{-i\frac{2\pi}{7}} \\ 1 \\ e^{i\frac{2\pi}{7}} \\ e^{i\frac{4\pi}{7}} \\ e^{i\frac{6\pi}{7}} \end{bmatrix} \tag{5-18}$$

To solve (5-16) for this current distribution simulation was performed with an initial set of capacitor values (all capacitors in $\mathbf{Z}^H$ and $\mathbf{Z}^L$ set to 25 pf) and all meshes fed from a central port to determine $\mathbf{Z}_G$. Based on the simulated impedance matrix the minimization in (5-16) was then carried out. Since the asymmetric capacitor values altered the distributed nature of the coil's electrical symmetry it was observed that the geometrically dependent impedance matrix $\mathbf{Z}_G$ was also slightly altered. The simulation was repeated with newly calculated capacitor values iteratively until the simulated impedance matrix remained constant.

5.4.3 6-mesh Ladder/Transceive Array Hybrid

The coil displayed in Figure 5-2b is a hybrid design of a transceive array and ladder array similar to that presented as a conceptual diagram in Figure 5-1d: fed from the two ports labelled 0° and 180° to excite the current distribution of (5-15) on the six meshes. For the meshes that are adjacent to each other and not part of the same two 3-element ladder structures decoupling was achieved by critical overlap.

The separate resonators are treated as a 6-mesh system. The symmetry of the coil design means that the lumped impedances on the separate 3-mesh ladder networks are the same so that (5-17) can be re-written as:

$$\mathbf{Z^L} = \begin{bmatrix} Z_{01}^{Lr} \\ 0 \\ Z_{01}^{Ll} \\ Z_{01}^{Lr} \\ 0 \\ Z_{01}^{Ll} \end{bmatrix}, \mathbf{Z^H} = \begin{bmatrix} Z_0^H \\ Z_1^{Hr} \\ Z_1^{Hl} \\ Z_0^{Hlr} \\ Z_1^{Hr} \\ Z_1^{Hl} \end{bmatrix} \tag{5-19}$$

Finally, to replicate the current distribution of a 6-mesh birdcage, with quadrature excitation, the desired $\mathbf{I}$ is:

$$\mathbf{I} = I_0 \begin{bmatrix} 1 \\ e^{i\frac{\pi}{3}} \\ e^{i\frac{2\pi}{3}} \\ -1 \\ e^{-i\frac{2\pi}{3}} \\ e^{-i\frac{\pi}{3}} \end{bmatrix} \tag{5-20}$$

Asymmetries in loading may lead to differences in the required tuning impedances found solving (5-16) for of $\mathbf{Z^L}$ or $\mathbf{Z^H}$, but for the specific implementation of the coil shown in Figure 5-2b these differences were negligible.
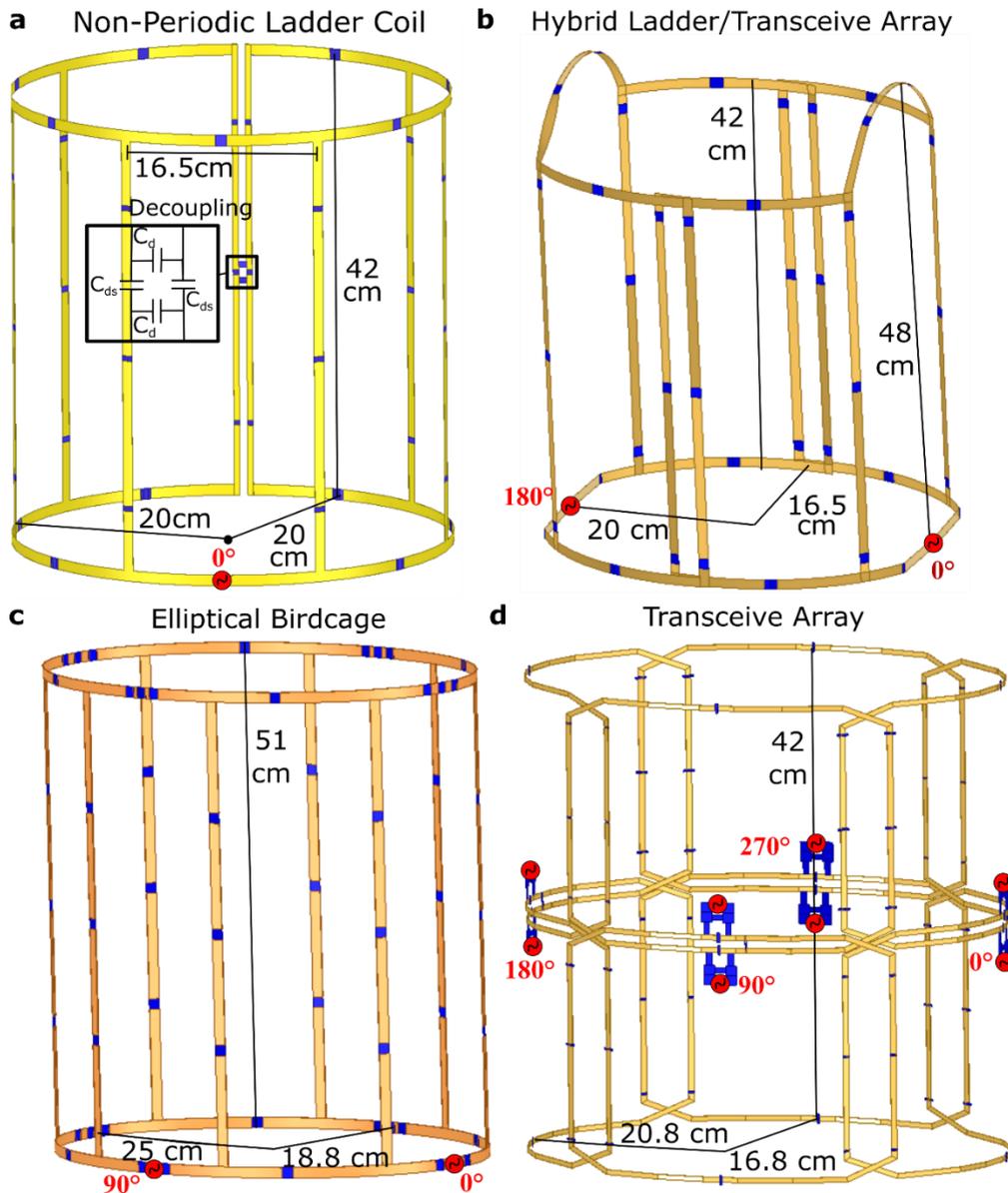
Figure 5-2: Simulation models of a) a 7-mesh non-periodic ladder coil with single port excitation, b) 6-mesh non periodic ladder/transceive array hybrid with two port excitation, c) conventional 8-mesh elliptical birdcage volume resonator and d) 8-element dual row transceive array.

The coil is designed to fit the form of to the human torso and therefore includes a curved top element to accommodate the arms and is of smaller dimensions than the 7-mesh ladder coil or the elliptical birdcage shown in Figure 5-2c. This is expected to be at the detriment of field homogeneity (due to smaller size and theoretically non-optimal geometry of current carrying paths) for the benefit of subject comfort. Due to the smaller size and larger filling factor there should also be an increase in receive sensitivity and transmit efficiency. Derivation of the required capacitor values was carried out as with the 7-element resonator. There is a separate receive channel for each mesh. For the calculation of $\widehat{B}_1^-$ the ports were replaced with current sources to determine the receive sensitivities of the individual meshes.

5.4.4 Simulation of 8-mesh Elliptical Birdcage Coil

As a standard for comparison with the novel ladder-coils introduced here an 8-mesh elliptical birdcage coil was simulated with the dimensions labelled in Figure 5-2c, which is similar to that of commercial MRI coils (Rapid Biomedical) previously employed for ^{19}F imaging at 1.5T (123). The separation/placement of rungs followed the theoretically derived optimal values for the current distribution in (5-11) (188).

The derivation of capacitor values was carried out as for the non-periodic ladder resonator coils, with central parts of the coil replaced with ports and iterative simulation with capacitor values derived with equation (5-12). In contrast to the 7-mesh non-periodic ladder resonator, only two capacitor values needed to be optimized since the coil has elliptical quadrature symmetry.

5.4.5 Simulation of 8-element Transceive Array

The simulation and design of the dual row 8-element transceive array in Figure 5-2d has been described previously (244). Superior and inferior adjacent coils are decoupled capacitively, while adjacent coils on the same row are decoupled by critical overlap. Matching is performed on each coil individually and they are driven by separate ports in simulation.

5.4.6 Fabrication and on-bench Measurement of Ladder Transceive Array

The ladder/transceive coil shown in Figure 5-2b was constructed from 11 mm wide copper tape. Capacitors were initially placed on the coil with values equal to those from simulation. To further tune the array on the bench the impedance matrix was first measured via calibrated S-parameter measurement (297). Inter-mesh capacitors were then changed to match the required mutual reactance between adjacent elements and tuning mesh capacitors were varied to match the reactive part of the self-impedance. Final capacitor values were found to be close to those simulated (±10%), with the variation observed likely due to differences introduced in construction and the phantom geometry using in measurement vs. simulation. In measurement, variability may also be introduced due to the introduction of BNC connectors on arm straps and the use of Velcro to join the anterior meshes so the coil opens up as shown in Figure 5-3.
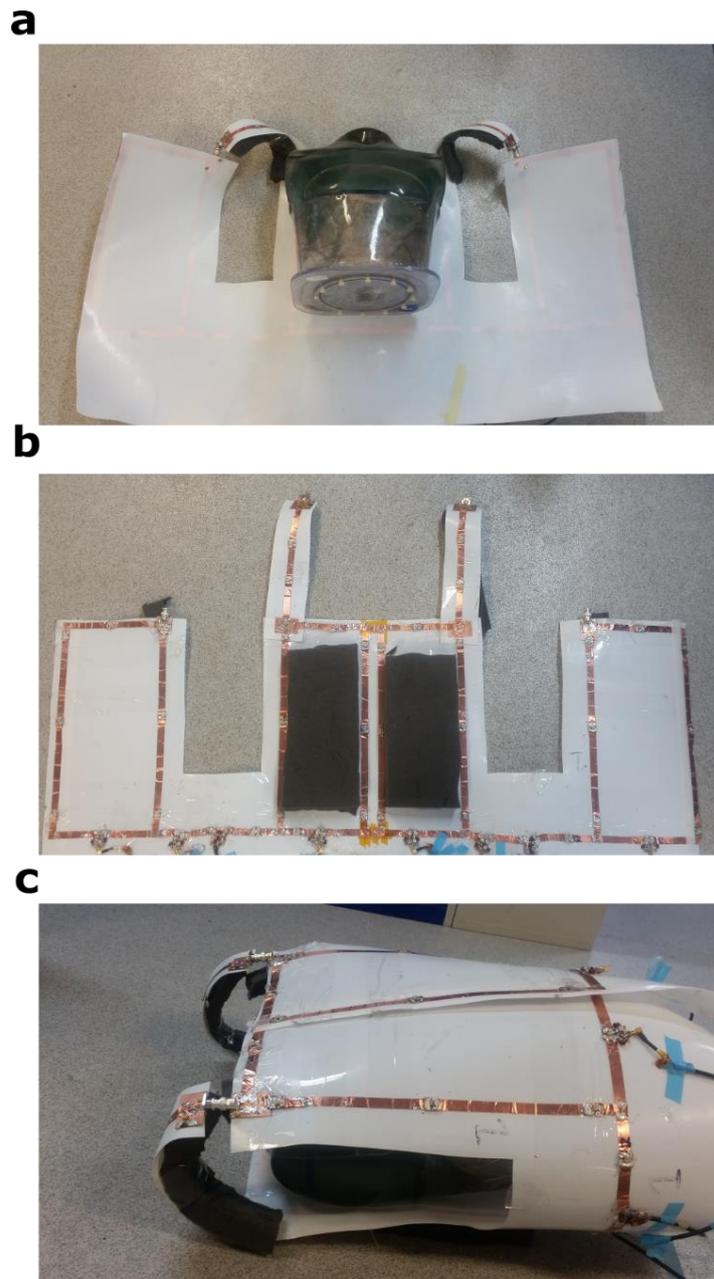
Figure 5-3: (a) Multinuclear ^{19}F and ^1H phantom (separate compartments) on coil when it is unfolded. (b) 6-element transceiver ladder array unfolded showing connection points for receive and transmit sections. Shoulder straps are connected with BCN female-male connectors and central overlap on one side is joined with by Velcro strips (c) Coil assembled with human torso phantom inside.

The circuit diagram for the constructed coil is shown in Figure 5-4, which includes the matching networks employed. During transmit all PIN diodes (MA4P7435F-1091T, MACOM, MA) are forward biased and act as small value resistors ($< 0.2\ \Omega$). The lattice balun employed for the receive network also isolates the preamplifier circuitry by acting as a larger parallel impedance with the diode in parallel with C_m. In reception the PIN diodes act as large capacitive impedances (< 2 pF) and the transmit circuitry is isolated from the coils. A 180^0 power combiner is used to split power between the two 3-element ladder resonators on opposing sides.

Preamplifier decoupling of coils is provided by the use of low impedance preamplifiers (~1.5 Ω for WanTCom WMM series, with measured noise Figure of ~1.5dB for both ^{1}H and ^{19}F frequencies) (252).
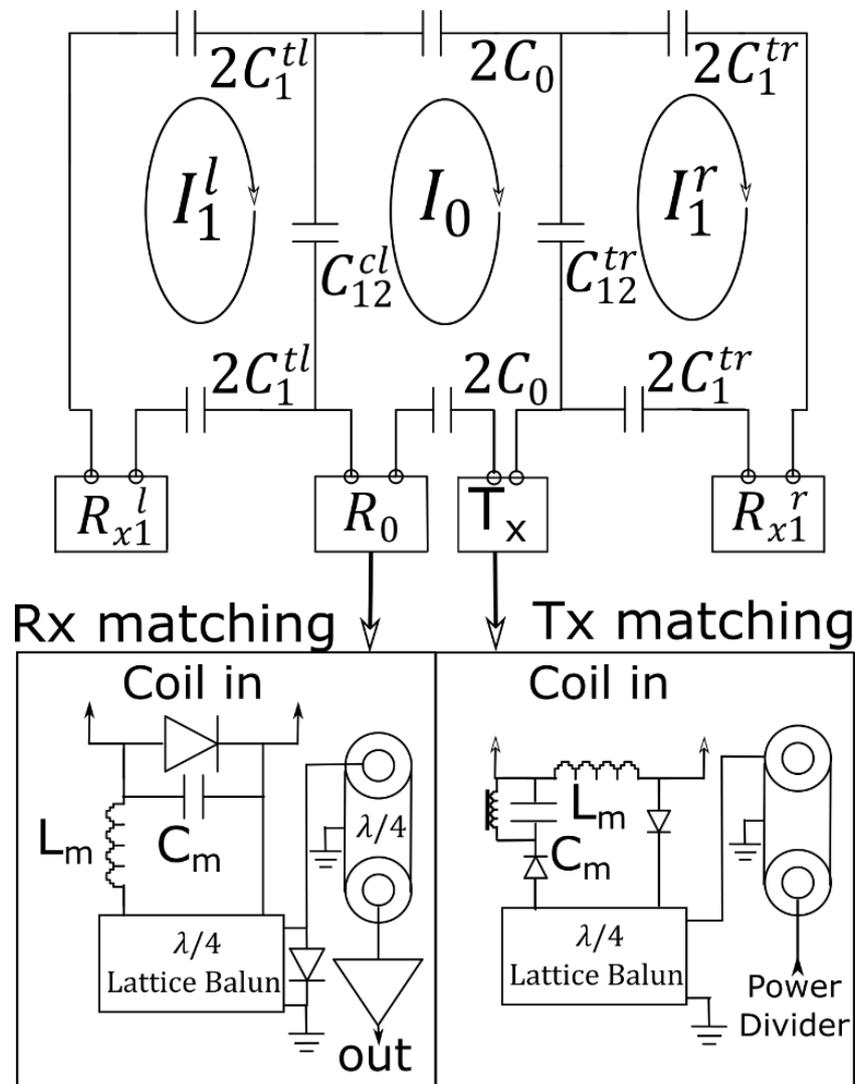
Figure 5-4: Circuit Schematic for 3-element ladder/transceive array with Rx/Tx matching and switching/detuning networks shown. In practice the capacitance was distributed along the coil with multiple capacitors as shown in Figure 5-2b.

The imaging/on-bench measurement phantom also shown in Figure 5-3 consisted of a torso shaped shell filled with 1.96g/L $CuSO_4$ and 3.6g/L NaCl solution and two separate bottles filled with 81% C_3F_8 + 21% O_2 to represent the lungs. The S-parameters of the two separate 3-element ladder resonators of the transceiver array were measured and compared in transmit mode to the simulated values over a range of 45 MHz-75 MHz. Measurements of the S-parameters in transmission were performed prior to matching and after matching with the series connection of a $\lambda/4$ T-line matching network and $\lambda/4$ lattice balun.

5.4.7 **MR Imaging**

To characterize the flip angle (FA) within the multinuclear torso phantom at ^{19}F and ^{1}H Larmor frequencies pixelwise fitting was performed as described in section according to the spoiled-gradient echo (SPGR) signal equation as in reference (257) and detailed in section 3.3.4. For ^{1}H imaging the repetition time (TR) was long relative to T_1 so that the signal was T_1 independent, while for ^{19}F imaging a T_1 of 17.5 ms was used for fitting. In-vivo FA mapping was also performed by varying the input power in three steps with a T_1 of 35 ms. The in-vivo images were filtered prior to fitting to improve the SNR for improved fitting accuracy. Based on the derived mean FA for given input power at both frequencies in-vivo ventilation and anatomical imaging was performed. The sequence parameters used are provided in Table 5-1.

Table 5-1: Imaging parameters of the phantom FA mapping and in-vivo ventilation and anatomical imaging

	Sequence	TE (ms)	TR (ms)	BW (±KHz)	Resolution (mm^3)	FOV (cm^3)	Target FA (°)	Avg.
Phantom FA mapping
^{1}H	2D SPGR	3.1	400	10	6.25x6.25x10	40x40x29	20-145	1
^{19}F	3D SPGR	2.9	6.8	3.01	10x10x15	40x36x24	4-30	15
In-Vivo Anatomical + Ventilation Imaging
^{1}H	2D SPGR	2.1	120	19.3	4x4x10	40x40x24	30	1
^{19}F	3D SSFP	1.4	4	8.96	10x10x10	40x32x24	76	10
In-vivo FA mapping
^{19}F	3D SSFP	1.4	35	3.01	12.5x12.5x20	32x26X12	20/40/60	1

5.5 **Results**

5.5.1 **Simulation of Tuning Capacitor Values**

Final values of the capacitors used in simulation of the 7-element resonator are provided in Table 5-2. Additionally, the final simulated self-impedance and next nearest meshes mutual impedance (from $\boldsymbol{Z_G + Z_C + Z_T}$) are included. The difference in tuning a non-periodic resonator for the current distribution in equation (5-15) compared to a conventional birdcage is apparent in the asymmetry of tuning capacitor values about the central feed mesh. Although not explicitly clear from equation (5-16), the tuning capacitor on the central mesh (C_0^t) has no impact on the resulting current distribution.

Table 5-2: Tuning capacitor values and simulated impedance parameters (self-impedance and next-nearest neighbour mutual impedance) of 7-mesh linear ladder resonator when simulated with the realistic body model.

Inter-mesh Capacitors (pF)						
C_{23}^l	C_{12}^l	C_{01}^l	C_{01}^r	C_{12}^r	C_{23}^r	
19.8	15.2	12.4	49.1	44.2	33.2	
Self-Impedance Tuning Capacitors (pF)						
C_3^l	C_2^l	C_1^l	C_0	C_1^r	C_2^r	C_3^r
23.4	27.3	39.5	16.6	14.4	13.7	17.7
(Self-Impedances (Ω))						
Z_{33}^l	Z_{22}^l	Z_{11}^l	Z_{00}	Z_{11}^r	Z_{22}^r	Z_{33}^r
9.52-25.9j	12.2-81.0j	8.76-126j	9.43-29.8j	12.1+51.9j	16.6+12.0j	10.3-5.28j
(Mutual Impedances of Neighbouring Meshes (Ω))						
Z_{23}^l	Z_{12}^l	Z_{01}^l	Z_{01}^r	Z_{12}^r	Z_{23}^r	
0.28+33.2j	1.57+62.0j	5.44+101j	3.14-63.1j	1.2-46.1j	-5.22-7.29j	

The self-resistance of the meshes is also asymmetric, partially due to simulation with the non-symmetric human body model, and partially due to the change in conservative electric field losses in the loading phantom due to asymmetric voltage/electric field distribution introduced on the different current meshes for the asymmetrically placed tuning capacitors (298).

The tuning capacitor values for the ladder/transceiver array and resulting impedance parameters are shown in Table 5-3. Again, the asymmetry between left and right sides is apparent. If there was no coupling between non-adjacent meshes, or asymmetric loading, the impedance matrix would be conjugate symmetric ($Z_{11}^r = Z_{11}^{l\,*}$ and $Z_{01}^l = Z_{01}^{r\,*}$).

Assuming that the mesh corresponding to the 0^0 feed point is the central mesh (mesh with current I_0 in Figure 5-1b) the value of capacitors used to tune the elliptical birdcage were $C_2^l = 1000\,pF$, $C_1^l = 2400\,pF$, $C_0 = 1000\,pF$, $C_{01}^l = 6.6\,pF$ and $C_{12}^l = 6.8\,pF$. Due to the geometric quadrature symmetry the other capacitors included are the same as these values.

Table 5-3: Tuning capacitor values and impedance parameters (self and mutual impedance) of the 3-element linear ladder resonators for the ladder/transceive array hybrid simulated with male body model.

Inter-mesh Capacitors (pF)		
C_{01}^l	C_{01}^r	
15.9	44.7	
Self-Impedance Tuning Capacitors (pF)		
C_1^l	C_0	C_1^r
11.9	14.2	8.46
Self-Impedances (Ω)		
Z_{11}^l	Z_{00}	Z_{11}^r
22.4-29.5j	26.5-15.6j	21.0+0.91j
Mutual Impedances of Neighbouring Meshes (Ω)		
Z_{01}^l	Z_{01}^r	
6.2+49.0j	-4.5-55.6j	

5.5.2 Variation of Transmit Field with Load

Figure 5-5 shows the resulting B_1^+ and $\hat{B}_1^-$ fields with a 1 kW RMS excitation in an axial slice as the phantom size and type is varied. The capacitor tuning was optimized for all coils to produce the desired current distribution when simulated with the human body model. It is clear that the 7-mesh non-periodic resonator is highly sensitive to the loading and inhomogeneity and non-quadrature excitation arises when the loading is varied, with greater excitation of meshes on the side of coil to the right of the central feed port. The reason for this asymmetry can be attributed to the different levels of mutual and self-reactance required for the desired current distribution with the human load. Lower self and mutual reactance is present on the right side meshes so that changes in the self-resistance leads to larger variations in the currents on these meshes. The ladder/transceive coil is less sensitive, but the same observed asymmetry of excitation is observed. In contrast, the fields produced by the elliptical birdcage coil visually appears to maintain an elliptical symmetry. The ladder/transceive coil shows greater field inhomogeneity in the body than the other two, but this may be attributed to the lower number of meshes and a geometry that is optimized to be form fitting.

a **Non-Periodic Ladder Coil**

semi-minor radius=12cm
$B_1^+=10.3\pm12.3\%$ $B_1^+/B_1^-=2.7$

semi-minor radius=14cm
$B_1^+=7.53\pm25.9\%$ $B_1^+/B_1^-=2.3$

B_1^+ B_1^- B_1^+ B_1^-

semi-minor radius=16cm
$B_1^+=5.71\pm44.6\%$ $B_1^+/B_1^-=2.0$

Human Body Model
$B_1^+=11.5\pm10.2\%$ $B_1^+/B_1^-=3.8$

B_1^+ B_1^- B_1^+ B_1^-

0   0.4µ   0.8µ   1.2µ   1.6µ   2µ
Transmit Field

b **Hybrid Ladder/Transceive Array**

semi-minor radius=12cm
$B_1^+=10.2\pm21.4\%$ $B_1^+/B_1^-=2.2$

semi-minor radius=14cm
$B_1^+=8.05\pm24.2\%$ $B_1^+/B_1^-=2.6$

B_1^+ B_1^- B_1^+ B_1^-

semi-minor radius=16cm
$B_1^+=6.36\pm46.1\%$ $B_1^+/B_1^-=2.0$

Human Body Model
$B_1^+=12.0\pm18.9\%$ $B_1^+/B_1^-=3.8$

B_1^+ B_1^- B_1^+ B_1^-

0   0.4µ   0.8µ   1.2µ   1.6µ   2µ
Transmit Field

c **Elliptical Birdcage**

semi-minor radius=12cm
$B_1^+=8.67\pm9.38\%$ $B_1^+/B_1^-=2.7$

semi-minor radius=14cm
$B_1^+=6.56\pm13.8\%$ $B_1^+/B_1^-=2.2$

B_1^+ B_1^- B_1^+ B_1^-

semi-minor radius=16cm
$B_1^+=4.92\pm20.0\%$ $B_1^+/B_1^-=2.0$

Human Body Model
$B_1^+=10.2\pm12.9\%$ $B_1^+/B_1^-=3.8$

B_1^+ B_1^- B_1^+ B_1^-

0   0.4µ   0.8µ   1.2µ   1.6µ   2µ
Transmit Field

Figure 5-5: Simulated B_1^+ and B_1^- fields in a central axial slice produced by the a) 7-mesh non-periodic resonator, b) ladder/transceive resonator and c) elliptical birdcage. For each coil the fields maps are displayed for three different sizes of an elliptical phantom and a human body model. The mean and standard deviation of the B_1^+ within the phantom is listed above the maps.

116

The simulated reflection coefficient for the non-periodic ladder coil, hybrid ladder/transceive array and elliptical birdcage coil with human body model over a broad frequency range are shown in Figure 5-6. Although the elliptical birdcage coil isn't strictly lowpass the endring capacitors are of low enough impedance that 4 distinct modes, and the end-ring mode, can be separated and appear with a distribution similar to that of the lowpass birdcage (293). For the non-periodic ladder coil and hybrid ladder transceive array there is no familiar mode distribution and the frequency of interest (60MHz) does not correspond to specific resonance but the coil appears to operate between multiple resonances.
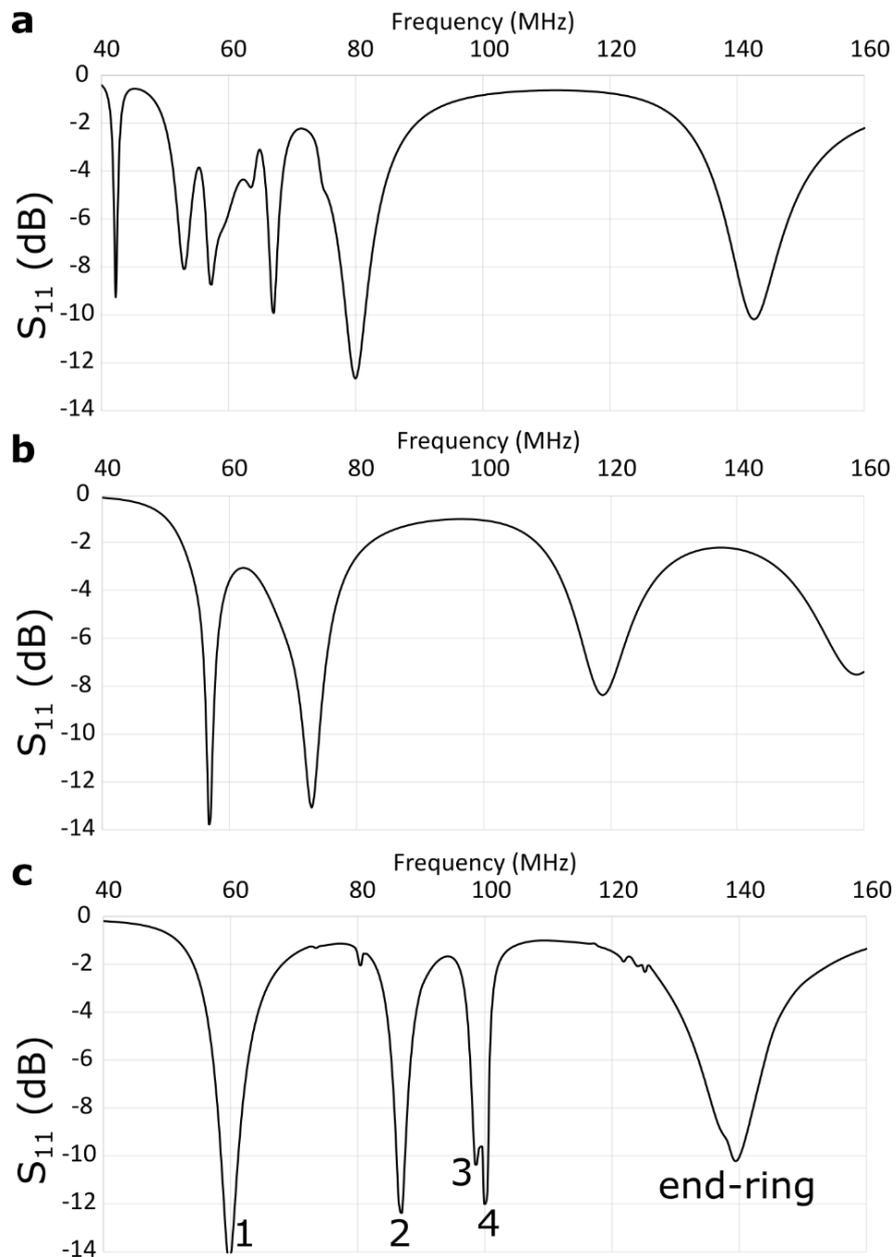
Figure 5-6: Simulated reflection coefficient (without matching) for a: 7-mesh non-periodic resonator, b: 3-mesh half of 6-mesh ladder/transceive resonator and c: elliptical birdcage coil with specified modes.

5.5.3   **Transmit Efficiency of Coil Designs**

Transmit efficiency in coronal and axial slices and SAR maps in axial slices for the elliptical birdcage coil, ladder/transceive array and conventional transceive array are displayed in Figure 5-7. The mean and standard deviation of the transmit efficiency displayed above slices is found inside the outlined lung volume, which was derived from previously acquired ventilation images in a healthy male volunteer of a similar size to the simulated human body phantom.

The mean transmit efficiency of the ladder array is higher, with poorer spatial homogeneity than the transmit array. The homogeneity of the ladder/transceive array is lower than the elliptical birdcage, but the ratio of transmit efficiency to SAR is higher. Figure 5-7b shows the distribution of SAR is more homogeneous for the ladder array and birdcage when compared to the transmit array, while having a lower maximum 10g averaged SAR.
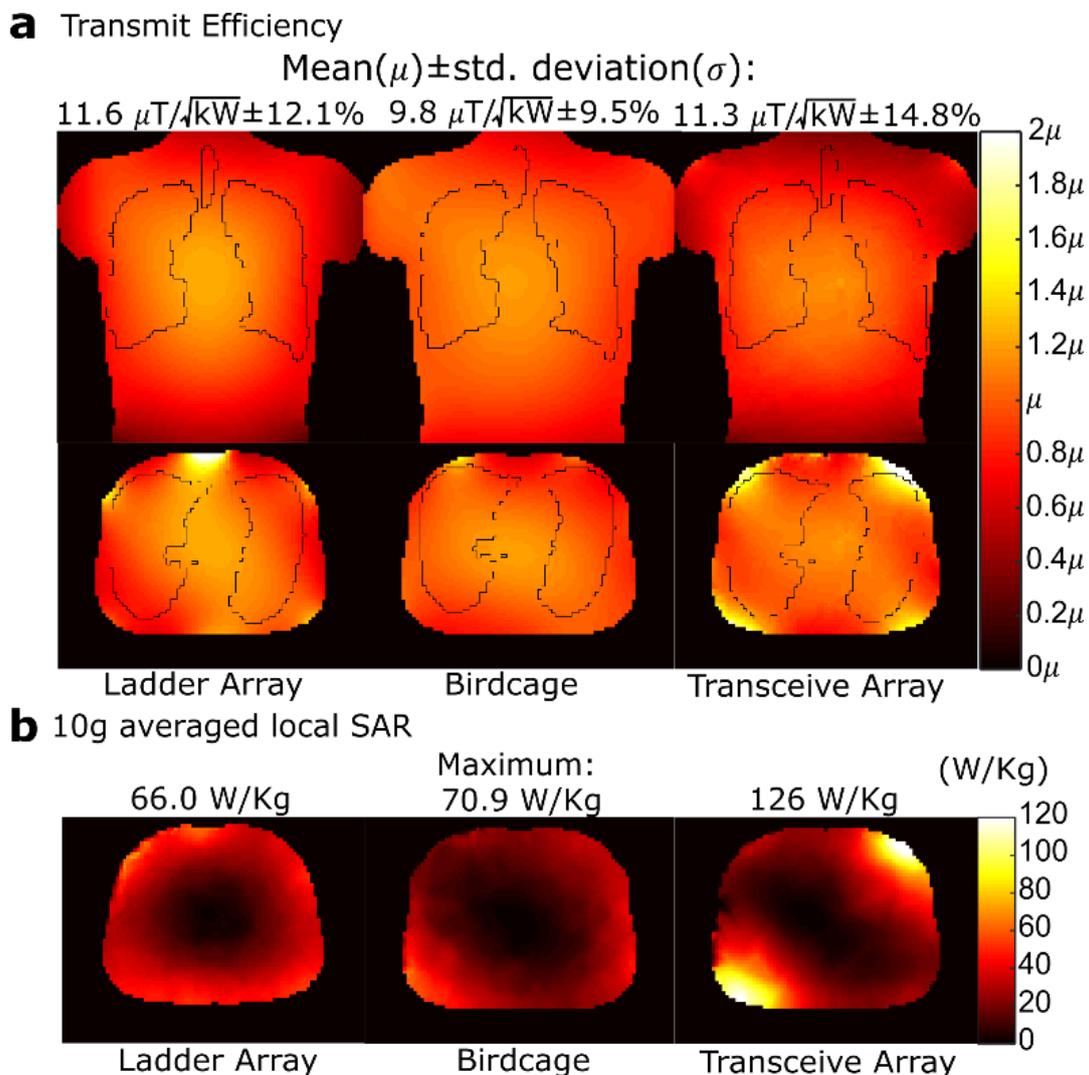
Figure 5-7: (a) Simulated transmit efficiency for a given 1 kW RMS input power for the 6-mesh ladder/transceive array coil, elliptical birdcage coil and 8-element transceive coil. (b) Also, the corresponding 10g averaged local SAR is shown in a central axial slice both, where the maximum within the entire body is labelled above.

5.5.4 Receive Sensitivity of Coil Designs

The simulated receive sensitivity according to (2-50)) for the elliptical birdcage coil, ladder/transceive array and conventional transceive array are displayed in Figure 5-8. The mean and standard deviation that are displayed above the maps are measured from the same lung volume as for the transmit efficiency plots in Figure 5-7. As may be expected, the receive sensitivity of the arrays is much higher than that of a single volume resonator (the elliptical birdcage). The 6-element ladder/transceive array has lower mean receive sensitivity than the 8-element dual row transceive array, but the amount is commensurate with the difference in the number of elements. The increase also appears to be primarily due to higher sensitivity in the peripheral regions of the lungs, due to the smaller size of the coils in the transceiver array design, while the receive sensitivity in the central region is close.
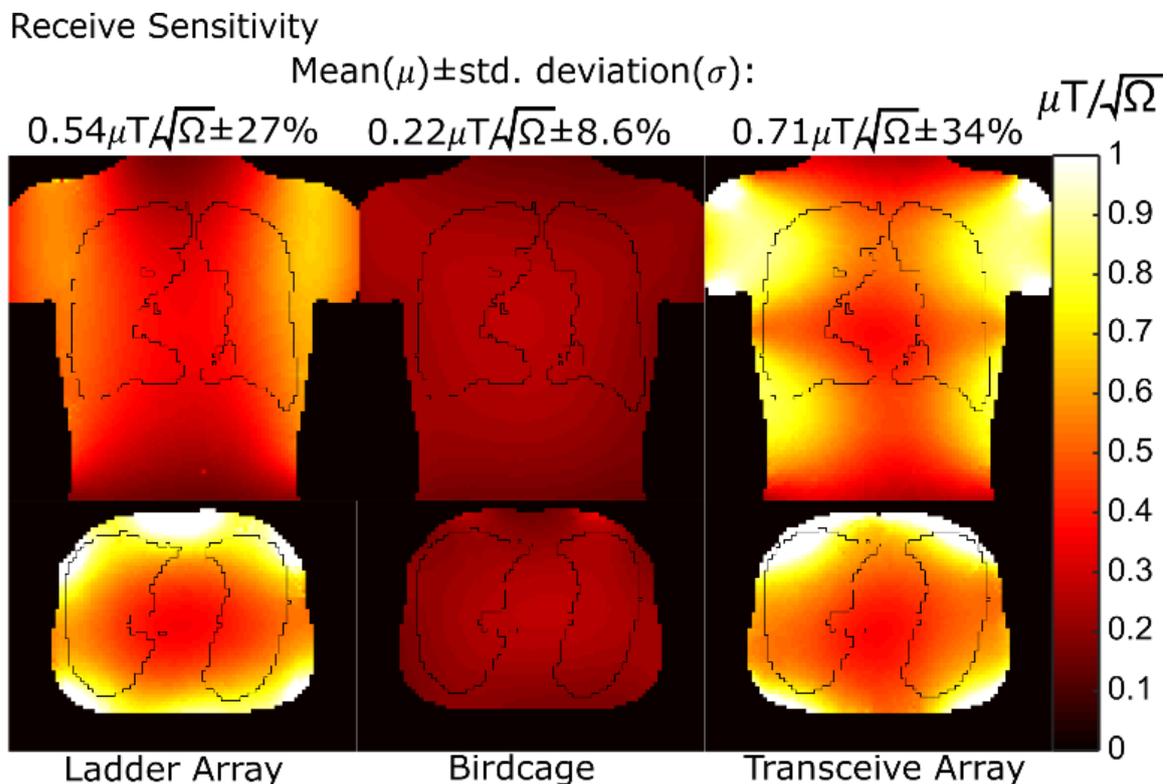
Figure 5-8: Simulated receive sensitivity of the 6-mesh ladder/transceive array coil, elliptical birdcage coil and 8-element transceive coil in central coronal (top) and axial (bottom) slices.

There was a small difference in the simulated homogeneity of the receive sensitivity when compared to the transmit field for the elliptical birdcage. This is due to the simulation in transmit sensitivity assuming equal power is delivered to each port in transmission, while in simulation of the receive sensitivity there is expected to be equal current magnitude. Thus, the discrepancy arises due to the different loading of the two quadrature modes, which in practice

may be compensated by use of a feeding network that delivers unequal power to the two ports (188).
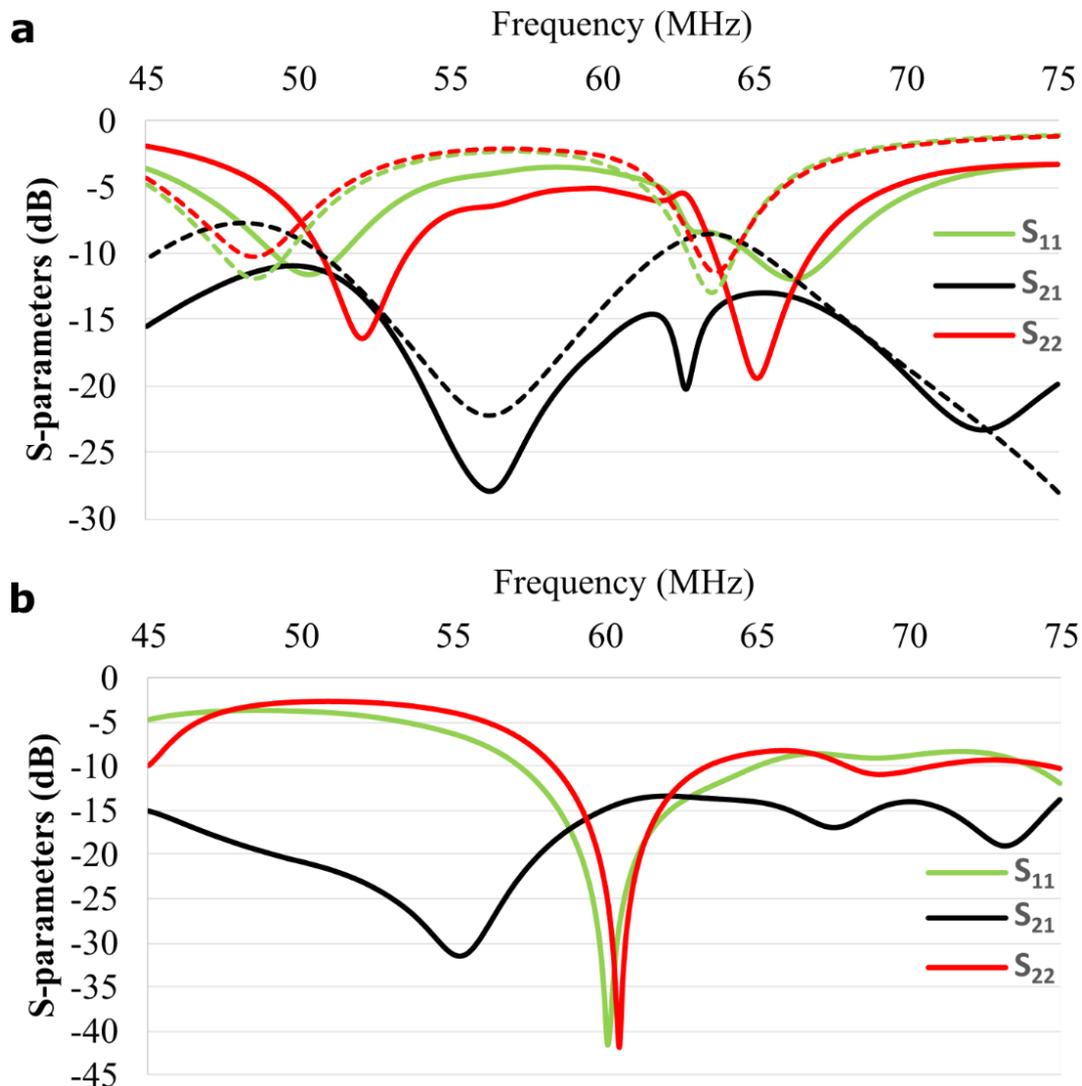
Figure 5-9: (a) Simulated (dashed) and measured (solid) scattering parameters prior to matching of the pair of 3-element ladder resonators. Differences in the resonant frequencies for simulation and measurement are expected due to differences in the geometry conformation during measurement and the tuning capacitors on the central current mesh coil. (b) The resulting S-parameters when each of the ladder resonator pair is matched is shown, where matching remains ~10 dB at the ^{1}H Larmor frequency of 64 MHz and isolation is ~15 dB.

5.5.5 Ladder Array Transmit Matching

The results of measuring the S-parameters at the transmit ports of the ladder/transceive coil hybrid before and after matching is shown in Figure 5-9a and Figure 5-9b, respectively. The trends of the simulated S_{11}, S_{22} and S_{12} match those of the measured, with some difference expected due to variations in the constructed vs. simulated geometry. The isolation between ports is relatively high at 60 MHz ($\sim 15 \, dB$), but since this is taken into account in the derivation of capacitor values with (5-16), for the current distribution of (5-20), it should not

significantly alter the imposed current distribution. The resonances of the coils to the left and right of the feed mesh is observed in the dips at higher and lower frequencies. After matching the dips are not observed as the matching network is narrowband. The reflection coefficient of the ports is $\sim -10\ dB$ at the Larmor frequency of ^{1}H indicating that power reflection should not be detrimental to safety or equipment after the inclusion of the 180^0 power combiner.
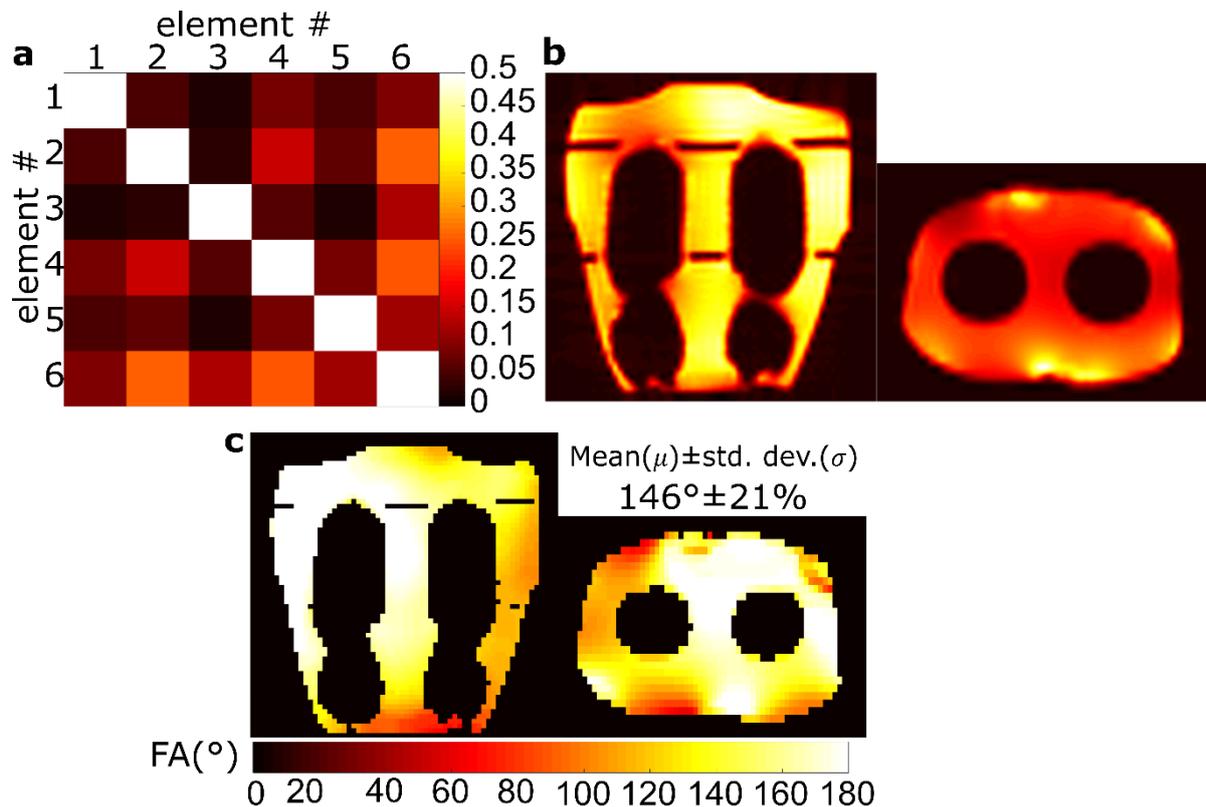
Figure 5-10: For the ladder/tranceive array hybrid measured (a) noise correlation matrix, (b) SNR maps and (c) FA maps in a central coronal and axial slice at ^{1}H frequency (64 MHz) with the mean and standard deviation of FA displayed calculated within the entire imaging phantom.

5.5.6 Phantom Imaging

Results of FA mapping with the multinuclear human torso phantom using the hybrid ladder/transceiver array with ^{1}H are shown in Figure 5-10. Noise correlations between the different elements are shown, which are generally less than 0.25. The pattern of the SNR maps shown with the FA maps are similar to the simulated receive sensitivity in Figure 5-8. The standard deviation of the FA is ±21% throughout the volume of the torso phantom, which is comparable to the 18.9% simulated in an axial slice in Figure 5-5 considering the coil is operating off-resonance, with some difference in power delivered to the two ports observed due to mismatch.

The noise correlation when imaging the multinuclear torso phantom at the Larmor frequency of ^{19}F is shown in Figure 5-11. The noise correlation between elements was generally lower

than 0.25, which was also observed with the ^{1}H phantom imaging. Additionally, the individual SNR maps from each channel shown in Figure 5-11c demonstrate distinct sensitivity patterns are obtained with each channel. The standard deviation of the FA within the imaging phantom bottles is close to that found with simulation in the lung region shown in Figure 5-7a (±12.9% in measurement vs. 12.1% in simulation). Some greater variation in the measurement fitting may be due to the effects of pixels on the edge having part of their volume outside of the phantom, which appears to result in an inaccurate increase in the fitted FA.
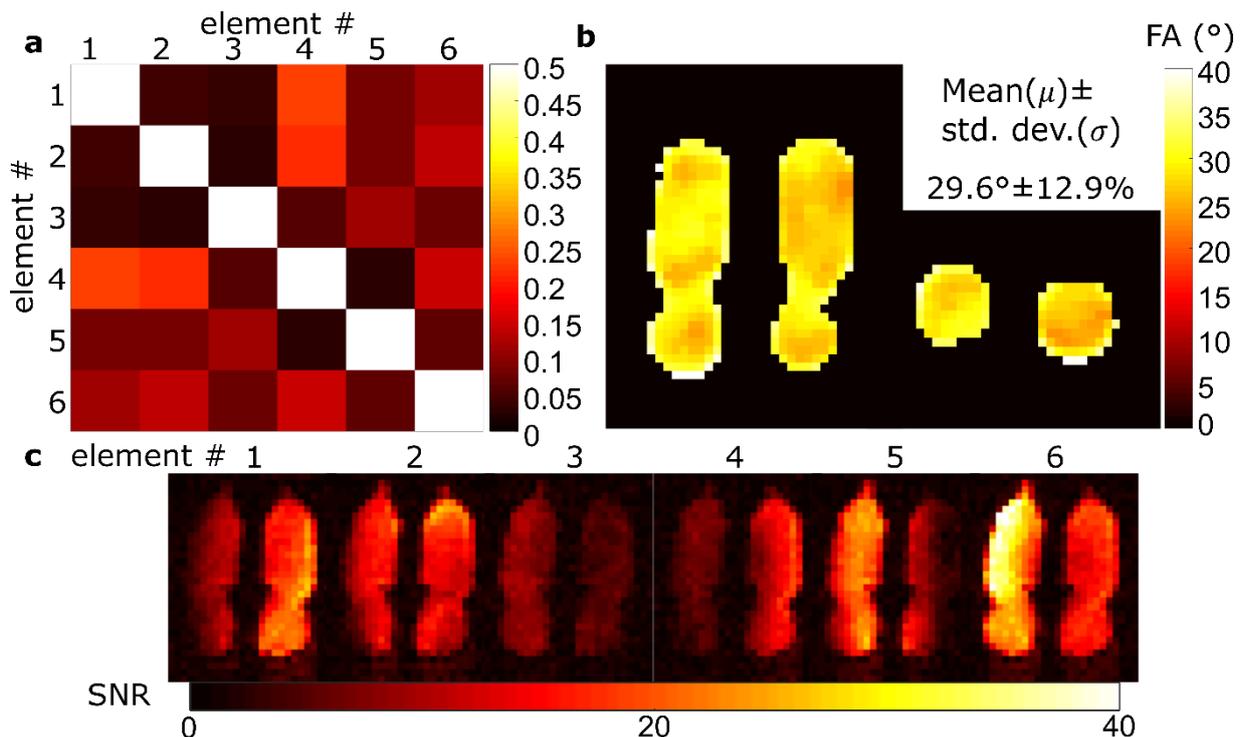
Figure 5-11: For the ladder/tranceive array hybrid measured (a) noise correlation matrix, (b) individual channel SNR maps and (c) FA maps in a central coronal and axial slice at the ^{19}F frequency (60 MHz) with the mean and standard deviation of FA displayed calculated within the entire imaging phantom.

5.5.7 In-Vivo Imaging

In-vivo ^{19}F ventilation images acquired with the long T_1 SPGR imaging for FA mapping are showed in Figure 5-12a, with the corresponding FA maps. Higher than simulated variation is found, which may come from two sources. The flexibility of the coil distorts the geometry, leading to observer high FA regions in the very anterior of the lungs and low SNR regions may have more variation due to the impact of noise on the least-squares fitting.
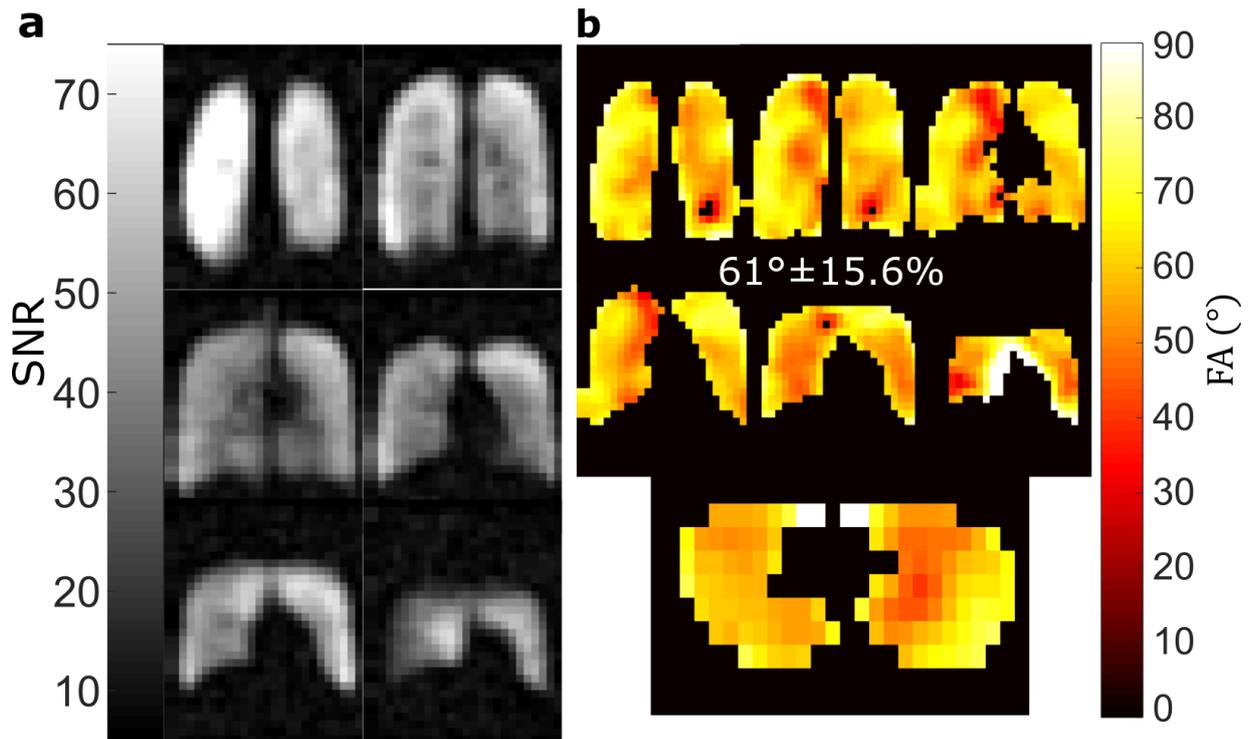
Figure 5-12: ^{19}F in-vivo a: SPGR images and b: FA maps.

Co-registered ^{1}H anatomical and ^{19}F ventilation in-vivo images are displayed in Figure 5-13. The ^{1}H images have higher SNR than obtainable using a single volume coil with the same imaging sequence, and no regions of signal dropout due to inhomogeneity in the receive or transmit fields was observed. In the ventilation image the presence of banding artefacts are observed. These artefacts are not observed in the FA maps or SPGR images so they can be attributed to the use of SSFP imaging due to the B_0 inhomogeneity and are unrelated to the coil's operation. The SNR is largely uniform between left and right lungs with higher SNR observed in the anterior and posterior slices as expected from the receive sensitivity maps shown in Figure 5-8.
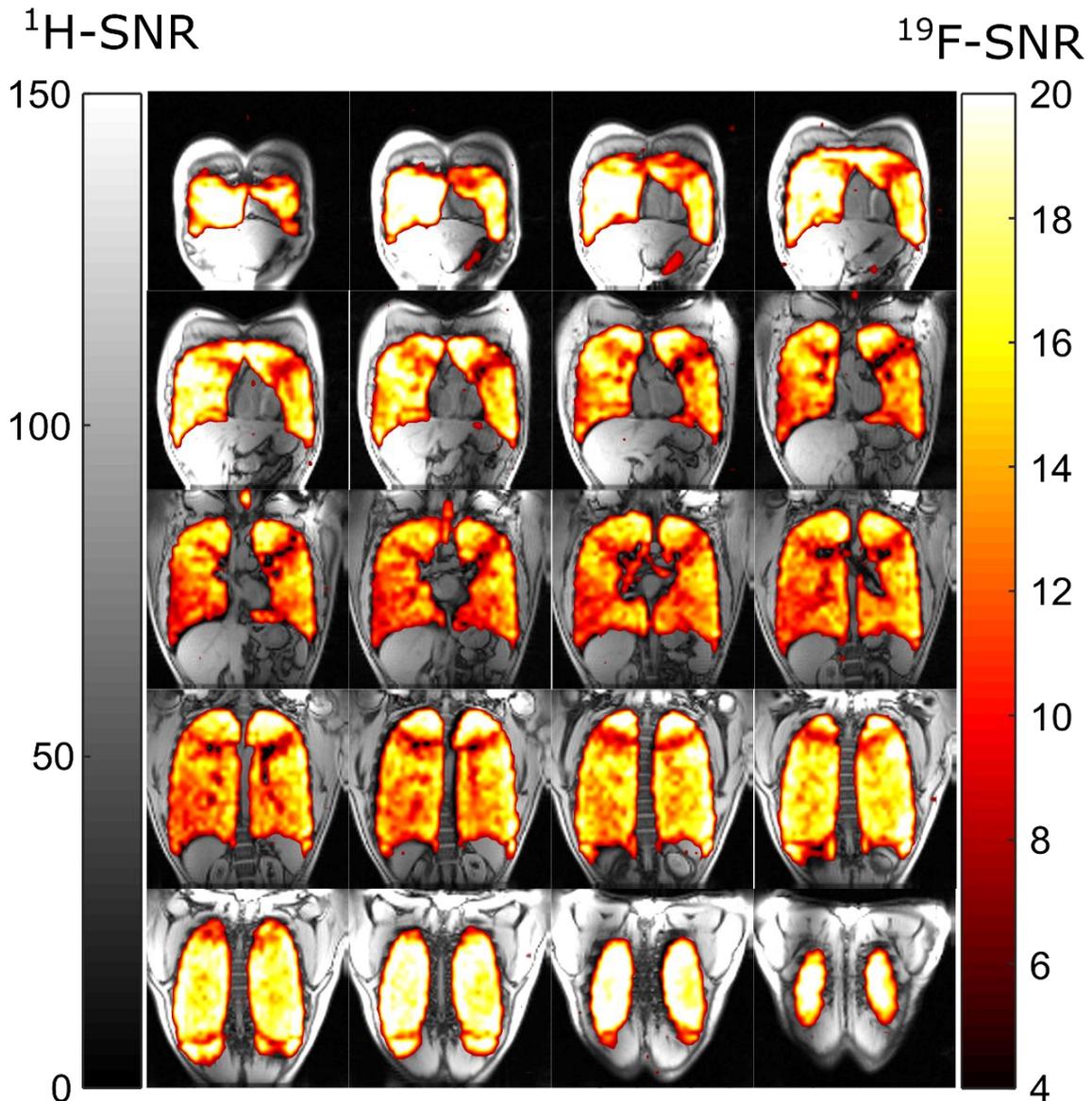
Figure 5-13: ^{19}F Ventilation images of $81\%C_3F_8+21\%O_2$ overlaid on anatomical ^1H images acquired with ladder/transceive array.

5.6 Discussion

The formalism presented in section 5.3 demonstrates a novel method to derive tuning impedances for any network that can be represented by (5-2). Using this formalism, the investigation of the non-periodic ladder coil for producing a current distribution analogous to that of the birdcage coil was enabled, including quadrature modes for circular polarization, which has not been attempted or demonstrated before. Furthermore, a direct consequence of the theoretical framework presented is the concept of a hybrid design combining a transceive array and non-periodic ladder resonator, which has not been presented previously. This was motivated by the potential to combine the benefits of better SAR and transmit homogeneity

characteristics of a volume resonator at 1.5 T, with the transmit efficiency and form fitting nature of the transmit array.

At higher field strengths (>1.5 T) transmit arrays have proven to be crucial for improving transmit homogeneity and reducing SAR as the dimension of the body relative to the wavelength becomes comparable (299, 300). However, even at 1.5T the use of transceive arrays has benefits of improved transmit efficiency, capability to be form fitting and improvement in receive sensitivity from using the individual transmit coils in reception. However, at 1.5T volume resonators still yield very homogeneous fields. In this study the comparison of a previously employed dual-row transceive coil design (244) and an elliptical birdcage showed better SAR and transmit homogeneity for the birdcage, with greater transmit efficiency and receive sensitivity for the array. A large part of this difference is due to the relative size difference of the two coils, with a larger sized transceive array a greater homogeneity and lower SAR could be achieved (at the expense of transmit efficiency).

The method of excitation and operation of the non-periodic ladder array introduced here is fundamentally different than the canonical theory of excitation of eigenmodes with birdcage coils (292), half-birdcage coils (301) or for more general 2D ladder networks (205, 296), generalized 2D meshed circuits (302) and TEM coils (191). The concept of resonance modes is not explicitly employed. This is expressed by the resonances occurring off-center of the imaging frequency observed in the S-parameters (Figure 5-9), and the asymmetric impedance parameters listed in Table 5-1 and Table 5-2. Furthermore, the resistive component of the impedance/coupling matrices is crucial for achieving the desired distribution, which is in contrast to typical ladder resonator eigenmode analysis where the resistive component is either neglected or assumed to only have a small perturbation on the resonance modes (187, 188, 255, 274). The formalism presented here doesn't require any such simplification of the network model.

The schematic representation and circuit formulation developed here ignored the effects of parasitic capacitance, coupling with other elements present in the MR environment (cables, coils, human body etc.) and wavelength dependent effects with large distributed coils resulting in alternative current paths. At higher frequencies difficulties may arise in maintaining the expected current distribution on the ladder resonators without accounting for these factors.

The sensitivity of the operation of the ladder resonator to the resistive portion of the impedance matrices is revealed by the variation in field patterns with loading. The extreme sensitivity of the 7-mesh non-periodic ladder coil tested here precluded its consideration as a viable design for the application of $^{19}F/^{1}H$ lung imaging. However, due to the fewer number of

meshes, and inclusion of two feed points as in a transmit array, the ladder/transceive coil was found to be viable.

The ladder/ladder array is tunable on the bench through referencing the measured S-parameters to the simulated S-parameters during construction. Without obvious "on-resonance" behaviour at the imaging frequency as observed with other surface or birdcage type coils the measurement of impedance parameters was critical for guiding the tuning. However, as found here the simulated and measured capacitor values should match very closely if the simulation model is suitably accurate.

Currently, the accuracy of the simulation has been verified through experimental results with the 6-element adder array and the 8-element transceive array (Chapter 4). The performance of the elliptical birdcage coil was not verified experimentally. However, the simplicity of the birdcage coil relative to the ladder coil and the many previous studies demonstrating the simulation accuracy of birdcage coils indicate further experimental comparison is not required(189, 197, 213, 292).

Although the ladder/transceive design poses additional challenges in the complexity of tuning and simulation, a number of benefits were observed.

(i) For a lower number of feed points than that of a transceive array a greater amount of meshes are excited, resulting in a more distributed current distribution.

(ii) a lower SAR

(iii) improved transmit homogeneity for a coil of similar dimensions to the simulated 8-element transceive array.

This is important for ^{19}F gas lung MRI where rapid imaging with a relatively large FA is required to increase SNR (133) due to low spin density. Additionally, 6 receive channels were able to be incorporated with the form fitting ladder/transceive coil, which is important in ^{19}F lung MRI where the inclusion of multiple ^{1}H and ^{19}F transmit and receive arrays, which couple closely together, is problematic with limited space in the magnet bore.

In measurement the ladder/transceive coil showed the expected homogeneity and receive sensitivity patterns from simulation. Additionally, the coil matching and homogeneity at the ^{1}H frequency proved to be adequate for the purposes of ^{1}H anatomical imaging for co-registration with ventilation imaging. The homogeneity of the ladder coil may change as seen in Figure 5-5 with loading, but for the intended application this may not be significantly detrimental. Part of this change will also depend on the asymmetric loading that is present in the case of human loads. As an example, for the SSFP imaging sequences that may be routinely used in ^{19}F imaging a variation of 33% (60º FA compared to 90°) has been shown to result in

only a 10% decrease in signal (133). This is also general property of the rapid low FA SPGR sequences that would be used for ^{1}H anatomical imaging.

In the future, methods of stabilizing the variation of mesh current to load variation with such ladder coil designs may need to be introduced. The inclusion of resistive components/losses in the coil design during transmit is one method that may provide this stability, at the expense of transmit efficiency. A practical way of introducing this could be the use of conductive inks for the conductive portion of the coil, which although it would introduce some loss in the coil it would allow the mechanical robustness and flexibility of the coil to be improved (303). Furthermore, to improve stability a greater number of feed-points may be introduced to both increase the number of meshes and force the desired phase/power at a greater number of points along the coils. For example, using a power distribution network to feed 4-ports with 0°,90°,180° and 270° phase difference, as in reference (257), to four 3-mesh ladder/transceive coils for a total of 12 meshes to improve baseline transmit homogeneity as well as stability.

5.7 Conclusion

In this study a novel scheme of ladder network operation using a novel method of quadrature excitation was explored. After determining that the impact of loading variation on the current distribution with such a network could be problematic the inclusion of multiple coils/power distribution feed points, as with transmit arrays, was introduced to mitigate the issue. In the application investigated here of dual ^{19}F ventilation and ^{1}H anatomical lung imaging the resulting ladder/transceive array was found to provide a more homogeneous field and lower SAR than a comparable transceive array design, and greater flexibility, transmit efficiency and receive sensitivity than an elliptical birdcage coil of similar dimensions. In future, this new class of coil, the ladder/transceive hybrid, should prove to have other applications in MR coil design.

5.8 Appendix: Explicit Solution for Non-Periodic Linear Ladder Resonator Applied to 3-Meshes

This section details the explicit equations to solve for Z^L and Z^H for a given mesh current distribution and directly solves them for the case to a 3-mesh non-periodic resonator. Equation (5-16) can explicitly as:

$$\boldsymbol{Z^H} = - \begin{bmatrix} \sum_{i=1}^{N^r+N^l+1} \frac{I_i Z_{G1i}}{I_1} + Z_1^L(1 - \frac{I_2}{I_1}) + Z_{N^l+N^r+1}^L(1 - \frac{I_{N^l+N^r+1}}{I_1}) \\ \sum_{i=1}^{N^r+N^l+1} \frac{I_i Z_{G2i}}{I_2} + Z_2^L(1 - \frac{I_3}{I_2}) + Z_1^L\left(1 - \frac{I_1}{I_2}\right) \\ \vdots \\ \sum_{i=1}^{N^r+N^l+1} \frac{I_i Z_{G2i}}{I_{N^l+N^r+1}} + Z_{N^l+N^r}^L\left(1 - \frac{I_{N^l+N^r}}{I_{N^l+N^r+1}}\right) + Z_{N^l+N^r+1}^L(1 - \frac{I_1}{I_{N^l+N^r+1}}) \end{bmatrix} \tag{5-21}$$

If $\mathbb{R}e(\boldsymbol{Z^L}) = 0$ and the additional condition is placed that $\mathbb{R}e(\boldsymbol{Z^H}) = 0$, the set of equations for $\boldsymbol{Z^L}$ are found as:

$$\begin{bmatrix} 0 \\ 0 \\ \vdots \\ 0 \end{bmatrix} = \begin{bmatrix} \mathbb{R}e\left(\sum_{i=1}^{N^r+N^l+1} \frac{I_i Z_{G1i}}{I_1}\right) - Z_1^L \mathbb{I}m\left(\frac{I_2}{I_1}\right)j - Z_{N^l+N^r+1}^L \mathbb{I}m\left(\frac{I_{N^l+N^r+1}}{I_1}\right)j \\ \mathbb{R}e\left(\sum_{i=1}^{N^r+N^l+1} \frac{I_i Z_{G2i}}{I_2}\right) - Z_2^L \mathbb{I}m\left(\frac{I_3}{I_2}\right)j - Z_1^L \mathbb{I}m\left(\frac{I_1}{I_2}\right)j \\ \vdots \\ \mathbb{R}e\left(\sum_{i=1}^{N^r+N^l+1} \frac{I_i Z_{G(N^l+N^r+1)i}}{I_{N^l+N^r+1}}\right) - Z_{N^l+N^r}^L \mathbb{I}m\left(\frac{I_{N^l+N^r}}{I_{N^l+N^r+1}}\right)j - Z_{N^l+N^r+1}^L \mathbb{I}m(\frac{I_1}{I_{N^l+N^r+1}})j \end{bmatrix} \tag{5-22}$$

This set of equations can be rearranged as:

$$\boldsymbol{Z^L} = \begin{bmatrix} \frac{\mathbb{R}e\left(\sum_{i=1}^{N^r+N^l+1} \frac{I_i Z_{G1i}}{I_1}\right)}{\mathbb{I}m\left(\frac{I_2}{I_1}\right)j} - Z_{N^l+N^r+1}^L \frac{\mathbb{I}m\left(\frac{I_{N^l+N^r+1}}{I_1}\right)}{\mathbb{I}m\left(\frac{I_2}{I_1}\right)} \\ \frac{\mathbb{R}e\left(\sum_{i=1}^{N^r+N^l+1} \frac{I_i Z_{G2i}}{I_2}\right)}{\mathbb{I}m\left(\frac{I_3}{I_2}\right)j} - Z_1^L \frac{\mathbb{I}m\left(\frac{I_1}{I_2}\right)}{\mathbb{I}m\left(\frac{I_3}{I_2}\right)} \\ \vdots \\ \frac{\mathbb{R}e\left(\sum_{i=1}^{N^r+N^l+1} \frac{I_i Z_{G(N^l+N^r+1)i}}{I_{N^l+N^r+1}}\right)}{\mathbb{I}m(\frac{I_1}{I_{N^l+N^r+1}})j} - Z_{N^l+N^r}^L \frac{\mathbb{I}m\left(\frac{I_{N^l+N^r}}{I_{N^l+N^r+1}}\right)}{\mathbb{I}m(\frac{I_1}{I_{N^l+N^r+1}})} \end{bmatrix} \tag{5-23}$$

For a periodic ladder coil this means that the equations for the elements of $\boldsymbol{Z^L}$ are self-referential. For a non-periodic coil, where $Z_{N^l+N^r+1}^L = 0$, (5-22) may be used to determine the values of $\boldsymbol{Z^L}$, which can be put into (5-21) to solve for $\boldsymbol{Z^H}$. For a single excitation point the condition that Z_0^{Hlr}=0 can be removed, as it does not affect the relative phase or magnitude difference between meshes. Therefore, for the three-mesh coil of the pair in Figure 5-2b with known $\boldsymbol{I}$ and $\boldsymbol{Z_G}$ (here actual values are given) given by:

$$\boldsymbol{I} = I_0 \begin{bmatrix} e^{-i\frac{\pi}{3}} \\ 1 \\ e^{i\frac{\pi}{3}} \end{bmatrix}, \boldsymbol{Z_G} = \begin{bmatrix} 22 + 359j & 5.9 - 119j & -10.6 - 7.8j \\ 5.9 - 119j & 26 + 461j & -4.4 - 112j \\ -10.6 - 7.8j & -4.4 - 112j & 21 + 373j \end{bmatrix} \Omega \tag{5-24}$$

Equation (5-23) can be then written as:

$$\begin{bmatrix} \mathbb{R}e\left(\sum_{i=1}^{N^r+N^l+1}\frac{I_i Z_{G1i}}{I_1}\right)\Big/\mathbb{I}m\left(\frac{I_2}{I_1}\right)j \\ \mathbb{R}e\left(\sum_{i=1}^{N^r+N^l+1}\frac{I_i Z_{G3i}}{I_3}\right)\Big/\mathbb{I}m\left(\frac{I_2}{I_3}\right)j \end{bmatrix} = \begin{bmatrix} \mathbb{R}e\left(22+359j+\dfrac{5.9-119j}{e^{i\frac{\pi}{3}}}+\dfrac{-4.4-112j}{e^{i2\frac{\pi}{3}}}\right)\Big/\mathbb{I}m\left(e^{i\frac{\pi}{3}}\right)j \\ \mathbb{R}e\left(\dfrac{-10.6-7.8j}{e^{-i2\frac{\pi}{3}}}+\dfrac{-4.4-112j}{e^{-i\frac{\pi}{3}}}+21+373j\right)\Big/\mathbb{I}m\left(e^{-i\frac{\pi}{3}}\right)j \end{bmatrix}\Omega = \begin{bmatrix} Z_{01}^{Ll} \\ Z_{01}^{Lr} \end{bmatrix}$$

$$\begin{bmatrix} -162j \\ -92j \end{bmatrix}\Omega = \begin{bmatrix} Z_1^L \\ Z_2^L \end{bmatrix}$$

Therefore, the elements of $\mathbf{Z}^H$ can be found as:

$$-\begin{bmatrix} 22+359j+\dfrac{5.9-119j}{e^{-i\frac{\pi}{3}}}+\dfrac{-10.6-7.8j}{e^{-i2\frac{\pi}{3}}}-162j\left(1-e^{i\frac{\pi}{3}}\right) \\ \vdots \\ \mathbb{I}m\left(\dfrac{5.9-119j}{e^{-i\frac{\pi}{3}}}+26+461j+\dfrac{-4.4-112j}{e^{i\frac{\pi}{3}}}-92j\left(1-e^{i\frac{\pi}{3}}\right)-162j\left(1-e^{-i\frac{\pi}{3}}\right)\right)j \\ \vdots \\ \dfrac{-10.6-7.8j}{e^{-i2\frac{\pi}{3}}}+\dfrac{-4.4-112j}{e^{-i\frac{\pi}{3}}}+21+373j-92j\left(1-e^{-i\frac{\pi}{3}}\right) \end{bmatrix}\Omega = \begin{bmatrix} -219j \\ -210j \\ -288j \end{bmatrix}\Omega = \begin{bmatrix} Z_1^{Hl} \\ Z_0^{Hlr} \\ Z_1^{Hr} \end{bmatrix}$$

This results in a total impedance matrix of:

$$\mathbf{Z} = (\mathbf{Z_G}+\mathbf{Z_C}+\mathbf{Z_T}) = \begin{bmatrix} 22-21.3j & 5.9+43.0j & -10-8j \\ 5.9+43.0j & 26-2.6j & -4.4-19.9j \\ -10-8j & -4.4-19.9j & 21-7.0j \end{bmatrix}\Omega$$

and it can be verified that with a single voltage source the resulting current is:

$$\mathbf{I}\Big/I_0 = \begin{bmatrix} e^{-i\frac{\pi}{3}} \\ 1 \\ e^{i\frac{\pi}{3}} \end{bmatrix} = \mathbf{Z}^{-1}\begin{bmatrix} \mathbf{0} \\ \mathbf{1} \\ \mathbf{0} \end{bmatrix}\Big/I_0 \text{, where } I_0 = I_2$$

Chapter 6: Optimization of steady-state free precession MRI for lung ventilation imaging with 19 F C3 F8 at 1.5T and 3T[4]

6.1 Overview

Purpose: To optimize ^{19}F imaging pulse sequences for perfluoropropane (C_3F_8) gas human lung ventilation MRI considering intrinsic in-vivo relaxation parameters at both 1.5T and 3T.

Methods: Optimization of the imaging parameters for both 3D spoiled gradient (SPGR) and steady-state free precession (SSFP) ^{19}F imaging sequences with inhaled 79% C_3F_8 and 21% oxygen was performed. Phantom measurements were used to validate simulations of signal-to-noise (SNR). In-vivo parameter mapping and sequence optimization/comparison was performed with a healthy adult volunteer. T_1 and T_2^* mapping was performed in-vivo to optimize sequence parameters for in-vivo lung MRI. The performance of SSFP and SPGR was then evaluated in-vivo at 1.5T and 3T.

Results: The in-vivo T_2^* of C_3F_8 was shown to be dependent upon lung inflation level (2.04ms±36% for residual volume and 3.14ms±28% for total lung capacity measured at 3 T), with lower T_2^* observed near the susceptibility interfaces of the diaphragm and around intrapulmonary vessels. Simulation and phantom measurements indicate that a factor of ~2-3 higher SNR can be achieved with SSFP when compared to optimized SPGR. In-vivo lung imaging showed a 1.7 factor of improvement in SNR achieved at 1.5 T, while the theoretical improvement at 3T was not demonstrable due to experimental SAR constraints, shorter in-vivo T_1, and B_0 inhomogeneity.

Conclusion: SSFP imaging provides increased SNR in lung ventilation imaging of C_3F_8 demonstrated at 1.5T with optimized SSFP similar to the SNR that can be obtained at 3T with optimized SPGR.

---

[4] The work presented in the chapter has been published in the journal Magnetic Resonance in Medicine: A. Maunder A, Rao M, Robb F, Wild JM. Optimization of steady-state free precession MRI for lung ventilation imaging with ^{19}F C_3F_8 at 1.5T and 3T Magn Reson Med. 2018; 81(2):1130-1142. All experiments, simulations and analysis on data were carried and described in the written manuscript by AMM. Manuscript revisions performed with JMW and AMM.

6.2 **Introduction**

MRI of lung ventilation with inhaled inert hyperpolarized (HP) gases has a proven sensitivity for the assessment of lung ventilation changes in obstructive airways disease (125). MRI with fluorinated gases (e.g. SF_6, C_2F_6 and C_3F_8) shows promise as a complementary or alternative method for lung ventilation imaging, but in contrast to HP gas MRI, does not require additional polarization equipment (106). Additionally, fluorinated gases may be mixed with oxygen (O_2) and continuously breathed, possibly allowing simpler investigation of dynamic lung physiology, such as the measurement of fractional ventilation by multi-breath washout (58, 108, 304) without the complication of gas depolarization observed with HP gas. Efforts to improve the quality of fluorinated gas ventilation images has been ongoing (106, 124-126). However, obtaining high-resolution ventilation images with fluorinated gases at thermal equilibrium is challenging because of the low spin density, short T_2^* and constrained imaging time (126).

For SPGR imaging with the repetition time $TR \ll T_1$, and where the acquisition time (T_{aq}) is approximately that of T_2^* (28, 305), the SNR per-unit-time is nearly constant with TR due to the competing factors of averaging, T_{aq} and longitudinal recovery (305, 306). However, if TR is of the same order as T_1, the optimization of single-echo SPGR sequences generally requires minimizing TR so that the rate of longitudinal recovery for each TR is maximized (306). Past strategies of fluorinated gas imaging have focused on the use of short echo time (TE) SPGR sequences with TR relatively close to T_1, due to the constraints posed by the relatively short T_2^* of fluorinated gases in the lungs and by the SAR considerations at 3 T; the most common field strength used for imaging of fluorinated gases to date. For example, TR values of 20 ms (121, 131) for SF_6 with $T_1 < 2$ ms (307), and 20 ms (98) or 13 ms (121) for C_3F_8 with $T_1 \sim 12.4$ ms (98). More recently, studies of C_3F_8 imaging have been performed at 1.5T using a 16-element receive array (123, 308). However, imaging was still performed with $T_1 \sim TR = 12$ ms, and a frequency encoding gradient readout duration of 7.1 ms, which is significantly longer than the T_2^*. Therefore, future fluorinated gas imaging can clearly benefit from imaging parameter optimization as presented here.

In free-gas phantoms C_3F_8 gas has a longer T_2 (~ 17 ms (117)) when compared to other fluorinated gases (~ 4.2 for SF_6 (114) and ~ 5.9 for C_2F_6 (106)), so improved signal to noise may potentially be achieved with the use of steady state free precession (SSFP). The optimization of imaging parameters for SPGR (28) and SSFP (309) ^{1}H MRI has been detailed previously. Also, the optimization of SSFP imaging parameters (310) has been investigated for

the imaging constraints of HP gas ventilation MRI with both ^{3}He and ^{129}Xe (34). Sequence optimization for perfluorocarbon emulsions has also been performed previously (311, 312), but in this instance the T_2 and T_1 relaxation parameters are significantly longer than for gas phase perfluorocarbons.

In this work we demonstrate the application of SSFP sequences for ^{19}F lung ventilation imaging using C_3F_8/O_2 gas at 1.5T and 3 T. Optimization of SSFP and SPGR imaging parameters was carried out by simulation with the specific relaxation parameters of C_3F_8/O_2 gas as found in phantoms. The additional consideration of k-space filtering (313) from T_2^* decay was explored by simulation of the 1D point spread function (PSF) (40). Simulations of the SSFP signal were performed and compared experimentally to those achievable with a SPGR sequence. Constraints posed by SAR for in-vivo applications are highlighted and the relaxation parameters T_1 and T_2^* were mapped in-vivo to verify the parameters used in simulation. Finally, in-vivo lung imaging was performed with both sequences at 1.5T and 3T in order to test the theoretical/experimental predictions of SNR improvement. This study is to benchmark optimal imaging parameters.

6.3 Theory

6.3.1 Simulations of SPGR and SSFP Signal for C_3F_8

The two sequences considered here for 3D lung ventilation imaging with ^{19}F perfluoropropane were SPGR and SSFP as described in sections 2.8.2 and 2.8.3. Simulations of M_{xy} with SSFP were performed according to Hargreaves et al. (310), with an effective transverse decay rate term of T_2 (31). In the simulations presented transverse magnetization (M_{xy}) was evaluated at TE, which correlates with the center of k-space and thus determines image signal intensity. For the sake of a fair SSFP and SPGR comparison the spatial resolution, imaging time and y and z phase encoding steps remained the same. The effects of SSFP signal transient behaviour on the final SNR were ignored, which was justified by the relatively short T_1 and T_2 when compared to TR, resulting in a steady state being reached rapidly.

With HP ^{3}He gas it has been demonstrated that dephasing from the imaging gradients has a significant effect on the effective transverse relaxation rate (313), while the effect is less significant when imaging with ^{129}Xe because of the much lower diffusion coefficient (84). Calculations with the even lower diffusion coefficient of C_3F_8 (117), with its relatively low T_2, indicate that this effect is small when compared to the uncertainty/variability in the T_2 and

therefore the effect of diffusion dephasing due to the imaging gradients themselves was neglected here.

To emulate practical imaging sequence timings, the simulated RF pulse widths were matched to the measurement values, while T_{D1} and T_{D2} were selected to be 0.6 ms throughout the comparison to closely match those used in measurement (see section 2.8.2).

6.3.2 Quantification of T_2^* Decay Induced k_x Filtering

Insight into the reduction in image quality due to T_2^* filtering during frequency encoding (k_x) was attained by comparison of the 1D PSF of the different sequences. For SPGR the signal decays exponentially from the center of the RF excitation pulse with a time constant T_2^*. For SSFP the signal is modelled as decaying exponentially with time constant T_2, as well as decaying symmetrically away from TE with the time constant T_2^*, similar to simulation/measurement performed in reference with a spin-echo sequence (41), as the transverse magnetism ideally decays similarly in a bSSFP sequence (31) (see Figure 2-6).

6.3.3 Relaxation Parameters of C_3F_8/O_2

For the phantom simulations presented here the T_1 and T_2 of C_3F_8 gas mixed with 21% O_2 are assumed to be 17 ms (117). Within the lung the T_1 of fluorinated gases is known to depend more upon regional differences in partial-pressure (116, 118) of O_2. Consequently, the mean in-vivo T_1 has been reported as 12.4 ms at 3T (98). Additionally, the intrinsic T_2 of C_3F_8 gas within the lungs has not been reported, but is expected to remain comparable to T_1 (117, 118). Additionally, the mean in-vivo T_2^* relaxation constant of C_3F_8 has been reported as $\sim$2.2 ms at 3T (98).

6.4 Materials and Methods

6.4.1 Simulation of Steady-State Magnetization with SSFP

The relation between steady-state magnetization, FA and RF frequency offset from resonance were simulated with MATLAB considering the particular relaxation parameters of C_3F_8 for 3D imaging with a TR of 3.4 ms. Additionally, to assess whether transient oscillations in the magnetization during initial RF excitations are significant, the transverse magnetization for successive RF excitations was simulated for different values of TR. Furthermore, to quantify the expected 1D PSF arising from transverse magnetization decay the PSF was simulated for varying T_{aq}.

6.4.2 Validation of Simulated Magnetization with Phantom SNR Measurements

To compare the simulations of signal for C_3F_8 for SSFP vs. SPGR, phantom experiments were carried out with a 2 L glass cylinder (12 cm diameter, 20 cm length) filled with 79% C_3F_8 and 21 % O_2 at 1.4 bar pressure. Rectangular (24 cm x16 cm) transceive single loop coils were constructed from 11 mm width copper strip, tuned and matched at the 1.5T (GE Signa HDx) (60 MHz) and 3T (Philips Ingenia) (120 MHz) frequencies and centered with the cylinders during imaging. Prior to the phantom studies at 1.5T and 3T, FA maps were generated by varying the input power in SPGR imaging with TR 100 ms $\gg T_1$ and fitting the received signal according to equation (2-50)), as in reference (257). The prescribed FA recorded in Table 1 for the imaging performed with the glass phantoms was based on the fitted FA at the center of the phantom. Furthermore, to ensure that SNR and relaxation parameters were not inaccurately calculated due to B_1 inhomogeneity, voxelwise parameter mapping was calculated using the voxelwise fitted FA map (315) rather than a prescribed mean value.

The assumed T_1 and T_2 relaxation parameters were verified by comparing the variation of image SNR and simulated steady-state transverse magnetization with RF excitation frequency offset. The offset frequency was varied from $-1/TR$ to $1/TR$ (TR=4.6 ms) in steps of 30 Hz with two FAs (22.5° and 75°) and the SNR was evaluated within a central voxel of the glass cylinder phantom at 3T. Furthermore, the simulated transverse magnetization of SPGR and SSFP sequences were compared to measured image SNR with varying FA. The image SNR was averaged within a $1.2 \times 1.2 \times 3$ cm^3 voxel with either 3D SSFP or SPGR imaging at 1.5 T.

The restrictions on FA due to regulatory SAR contraints (147), when applying the same imaging sequence in-vivo with a thoracic vest transceiver coil (230, 257) were also considered in the SPGR and SSFP SNR vs. FA comparison. The vest transceiver coil is similar in geometry to the one used here and should have comparable SAR characteristics. For a 1 kW RMS input power the maximum local 10g averaged SAR was simulated within a realistic human body model (SIM4LIFE Zurich Med Tech, Duke model (240)) as 125 W/kg, with a 11.8 $\mu T/\sqrt{kW}$ transmit efficiency at 60 MHz. The global SAR was calculated conservatively as the input power to the coil being completely deposited into a 70 kg patient. A constant 500 μs hard pulse width was assumed, while pulse amplitude was varied to match the FA. All simulated FAs were therefore acheivable with the 4 kW peak power amplifier used in in-vivo imaging at 1.5 T. The specific imaging parameters for these and the in-vivo imaging experiments detailed later are provided in Table 3-2.

Table 6-1: Imaging parameters for phantom and in-vivo SSFP and SPGR performance verification with C_3F_8

Measurement	Sequence	TE (ms)	TR (ms)	BW (± kHz)	Matrix size (pixels^3)	FOV (cm^3)	Prescribed FA (°)	Avg.	T_{pw} (µs)
1.5 T									
Phantom Study									
SNR vs. FA	3D SPGR	1.6	4.3	10	50x50x10	20x20x16	13-91	10	468
SNR vs. FA	3D SSFP	1.6	3.9	10	50x50x10	20x20x16	18-120	10	616
FA mapping	3D SPGR	6.8	100	2.0	52x52x12	24x24x12	9-103	1	1600
T_1 mapping	3D SPGR	1.4	5	12.5	52x52x12	24x24x12	8.5-52	40	1600
T_2^* mapping	2D SPGR	1.5-11	250	31.25	52x52x12	24x24x12	47	2	1600
SNR vs. TR	3D SPGR	6.8-0.7	15.4-3.2	2-62.5	52x52x12	24x24x12	66-34	5	1600
SNR vs. TR	3D SSFP	6.8-0.7	15.4-3.2	2-62.5	52x52x12	24x24x12	89.6	5	1600
In-Vivo Comparison									
FA mapping	3D SPGR	2.2	35	3.97	32x26x10	40x32x30	27.5/55/82	1	832
T_1 mapping	3D SPGR	2.2	5.7	-	-	-	27.5/55/82	10	856
Optimal SNR comparison	3D SSFP	1.7	4.0	5.21	32x27x18	40x32x36	72	4	616
Optimal SNR comparison	3D SPGR	1.7	4.0	5.21	32x27x18	40x32x36	45	4	468
Ventilation Image	3D SSFP	1.72	4.0	6.76	40x34x32	40x32x32	72	8	616
3 T									
Phantom Study									
FA mapping	3D SPGR	6.4	100	3.1	52x52x12	24x24x12	10.6-85	1	1600
T_1 mapping	3D SPGR	2.1	5	22.6	52x52x12	24x24x12	22-82	10	1600
T_2^* mapping	3D SPGR	1-30	80	45.1	52x52x12	24x24x12	42.5	5	1600
SNR vs. TR	3D SPGR	6.9-1.8	13-4.0	3.1-35.3	52x52x12	24x24x12	57.5-35	5	1600
SNR vs. TR	3D SSFP	7.2-2.1	13-4.0	3.1-32.2	52x52x12	24x24x12	85	5	1600
SNR vs. offset frequency	3D SSFP	2.1	4.6	12.2	50x50x5	20x20x10	22.5/ 75	10	1600
In-Vivo Comparison									
FA mapping	3D SPGR	1.48*	50	4.3	28x27x12	40x40x24	30/90	2	1350
T_1 mapping	3D SPGR	-	6.5	4.3	28x27x12	40x40x24	25/37.5/50	5	1350
T_2^* mapping	3D SPGR	1.0-6.0	7	46.3	32x29x14	40x35x29.3	26	12	1350
Optimal SNR comparison	3D SPGR	1.8	4	9.5	40x32x28	40x32x28	30	4	780
Optimal SNR comparison	3D SSFP	1.8	4	9.5	40x32x28	40x32x28	30	4	780
Ventilation Image	3D SSFP	1.8	4	9.5	40x32x28	40x32x28	30	8	780

6.4.3 Phantom Relaxation Parameters

The T_2^* of C_3F_8 within the glass cylinder phantoms is not representative of in-vivo values measured in the lung where tissue-airspace field inhomogeneity plays a significant role. Therefore, a spatially varying T_2^* inhomogeneity was introduced by placing a paramagnetic wire in close proximity to the glass canister. At 1.5 T, T_2^* maps were calculated by varying the *TE* in multiple image acquisitions, while fixing the *BW, FA* and *TR*, then fitting according to equation (2-50)). The range of *TE* available at 1.5T was not high enough to accurately distinguish between T_2^* values >14 ms. However, at 3 T, T_2^* maps were fit from the signal decay during multi-echo SPGR imaging (multiple echoes per *TR*) with *TE*s up to 30 ms. To determine that the paramagnetic inhomogeneity did not alter the T_1 relaxation parameter, and that the in-phantom T_1 agreed with previous literature (117), T_1 was mapped throughout the cylinder by varying the FA, with a short *TR* (5 ms at 3T and 1.5 T) and fitting pixel-wise according to equation (2-50)) (238).

6.4.4 Simulated and Measured Optimization of SPGR and SSFP Imaging Parameters

To determine the optimal *TR* for 3D SPGR and SSFP imaging sequences, measurements were performed at 1.5T and 3T with varying *TR*. The same FA was used for SSFP imaging (approximately 90°), while the input RF power was varied with SPGR imaging to maintain the optimal Ernst FA at the center of the phantom. Three different regions of interest covering a range of T_2^* values were investigated.

The simulated steady-state transverse magnetization was multiplied by the factor $\sqrt{\frac{T_{aq}}{TR}}$ to represent the SNR per-unit-time efficiency due to trade-off between acquisition bandwidth and averaging. The simulated magnetization and measured SNR were plotted against *TR*. The previously acquired FA maps were used to verify that within the representative voxels the difference in SNR due to potential mismatch in prescribed FA and optimal FA was less than 5%.

6.4.5 In-vivo Relaxation Parameter Mapping

In-vivo lung ventilation imaging was performed in a healthy male adult volunteer (29 years old) following informed consent and adhering to protocols approved by UK National research ethics committee. An 8-element in-house constructed transceive array was used for 1.5T ^{19}F and ^1H in-vivo imaging (244). An elliptical birdcage coil (Rapid Biomedical, Rimpar, Germany) was used for ^{19}F and ^1H imaging at 3 T. The global FA was measured prior to

imaging by performing whole-lungs spectroscopy with a varying input power and long *TR* (268 ms at 1.5T and 200 ms at 3 T) and then fitting the resulting signal according to equation (2-50)). Saturation of the lungs with the C_3F_8/O_2 mixture was achieved by directing the volunteer to take three inhalations from a Douglas bag then perform a breath-hold.

To compare the global and regional variation of T_1 in-vivo at 1.5T and 3T to that obtained in phantoms at 3 T, T_1 and FA parameter mapping was performed. In the same breath-hold two 3D SPGR imaging sequences were performed with a long *TR* relative to T_1 (*TR*=50 ms at 3T and *TR*=35 ms at 1.5 T) and prescribed mean FAs of $\sim$90° FA and $\sim$30° FA (for 1.5T an additional point of $\sim$ 60° was included). The resulting pixel-wise FA was calculated based on the signal intensity difference according to equation (2-50)) (316). In a second breath-hold, three 3D SPGR imaging sequences were performed with *TR* shorter than T_1 (*TR*=6.5 ms at 3T and *TR*=5.7 ms at 1.5 T) and the resulting pixel intensity variation used to fit T_1 (317).

In addition, at 3 T, $T_2{}^*$ mapping was performed to corroborate the presumed values. A multi-echo SPGR acquisition was made with *TE* in the range of 1-6 ms in 1 ms steps, and the resulting images were fit on a voxel by voxel basis. $T_2{}^*$ mapping was performed at the two lung volumes of total lung capacity (TLC) and residual volume (RV).

6.4.6   In-vivo Comparison of SPGR and SSFP Image SNR

At 1.5 T, SNR comparisons were made between a SPGR sequence with an approximately optimal prescribed FA ($\sim$45° with TR=4 ms), and a 3D SSFP imaging sequence with $\sim$70° FA, which was limited due to SAR constraints. At 3 T, SPGR and SSFP imaging were performed with nearly identical imaging parameters, since SAR constraints restricted the FA to 30° with a TR of 4 ms. The direct comparison of SPGR and SSFP sequences at each field strength was carried out within the same breath-hold to avoid inconsistencies in co-registration or possible differences in the PFP: air concentration ratio in the lungs that may arise between breath-holds (20 s at 1.5T and 28 s at 3T plus inter-scan delay of approximately 5 s). Images were obtained with fully optimized sequences using the same resolution at both 1.5T and 3T for final comparison. Finally, to accurately compare the imaging methods k-space was filtered with an identical Hamming filter prior to FFT reconstruction (131). As a final comparison between the two field strengths, imaging was performed at 1.5T and 3T with the same resolution (10x10x10 mm^3) TR (4 ms) and 8 averages. To reduce the breath-hold time, 4 averages were obtained in two separate breath-holds to total lung capacity (20 s at 1.5T and 14 s at 3T which included an elliptical shutter).

6.5 Results

6.5.1 Simulations for Informing Experimental Optimization

Simulation of the C_3F_8 phantom steady state transverse magnetization with a TR = 3.4 ms is shown in Figure 6-1a, with varying flip angle (FA) and RF excitation offset frequency. Since T_1 is approximated as $T_1=T_2$ the transverse decay is equal to the longitudinal recovery rate and the optimal FA remains 90° for the central (0 Hz) offset frequency in all cases (32).
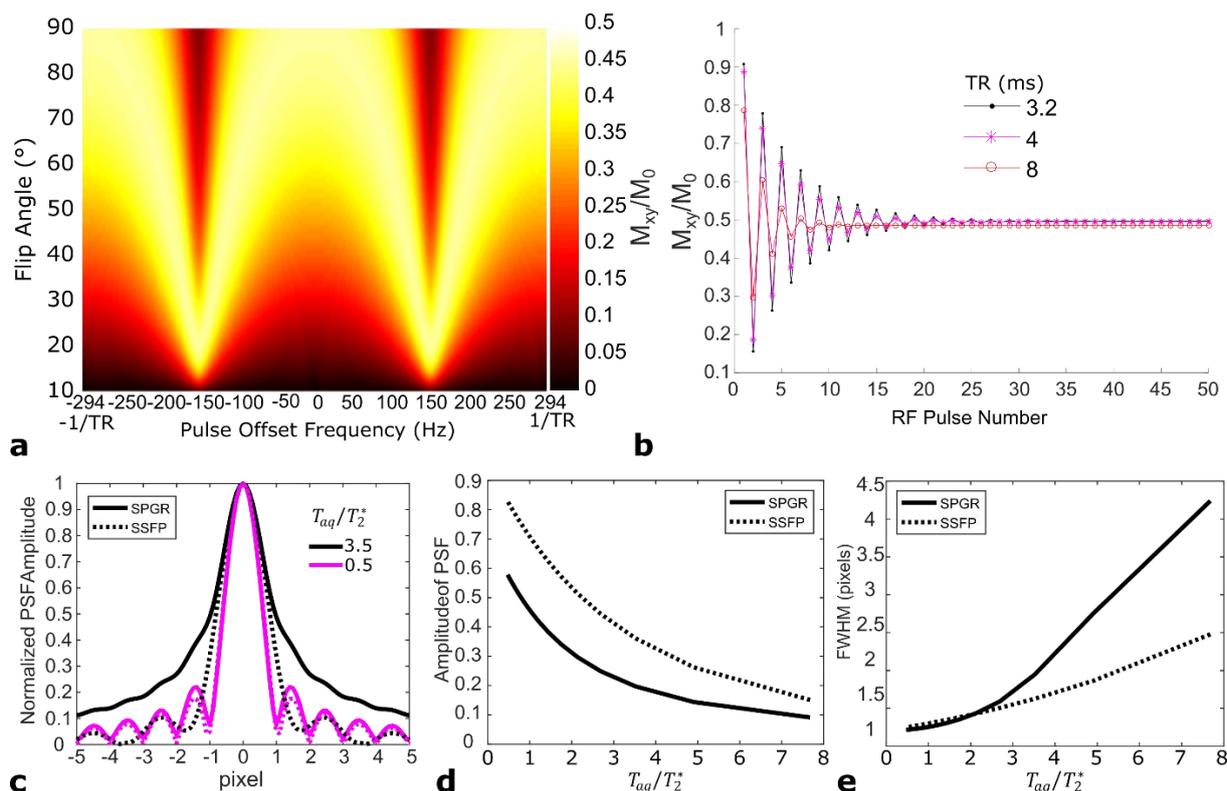
Figure 6-1: **a:** Simulated steady state magnetization as a function of FA and offset frequency for TR=3.4 ms **b:** Simulated transverse magnetization evolution for successive RF pulses (effective k_y/k_z filter) for a bSSFP sequence with C_3F_8. **c:** The simulated normalized 1D PSF in the k_x direction from T_2^* decay for both SSFP and SPGR sequences with relaxation parameters of C_3F_8 **d:** The corresponding simulated PSF amplitudes and **e:** FWHMs of PSFs with increasing T_{aq}.

The simulated oscillating transverse magnetization during the initial series of excitations is shown in Figure 6-1b for varying TR. The rapid longitudinal recovery of C_3F_8 means that a steady-state is reached within a short number of RF pulses for the TRs shown, reducing the amount of k_y & k_z filtering to a negligible level when SSFP imaging with C_3F_8 (313). Therefore, the application of 10 stabilization excitations prior to imaging performed in this study reduced the variation in magnetization with subsequent RF pulse excitations to less than 10%, even for a relatively short TR of 3.2 ms.

The simulation of the 1D PSF during frequency encoding readout is shown in Figure 6-1c for both SPGR and SSFP. The resulting amplitudes of the PSFs for the different sequences is

also shown in Figure 6-1d, and the FWHM of the PSF in Figure 6-1e. SPGR is deficient in terms of lower PSF amplitude and increased FWHM when compared to the SSFP PSF as the T_{aq} is increased. However, if T_{aq} is kept short relative to the T_2^* the FWHM remains low and blurring is minimal. For SPGR and SSFP sequences with C_3F_8 if $T_{aq} < 2T_2^*$ the FWHM of the PSF remains comparable.
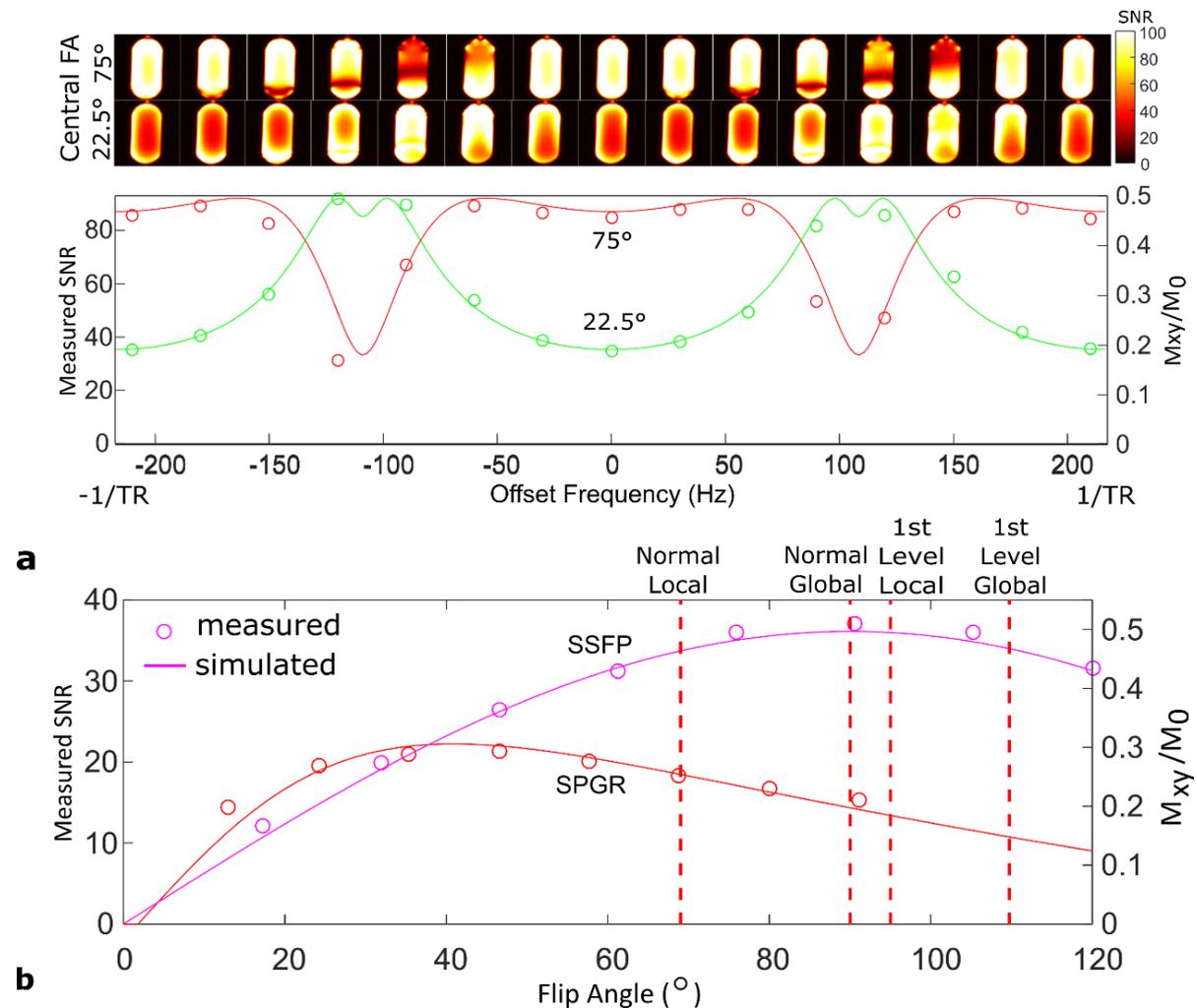
Figure 6-2: **a**: Simulated SSFP transverse magnetization and measured SNR vs. offset frequency at 3T for a central ROI within the C_3F_8 gas phantom at 3T with TR of 4.3 ms. SNR maps of a central slice are shown (above) as the offset frequency is varied for both 22.5° and 75° FAs **b:** Simulated steady state magnetization and measured SNR at 1.5T in a central ROI of the PFP cylinder with 3D SPGR and SSFP sequences plotted as a function of varying FA demonstrating the close relation with simulation. Red dotted vertical lines indicate the calculated SAR limits based on FA if the same sequence were performed in-vivo at 1.5 T.

6.5.2 Simulation Investigation and Validation

Figure 6-2a shows the measured SNR of the SSFP signal at 3T with varying offset excitation frequency. As expected, the simulated magnetization displays a similar trend vs. offset frequency when compared to measurement. Central slices are displayed for the varying offset frequency, demonstrating the introduction of banding artifacts arising from field inhomogeneity as the excitation frequency is offset from the center. In Figure 6-2b the relation

between SNR and FA for both SPGR and SSFP sequences is demonstrated at 1.5T for a central region of interest (ROI) of the phantom. Here, a close relation between SNR and the simulated steady-state magnetization is demonstrated, further validating the values of the relaxation parameters used in the simulations. The calculated SAR levels are displayed showing that a 90° FA could be used within 1st level controlled SAR constraints. However, to maintain more conservative local SAR levels, FA<70° should be used for the specific TR and pulse width presented in this case.

6.5.3   C$_3$F$_8$ Phantom SSFP vs SPGR SNR Comparison

Maps of the FA homogeneity that all subsequent phantom parameter mappings are based upon are displayed in Figure 6-3a. The T_1 map for the phantom at 1.5T and 3T is displayed in Figure 6-3b, and is in agreement with the range reported in reference (117) at 60 MHz. The T_1 is expected to increase slightly with Larmor frequency (<1 ms larger at 176 MHz vs. 60 MHz reported in reference(117)). Here, the standard deviation in the measurement was greater than the expected increase from 1.5T to 3 T. The T_1 maps do not show any regional variation with proximity to the paramagnetic wire. In Figure 6-3c the T_2^* maps for a central slice of the phantom with the paramagnetic wire added at both 1.5T and 3T. The T_2^* map measured at 3T when the wire is excluded is also shown.

The main comparison of image SNR obtained with SPGR and SSFP sequences is displayed for varying *TR* in Figure 6-4a (at 1.5 T) and Figure 6-4b (at 3 T). The central ROIs were chosen to demonstrate the SNR variation with T_2^* and are displayed on the T_2^* maps in Figure 6-3c. As TR is varied the measured SNR remains significantly higher for SSFP when compared to SPGR. SPGR optimization is highly dependent on T_2^*, with maximal SNR occurring when the T_{aq} is slightly greater than T_2^*.
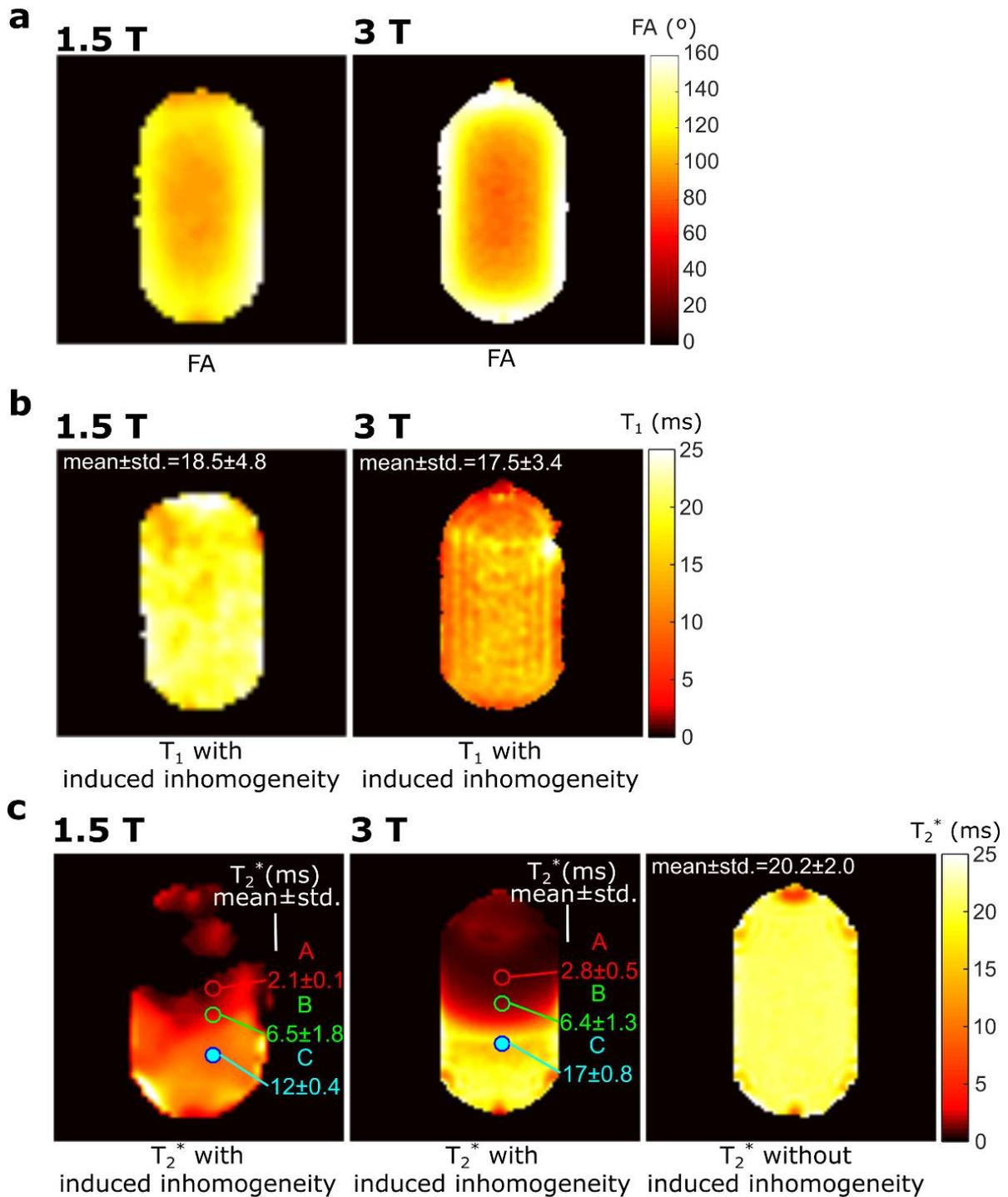
Figure 6-3: **a:** FA maps through a central slice at 1.5T and 3 T. **b:** T_1 maps through a central slice are displayed with the placement of a paramagnetic wire at 1.5T and 3T. **c:** T_2^* maps are also displayed for 1.5T and 3T originating from the placement of the paramagnetic wire. The T_2^* map without the variation from the paramagnetic wire is shown for 3T as well. ROIs where SNR variation is evaluated as TR is varied and the corresponding T_2^* for specific locations are displayed with the T_2^* maps.

The simulated transverse magnetization (normalized for the time available time for acquisition and averaging) closely matches the measured ROI SNR. However, since the pixel ROIs include a range of T_2^* the SNR behaviour with TR does not match exactly. In simulation the signal was assumed to correspond to the transverse magnetization amplitude at $k_x=0$ (center

141

of the frequency encoding gradient), but in fact is also dependent on the PSFs as presented in Figure 6-1d.
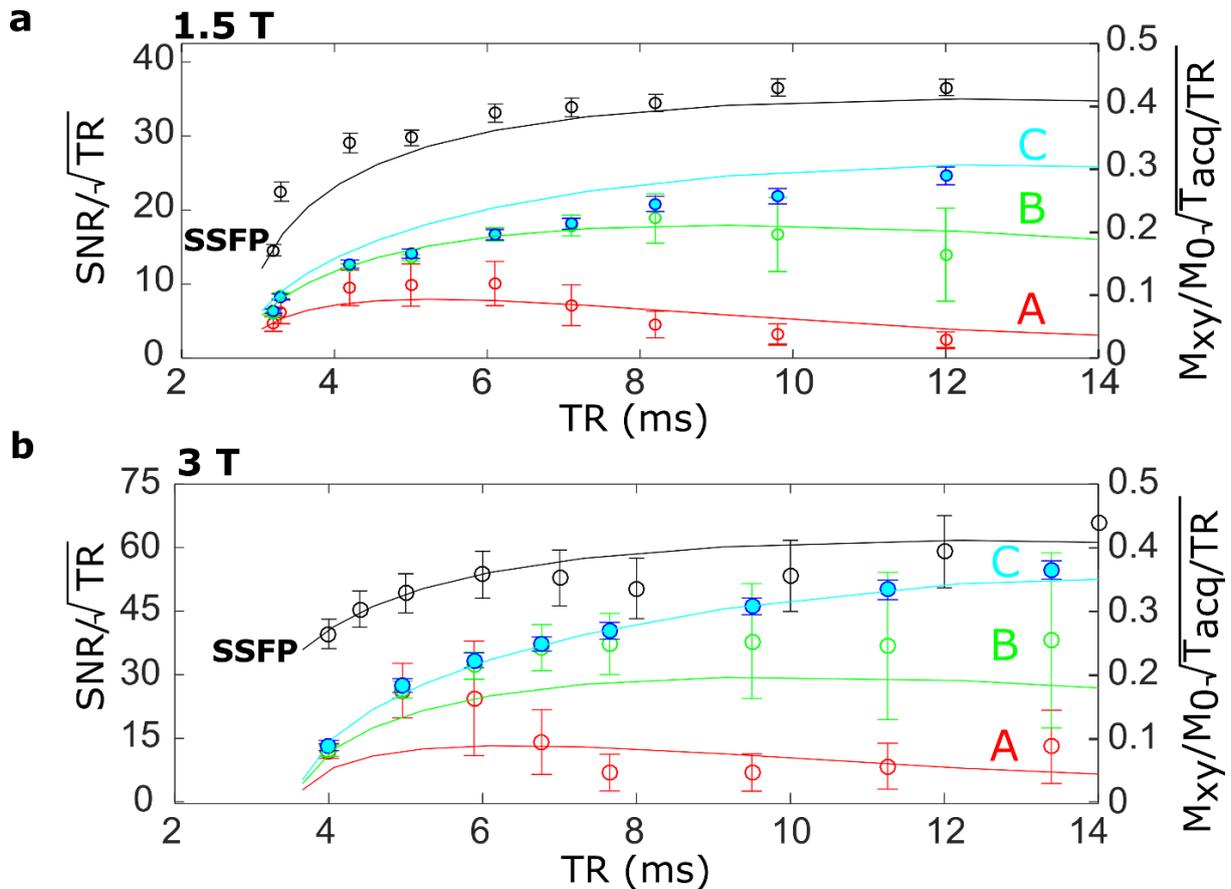
Figure 6-4: The measured variation (circular markers) of SNR with TR for SSFP (black) or SPGR (blue, green and red) sequences at **a:**1.5 T or **b:** 3T are displayed. For SPGR, labels of A, B and C correspond to the ROIs in T_2^* maps labelled similarly in Figure 6-3c. Image SNR is normalized by the time for averaging ($\sqrt{TR}$), while the simulated transverse magnetization (solid lines) is normalized by the predicted T_{acq} and TR.

6.5.4 In-vivo Parameter Mapping

Mapping of FA is displayed in Figure 6-5a, and the corresponding co-localized T_1 map in Figure 6-5b. The mean T_1 is lower than that found in the phantom (Figure 6-3), which is in agreement with previously reported in-vivo T_1 from whole lungs (12.4 ms at 3T (98)). Regional variation is apparent, with the greatest variation observed at the lung-tissue interfaces.
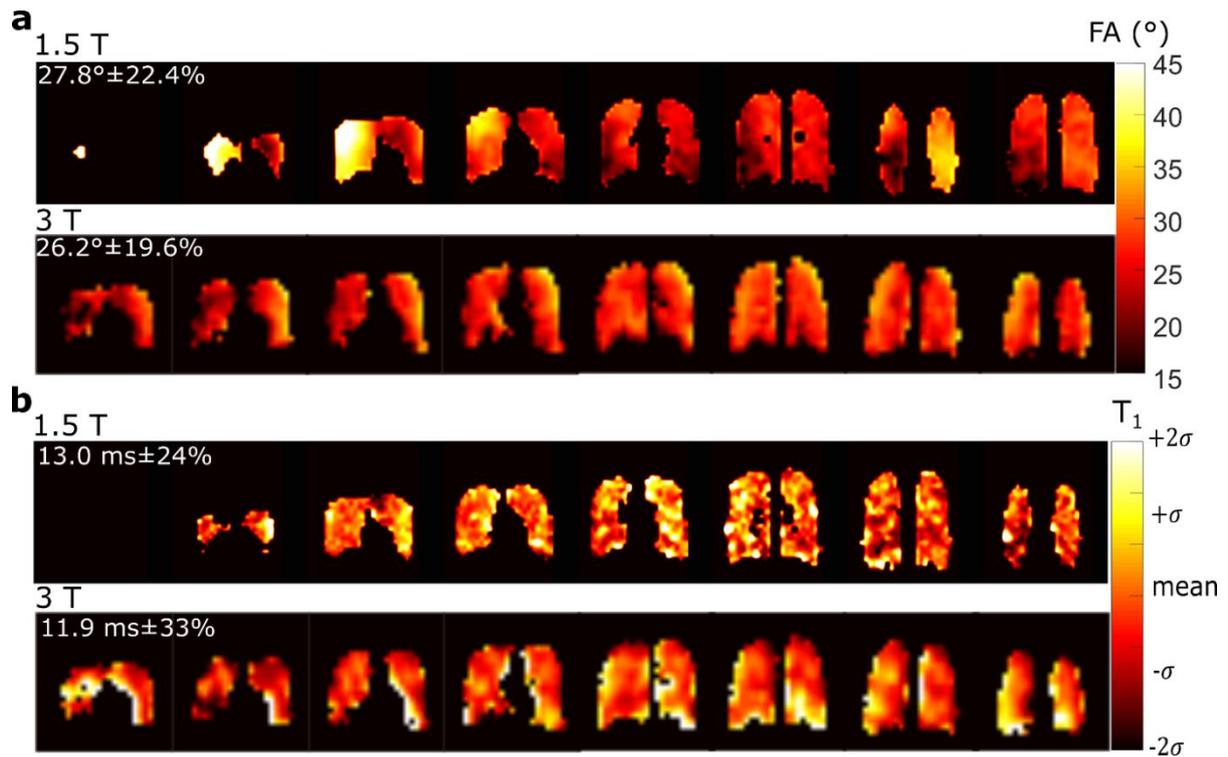
Figure 6-5: Maps of **a:** FA for a prescribed 30° and **b:** T_1 at 1.5 T and 3T, for images acquired at a lung volume of TLC in a healthy volunteer. Parameter mapping results where the image SNR was < 20 were excluded from analysis. Maps include the mean and standard deviation of parameters throughout the lungs in the top left corner.

T_2^* maps are shown in Figure 6-6a and Figure 6-6b for lung inflation levels TLC and RV, respectively. The in-vivo T_2^* is systematically less than in the glass cylinder phantoms (average of 2.04 ms vs. 20 ms in the phantom with undistorted field). The average T_2^* at 3T is in agreement with previous global measurements for the PFP T_2^* in the lungs (2.2 ms (98)), but the regional variation and dependence on inflation level is significant. There does not appear to be a visually observable correlation between regions of varying T_2^* and T_1, while T_2^* seems to be lowest in regions near the susceptibility interfaces of the pulmonary blood vessels and at the inferior portion of lung where perfusion is highest.
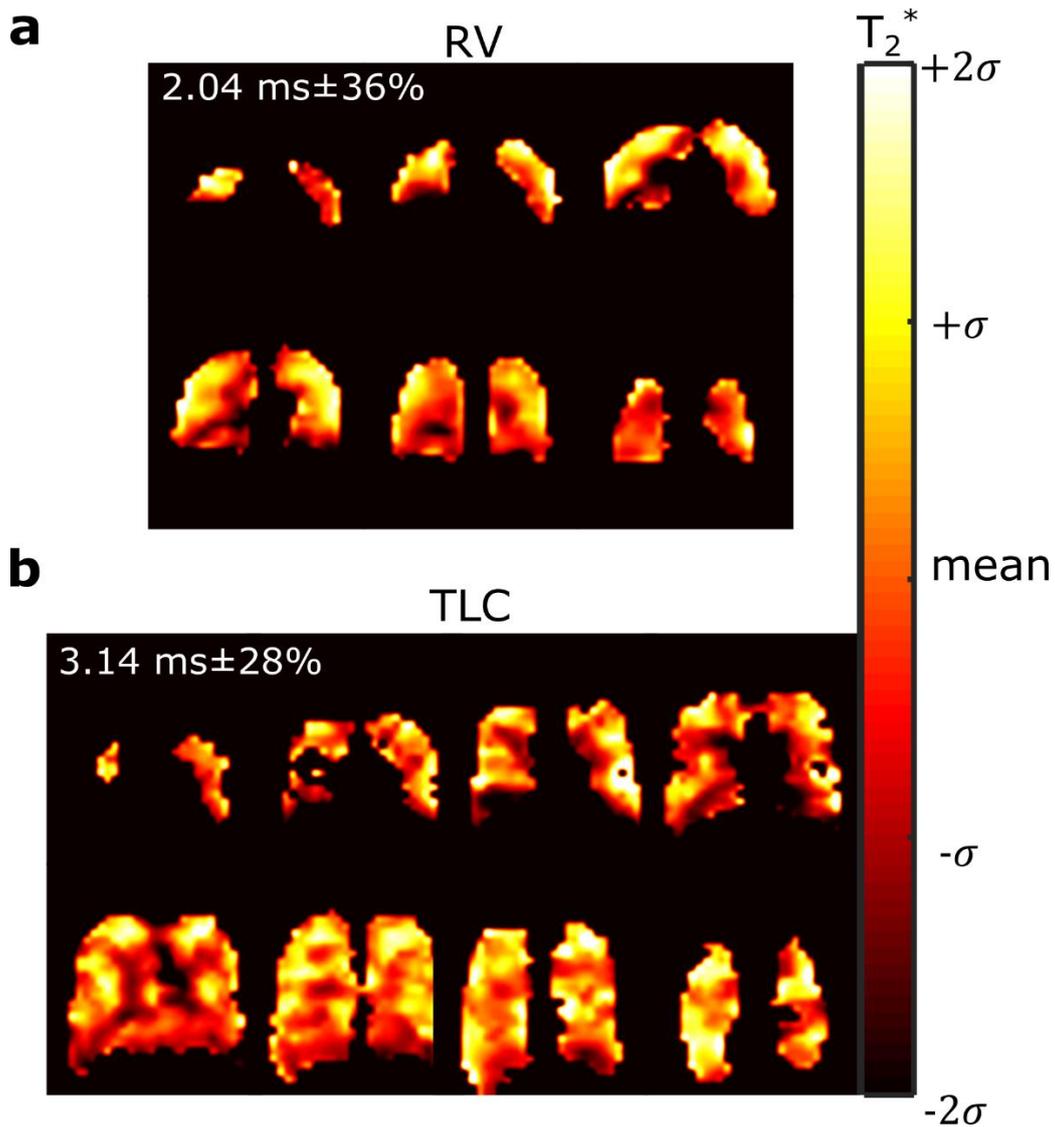
Figure 6-6: Maps of T_2^* in-vivo at 3T for lung volumes of **a:** RV and **b:** TLC are displayed with the mean and standard deviation of parameters throughout the lungs in the top left corner.

6.5.5   In-vivo SNR performance: SSFP vs. SPGR

An average increase in SNR by a factor of 1.7 was found at 1.5T (Figure 6-7a compared to Figure 6-7b). However, there are some off-resonance bands of high vs. low increases in signal intensity (Figure 6-7c) demonstrating the possible impact of field inhomogeneity. At 3T, no overall increase in SNR was observed with SSFP when performed under the SAR conservative settings (FA of 30° and *TR* of 4 ms) when compared to SPGR imaging (Figure 6-7c compared to Figure 6-7d). The significant regional variation in the SNR increase throughout the lungs with SSFP sequence vs. SPGR is reflective of the local B_0 inhomogeneity.
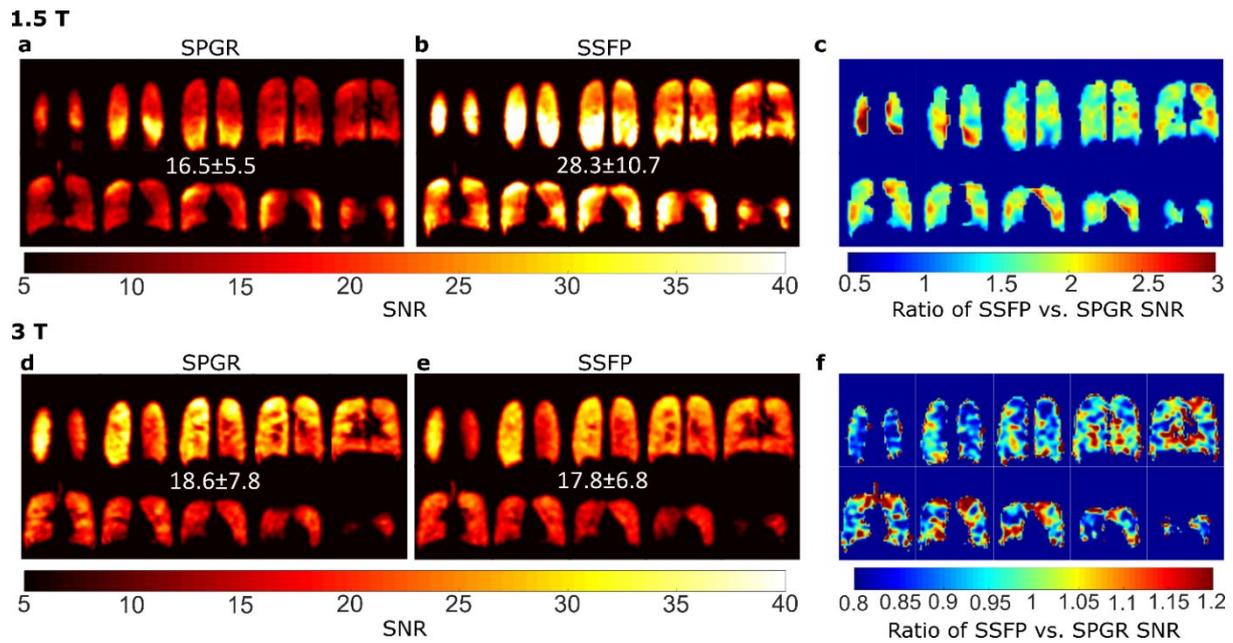
Figure 6-7: SNR maps of PFP in the lungs acquired at 1.5T using either **a:** SPGR or **b:** SSFP imaging and **c:** the relative improvement in SNR with SSFP imaging. Additionally, SNR maps acquired at 3T using **d:** SPGR or **e:** SSFP sequences with **f:** maps of the relative ratio of SNR of SSFP vs. SPGR imaging.

6.5.6 In-vivo Ventilation Imaging: 1.5T and 3T comparison

SNR maps of the in-vivo ventilation images obtained at 1.5T and 3T are shown in Figure 8. Through the use of a transceive array and increased SNR with SSFP imaging the mean SNR at 1.5T is higher than that of 3T for the same resolution. The increase in SNR is dominated by the regions of increased coil sensitivity at the anterior and posterior regions of the lung and much of the periphery, so the variation is higher at 1.5T as well. Due to B_1 inhomogeneity in the anterior of the lung at 3T there is significant signal drop-out.
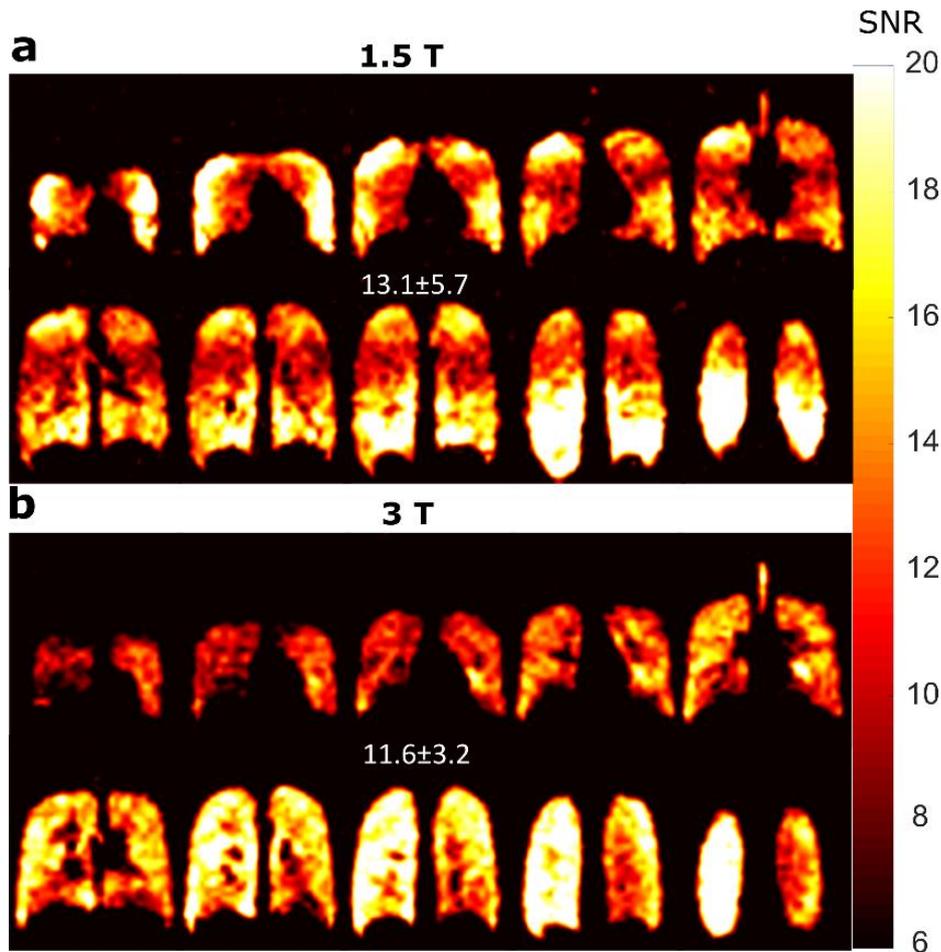
Figure 6-8: SNR maps for fully optimized imaging at equal resolution **a:** with SSFP imaging at 1.5T and an 8-element array or **b:** at 3T with SPGR and a quadrature birdcage coil are shown for final 1.5T and 3T comparison.

6.6 Discussion

The close agreement between the simulated and measured SSFP vs. SPGR signals, with both varying FA and offset frequency, indicates that the expected parameters of T_2, T_1 and T_2^* within the glass phantom are valid. Additionally, the direct measurement of T_1 and T_2^* matched the expected in-phantom values, with measurably smaller mean values of T_1 and T_2^* measured in-vivo. T_2 was indirectly validated by the close agreement between SSFP simulations and measurements since measuring T_2 with established spin echo sequences was constrained by the SAR limitations. For short sequence TR, variations in the simulated T_2 and T_1 for C_3F_8 have minimal influence on the simulated steady-state magnetization, since they are expected to remain comparable (117). However, lower T_1 results in a predicted greater steady-state magnetization with SPGR. This manifests as a reduction in the relative improvement of SSFP imaging of C_3F_8 in the lungs when compared to in a C_3F_8 gas phantom, which was observed at both 1.5T and 3 T. It was also demonstrated that the improved SNR achieved using SSFP when

146

compared to SPGR is strongly dependent upon the $T_2{}^*$ expected in-vivo and the k_x filtering effect of $T_2{}^*$ reduces the expected image quality when $T_2{}^* < T_{acq}$.

The in-vivo T_1 (317) and $T_2{}^*$ mapping results add to the data in the literature for C_3F_8 in lungs. The T_1 of fluorinated gases has previously been attributed to have a direct correlation with ventilation-perfusion (118, 318). Consequently, the differences in mean values for T_1 measured at 1.5T and 3T (Figure 6-5b) may be due to the level of saturation with the $C_3F_8+O_2$ mixture. $T_2{}^*$ correlates with lung inflation/filling level and may be related to alveolar size (319), which can change in diseases such as emphysema. Therefore, the parameter mapping techniques followed here may have direct relevance for future study.

Figure 6-2b demonstrates that at 1.5T using the optimal imaging parameters, the conservative SAR limits (147) are exceeded since the optimal SSFP FA is high due to the near equivalence of T_1 and T_2 for the gases used in these experiments. Nevertheless, the sequence when run with a sub-optimal flip angle of 72° still provides significant SNR gains over SPGR. However, at the higher field strength of 3T, SAR constraints are expected to further limit the potential advantage of SSFP for human ^{19}F ventilation imaging. A prescribed FA during in-vivo imaging at 3T of 30° was shown in phantom experiments (Figure 6-2a) to result in nearly the same SNR with SPGR and SSFP imaging.

There is a likelihood of some off-resonance banding artifacts occurring in routine imaging, as may be observed near the diaphragm in some of the 1.5T SSFP images in Figure 6-7b and Figure 6-8a. Even in the geometrically uniform and relatively small cylindrical glass phantoms banding can be observed at the susceptibility interfaces and as resonant frequency is offset (Figure 6-2a). Increased B_0 and RF inhomogeneity, especially with FOVs as large as the human torso (38-52 cm), increases this likelihood at the higher field strength of 3T. Previously, B_0 mapping within the lungs with inhaled ^3He gas at 1.5T and 3T demonstrated a variation in Larmor frequency at 3T of > 120 Hz across the lungs (320). Therefore, the B_0 inhomogeneity in the lungs makes the application less robust at 3T. Future investigations to test SSFP vs. SPGR imaging at higher field strengths may show the expected improvement if the same imaging methods are reproduced in a rat model where SAR limits are not exceeded and FA and B_0 inhomogeneity can be reduced.

The expected SNR gains of using SSFP over SPGR imaging at 1.5T are comparable to the improvements seen with SPGR when going from 1.5T to the higher field strength of 3 T. Therefore, equivalent quality human ventilation images may be obtained with the lower field strength without the same constraints of SAR. Especially, if at 1.5T a multi-channel receive array is employed as in this work and others (304). The use of a receive array for imaging of

the thorax/torso may result in further SNR increases in the range of $50 - 100\%$ (250, 268), with the majority of the increase obtained at the periphery. Therefore, a mean SNR of 15-20 may have been expected at 1.5T by combining the following factors: a measured SNR increase of 70% by use of SSFP, the approximate linear dependence of SNR with field strength (183), and the use of a receive array. We note that, at 3T k-space was sampled with the use of an elliptical shutter where the corners of k-space were not sampled (22% undersampling). Hence, despite the same nominal resolution of 1.5T and 3T for images in Figure 6-8 the SNR was slightly enhanced for the 3T images.

Here, the in-vivo imaging at 1.5T was performed with a flexible vest coil (244), which typically would have a worse transmit homogeneity than rigid volume coils as demonstrated with direct comparisons with ^{3}He hyperpolarized gas imaging at 1.5T in reference (189) (the variation was 7.3% within lungs with an asymmetric birdcage coil), or in comparisons made with simulation in Chapter 5. Despite the lower frequency of 1.5T the flexible transceive array showed lower in-vivo transmit homogeneity during in-vivo imaging, while the transmit homogeneity with the birdcage coil at 3T was also not ideal ($\sim$20% variation). The FA variation should not affect the in-vivo T_2^* parameter mapping, or the T_1 mapping since the co-localized FA maps were used in the fitting. The in-vivo comparison of SPGR and SSFP imaging is confounded by the coil related percent variation of FA (22.4% in Figure 6-5a) and natural variation of T_1 (24% in Figure 6-5b) and T_2^* (28% in Figure 6-6b) throughout the lungs. These three factors lead to the range of variations in improvement with SSFP vs. SPGR shown in Figure 6-7c and Figure 6-7f, and in future may be investigated further.

Comparison of the in-vivo ventilation image quality obtained here to previous studies is difficult due to differences in the imaging resolutions used and in the method of reporting and measuring SNR in images. Often, SNR is reported within a ROI with the highest signal. Further complicating the comparison, the longer T_{aq} employed in previous studies results in broadened PSF as simulated in Figure 1(d-e), which imparts a higher image SNR whilst degrading image quality due to blurring (40), and may be additionally modified by filtering during post-processing (98). Additionally, different studies have used different RF transmit/receive coils that may contribute to more than a factor of 3 in SNR variation. Nonetheless, in our study the measured SNR of 13.1$\pm$5.7 throughout the lungs at 1.5T (8-element transceive array with image resolution of 10x10x10 mm^3 and $T_{aq} = 3.3\ ms$) is equivalent to the SNR of $\sim$30 reported by Gutberlet et al. (123) (transmit birdcage and 16-element receive array with image resolution of 7.8x7.8x20 mm^3 and $T_{aq} = 7.1\ ms$). At 3T, the SNR achieved in our study of

11.6$\pm$3.2 throughout the lungs (elliptical birdcage coil with image resolution of 10x10x10 mm^3 and $T_{aq} = 2.1\ ms$) is also comparable to 32$\pm$6 in a chosen central region reported by Couch et al. (131) with a transceive vest coil and image resolution of 7.1x7.1x22 mm^3 and $T_{aq} = 7.1\ ms$ with half-fourier echo. Although the in-plane resolution reported here at 3T is lower, visual comparison of the images in Figure 8 with those in (12) show more clearly defined edges and features, similar to those obtained by Halaweish et al. (121) at 3T, which did not report SNR values (with transceiver vest coil and image resolution of 6.25x6.25x15 mm^3 and $T_{aq} = 7.7\ ms$).

The benefits shown here for SSFP of C_3F_8 are less applicable to the other common fluorinated gases of SF_6 or C_2F_6 because of their shorter T_1 and T_2 values. Therefore, the use of C_3F_8 over other fluorinated gases has an increased benefit in terms of SNR achieved with SSFP and longer T_2^*. Consequently, the use of ultrashort echo time (UTE) sequences for SF_6 or C_2F_6 is logical (98), while not providing as dramatic an improvement for ^{19}F lung imaging with C_3F_8 since T_2^* is greater than gradient encoding and RF pulse times that may be used. Additionally, T_2^* filtering in UTE SPGR imaging with fluorinated gases in 3D radial or 1D Cartesian UTE (131) is another concern somewhat circumvented by the use of C_3F_8 with short TR SPGR or SSFP.

6.7 Conclusion

With optimized SSFP images we have demonstrated improved lung ventilation images with ^{19}F C_3F_8 gas at 1.5T. We believe the image quality shown here to be equivalent or superior to images published previously at 1.5T or 3T and this work bodes well for the emergence of ^{19}F gas MRI as a complementary modality to ^{129}Xe or ^{3}He MRI for directly imaging lung ventilation. However, benefits of SSFP at 3T are less clear.

Chapter 7: Application of Sparse Incoherent Undersampling for C_3F_8 Lung Ventilation Imaging: Investigation of Reconstruction and Sampling Methods[5]

7.1 Overview

Purpose: To investigate the use of compressed sensing (CS) via sparse sampling and different reconstruction methods for ^{19}F perfluoropropane (C_3F_8) gas human lung ventilation MRI to best reproduce the spatial-information obtained with high-resolution hyperpolarized (HP) gas imaging.

Methods: Retrospective simulation was performed using a ^3He lung MRI ventilation dataset with different sampling, reconstruction and image parameters: sampling pattern sparsity, nominal imaging resolutions, reconstruction method, and levels of noise. To determine the applicability of sparse sampling towards ^{19}F C_3F_8 ventilation imaging a 3D printed phantom was designed based on the ^3He dataset for in-vitro image optimization experiments with a fully sampled ^{19}F image of equal resolution to the ^3He image, which would not be feasible with in-vivo imaging. For validation of the simulation method, acquired data is compared to simulated. Sparse sampling was then applied in experiments with in-vivo ^{19}F imaging using receiver arrays.

Results: The SNR level and AF was found to change the optimum reconstruction parameters promoting the idea that a parameter free reconstruction method of the sparse data for ^{19}F imaging may be beneficial. Sparse sampling with AFs higher than 2 were found to be less beneficial than performing conventional lower resolution imaging. Overall, ^{19}F imaging with lower resolution was found to result in unrecoverable loss of detail in ventilation imaging.

Conclusion: Some degree of undersampling was observed to be beneficial for image quality with the SNR limited method of fluorinated gas ventilation imaging. The comparison of sampling and reconstruction strategies and experimental results described here may also be applicable to HP gas imaging where image resolution or sampling time is reduced when compared to ventilation imaging, such as with dissolved phase ^{129}Xe imaging or the measurement of the ADC.

---

[5] All experiments, simulations and analysis on data were carried and described in the written manuscript by AMM. Manuscript revisions performed with GC, JMW and AMM. Code to perform reconstructions with NLCG was developed my Michal Lustig and modified in its usable form by GC.

7.2 **Introduction**

Fluorinated gas (^{19}F) MRI is a promising method for the assessment of lung ventilation in obstructive lung diseases (121, 126). Fluorinated gas ventilation imaging provides direct functional information of lung physiology and can be mixed with oxygen for safe continuous breathing. Also, fluorinated gas imaging does not require specialized hyperpolarization (HP) equipment as with ^{129}Xe and ^{3}He ventilation imaging. However, the substantially weaker MR signal with TP when compared to HP gas MRI (124) has so far necessitated the acquisition of much lower resolution images for sufficient signal-to-noise ratio.

With HP gas lung imaging, CS has been used to reduce acquisition time whilst maintaining most of the imaging quality (33). This has been critical in current applications that involve for instance the acquisition of both anatomical ^{1}H and HP ventilation images within the same breath-hold (321) or in diffusion weighted acquisitions which require multiple b-value interleaves of a 3D data-set (85, 139). The CS method is especially beneficial for ventilation imaging since the images are naturally sparse in the wavelet and/or image domain (322). As such, the comparison of fully sampled images and those obtained with CS can have low error (323).

Previously, it has been shown that in the presence of low SNR, CS may also improve the effective resolution with improved effective SNR for better quality diagnostic proton images (324). Here we investigate under what conditions the application of CS may be advantageous in ^{19}F lung MRI with the motivation of narrowing the gap in ^{19}F ventilation imaging quality compared to routinely obtained HP ^{129}Xe/^{3}He ventilation images, despite the lower inherent SNR(325). This goal is in contrast to typical motivations for using CS or parallel imaging which are generally geared towards increasing temporal resolution (326), reducing motion artefacts (327-329) and reducing SAR (330) .

In addition to the numerous techniques of image acceleration via parallel imaging with multiple receiver coils (42, 45), there are a large, and ever increasing, number of algorithms for reconstructing k-space data that is acquired via sparse incoherent semi-random sampling of k-space. These include, but are not limited to: various method based on NLCG algorithms (48), iterative soft thresholding (IST) (331), other linear algebraic methods based on thresholding coefficients (332), and generalized hybrid methods of parallel imaging and L$_1$-minimization with incoherent undersampling (49, 333) and auto calibrating of the reconstruction parameters (334). In the limited number of comparisons of various algorithms to date, no single algorithm has been found to perform best in all cases (335, 336).

Furthermore, the reconstruction algorithm, method of quantifying reconstruction accuracy, sparsifying domain, sampling method/pattern employed, and the imaging object/application of CS vary significantly in the literature, so that direct comparison is challenging (in reference (337) which reviewed 18 relevant clinical studies of CS, out of a potential 269 considered, the listed variables were not compatible between the different studies). Therefore, it is unlikely that all the algorithms developed, or even a significant proportion of them, have or will be systematically compared.

For the reconstruction of undersampled k-space in MRI the optimization of weighting parameters for different algorithms requires comparison of the reconstructed image to that of a fully sampled dataset with specific indices, such as the root mean square error (RMSE) or structure similarity index (338, 339). However, as noted in reference (51), often "values of the regularization parameters are simply quoted, or perhaps the issue is simply omitted". In addition, algorithms have been developed that avoid the use of weighting parameters (331), or use prior knowledge or information from the images being acquired to calibrate the weighting/reconstruction (334, 339). Therefore, the work presented in this chapter aims to investigate the optimization of weighting parameters for different levels of SNR and sampling resolutions and patterns for the specific application of ^{19}F lung ventilation MRI. For the case of fluorinated gas imaging, where a fully sampled high-resolution image may not be obtained in the time course of a breath-hold, determination of the optimal weighting parameters is difficult and an algorithm that doesn't require weighting parameters may be beneficial. Consequently, an algorithm was developed here that uses thresholded coefficients from the wavelet and/or image domain to calculate the transform point spread function (TPSF) and remove the interference produced due to the sparse sampling of k-space. The performance of this algorithm is compared to the NLCG algorithm (48), which has previously been employed for numerous studies involving HP lung and lung related imaging (33, 87, 139, 322, 323, 340) and is therefore the most applicable for direct comparison to the state-of-the-art. The stability of the optimal regularization parameters to the SNR in ventilation imaging and nominal resolution is evaluated for the commonly employed NLCG algorithm. Additionally, the response of the newly developed algorithm under similar conditions is compared.

Without comparing ^{19}F lung ventilation images of similar resolution to those obtained with HP gas it is not possible to determine if fluorinated gas imaging can provide a clinically useful and potentially cheaper alternative. Previously, 3D printed anatomical phantoms of the lung (341) heart (342), breast, brain (343) etc. have been developed for rapid evaluation of MR techniques and methods that could not be practically or safely studied through in-vivo study.

In these models it is desirable to reproduce the structural and MR parameters as closely as possible, to enable valid comparisons with expected in-vivo results. Hence, we also present a 3D printed lung phantom based on a lung ventilation scan acquired from ^{3}He MRI used to explore the limits of fluorinated gas MR in terms of spatial resolution and SNR. With a lung model containing suitable spatial structure we aimed to compare the lower-resolution imaging obtainable in-vivo with ^{19}F ventilation imaging to higher-resolution imaging typically obtained with HP gas imaging, but not practically achieved in-vivo with ^{19}F MRI due to constraints of in-vivo scanning time. The 3D printed phantom allowed prospective investigation of sparse sampling for ^{19}F with comparison to a fully-sampled dataset.

The investigation into sparse sampling for ventilation imaging taken here differs from previous works in a number of ways. First, in previous scanning the AF and resolution is usually predetermined for the desired number of scans required for a set-imaging time, while here the resolution and AF are not known ahead of time and are being chosen based on what results in the best image for a given imaging time based on limited SNR. Second, since a fully-sampled high-resolution in-vivo data-set isn't obtainable for the C_3F_8 ventilation imaging different approaches to finding the optimal reconstruction had to be investigated here so the following steps were taken: a different reconstruction method was tested, retrospective sampling with a HP dataset was used, prospective sampling with a lung phantom was attempted and also prospective in-vivo imaging was performed attempting to use the visual comparison of the reconstructed images to determine the optimal weighting. Finally, for in-vivo C_3F_8 ventilation imaging the reconstruction algorithm was performed with multi-element arrays rather than a single transceive element, though coil sensitivity was not used explicitly in the reconstruction method.

7.3 Theory

7.3.1 SNR difference in HP gas and TP Fluorinated Gas MRI

As this study is based on the evaluation of CS in ventilation imaging with fluorinated gas, the SNR that may be expected with ^{19}F MRI when compared to the more established experimental evidence base of HP gas imaging experiments is required as a theoretical starting point. Therefore, Equations 2.35-2.39 in Chapter 2 are used to evaluate the relative SNR difference between HP and thermal equilibrium imaging with C_3F_8 here.

7.3.2   **SNR-Resolution Relation for 3D imaging**

There are fundamental differences between fluorinated and HP gas imaging contrast due to dissimilar MR relaxation parameters and imaging methods. In addition, the density of fluorinated gas in the lungs can be artificially enhanced to high levels because it has negligible anaesthetic effects and its T_1 relaxation time is reduced by mixing with oxygen in the lungs allowing more rapid recovery of longitudinal magnetization after excitation. In reference (117) it is shown that for C_3F_8 gas mixed with O_2 the T_1 varies from 6ms-20ms for a concentration of 0-100% C_3F_8 (at 60 MHz, 0.94 atm and $22°C$). Thus the lungs can be saturated with ^{19}F gas before image acquisition, whilst the concentration of HP gases used is generally lower (because the signal is higher) and thus the regional distribution of gaseous tracer in the lungs may have a greater dependence on breathing pattern, and collateral and fractional ventilation (123, 344). However, for the purpose of performing retrospective analysis with a HP gas image dataset it is assumed that fluorinated and HP ventilation images contain fundamentally the same spatial information. Therefore, the dominant factor considered in simulation is the lower SNR of fluorinated gas compared to HP gas imaging, necessitating lower resolution imaging. The SNR-resolution relation in TP 3D imaging, assuming constant; FA, TR, TE, and T_{aq} is (345):

$$SNR \; \alpha \; \frac{FOV_x FOV_y FOV_z}{\left(N_{fx} N_{py} N_{pz} \right)^{3/2}} T_s \tag{7-1}$$

where $FOV_{x,y,z}$ is the field of view in the x, y, z direction, N_{py} and N_{pz} are the number of phase encoding points, N_{fx} is the number of frequency encoding points and T_s is the imaging time. In the work presented here this conversion is used in comparing the level of SNR for different resolutions and AFs to that of a fully-sampled dataset matching the typical resolution of a HP gas ventilation image.

7.3.3   **Algorithm for Threshold Based Cancellation of Incoherent Interference**

The NLCG method (detailed in section 2.8.8) is robust and has been applied previously for ventilation imaging (85, 139, 322), and in other MRI applications (51, 338). However, for the purpose of TP fluorinated gas imaging there are a number of obstacles to its use. For the optimization of λ_{Xfm} and λ_{TV} , a fully sampled data-set must be acquired, which is not possible in-vivo for the desired resolution investigated here due to the inherently low spin density and hence low SNR of fluorinated gas imaging. Also, the optimal weighting parameters may change as lung physiology (and hence the regional appearance of the image) changes with diseased vs. healthy lungs, or SNR changes (such as during wash-out/wash-in imaging) as such

a reconstruction method with no free parameters may be preferred (331, 334). Therefore, in this work a new reconstruction method is developed and presented that may be less sensitive to differences in image structure/variation.

The proposed method is part of the IST framework, which uses the reconstructed data as the best approximation available to calculate and remove the interference caused by undersampling k-space. A basic example of this is used as an illustration in reference (48), forms part of the theoretical basis for the method in references (332) and is similar to the method employed in reference (346). The theoretical basis for this method relies on the following principles:

(i) The incoherent noise introduced by undersampling can be estimated using the reconstructed data

(ii) Only a limited number of coefficients have sufficient SNR to contribute to the approximation

(iii) The best estimation for removing the interference results in the highest sparsity, while maintaining data consistency

The algorithm attempts to maximize the sparsity of the data in some domain. This can be compared to the method proposed in reference (346), which uses the image entropy as the focus criterion, since incoherent noise produced by undersampling increases the entropy. The objective function the algorithm attempts to minimize is quantified by:

$$g\left(\psi_{Xfm}x\right) = \frac{\|\mathcal{F}_u x - y\|_2^2}{AF \times N_{fx} \times N_{py} \times N_{pz} \times \sigma_k^2} + \frac{\|\psi_{Xfm}x\|_1}{\|\psi_{Xfm}x_{zf}\|_1} + \frac{\|\psi_{TV}x\|_1}{\|\psi_{TV}x_{zf}\|_1} \tag{7-2}$$

where the subscript *zf* denotes the quantity derived when the unsampled k-space data is zero-filled and additional variables are described in Chapter 2 with the NCGD algorithm. The L1 norms in the sparsifying domain, $\frac{\|\psi_{Xfm}x\|_1}{\|\psi_{Xfm}x_{zf}\|_1}$, and total variation domain, $\frac{\|\psi_{TV}x\|_1}{\|\psi_{TV}x_{zf}\|_1}$, quantify the level of sparsity in those domains, while $\frac{\|\mathcal{F}_u x - y\|_2^2}{AF \times N_{fx} \times N_{py} \times N_{pz} \times \sigma_k^2}$ is a normalization of the data consistency in the k-space domain. The change in the sampled k-space data is normalized by the total variation considering the standard deviation of noise in the sampled k-space points and 3D matrix size ($AF \times N_{fx} \times N_{py} \times N_{pz} \times \sigma_k^2$), while the L1 norms of the sparsifying domain and TV domain are normalized by the reconstruction obtained from the zero-filled k-space. Equation (7-2) is used as the minimization criteria for all steps of the algorithm.

A detailed algorithm flow chart and visual representation of the proposed method is provided in Figure 7-1. Figure 7-1a demonstrates that ventilation images are potentially sparse in both the image and wavelet domain, so that information from both is combined in the reconstruction

algorithm as described in Figure 7-1b. Steps 1-5 describe the acquisition and reconstruction of the zero-filled k-space and initial calculation of the L1 norms. Step 1 shows an example sampling pattern, which is smaller in the k_z phase encoding direction due to the typically reduced FOV and resolution in the anterior-posterior direction for lung ventilation imaging. In step 6, a fraction of the highest value coefficients is used to calculate the interference caused by the sampling pattern with:

$$h(\psi_{Xfm}x) = \psi_{Xfm}x_{rec} - \psi_{Xfm}\mathcal{F}_u\mathcal{F}^{-1}\psi_{Xfm}^{-1}Th_i(\psi_{Xfm}x_{rec}) \tag{7-3}$$

where x_{rec} is the current best estimate of the un-aliased image and Th_i denotes the thresholding operation for the fraction of coefficients up to the value of $0 < i < 1$. In step 7, a fraction (1/n_{iter}) of the calculated interference is subtracted and the current best estimate of the data, $\psi_{Xfm}x_{rec}$, is updated. Afterwards, the same process is repeated with a slightly increased number of coefficients of the domain representation ($i = i + di, 0 \le di$); this process is performed n_{iter}. The same procedure is repeated for increasing values $di = di + \Delta di$ until $g(\psi_{Xfm}x_{rec}]_{di}) < g(\psi_{Xfm}x_{rec}]_{di+\Delta di})$. In step 8, $\psi_{Xfm}x_{rec}$ is repeatedly used to estimate equation (7-3), and then update it with $\psi_{Xfm}x_{rec} = \psi_{Xfm}x_{zf} - h(\psi_{Xfm}x)$, until the updated $g(\psi_{Xfm}x_{rec})$ is greater than the previous. Steps 6-8 are then repeated with $i = i + \Delta i$, until $g(\psi_{Xfm}x_{rec}]_i) < g(\psi_{Xfm}x_{rec}]_{i+\Delta i})$.

Since this method obtains reconstructions from both the wavelet ($[x_{rec}]_{wave}$) and image ($[x_{rec}]_{img}$) representations of the data, with noticeable differences in both, the final image is a weighted average, $x_{rec} = \frac{\alpha[x_{rec}]_{wave}+\beta[x_{rec}]_{img}}{\alpha+\beta}$, where the function $g(\psi_{wave}x_{rec})]_{\alpha+\beta=1} + g(\psi_{img}x_{rec})]_{\alpha+\beta=1}$ is minimized.

7.4 Methods

7.4.1 Sampling Patterns

The following method of sparsely sampling phase-encoding (k_y and k_z) lines in MRI has been employed in previous research (85, 322). The 2D phase encoding sampling pattern follows a probability distribution function (PDF) with full sampling of the Cartesian grid within a given fully sampled radius (r_ρ) around the centre of k-space and a sampling probability density that scales according to a power (p_ρ) with distance away from the centre outside that radius (322). For every choice of p_ρ and r_ρ many potential patterns are evaluated, and the pattern that produces the smallest side-lobes in the TPSF is used. In retrospective analysis,

variations of r_ρ and p_ρ were performed to determine the impact of both of these parameters on reconstruction accuracy. Additionally, with a single value of p_ρ many patterns with varying values of r_ρ, different AFs and nominal resolutions were compared. Figure 7-2 shows the different k_y/k_z phase encoding sampling patterns evaluated in simulation. The imaging FOV is assumed to remain the same in all cases. The highest imaging resolution investigated matches the one currently employed in our group with ^{129}Xe HP gas 3D SSFP ventilation imaging (142), and is that of the fully-sampled dataset used for retrospective analysis.
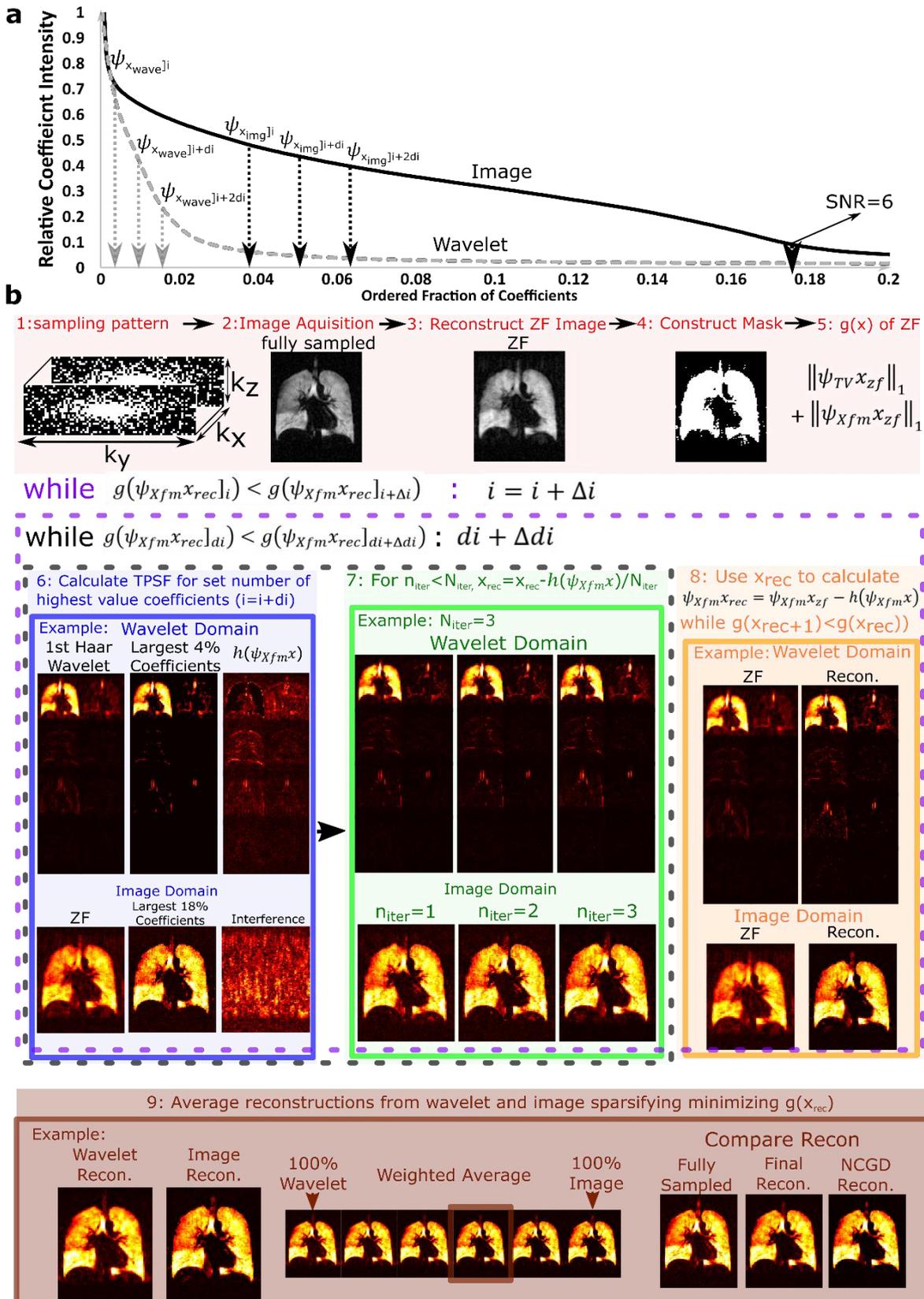
Figure 7-1: a: Diagram demonstrating the relative sparsity of coefficients in image domain and wavelet domain for lung ventilation imaging. b: The algorithm followed for reconstructing sparsely sampled data to remove noise from incoherent sampling.

7.4.2 Reconstruction Accuracy Metrics

The quality of the reconstructed images was compared using the normalized root mean square error (RMSE) calculated as where x_{ij} and z_{ij} are the pixel values of:

$$RMSE = \sqrt{\frac{\sum\left(x_{ij} - z_{ij}\right)^2}{\sum\left(x_{ij}\right)^2}} \qquad (7\text{-}4)$$

the fully and under sampled images, respectively. In the analysis the image is masked so that regions outside of the lung are set to zero (x_{ij}=0 and z_{ij}=0 outside of the lung). In retrospective analysis the mask is created from thresholding the fully sampled image, while in prospective analysis the mask is created by thresholding the filtered zero-filled image.

SNR was evaluated by determining a region of interest containing no signal (just noise) and evaluating the standard deviation of pixel intensity. Images were then scaled in SNR units by dividing by the standard deviation of the noise. For sparsely sampled data the same procedure was carried out using the zero-filled data where no visible undersampling based aliasing appeared, and the reconstructed data was scaled according to the standard deviation of noise found in this region. Regions where undersampling did not occur were found manually, and chiefly included the corners of the outermost slices. For data acquired with coil arrays, data from each element was scaled to SNR units so that the sum-of-squares reconstruction was also in SNR units. For reporting the SNR of image datasets the mean of the entire masked lung volume is quoted.

The coefficient of variation (CoV) has been shown to change in the presence of respiratory pathology, and with lung inflation level, and been used as a marker of
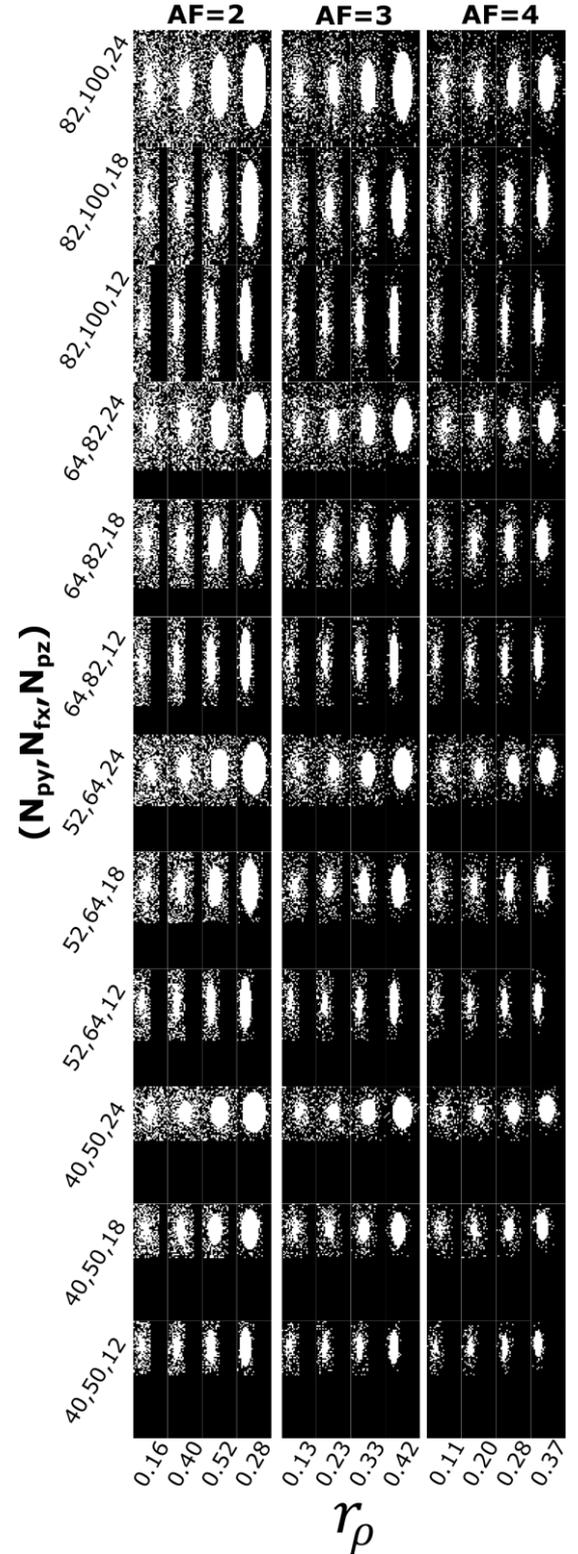
Figure 7-1: Sampling patterns that are compared for reconstruction accuracy with different levels of SNR. Crucial parameters that are varied include r_ρ, AF and nominal resolution ($N_{fx} \times N_{py} \times N_{pz}$).

ventilation heterogeneity (347). It is also an important parameter for characterizing the level of edge definition and detail in an image. Since regions of low CoV are both less crucial for image quality and more likely to be well represented as image resolution decreases reconstruction accuracy is compared in three binned levels of CoV of the original fully-sampled image: low CoV, medium CoV and high CoV.

The CoV of signal intensity was within 3x3 in-plane kernels, calculated as:

$$CoV = \frac{\sigma}{\mu}$$ (7-5)

where σ is the standard deviation and μ is the mean. Binned CoV maps were derived from the images where CoV was between 0.15<0.35 (described as medium CoV) and >0.35 (described as High CoV). RMSE was compared for regions of interest (ROIs) where CoV was high in order to investigate the reproduction of structural detail in the images.

7.4.3 Retrospective Simulation from Fully Sampled Dataset

Using a flexible transmit/receive vest coil (CMRS, Brookfield, Wisconsin, USA) on a 1.5T GE Signa HDx scanner, a 3D ^{3}He ventilation image with the desired imaging resolution was obtained as a ground truth data set (150ml ^{3}He, 3D steady-state free precession, BW = ±43 KHz, FA = 15°, TE = 0.8 ms, TR = 2.0 ms, 100×82×24 matrix, 4x4x10 mm^3 resolution).
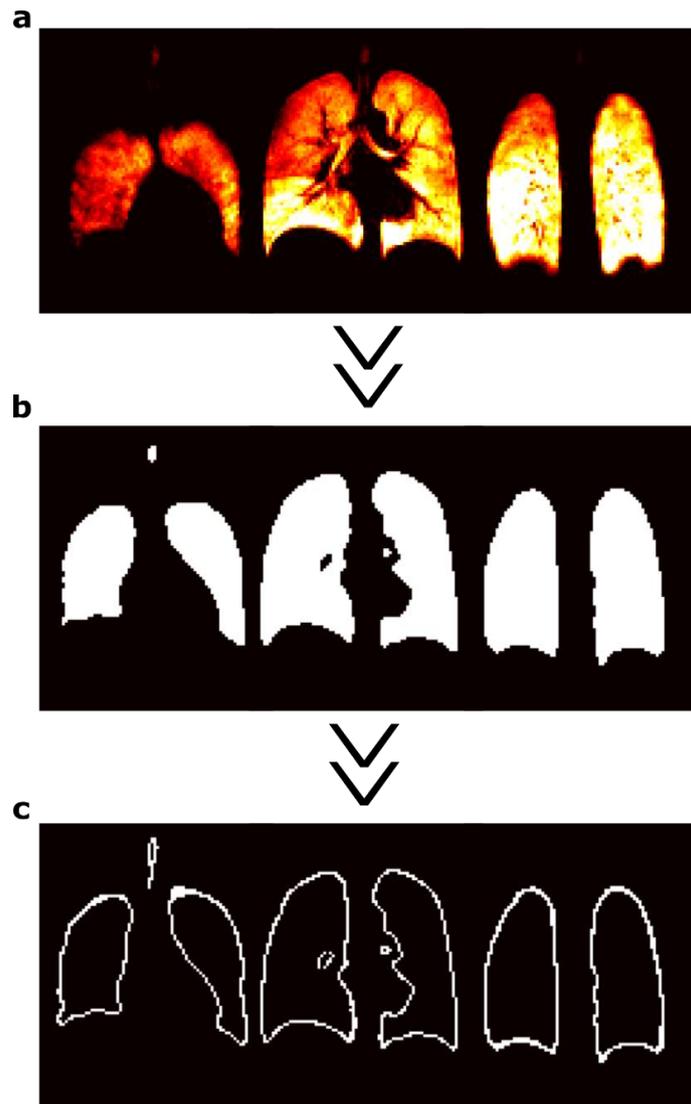
Figure 7-3: Demonstration of the method used here to convert a: a ^{3}He ventilation image to derive b: a 3D volumetric surface by median filtering the image, then thresholding the image to exclude noise to create c: a 3D shell of the lungs.

7.4.4 **Design of 3D Lung Phantom for Prospective Measurement of Sparse Reconstruction Accuracy**

Using the ^{3}He imaging dataset obtained for a retrospective analysis a 3D lung phantom was produced. The lung phantom was constructed in order to:

- provide a repeatable test object to allow for prospective sparse imaging,
- validate simulated predictions with experiment,
- allow the acquisition of a fully-sampled image acquired with ^{19}F imaging of sufficient quality to perform retrospective simulation.

To design the 3D lung phantom a 3D volumetric surface was derived by median filtering of the ^{3}He image, then excluding voxels in the model with neighboring voxels of intensity greater than the threshold of noise. This process is outlined in Figure 7-3. The shell was printed with

a Dimension SST 1200 es^{TM} 3D printer using a substrate polymer (ABS) with MRI compatible EM properties. Then, 4 mm tubing was inserted in the lung model airspaces to represent small vessels/arteries and defects that may be observed in diseased lungs.
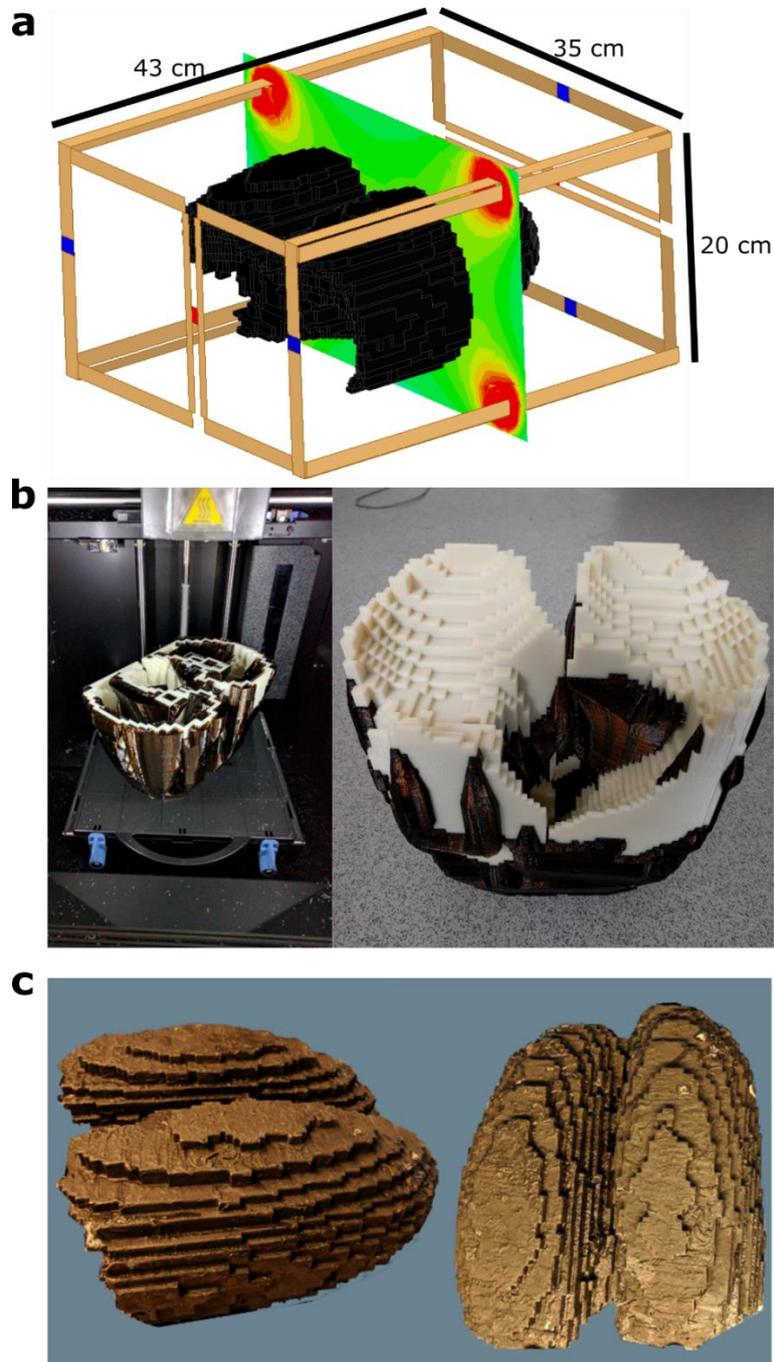
Figure 7-4: (a) Simulation model of parallel driven quadrature coil with 3D lung model, (b) and printing of phantom with Dimension SST 1200 es^{TM} 3D printer using a substrate polymer (ABS with $\varepsilon_r = 2.6$ - 2.86, Dissipation factor = 0.0048 - 0.0054) and sacrificial support material. (c) Manufactured 3D lung phantom.

In order to image the lung phantom a homemade ^{19}F coil with two sets of parallel coils driven in quadrature was designed and built for homogenous excitation and reception. The coil simulation model is shown in Figure 7-4 with the constructed 3D printed lung model.For

imaging the 3D printed lungs were filled with 79% C_3F_8 and 21% O_2 then a fully-sampled dataset was obtained with the following parameters: 3D SPGR, TE = 2.95 ms, TR = 6 ms, BW = ±9.6 KHz, FA = 60°, 100x82x24, 4x4x10 mm^3 resolution and 120 averages for a resulting 23:40 minutes of imaging. With the same imaging parameters, but 80 averages, sparsely sampled data was acquired for AF=6 (2:37 minutes), AF=4 (3:56 minutes) and AF=2 (7:52 minutes). The resulting images were compared to the fully sampled dataset and to retrospective simulations performed with the fully-sampled data. A ^{19}F image was also acquired with half the spatial resolution in all three Cartesian dimensions, half the acquisition bandwidth and half the averages. The k-space data of low-resolution images were zero-filled to the equivalent dimensions as the k-space data of the high-resolution images.

7.4.5 **Parameter Optimization with Added Noise**

In retrospective analysis, Gaussian noise was added to the complex raw data of images with a standard deviation (σ) to simulate the acquisition of images with lower SNR. Also, to emulate lower resolution imaging the points that are not sampled in k-space are removed and Gaussian noise is added to the remaining data with a standard deviation $\sigma_{low} = \frac{\sigma}{\sqrt{AF}\sqrt{N_{fx}N_{py}N_{pz}}}$, which is reduced due to the lower BW required to maintain the same acquisition time and increased number of averages available for the same imaging time. The reconstruction accuracy of images with varying levels of SNR was compared to the fully sampled image with equation (7-4), using only pixels in the original image with SNR>8.

7.4.6 **In-vivo Experiments with Sparse Sampling**

In-vivo imaging with 4 healthy volunteers was performed to explore the imaging quality with ^{19}F C_3F_8 ventilation imaging using sparse sampling compared to using standard lower resolution imaging. Experiments were carried out with the use of a single element transceive coil, an 8-element transceive array and the same 8-element transceive array with an additional 6 receive-only loops included (total of 14 receive elements). Images were reconstructed from each element separately, since the level of sparsity in the image domain should be greatly reduced for each, and then a sum of squares combination was used to combine the images.

In the measurements with the custom built ^{19}F vest coil (257), 40 averages were obtained over twenty 4-second breath-holds in an attempt to increase the image SNR to the point that sparse sampling could be applied successfully. The resulting image was compared qualitatively to a ^{3}He dataset acquired with the same volunteer. In imaging performed with the arrays, the

data from two breath-holds were averaged. Each breath-hold was approximately 17-19 second and for the "low-resolution" images 4 averages were obtained each time, while for the sparsely sample data 8 averages were obtained. The imaging parameters are listed in Table 7-1.

Table 7-1: Imaging parameters used in in-vivo experiments with ^{19}F 3D SSFP ventilation imaging with FOV of 40x32x24cm^3 ($r_\rho = 0.25$ and $p_\rho = 4$ for the sampling pattern used).

TE (ms)	TR (ms)	BW (±KHz)	Resolution (mm^3)	fully-sampled Encoding Steps (N_xxN_yxN_z)	AF	Target FA (°)	Avg.
V1 - Volume Transceive Coil							
1.4	3.5	12	8x4x10	50x82x24	4	62	40
V2 – 8-element Transceive Coil							
1.7	4	6.76	10x10x10	40x34x24	1	72	8
2.3	5	6.58	8x4x10	50x82x24	4	72	16
V3 – 14-element Transceive Coil							
1.9	5	5.95	10x10x10	40x34x24	1	72	8
1.9	5	8.06	8x4x10	50x82x24	4	72	16
V4 – 14-element Transceive Coil							
1.9	5	5.95	10x10x10	40x34x24	1	72	8
1.9	5	8.06	8x4x10	50x82x24	4	72	16

7.5 **Results**

7.5.1 **RMSE comparison with Retrospective Simulation from ^{3}He In-vivo and ^{19}F Phantom Data**

Histograms of the CoV for the ^{3}He ventilation dataset and the ^{19}F 3D phantom data set are displayed in Figure 7-5a. The tubing was found to introduce additional variation as might be expected from volume defects; potentially from masses or from unfilled airways in diseased lungs. This is desirable since the experiments performed are focused on the ability to reconstruct high variation areas of the lungs, which may be more prevalent in diseased lungs (57). Figure 7-5b shows masks of the regions of low CoV (white background), medium CoV (green) and high variation (red).
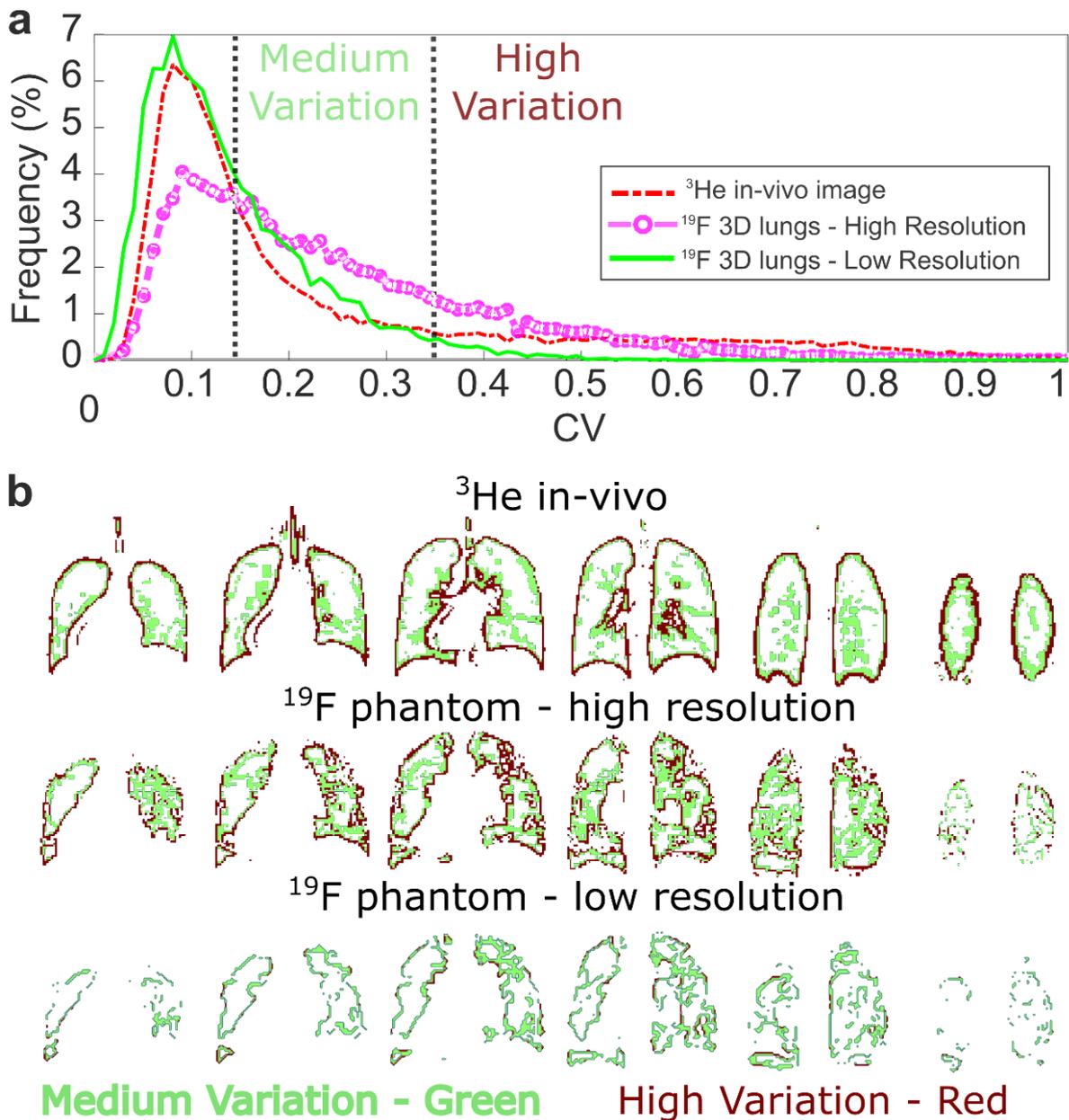
Figure 7-5: a: Histograms of CoV in ³He ventilation lung image and ¹⁹F image of the 3D phantom derived from the ³He dataset. The low resolution image of ¹⁹F phantom imaging is found by reducing the resolution by half in each spatial dimension for the original high-resolution image. b: Representative slices of 3D ³He b-SSFP and 3D ¹⁹F SPGR images used as a basis for retrospective simulation and optimization of CS sampling patterns.

For the NCGD algorithm the variation of the optimal weighting parameters with different levels of SNR is demonstrated in Figure 7-6. Naturally, the RMSE of the reconstruction is higher with lower SNR. Also, as the SNR is lowered a higher weighting for sparsity of the TV is optimal, which results in greater smoothing. This example demonstrates the need to optimize the weighting parameters for consideration of SNR, as well as for different nominal resolution, AF and sparse sampling patterns.
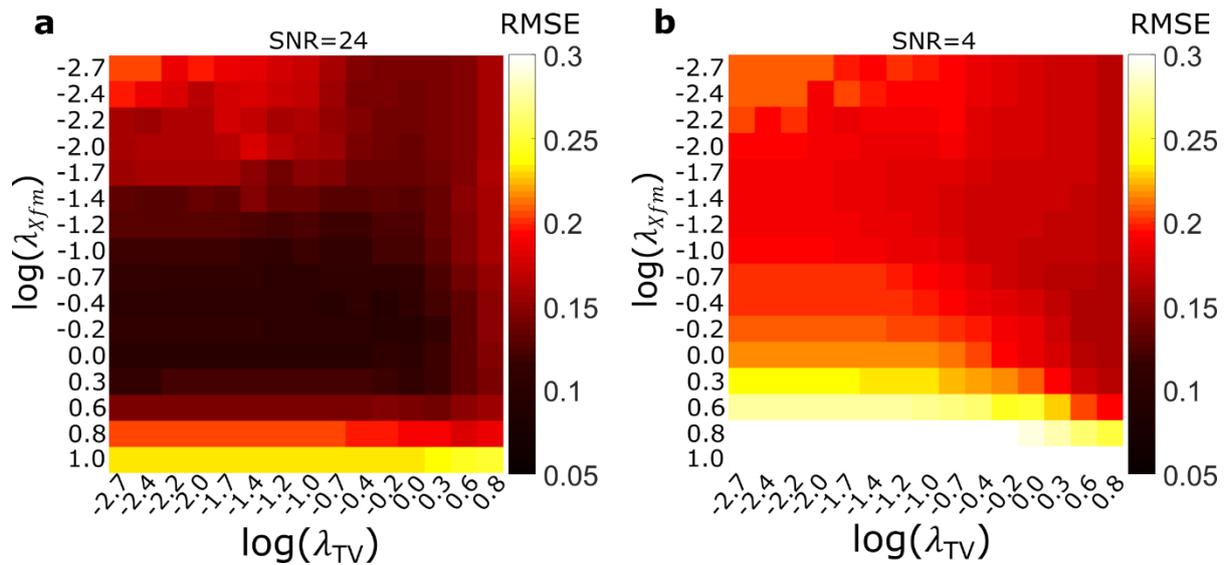
Figure 7-6: Retrospective simulation of the variation of RMSE with the TV and Xfm weighting parameters from reconstructed undersampled data with the NCGD algorithm when a: SNR=24, and b: SNR=4. The sparse sampling parameters are AF=3, r_ρ=0.2, p_ρ=3.

The variation of the RMSE with AF and SNR using the NCGD algorithm for retrospective simulation with the ^{3}He dataset (nominal resolution of 82x100x24) is shown in Figure 7-7. As shown in Figure 7-2, simulation with four different values of r_ρ were performed for every AF. The effect of different values of r_ρ on the reconstruction accuracy is shown with the use of error bars; the difference in minimum and maximum RMSE with the same AF, but different r_ρ, are shown as the lower and upper edges of the error bars. The resulting difference in the RMSE with varying r_ρ is found to be small relative to the influence of SNR and AF. As expected, with higher SNR more accurate reconstruction is obtained with lower AFs. Also, the RMSE is higher for higher CoV as AF increases. However, for low SNR the RMSE becomes mostly invariant with AF, and this range of SNR corresponds with the range expected for ^{19}F ventilation imaging (an SNR range of 0.4-4 considering an SNR of 20 was achieved with the fully sampled ^{3}He image). The results presented in Figure 7-7 contextualize the impact of AF, SNR and sampling pattern have on the quality of image reconstruction with varying levels of CoV. Based on this in future results the RMSE is either shown as the total from all binned values of CoV, or just for the region of medium CoV, since the conclusions derived for optimization are mostly the same.
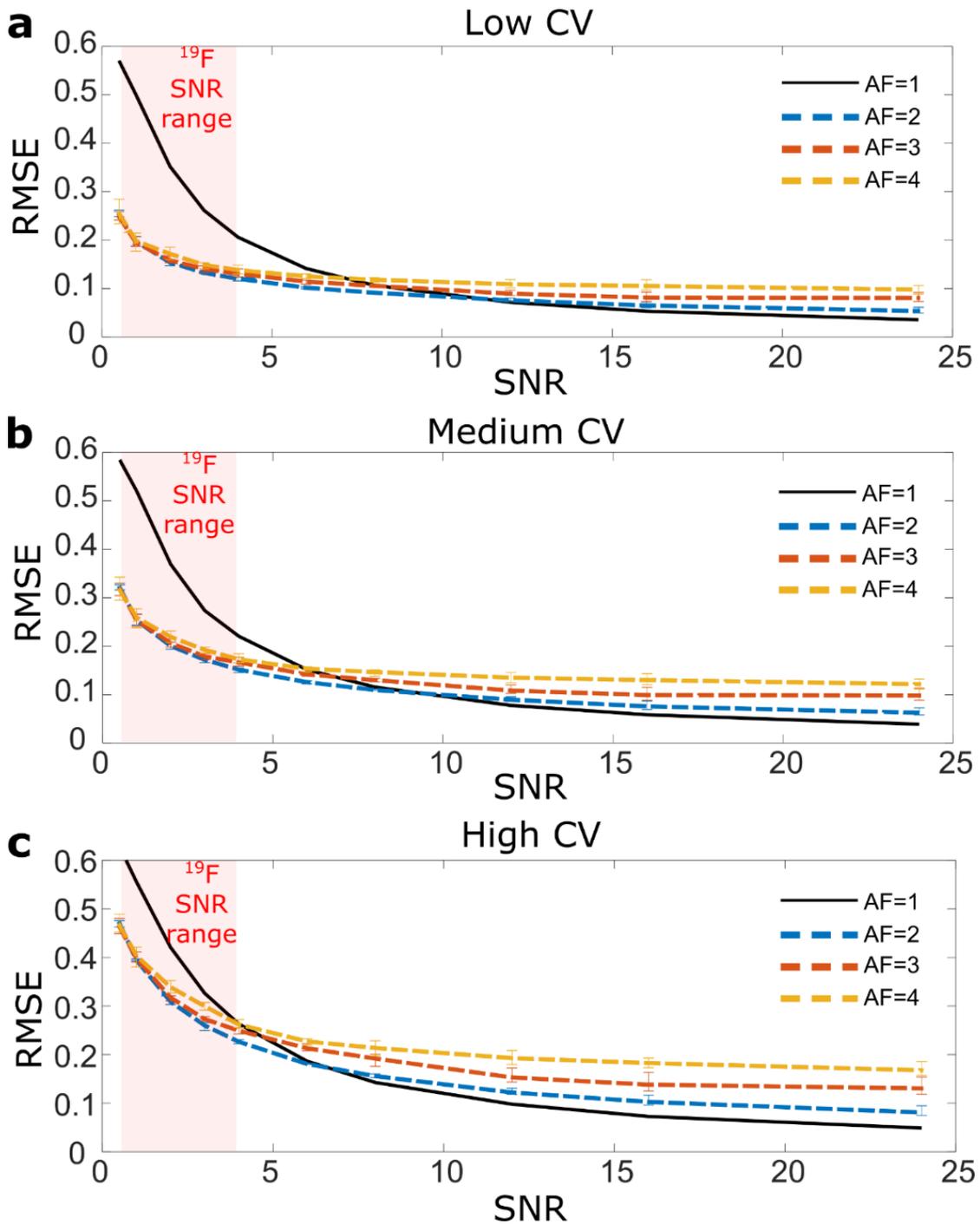
Figure 7-7: Retrospective simulation of the variation of RMSE with SNR for sparsely sampled data with varying AFs for regions of a: low CoV, b: medium CoV and c: high CoV. Error bars indicate the range of RMSE found with different sampling patterns. Based on the known approximate value of SNR for ^{129}Xe imaging, and the ^{3}He image used in this analysis, the range of expected ^{19}F image SNR for a fully-sampled image is displayed.

Figure 7-8 provides a comprehensive summary of the results reconstructed RMSE from retrospective analysis of the ^{3}He dataset with varying SNR and AF, similar to Figure 7-7, but including variation of the nominal imaging resolution. In the Figure 7-8 it can be observed that there is a nominal imaging resolution and AF that results in minimal RMSE for each level of SNR. For a given SNR and for each CoV region the nominal imaging resolution and AF

resulting in the smallest RMSE is surrounded with a green border. For each pixel only the sampling pattern with r_ρ resulting in the smallest RMSE is considered, however from Figure 7-7 it was found that the difference was marginal.
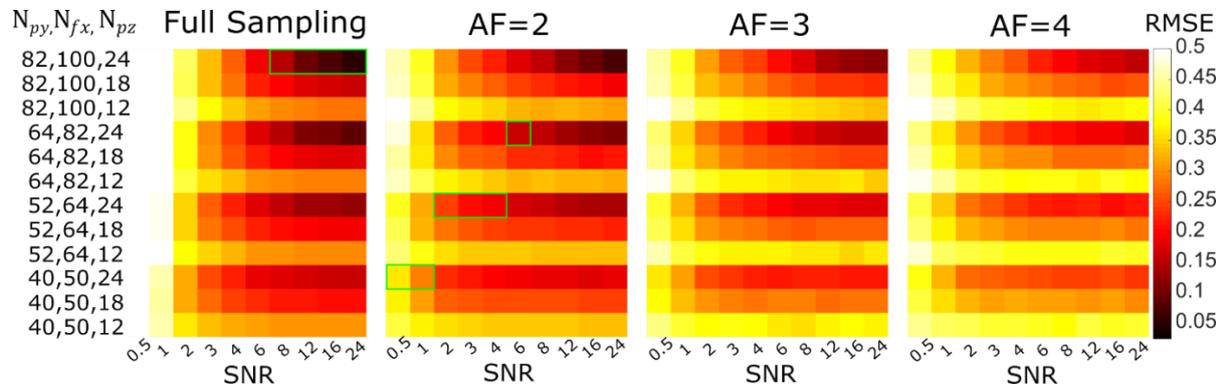
Figure 7-8: Results of retrospective simulation with ^{3}He ventilation image for varying SNR, nominal resolution and AF with the NCGD algorithm. The resulting RMSE of the reconstructed image is shown for the binned region of highest CoV. The result with minimal RMSE for varying $\boldsymbol{r_\rho}$ is shown in each pixel, while a constant $\boldsymbol{p_\rho}$=3 is used. Green boxes surround pixels that correspond to the nominal resolution and AF that results in the lowest RMSE for a given SNR.

Based on the results from Figure 7-7 and Figure 7-8 it can be inferred that the optimization of the nominal resolution and AF for imaging may be specified for each SNR value. Thus, Figure 7-9 provides line plots detailing the minimal RMSE achieved during retrospective reconstruction using the NCGD (Figure 7-9a) and IST (Figure 7-9b) algorithm and the ^{3}He image dataset, as well as with the 3D ^{19}F phantom (Figure 7-9c) using the NCGD algorithm. The minimum RMSE achieved with the IST or NCGD algorithm is also shown side-by-side in Figure 7-9d demonstrating the difference in reconstruction success.

From this, the optimal nominal imaging resolution and AF for sparse sampling to best reproduce the gold-standard/ground truth imaging resolution may be inferred. For all variations it appears that AFs greater than 2 have reduced image quality as measured by the RMSE, and that instead a reduction in nominal imaging resolution is more effective as SNR decreases. Also, it appears that a reduction in the N_{pz} resolution results in a greater decrease in the RMSE compared to reduction in the N_{fx} or N_{py} resolution, for the ^{3}He image data set. For the ^{19}F phantom images this was found as well, but to a lesser amount as in some cases a nominal resolution of 15 mm resulted in the lowest RMSE (N_{pz}=18). This is likely because the N_{pz} dimension is already the lowest resolution dimension in the analysis performed here for the fully-sampled case (10mm vs. 4 mm for the N_{fx} and N_{py} encoding resolution).

Figure 7-9 shows the comparison of RMSE and SNR variation as in Figure 7-8, but instead using the IST algorithm for reconstruction. It is observed that generally the IST algorithm

provides a less consistent reconstruction than the NCGD algorithm, with RMSE increasing to larger values as SNR decreases, furthermore the image coefficients have less predictive power for the incoherent noise introduced by sparse sampling. For AFs greater than 2, the difference is more pronounced, while for an AF of 2 they perform nearly on par. However, from Figure 7-6 it is observed that the minimal RMSE of the NCGD algorithm can vary greatly if the weighting parameters are not optimal, while the IST algorithm has no weighting parameters. The comparison of the minimal RMSE achieved with different levels of SNR for the two reconstruction methods is shown in Figure 7-9b, where it is observed that unless the baseline fully sampled SNR < 2, the difference in minimal RMSE is small between the two methods.
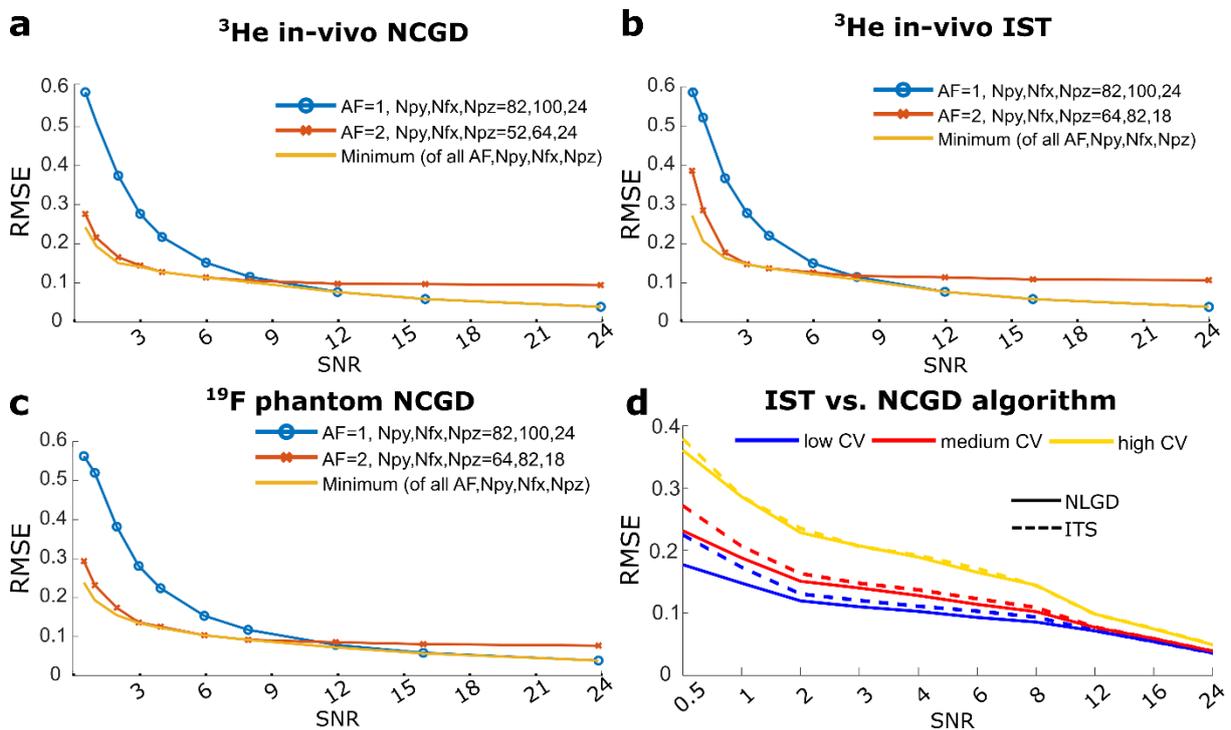
Figure 7-9: Retrospective simulations performed with ^{3}He ventilation imaging k-space demonstrating the change in *RMSE* in the medium CoV regions as SNR, nominal resolution and AF are all varied using the a: NCGD or b: ITS algorithm. c: The same analysis is shown using the NCGD algorithm with the ^{19}F phantom images d: The lowest RMSE achieved with SNR variation for the NCGD algorithm (solid line) and IST (dashed line) is plotted together to demonstrate the difference in reconstruction performance.

Figure 7-10 shows the reconstructed images from the ^{3}He data for a select number of cases with varying nominal resolution, AF and SNRs of either 3 or 24 of the equivalent fully sampled image. As AF increases or nominal resolution decreases, features such as vessels are obscured, while noise in the images also obscure the spatial. When SNR is lower there appears to be a greater weighting towards more TV regularization of the image during reconstruction, as also found in Figure 7-6 with greater TV weighting leading to lower RMSE.
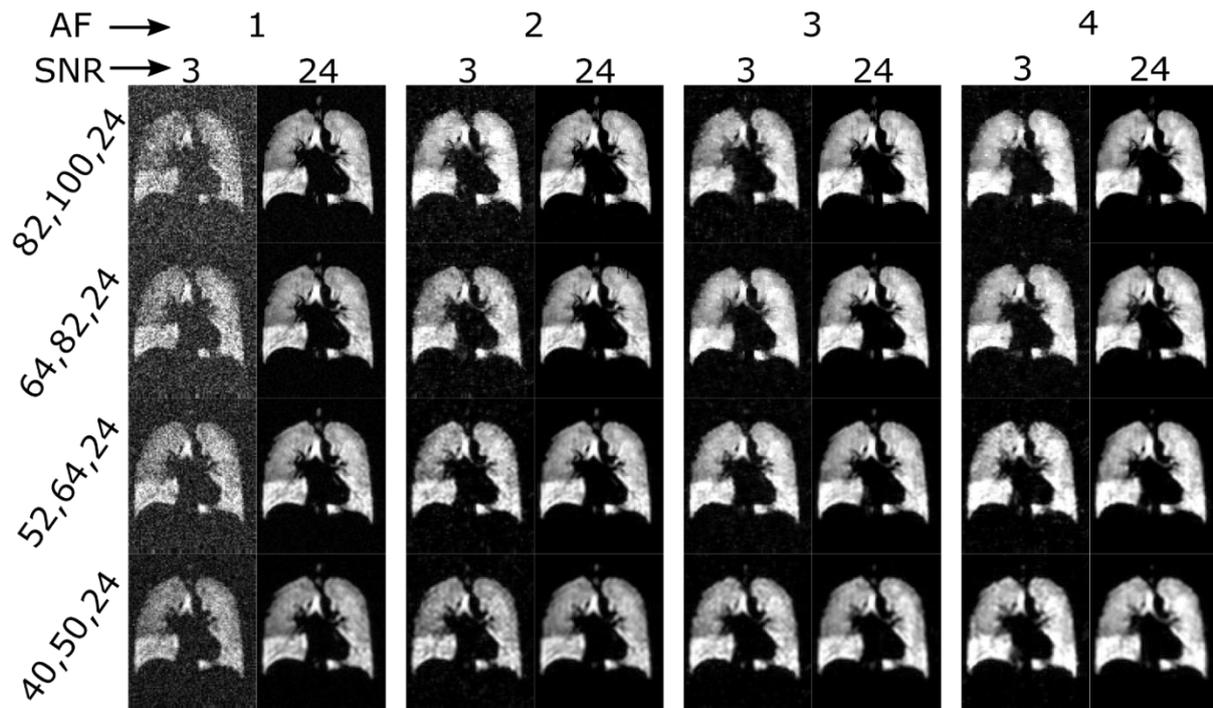
Figure 7-10: Reconstructed images using the NCGD algorithm with varying nominal resolutions and AFs when the SNR of a fully sampled image would be 3 or 24; p_ρ=3.

The basis for the IST algorithm presented in Figure 7-1 is that minimization of $g(x)$ in equation (7-2) corresponds to the minimization of the RMSE; leading to the best possible representation of the ground truth image. To test this hypothesis the variation of RMSE and the L1 norms of the different transforms (wavelet, image and TV), which are components of $g(x)$, are plotted together in Figure 7-11 for three example reconstructions. As the number of image or wavelet coefficients
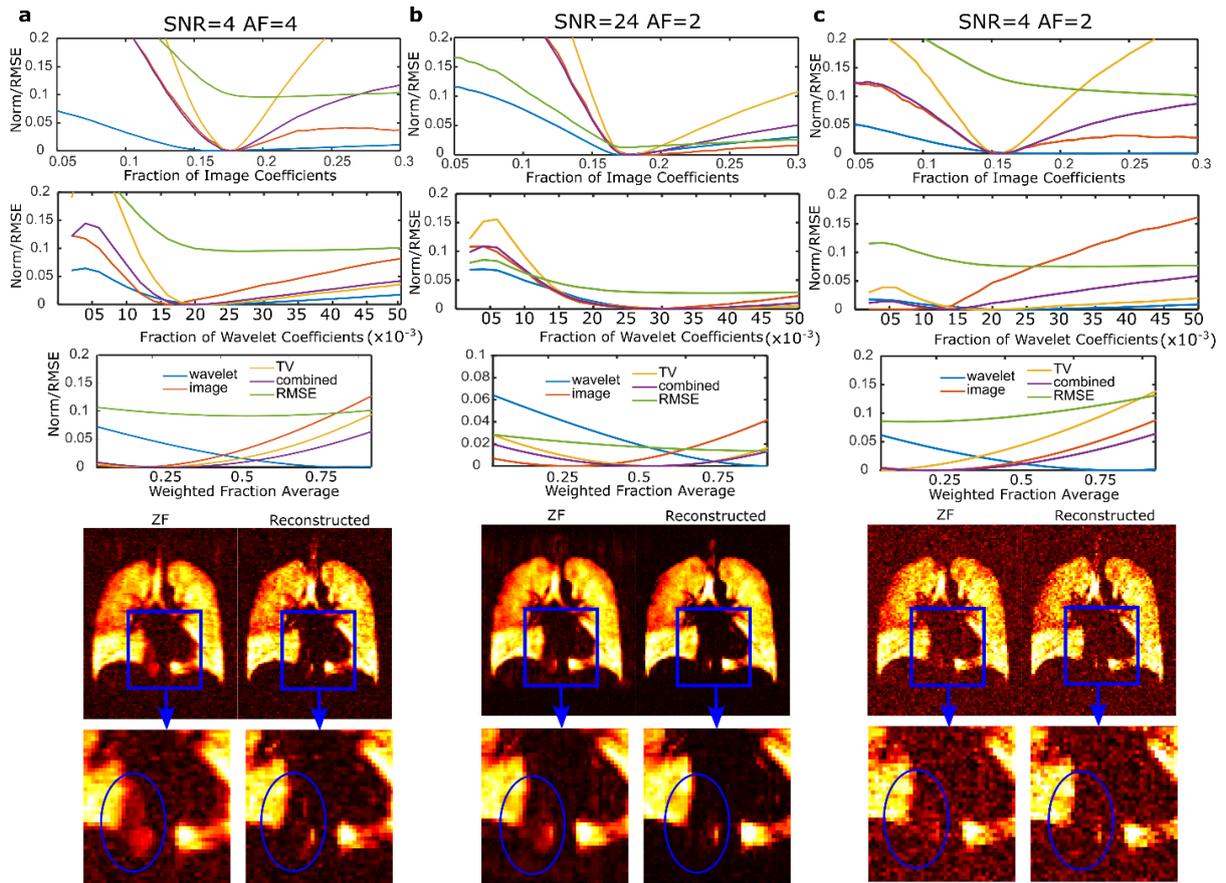
Figure 7-11: Variation of RMSE and L1 norms of different transforms for retrospective simulations performed on a ^{3}He imaging dataset using the IST algorithm for example cases where $r_\rho = 0.5$, $p_\rho=3$ and a: SNR=4 and AF=4, b: SNR=24 and AF=2 and c: SNR=4 and AF=2. Also shown is the variation of the RMSE and L1 norms as the average weighting is varied in the images reconstructed either by sparsifying the image or wavelet domain representation. The final reconstructed image is displayed next to the initial zero-filled image at the bottom. The L1 norms and RMSE are normalized by subtracting the minimum value obtained.

included in the IST algorithm increases the RMSE increases, until a point where inclusion of further coefficients result in inaccurate prediction of the incoherent noise and the RMSE begins to increase. Also, the result of the RMSE and L1 norms are shown for the weighted average of the reconstructed images using the image or wavelet domain for calculating the incoherent noise. The initial zero-filled image in a representative slice and final reconstructed image is shown for each case where it is clear that the artefacts due to incoherent undersampling that appear as aliasing (see circled region in enlarged image) are reduced in the reconstructed image, but that the performance of the algorithm is worse with lower SNR.

Generally, the minimization of $g(x)$ occurs close to the minimum of RMSE, but not precisely. This may account for the better performance of the NCGD algorithm. Neither the reconstruction using the wavelet or image domain performs consistently better. However, it appears that the averaging procedure weights towards the reconstruction with the lowest RMSE in the cases observed. Additionally, the RMSE of the average has the potential to be lower than

171

either reconstruction on their own. This suggests that an average of the images constructed with the NCGD and IST algorithm may also perform better than those performed by averaging the outputs of the individual algorithms separately since they operate using different methods of non-linear reconstruction.

7.5.2 Prospectively Sampled Sparse Imaging with ^{19}F and 3D printed lungs

The quantitative results from prospective sparse sampling imaging with the 3D phantom are shown in Figure 7-12. In Figure 7-12a, the variation of the RMSE with AF and imaging time is similar to that of the retrospective simulation presented in Figure 7-7. In addition, although the NCGD algorithm performs consistently better than the IST algorithm (since the weighting parameters could be optimized for RMSE by referencing the fully sampled image) the RMSE of the averaged image is either only marginally higher, or lower than the minimum of either method used separately. Furthermore, in some cases with low SNR/averaging time the IST does perform better. When comparing the reconstructed image in Figure 7-12b with high SNR, as AF increases greater blurring is observed as expected. Fine details of the pattern introduced by the tubing inserts are lost, but the impact is less than having a low SNR image as shown in Figure 7-5b.
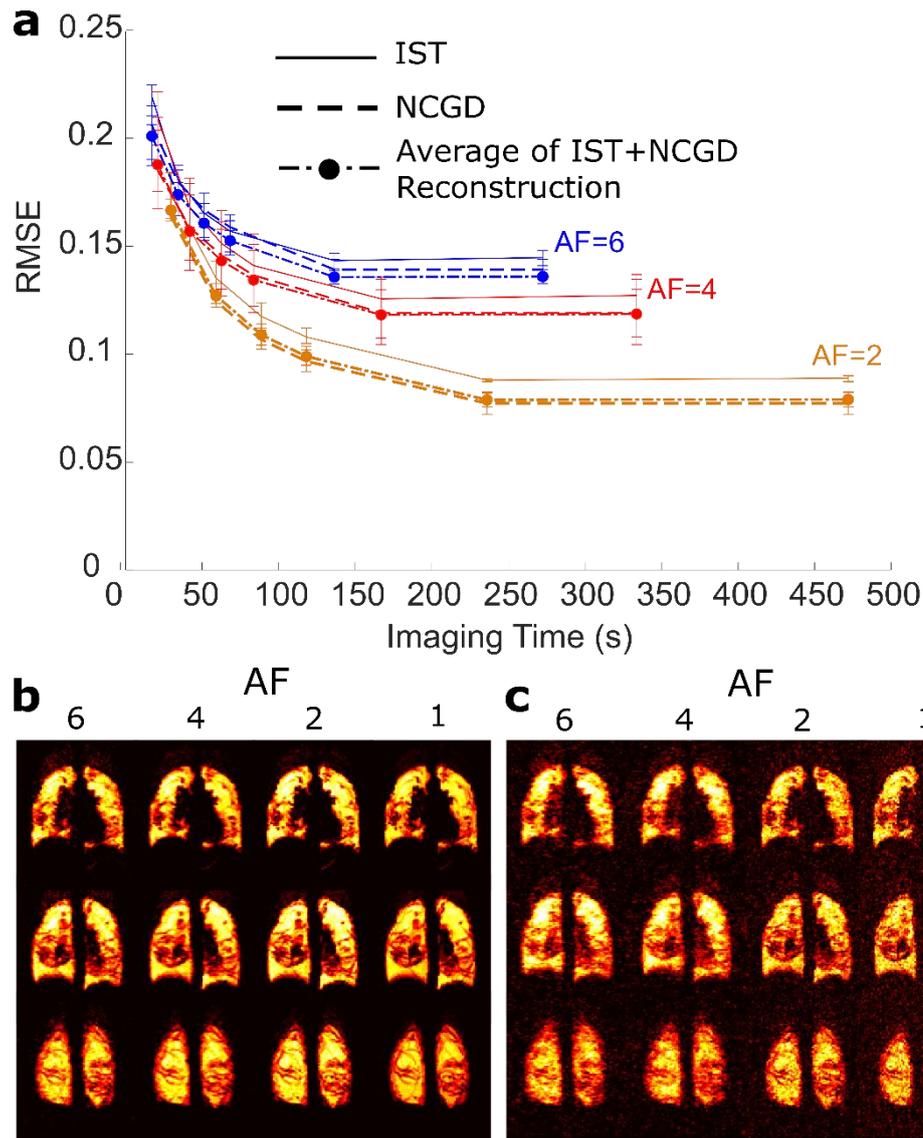
Figure 7-12: a: RMSE with varying imaging time for different AFs (a discrete number of averages are included in the reconstruction for each AF: 5,10,15,20,40 or 80). Error bars represent the minimum and maximum RMSE for the three sampling patterns tested for each AF. For each AF the results when reconstructing with the IST or NCGD algorithms and the average of both are shown. The reconstructed images in representative slices are shown for different AFs when b: 80 averages are used or c: 5 averages. They can be compared to the fully sampled image (AF=1) with b: 240 averages or c: 20 averages.

7.5.3 **In-vivo ^{19}F imaging: Array vs Transceive Coil**

A visual comparison of an in-vivo ^{3}He ventilation image and the ^{19}F undersampled in-vivo image obtained in the sample volunteer is shown in Figure 7-13. The ^{19}F image is reconstructed from sparsely sampled data with AF=4 and has half the nominal resolution in the frequency encoding direction as well. Motion related blurring is also observable at the diaphragm in the ^{19}F image since the results were averaged over 20 consecutive breath-holds. Despite some clear spatial discrepancies (see arrows) the CoV histograms generated from the in-vivo images are shown in Figure 7-13b and have similar distributions.
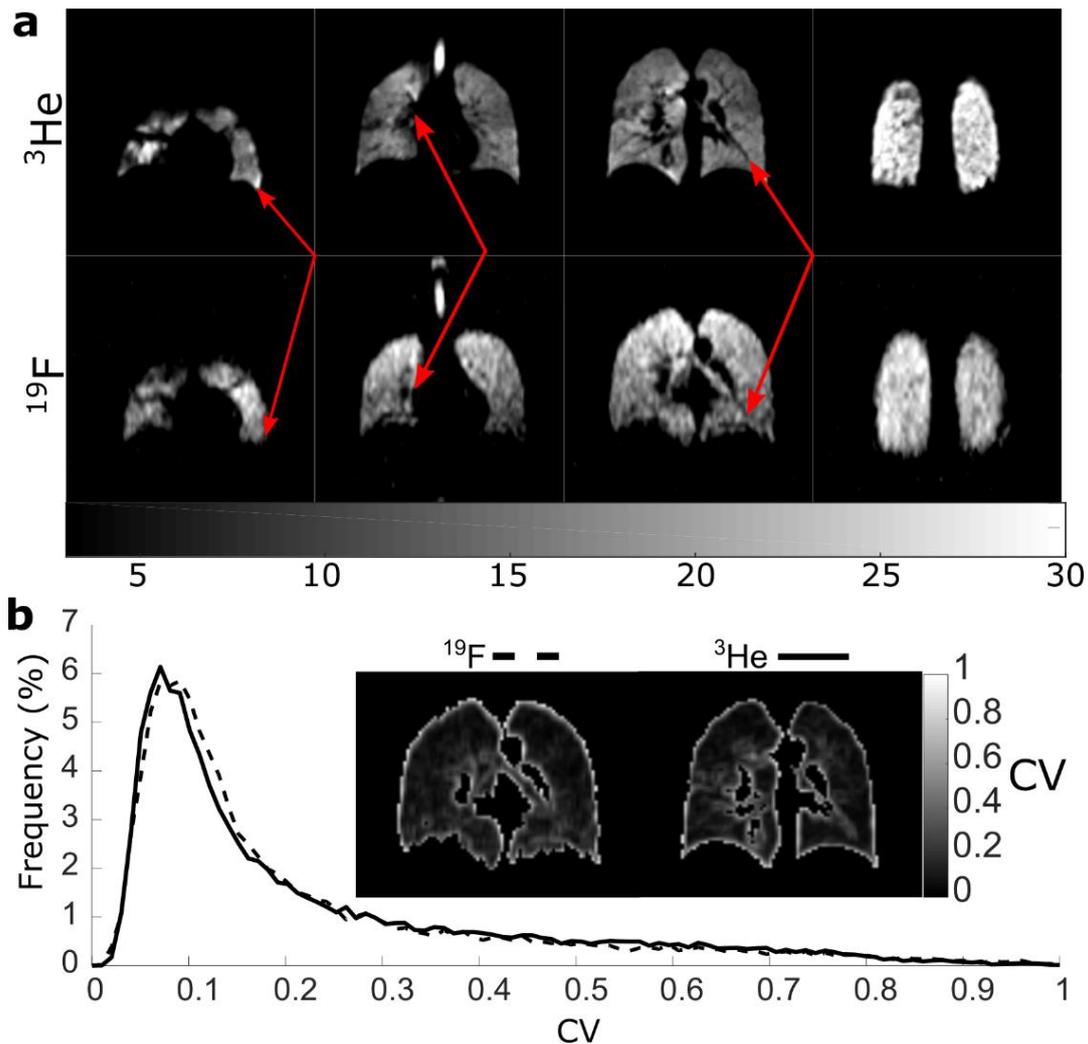
Figure 7-13: a: Representative slices in similar anatomical regions from a volunteer using ³He ventilation imaging or ¹⁹F with sparse sampling (AF = 4, $r = 0.2$ and $p = 4$) b: The resulting CoV histograms from the in-vivo imaging as well as CoV maps in a central slice.

The resulting reconstructed images in representative slices from volunteer 2 (8-channel transceive array), volunteer 3 and volunteer 4 (8-channel transceive array with additional 6 receive-only loops) are shown in Figure 7-14. For the NCGD algorithm the impact of weighting parameters on the final image is shown for a representative slice in Figure 7-14a. For in-vivo ¹⁹F images it is not possible to obtain a fully-sampled image for the means of comparison of RMSE during reconstruction, this is especially the case for an array as the sensitivities are highly dependent upon positioning and are consequently variable during every imaging session. Therefore, the resulting reconstruction was chosen based on the visual appearance of reconstructions, choosing ones that did not over-regularize the image or TV domain. The over-regularization of the TV domain is observed as excessive blurring, while in the image domain it is observed as a loss of detail in regions where the SNR/signal is lower. In contrast, the process with the IST algorithm remained consistent.
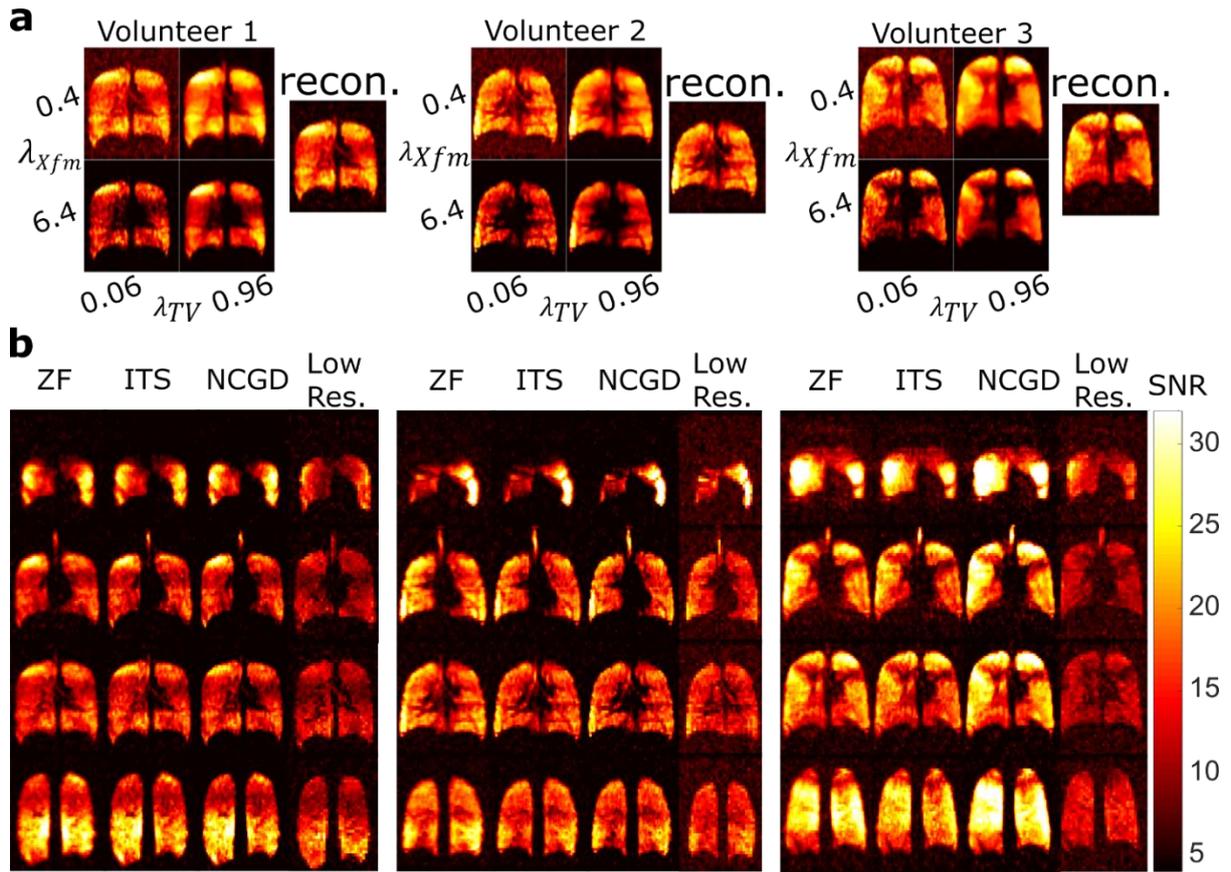
Figure 7-14: Imaging results for in-vivo application of sparse sampling ($r_\rho = 0.25$, p_ρ=4 and AF=4) for ^{19}F ventilation imaging acquired with the transceive array for three healthy volunteers. a: The resulting image in a representative slice as the weighting parameters in NCGD reconstruction is varied is shown for the three volunteers visually showing the impact on reconstruction. b: Represented slices of the reconstructed images using zero-filling, the IST algorithm, the NCGD algorithm and corresponding slices from a lower-resolution image taken with similar imaging parameters in the same imaging session.

Compared to the ZF image, both algorithms appear to reduce blurring and noise, however the difference is less dramatic than with a single coil. This is potentially because the incoherent noise from undersampling in each channel is different and therefore not additive during sum-of-squares combination. The low-resolution version for each volunteer has a consistently lower SNR, while not appearing to provide any better-defined features than the CS data. Note that the images obtained from volunteer 3 show the appearance of strong banding artefacts from the SSFP imaging indicating inadequate shimming, but also have the highest SNR.

7.6 Discussion

In the retrospective simulations performed to optimize sampling for ^{19}F lung ventilation imaging it was assumed that imaging with either [3]He or ^{19}F is a measure of the same ground truth ventilation image. However, the images obtained with ^{19}F may differ from [3]He imaging in a number of ways: the lungs may be fully saturated with ^{19}F gas during ventilation imaging,

MR relaxation parameters are different and the impact of the short T_2^* and associated blurring from the kx filter may limit the effective resolution due to the point spread function for ^{19}F imaging. However, since a fully-sampled ^{19}F image of sufficient quality cannot be imaged for the analysis presented here basing the analysis on a ^{3}He ventilation image is a reasonable approximation for ^{19}F imaging.

From the results presented in Figure 7-8 and Figure 7-9 a nominal 3D imaging resolution of 64x52x24 ($6.25 \times 6.25 \times 10$ mm^3) with AF=2 is predicted to provide the most accurate representation of the gold-standard HP gas ventilation fully sampled imaging resolution (100x82x24), with an expected SNR of $\sim 2 - 4$ if imaging with C$_3$F$_8$ was attempted at the same fully sampled resolution. However, from Figure 7-10, visual observation of the corresponding reconstructed image with this resolution and AF show a distinct loss of key features signifying ^{19}F gas imaging cannot completely match the image quality achieved with HP gas MRI.

In healthy volunteers, defects < 2 cm in size arise due to physiological effects attributed to posture (132, 348). Therefore it is difficult to attribute features smaller than this size to disease pathologies, except perhaps through the quantification of lung heterogeneity via CoV (347, 349), which is not yet a well-established method. Therefore, the exact threshold between physiological variations and pathology is unclear, but would generally be ~ 2 cm. Thus, the imaging resolution found to be obtainable with ^{19}F imaging here may prove to able to reproduce many of the key uses of HP gas imaging in monitor disease pathology related directly to ventilation, but further study is required.

Through prospective measurement with a ^{19}F 3D phantom it was possible to verify many of the retrospective simulation results. However, the comparison of retrospective simulation results with the ^{19}F 3D phantom images or ^{3}He ventilation imaging showed that the phantom does not act as a perfect representation and is missing some structural variation. In future, it would be best to include the smallest features in the 3D printing rather than median filtering the initial imaging and attempting to include structural detail with the addition of tubing as an ad hoc solution. On the other hand, many of the key results were replicated: the optimal imaging AF was typically only AF=2 and reconstruction with the NCGD algorithm was generally slightly better than the IST method, but dependent on weighting parameters. Although not explored here it future work may attempt to implement the NCGD algorithm without free-parameters to determine if the same level of reconstruction accuracy may be maintained. Through prospective imaging it was also possible to see that an average of the images resulting from both reconstruction methods results can result in a more consistent reconstruction, since in some cases the combined average performed better than the NCGD algorithm alone.

Previously, the methods of either acquiring as much data as possible under noisy conditions or averaging identical measurements to improve SNR was investigated, showing that theoretically it should be preferable to acquire more independent measurements (350). However, from the evaluation of CoV and RMSE under different AFs (with greater averaging relative to fully sampled) it appears that there is a range of SNR where increasing AF to allow for averaging is better than additional sampling of noisy data. In this study, reconstruction from less sparsely spread data (closely representing an elliptical shutter) did not differ significantly in MSE from data acquired with greater sparsity and the same AF. This indicates that the resolution being investigated may be larger than the scale of variation present in typical lung ventilation images and the use of an elliptical shutter may result in equivalent performance. This is also strongly corroborated by the finding that the optimal AF was typically 2, while the ideal nominal image resolution continued to decrease.

In the ^{19}F in-vivo ventilation imaging with multi-element arrays there was no explicit use of the coil sensitivities in the reconstruction algorithms used. Algorithms have been developed that combine methods of sparse sampling and k-space based parallel imaging (49), or including image domain based as well (50, 333), to reconstruct sparsely sampled data. However, here the fact that the data acquired from the individual elements is sparser in the image domain does help in the final reconstruction, while also reducing the effect of the undersampling based aliasing in the final zero-filled reconstruction since the noise does not add coherently. However, in future work comparison to these additional algorithms is necessary.

With the multiple algorithms for reconstructing sparsely incoherently sampled data available (48, 331-335, 339, 340, 351) there is still no clear best method for every MR imaging application. Additionally, often the differences between reconstruction accuracy with different methods can be small. In some cases, compared to a simple low-resolution alternative with equal imaging time the improvement may be insignificant (322), especially if the spatial variation in the image is inherently low. In-vivo measurements performed here showed that compared to low-resolution imaging performed, the SNR was enhanced, with no visual blurring. Additionally, there was not a significant visual difference in reconstructions performed with the two methods here, which may be due to the use of a receive array which masked the impact of incoherent noise added from sparse sampling. There is a reasonable case to be made that the use of the IST method, or any other parameter-free method, is preferable for ^{19}F imaging as no fully sampled in-vivo image can be obtained for optimization of the imaging parameters. Here an average of both techniques also appears to provide the potential benefit of better reconstruction with the NCGD algorithm, while avoiding some of the risk in

highly suboptimal weighting coefficients leading to over-regularization with the NCGD algorithm. The retrospective simulations of SNR presented here assumes that the target nucleus is TP, but for HP gases the loss of longitudinal magnetization with RF encoding step can be partially retrieved by the use of higher AFs with a higher associated FA thereby increasing the effective SNR per unit time (33).

Since the ^{19}F C$_3$F$_8$ imaging is now being performed with multi-element arrays a comparison must be made in the performance of the algorithms tested here to those that explicitly include coil sensitivity in the reconstruction (eg. L$_1$ SPIRiT). In order to perform the same analysis multi-element images must then be obtained with HP gas imaging to similarly perform retrospective analysis on. Similarly, prospective imaging using a phantom for fluorinated gas imaging may be used with a multi-element array to verify the retrospective analysis. Finally, the results presented here show the optimal AF and nominal resolution based on the expected SNR (an AF of 2-3 and nominal sampling resolution of 64x50x24 found here for the SNR obtained here). Therefore, imaging with these parameters may be carried out with a set of volunteers with different lung pathologies and compared to fully-sampled and similarly undersampled HP gas images.

7.7 Conclusion

Through retrospective simulation and prospective imaging incoherent sparse sampling was found to potentially provide some benefit to ^{19}F ventilation imaging. Two different reconstruction algorithms were compared, IST and NLCG, and it was found that the NLCG algorithm generally provides higher reconstruction accuracy, but only if the weighting parameters are optimal. An optimal imaging resolution and AF for ^{19}F imaging was determined for different levels of expected SNR, with a range specified based on the difference in polarization and MR imaging parameters compared to the gold standard of HP gas imaging. Experimental verification through prospective imaging with 3D printed lung phantoms and in-vivo images provided validation for the results obtained through simulation. For the purpose of ^{19}F lung ventilation imaging only a modest amount of undersampling appears to warranted. Furthermore, it appears that an appropriate choice of image resolution is more crucial than reconstruction method for accurately representing the fully-sampled image under conditions of lower SNR.

Chapter 8: Parametric mapping of ^{19}F C_3F_8 ADC, T_2^*, T_1 and lung ventilation in the Lungs of Healthy Volunteers at 1.5T and 3T Benchmarked with ^{129}Xe MRI [6]

8.1 Overview

Purpose: To optimize methods of ^{19}F C_3F_8 in-vivo lung MR parameter mapping at 1.5T and 3T and determine representative normal values and typical variation among healthy individuals.

Methods: Imaging parameters were determined, and breathing protocols were developed, for the mapping of the apparent diffusion coefficient (ADC), and T_1 at 1.5T and fractional ventilation (FV), T_1 and T_2^* at 3T. In addition, ^{19}F C_3F_8 values of ADC were compared with those obtained with ^{129}Xe at 1.5T in the same subjects. The evaluation of percent ventilated volume (%VV) was carried out using anatomical and ventilation images from the subjects, with C_3F_8 imaging performed at 1.5T and 3T and ^{129}Xe imaging at 1.5 T, to evaluate sources of discrepancy between the methods in evaluating the commonly used metric. Six healthy volunteers were recruited and imaged.

Results: A demonstrated increase in ADC between lung inflation levels of FRC and TLC of a factor of 1.22 and 1.36 was found in ADC mapping with ^{19}F C_3F_8 and ^{129}Xe, respectively. In measuring %VV a slightly reduced value was found when imaging ^{19}F at 3T when compared to ^{19}F or ^{129}Xe at 1.5T, which is attributed to reduced signal in the anterior portion of the lungs with the transceive birdcage coil used. The values of ^{19}F C_3F_8 T_1 obtained in healthy volunteers at 1.5T and 3T were generally within the expected range, though a large variation relative to the mean was observed, as well as a strong sensitivity to the accuracy of prescribed FA indicating some measurement dependence. T_2^* was demonstrated to be shorter with lower lung inflation levels. In addition, variation of the mean T_2^* between individuals was found, but with a similar % variance and distribution between subjects. The measurement of FV was found to be repeatable between volunteers and higher in the posterior and peripheral region of the lungs.

Conclusion: In this feasibility study, values of physiologically relevant MR parameters were established for C_3F_8 in-vivo ventilation imaging. In future work a greater number of volunteers

---

will be recruited to improve the reliability of results and comparison will be made to the same mapping performed in volunteers with known respiratory conditions.

8.2 **Introduction**

Currently, fluorinated gas human in-vivo lung imaging is not as well characterized as HP gas imaging, due to the greater research interest in HP gas because of higher attainable image quality and unique properties of the noble gases ([3]He is more diffuse (39), while [129]Xe dissolves into the blood-stream and can be further imaged/characterized (352)). Additionally, the relative lateness of fluorinated gas imaging being performed in humans compared to HP gas (2008 (120) versus 1994 (71)) has resulted in relative paucity in the literature. Thus, there have already been a number of longitudinal and clinical studies performed with HP gases (88, 129, 348, 353). In addition, typical values of MR measureable parameters for gas phase [3]He and [129]Xe have been characterized in-vivo, such as T_2^* (87, 129, 319, 354), T_1 (355), T_2 (125), ADC (39, 87, 139, 356-358) and the SNR and image quality obtainable for set imaging parameters (34, 36, 134, 142, 359). Also, models have been developed to further detail the complicated nature of the diffusion within the lungs (139, 142, 357).

For fluorinated gas imaging (focussed on C_3F_8 in this thesis) to follow a similar progression as HP gas imaging the typical values and range of in-vivo MR parameters must be similarly determined (98, 245, 360). Additionally, reproducible methods of mapping need to be outlined in a coherent way that allows them to be repeated at multiple sites (361). Consequently, this chapter details the imaging and characterization of T_2^*, ADC, T_1, %VV, fractional ventilation (FV) and typical values of SNR with ^{19}F imaging of 79% C_3F_8+21% O_2 in healthy volunteers at 1.5T and 3 T. In addition, the values of SNR, %VV and change in ADC between FRC and TLC obtained are compared to those obtained with [129]Xe imaging.

The two quantitative measures of lung function, %VV and the coefficient of variation of signal intensity (CoV) (347), have previously been derived from inhaled HP gases lung ventilation imaging. The inherently low MR signal and short T_2^* of fluorinated gases results in lower signal-to-noise ratio (SNR) and necessitates lower image resolution compared to HP gas imaging, so it is unknown if the same metrics obtained with fluorinated gas imaging can have the same utility. Recently, there has been significant improvements in sequence optimization for fluorinated gas imaging using ultrashort echo time and steady state free precession methods (98, 251). However, to date, there has been no clear demonstration that fluorinated gas imaging can be used routinely to provide suitably robust quantitative measures of lung function. Thus,

the derivation of the two metrics obtained with ^{19}F C$_3$F$_8$ imaging is compared to those obtained imaging with HP ^{129}Xe in healthy volunteers.

The T$_2^*$ relaxation parameter has been shown to depend on physiological changes in different tissues/organs with ^{1}H MRI (6, 361, 362). For example, in ^{1}H imaging of brain tissue, T$_2^*$ has been shown to correlate with physiological difference between healthy individuals and from disease-related differences (363). Previously, with HP gases no definite correlation between T$_2^*$ and lung physiology has been shown, though decreases around vessels and the diaphragm where perfusion is greatest has been demonstrated (87, 319, 354). Unlike HP gases, fluorinated gases more fully saturate the lungs and the T$_2^*$ of HP gases is expected to be more influenced by the presence of paramagnetic oxygen (319, 354). Additionally, the in-vivo T$_2^*$ of C$_3$F$_8$ has been found to be vastly different from that within phantoms (135), further indicating that it may be a sensitive marker of lung microstructure. Therefore, in this study T$_2^*$ is mapped in healthy volunteers to evaluate the range of values in the lungs and variation at different inflation levels.

For fluorinated gas imaging T$_1$ is predicted to correlate with V/Q since the partial pressure of other gases is the dominant factor affecting T$_1$ (118, 318). In previous research with fluorinated gases T$_1$ mapping has been linked to the concentration of O$_2$ in the lungs with C$_4$F$_{10}$ (318) or with C$_3$F$_8$ (60). However, if the variation within the lungs is greater than the change expected from variations in partial pressure, or the SNR is too low, a reliable method of V/Q mapping may prove difficult to implement. Currently, the variation of T$_1$ between individuals for C$_3$F$_8$+O$_2$ mixed in the lungs is not known. Therefore, in this work the T$_1$ at full lung saturation in healthy volunteers was characterized.

Through multiple studies it has been established that in progressive stages of emphysema and COPD the measured ADC can increase by a factor of 2-4 compared to healthy lungs. In addition, the distribution of ADC and effective mean diffusion length scale (L_{m_d}) measured through multiple b-value imaging have been shown to be heterogeneous in diseased lungs (141). Studies with both HP ^{3}He and ^{129}Xe imaging have shown that comparable results are obtained with diffusion imaging (142).

There are also changes in diffusion parameters that occur naturally due to affects such as posture and the physiological makeup of healthy lungs. For example, in healthy volunteers a 22% decrease in the mean ADC with ^{129}Xe imaging was found moving from the anterior to posterior of the lungs in healthy volunteers, which was not observed in volunteers with COPD (81). Furthermore, a decrease of 24% in the superior-inferior direction was also found, which

was potentially attributed to regional differences in ^{129}Xe concentration, since the partial pressure of gases greatly affects the diffusivity, and in a single breath the inhaled ^{129}Xe gas may not fully mix in the lungs. In previous works a similar gradient in ADC has been observed in the anterior/posterior direction as well as the craniocaudal direction (although <15% in the superior inferior direction) (143, 144), which changes depending on the posture during imaging. Also, regions of the lung next to the heart experience compression (145), which result in regional changes in ADC that can be observed in HP gas diffusion imaging. Furthermore, lung inflation has a similar effect on mean ADC values, while at TLC the anterior-posterior gradient is no longer observable (95). The changes in ADC observed with posture are smaller than those observed with disease. Therefore, by replicating the results of previous studies measuring the dependence of ADC on lung inflation and physiological distribution in healthy volunteers with ^{19}F C_3F_8 imaging the feasibility of detecting changes in diseased lungs may be extrapolated.

Currently, ADC mapping with C_3F_8 has not been performed reliably in-vivo. Utilizing improvements in receiver design, optimized imaging parameters and breathing manoeuvre 3D in-vivo ADC mapping was found to be feasible with a greater resolution than previously attempted. Thus, to determine the sensitivity of measuring ADC with C_3F_8 the differences obtained at either FRC or TLC, which has previously been shown to be significant with HP ^{3}He (95), was investigated in six healthy volunteers

In contrast to HP gas imaging ventilation mapping is possible without compensating for signal decay from RF magnetization destruction and MR relaxation as in HP(59, 364). Fractional ventilation mapping with C_3F_8 has previously been performed in-vivo in rats (131) and in humans (123). Here a modified breathing manoeuvre is employed so that FV is mapped at the lung inflation level of TLC in healthy volunteers to show the feasibility of performing the same in a future larger cohort of volunteers.

It is hoped that the resulting data obtained and methods outlined in this chapter for mapping the physiologically related parameters in healthy volunteers (T_2^*, ADC, T_1, %VV, FV) will provide a benchmark for future study in healthy and diseased lungs.

8.3 Methods

In total, 6 volunteer subjects (S1-S6) were images in a number of sessions following informed consent using a protocol approved by the UK National research ethics committee.

8.3.1 RF Coils

For ^{1}H and ^{19}F imaging performed at 3T (Philips Ingenia) an elliptical transmit/receive quadrature birdcage coil (Rapid Biomedical) was used, while imaging at 1.5T (GE HDx) was performed primarily with an 8-element transceiver vest coil (365), in most cases modified to include an additional 6 receive-only elements [Chapter 4], for a total of 14 elements. For one volunteer measurement was performed with a 6-element ladder resonator/transceive array hybrid [Chapter 5], because of the improved access provided. ^{129}Xe imaging at 1.5T was performed with a flexible transmit/receive vest coil (CMRS, Brookfield, Wisconsin, USA).

8.4 Imaging Parameters

Table 8-1 lists the various parameters used in the determination of ADC, T_2^*, T_1, FV and %VV with C_3F_8, as well as of ADC and %VV with ^{129}Xe. Details on parameter choice and scan procedures followed are included in following sections.

8.4.1 %VV, CoV and SNR

Discussion of the evaluation/determination and value of %VV from anatomical images registered to ventilation images and segmentation is provided in Chapter 9. During ventilation and proton imaging a 1 L bag of gas was inhaled from FRC to ensure equal lung inflation for ^{19}F imaging at 3T and ^{129}Xe imaging at 1.5 T. For ^{129}Xe imaging the 1L consisted of 400 mL N_2 gas mixed with 600 mL isotopically enriched ^{129}Xe (86%) gas hyperpolarized to a level of 30-40% (366). For ^{19}F, imaging at 1.5T was performed after the volunteer breathed to TLC, since it was determined this was a more reproducible lung inflation level with continual breathing from a Douglas bag. For fluorinated gas imaging 4-breaths were taken of the gas mixture prior to breath-hold to fully saturate the lungs. Each ^{19}F scan was repeated a second time after the volunteer recovered while breathing the fluorinated gas mixture and was then able to repeat the breath-hold manoeuvre, the resulting images were averaged for higher subsequent SNR.

Images were segmented and median CoV calculated as previously described (57). For ^{129}Xe imaging at 1.5T and ^{19}F imaging at 3T CoV maps were generated by subsampling ^{129}Xe images so that the image resolution was equal to the reconstructed ^{19}F image resolution. A 3x3 kernel of 3.125 mm reconstructed pixel resolution (higher than the acquired resolution for both) was used to calculate local CoV for every voxel within the ventilated lung volume. CoV calculation

was not carried out with ^{19}F imaging performed at 1.5T because the inhomogeneous receive field of the transceive array coil would not allow for comparable results to the imaging at 3T.

8.4.2 T$_1$

The following breathing manoeuvre was followed: two deep breaths were taken of the gas mixture to fully saturate the lungs. Then, during a subsequent breath-hold at TLC, three 3D SPGR imaging acquisitions were performed with a long *TR* relative to *T$_1$* and varying RF pulse amplitude (for targeted flip angles of 30º, 60º and 90º). The resulting pixel-wise FA was calculated based on the signal intensity difference according to equation (2-50) (43). The volunteer then recovered while still breathing from the gas mixture and once they felt comfortable to do so they performed another breath-hold during which three 3D SPGR imaging acquisitions were made (that were co-localized with the previous acquisitions), with TR shorter than T$_1$ (TR=5.7 ms at 1.5T and 6.5 ms at 3 T). The resulting pixel intensity variation and previously fitted FA map was used to fit T$_1$ (44). The estimation of T$_1$ using the variable flip angle method was performed according to reference (60), which is described in section 3.3.4.

8.4.3 T$_2$*

T$_2$* mapping was performed at 3T only due to the availability of a multi-echo sequence for multi-nuclear imaging. From multi-echo SPGR acquisition sequences the signal in each voxel for each echo ($S_{n_{echo}}$) was fit according to:

$$S_{n_{echo}} \propto S_1 e^{-\frac{\Delta TE(n_{echo}-1)}{T_2^*}} + c_\sigma \tag{8-1}$$

where ΔTE is the spacing between echos, n_{echo} is the echo number and c_σ is a constant to take into account the background noise in image reconstruction. In one volunteer T$_2$* mapping was performed at the two lung volumes of TLC and RV (see Figure 2-14), while for other volunteers mapping at just TLC was performed.

Table 8-1: Imaging parameters for specific volunteers for the characterization of different MR parameters.

Measurement and volunteers	Sequence	TE (ms)	TR (ms)	BW (±kHz)	Matrix size (pixels^3)	FOV (cm^3)	Prescribed FA (°)	Avg.
				1.5 T				
^{19}F %VV-S1/S4††								
Ventilation	3D SSFP	1.68	3.94	6.94	40x34x24	40x32x24	72	5**
Anatomical	3D SPGR	1.80	3.92	17.9	100x100x32	44x44x32	15	1
^{19}F %VV – S2/S6†††S3†								
Ventilation	3D SSFP	1.92	4.94	5.95	40x34x24	40x32x24	72	4**
Anatomical	3D SPGR	1.96	4.54	17.9	100x100x(28/30)	44x44x28	15	1
^{129}Xe %VV - S1/S2/S3/S4/S6								
Ventilation	3D SSFP	2.2*	6.7	8.06	100x82x(22/24)	40x32x(22/24)	10	1
Anatomical	3D SPGR	0.6*	1.9	83.3	40x40x(22/24)	40x40x(22/24)	5	1
^{19}F T$_1$ - S1/S2/S4/S5/S6†††								
FA mapping	3D SPGR	2.22	35	3.97	32x26x10	40x32x30	27/54/81	1
T$_1$ mapping	3D SPGR	2.22	5.6	3.97	32x26x10	40x32x30	27/54/81	4
^{19}F ADC S1/S2/S4/S5/S6†††S3†								
ADC Mapping (t=2.2 ms, b=1.79 s/cm^2)	3D SPGR	5.87*	10.4	3.01	32x26x10	40x32x30	81	4**
^{129}Xe ADC S1/S2/S4/S5/S6								
ADC Mapping - AF=4 (t=8.5ms, b=12,20,30 s/cm^2)	3D SPGR	14.1	17.4	6.94	64x53x18	40x32x24	3.1	1
				3 T				
^{19}F %VV- S1/S2/S3/S4/S5/S6								
Anatomical	3D SPGR	2.5	5.2	15.9	110x110x43	44x44x32.3	30	1
Ventilation	3D SSFP	3.2	7	6.03	50x42x19	40x33.8x28.5	52	5**
^{19}F T$_2$* - S1/S2/S3/S4/S5/S6								
T$_2$* mapping	3D SPGR	1:1:6	7	23	32x28x13	40x32x29.3	26	12**
Single session Washout FV/T$_2$*/T$_1$ – S1/S2/S3/S5								
FA mapping	3D SPGR	1.9/4.3/6.7	30	3.4	53x22x16	40x33x24	30/60/90	1
T$_1$/T$_2$* mapping	3D SPGR	1.3/2.8/4.3	6.5	11.7	53x22x16	40x33x24	22.5/30/45	4
FV/T$_2$* mapping	3D SPGR	1.3/2.8/4.3	6.5	11.7	27x22x16	40x33x24	45	1

*Partial Fourier encoding (87.5%) † 6-element array ††† 14-element array
** 2 dynamics, for double the number of stated averages †† 8-element array

8.4.4 **Apparent Diffusion Coefficient**

We perform experiments here with the ADC in the linear regime, where $S/V\, L_{diff} < 1$ (detailed are provided more fully in Chapter 2, as well as details on motivation of multi-inflation study). A diffusion time of 2.2 ms and b-value of 17.87 s/cm^2 was used as previously employed in experiments with C_2F_6 in excised lungs (97). To determine the sensitivity of measuring ADC with C_3F_8 the differences obtained at either FRC or TLC was investigated and

compared to the same measurement with ^{129}Xe using a 3D multiple b-value SPGR sequence with compressed sensing (85).

The following breathing manoeuvre was followed: 4 deep breaths were taken of the gas mixture to fully saturate the lungs and a breath-hold was performed at TLC during imaging, after recovery while breathing from the gas mixture the volunteers performed a second breath-hold at TLC once they felt comfortable to do so, the volunteer then recovered again and performed a breath-hold at FRC, then recovered once more and performed another breath-hold at FRC. All breath-holds were 18s and images obtained at the same inflation level were averaged together for increased SNR. A 25L Douglas bag was found to be sufficient for the breathing manoeuvre. According to general guidelines provided in reference (358) the resulting images were thresholded so that only voxels with SNR>15 were used in calculation of ADC.

To evaluate the distribution of ADC value histograms of the ADC values from ^{129}Xe and ^{19}F imaging were plotted for all volunteers at FRC and TLC. Furthermore, similar to the process carried out in references (81, 144) the ADC gradient in the anterior-posterior and superior-inferior directions were calculated by first manually placing the center of the lungs and then plotting the average ADC for each of the slices/pixels relative to the center for all volunteers together.

8.4.5 Fractional Ventilation

The rate of signal decay during the washout phase of imaging was used to evaluate FV according to (58, 131):

$$S(n) = c(1 - FV)^n + c_\sigma \qquad \text{(8-2)}$$

where $S(n)$ is the MR signal, c is a constant related to imaging parameters, n is the breath number, c_σ is a constant to take into account the background noise in image reconstruction and FV is the variable associated with fractional ventilation. Here, T_1 and T_2^* are measured prior to measurement of FV washout.

First, FA and T_1 parameter mapping was carried out at 3T using the same breathing manoeuvres as described earlier. Immediately after, constant dynamic imaging was carried out while the volunteers attempted to repeatedly breath to TLC, remain at that inflation level as long as they felt comfortable, and then breath out to FRC. The first breath to TLC during dynamic imaging was from the Douglas bag containing the fluorinated gas mixture, and subsequent breaths were from room air.

In post-processing the signal in a region that was in an inferior part of the lungs was averaged and the progression of the signal with the dynamic imaging was plotted. The images with highest signal were isolated as part of the individual breaths where the lung inflation level of the volunteers was at TLC. The signal and the resulting images at these isolated time points were averaged for each small breath-hold (about 3-7 seconds each, for 2-4 averages).

For evaluating the FV a Blackman filter was applied to k-space to provide suitably high SNR for fitting (367). Fitting was performed by least-squares via MATLAB (Mathworks, Natick, Massachusetts, USA). Only results with a linear regression correlation coefficient >0.95 are reported. In addition, pixels with SNR<10 were excluded for both FV and T_2^* analysis, while for T_1 and FA mapping SNR<15 were excluded.

8.5 **Results**

8.5.1 **%VV, CoV and SNR**

Figure 8-1 shows ventilation images acquired either with ^{19}F at 1.5T or 3T, and [129]Xe at 1.5 T, overlaid on anatomical images. The resulting %VV for the different cases is displayed above and a Bland-Altman plot of the difference between %VV derived from ^{19}F images at 3T or [129]Xe at 1.5T is shown in Figure 8-2. Compared to ^{19}F images acquired at 3T the %VV is systematically higher for [129]Xe images at 1.5T, as well as for ^{19}F images acquired at 1.5T with receive arrays. Comparison of the representative slices from the healthy volunteers in Figure 8-1 illuminates why a lower %VV was found. At 3T the lower %VV found with ^{19}F, when compared to [129]Xe, appears to be partially due to signal drop-off in the outermost anterior and posterior slices. Overall, fluorinated gas images are blurred due to lower resolution and lower relative signal in the major airways can be observed. For the imaging resolutions used the SNR is similar between all the [129]Xe and ^{19}F images at both field strengths. This is potentially a result of B_1 inhomogeneity as found in FA and sensitivity mapping of the birdcage coil in Chapter 8. The increase in SNR at 1.5T due to use of SSFP imaging and multi-element arrays appears to compensate for the decrease in SNR relative to 3T due to lower polarization/signal.
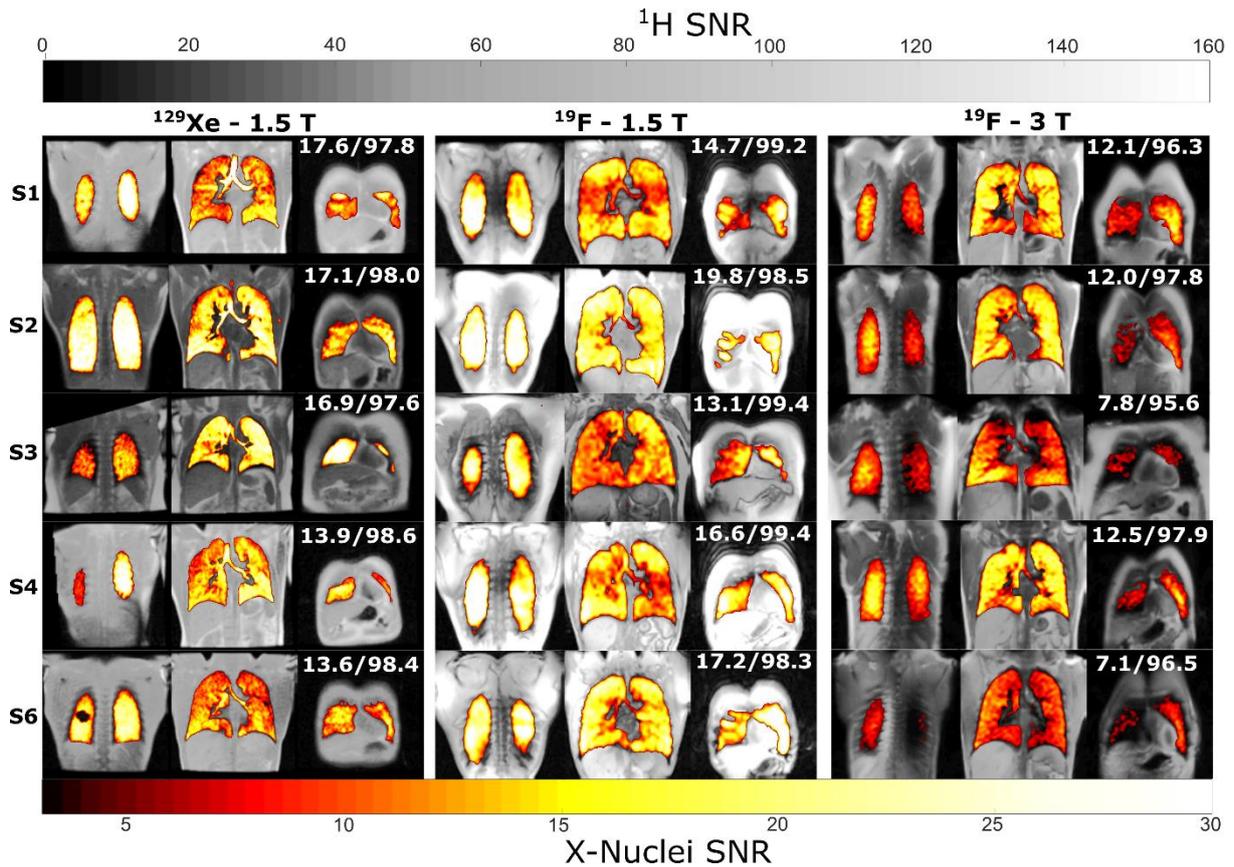
Figure 8-1: Inhaled inert gas ventilation SNR maps for representative coronal slices (^{19}F or ^{129}Xe) overlaid over registered anatomical ^{1}H images with calculated mean SNR within the segmented ventilation images shown next to %VV (SNR/%VV shown above anterior coronal slice).
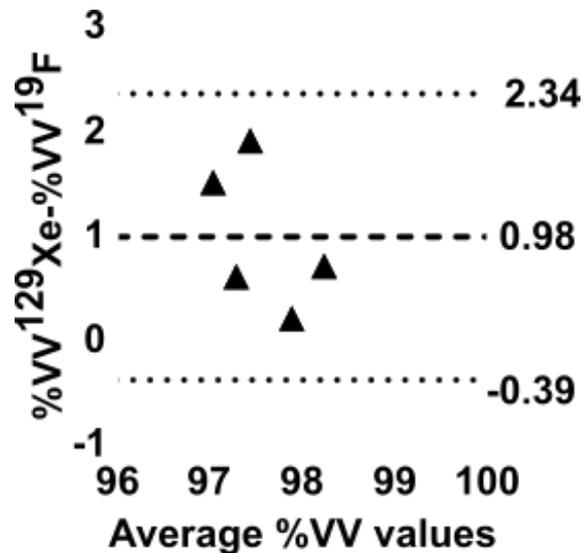
Figure 8-2: Bland-Altman plot of %VV values derived from images.

The results of CoV histogram analysis are displayed in Figure 8-3. In Figure 8-3 the CoV calculated from only a single dynamic image is higher than with two. Therefore, with only one

dynamic image sufficient SNR is not achieved for CoV to be independent of SNR (SNR $> \cong 20$). With the two dynamic images the median CoV is on average 1.6% lower than that calculated from ^{129}Xe MRI. From CoV histograms in Figure 8-3 this change can be clearly observed with the shift of the CoV distribution. This is indicative of the impact of lower sampling resolution resulting in reducing image variation.
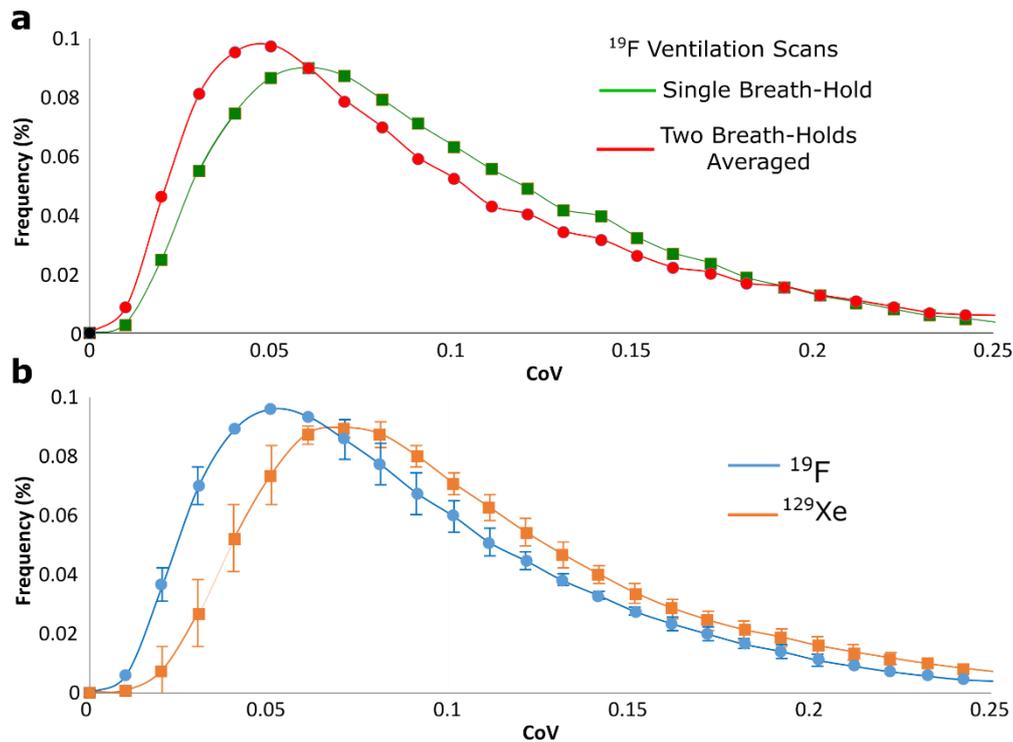
Figure 8-3: a: Mean CoV histogram of volunteers obtained from 3T imaging with ^{19}F using either a single breath-hold dynamic or the average of two. b: The mean CoV histograms of images acquired ^{19}F at 3T or ^{129}Xe imaging at 1.5T with error bars indicating the standard deviation of all volunteers for each histogram bin.

8.5.2 T_1

The resulting FA maps and T_1 maps obtained from volunteers at 1.5T are shown in Figure 8-4. Results from mapping in healthy volunteers at 3T are also shown in Figure 8-6. The SNR of images for FA and T_1 mapping, after filtering and for images acquired for peak FA, was 25-50 throughout the lung at 3T with the use of a birdcage coil and 30-100 at 1.5T with the use of a coil array. The FA homogeneity within the lungs at 1.5T is lower in some cases (but not always) relative to that of the birdcage at 3T, with a consistent drop-off towards the inferior where the coil coverage is potentially lacking. Black areas are regions where SNR<10 in the image with the highest FA, or the fitting was too unreliable due to low achievable FA or poor fitting. The mean T_1 found here in the lungs across volunteers is reasonable considering the

predicted range of T_1 with variation of partial pressure (117), but the standard deviation is significant relative to the mean.
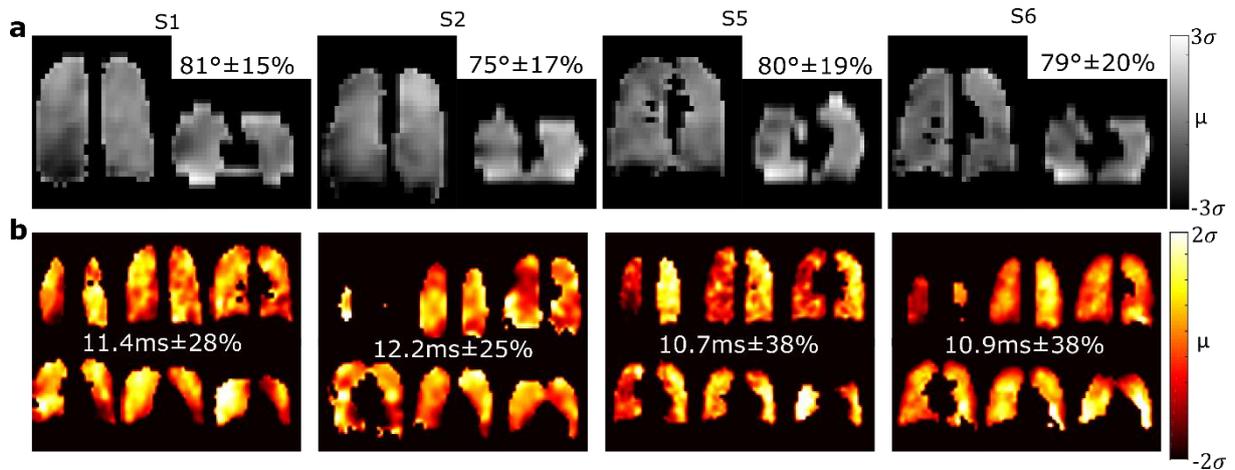
Figure 8-4: a: In-vivo FA maps for a prescribed 90° FA obtained for 4 healthy volunteers at 1.5T with 14-element array and b: co-localized T_1 maps for volunteers.
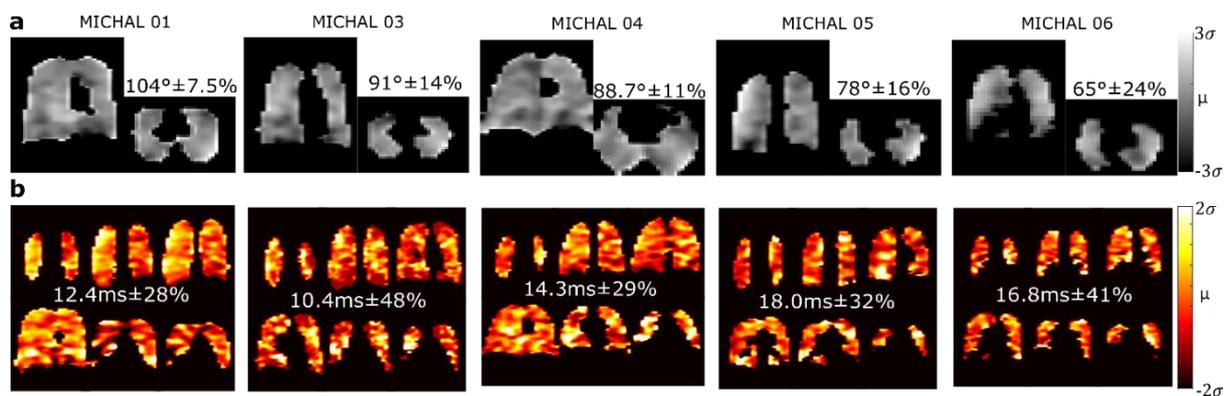
Figure 8-5: a: In-vivo FA maps for a prescribed 90° FA obtained for 4 healthy volunteers with elliptical birdcage at 3T and b: co-localized T_1 maps for volunteers.

8.5.3 T_2^*

Maps of T_2^* in representative slices are shown in Figure 8-6. Results are similar to those presented in Chapter 8, except measured at FRC+1L rather than TLC. It is clear that a decrease in T_2^* is observed around intrapulmonary vessels and the diaphragm where tissue-air magnetic susceptibility gradients are highest. The regional variation in T_2^* is significant, and much lower than that found in phantoms, indicating that it may be sensitive to structural/function changes in the lungs. The demonstrated lower T_2^* at RV compared to FRC+1L in one volunteer further supports this claim.
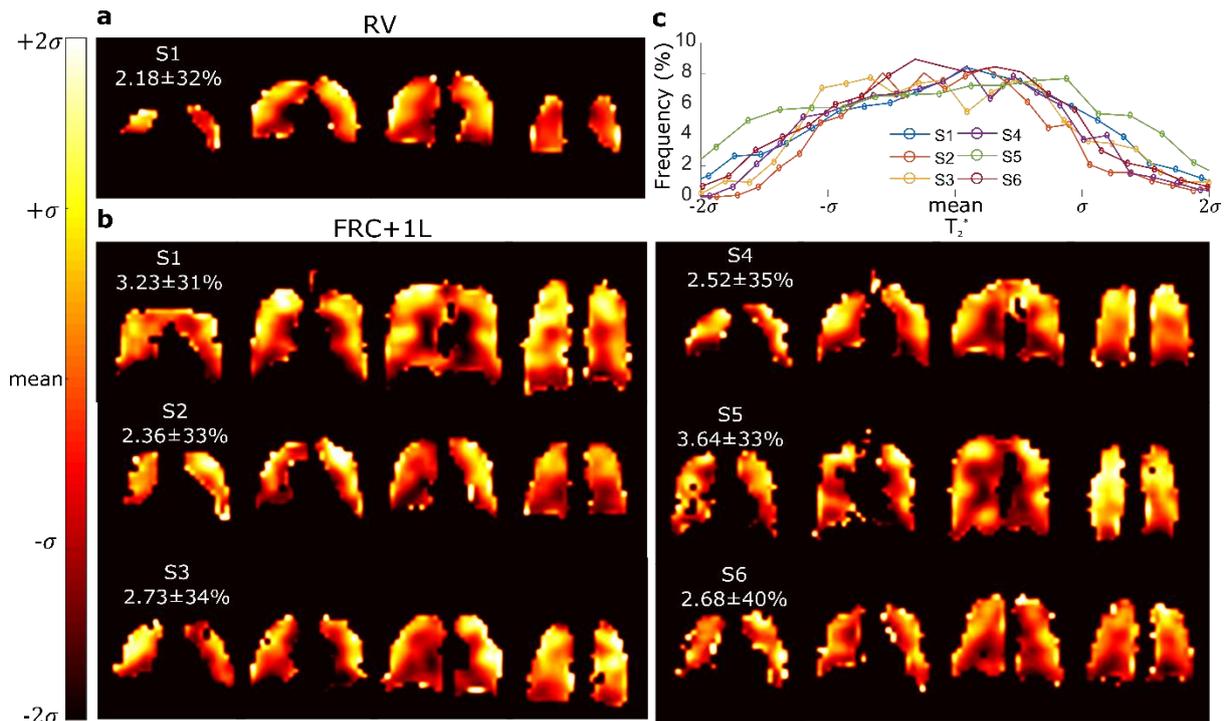
Figure 8-6: T_2^* maps for ^{19}F/C_3F_8 measured at 3T in anterior, central and posterior slices, and the mean and standard deviation within the lungs for each volunteer, a: at RV for one volunteer and b: FRC+1L for all 5 volunteers. Also. the c: histogram line plots for all the volunteers within the lungs normalized to the mean value.

8.5.4 Apparent Diffusion Coefficient

Maps of coronal slices of C_3F_8 ADC with lung inflation levels of FRC and TLC are shown for in Figure 8-7, which can be compared to maps generated with the same volunteers and lung inflations with ^{129}Xe imaging shown in Figure 8-8. For ^{19}F, the SNR found in ADC mapping (averaging from the two breath holds and minor filtering applied to k-space) was SNR > 70 in peripheral slices and lung regions, and SNR ~ 25 in central regions of the lung. Due to the rejection of low SNR regions in mapping ADC (358) there is a consistent exclusion of areas around the major pulmonary vessels and in some regions around the diaphragm of volunteers. This is due to the reduced SNR resulting from the lower T_2^* in these regions, as observed in Figure 8-6, and the long TE required for the ADC mapping sequence. For ^{129}Xe imaging there is a more uniform SNR distribution due to the use of a single volume transceiver, with a typical range of 20-40 in volunteers. For ^{19}F and ^{129}Xe imaging the average in ADC from FRC to TLC was by a factor of 1.22 and 1.36, respectively.

191
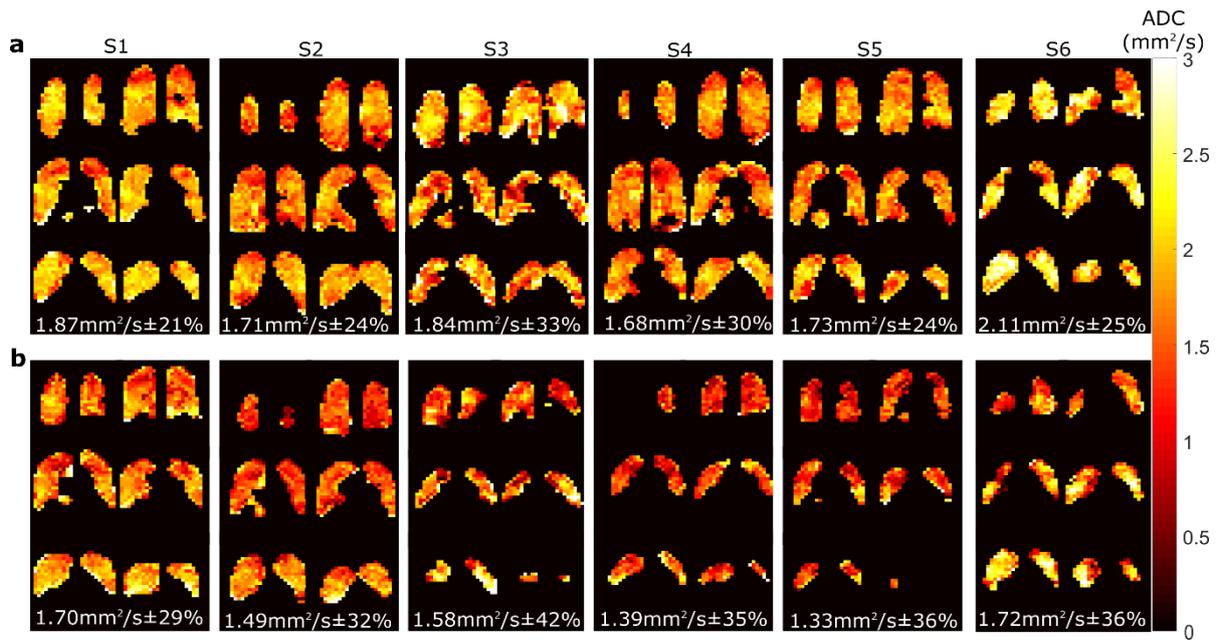
Figure 8-7: [19]F ADC maps in representative slices plotted from posterior to anterior (top to bottom) obtained with 6 healthy volunteers as a: TLC and b: FRC. Global mean values and standard deviation of ADC are displayed below representative slices.
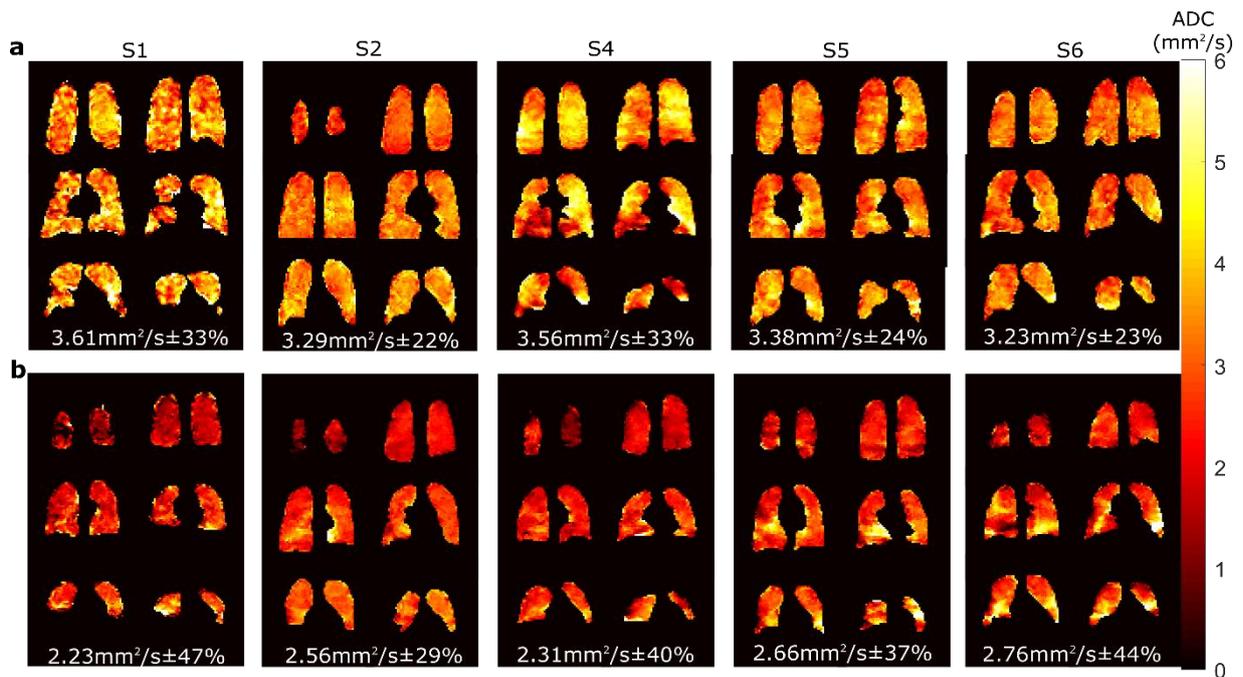
Figure 8-8: [129]Xe ADC maps in representative slices plotted from posterior to anterior (top to bottom) obtained with 5 healthy volunteers at a: TLC and b: FRC. Global mean values and standard deviation of ADC are displayed below representative slices.
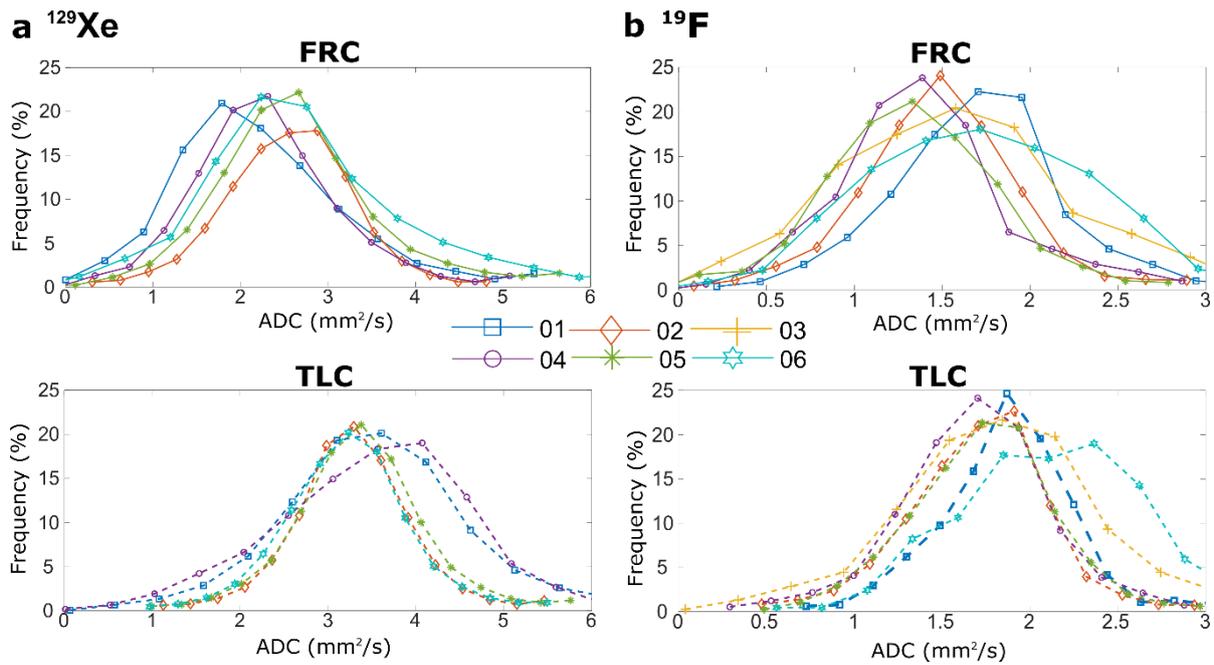
Figure 8-9: Histograms of ADC in healthy volunteers measured at lung inflation levels of FRC and TLC for a:^{129}Xe and b: ^{19}F.

A reduction in the gravitational (posterior-anterior) ADC gradient was observed from FRC to TLC with both gases (Figure 8-10). At FRC, the mean change with all volunteers plotted as described shows a maximum range increase of 107% (1.5→3.1) and 30% (1.38→1.8) increase in ADC in the posterior to anterior direction for ^{19}F and ^{129}Xe, respectively. Furthermore, with both C_3F_8 and ^{129}Xe ADC at TLC the posterior-anterior gradient is no longer discernible, as observed previously with ^{3}He (368). In contrast to previous studies the gradient in ADC in the superior-inferior direction is either not readily observable, or increasing rather than decreasing (144, 369). From the ADC maps in Figure 8-7 and Figure 8-8 it can be seen that that there are a number of regions with higher than average ADC that are near the heart and to the inferior of the lungs, as well as localized regions of lower than average ADC. These regional variations appear to mask any superior-inferior gradient observable with the limited number of volunteers and particular method of plotting the superior-inferior gradient used here.
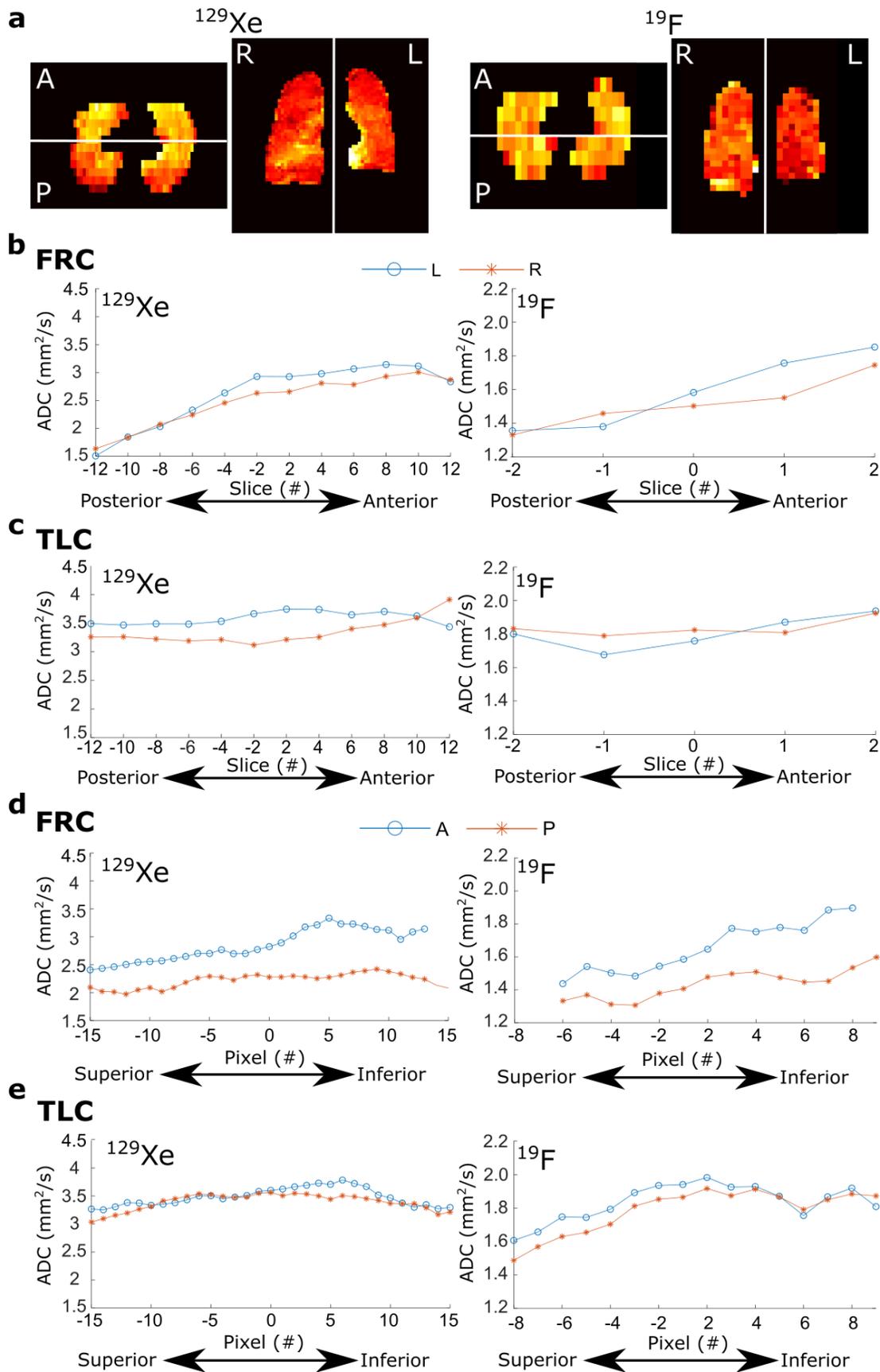
Figure 8-10: a: Labelled segmented regions for performing analysis of anterior-posterior (A-P) and superior-inferior (S-P) gradients in ADC with ^{129}Xe and ^{19}F imaging. The mean ADC in slices moving in the A-P direction is shown for b: FRC and c: TLC for both ^{129}Xe (left) and ^{19}F (right). The mean ADC in pixels moving in the S-I direction relative to the centre is shown for d: FRC and e: TLC as well.

194

8.5.5 Fractional Ventilation

Representative coronal slices of FV maps from healthy volunteers are shown in Figure 8-11a. An increase of FV towards the posterior was observed as well as to the inferior. This is expected as the inferior of the lung towards the diaphragm expands and contracts the most during tidal breathing, and because of the gravitational effect on the distribution of FV (370). This same effect has is well documented with ^{3}He and ^{129}Xe gas MRI (59, 364). With this method of FV mapping it was observed that approximately half of the fluorinated gas is washed out per breath from FRC to TLC, which is expected to be reduced for obstructed lungs. The SNR is fairly consistent across volunteers with a range of 40-50 at the first breath image. The rapid rate of washout found means that signal is typically too low to measure after the second breath (SNR is < 6 after the 3rd image). Figure 8-11b shows T_2^* maps obtained prior to washout from the imaging employed to map T_1.
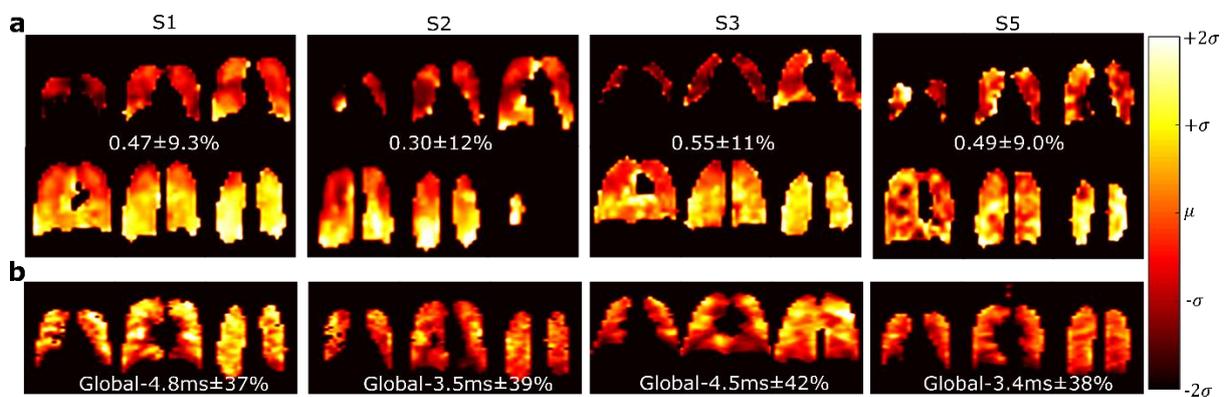
Figure 8-11: a: FV maps of fluorinated gas imaging during washout with labelled mean and standard deviation with lungs. b: Corresponding T_2^* maps in representative slices are shown prior to washout. The scale for the T_2^* maps are normalized to the mean (μ) of the T_2^* in each volunteer.

8.6 Discussion

In this study, for the first time systematic in-vivo mapping of T_1, T_2^* and ADC for C_3F_8 has been presented in a number of healthy volunteers. In addition, methods of mapping FV and %VV have been outlined, as well as comparison of SNR obtained with different imaging parameters and at the two clinically relevant MRI field strengths (3T and 1.5T).

In the evaluation of %VV of healthy volunteers, the systematic bias towards low %VV when imaging with ^{19}F at 3T when compared to ^{129}Xe appears to be primarily due to a combination of coil inhomogeneity and magnetic field inhomogeneity dependent effects leading to signal drop-off in the outermost anterior slices. Therefore, the same systematic bias was not found imaging ^{19}F at 1.5T using coil arrays (6/8/14 elements) for imaging, since high SNR was obtained in the outermost slices due to increased coil sensitivity. Since the %VV is expected

to be typically >97% in healthy volunteers (142, 347), to determine the true clinical viability of ^{19}F imaging for %VV a cohort of patients with respiratory diseases need to be imaged with HP and fluorinated gas imaging to determine the effects of different gas properties, and collateral and FV differences, on the measurement of %VV. This is work ongoing that I am taking forward as part of the LIFT study [Chapter 9]. In comparing CoV for ^{19}F and ^{129}Xe imaging, changes with increasing SNR and increasing imaging resolution were found indicating that the resolution and SNR achievable with ^{19}F imaging are not sufficient to fully represent the spatial variation inherent in lung ventilation as measured by MRI. However, since CoV remained consistent between healthy volunteers ^{19}F imaging may still be sensitive to changes in ventilation heterogeneity, as measured by CoV, which has been demonstrated to occur in different pathologies (371)

Previously, the measurement of ^{19}F gas T_1 in lungs has been performed assuming a uniform FA. Assuming accurate co-registration of images, the variation in FA should not affect the T_1 mapping, while with a highly homogeneous transmit coil the FA mapping step may be excluded. Considering the large variation in T_1 and FA found here it is clear that no compensation for FA inhomogeneity would introduce systematic bias into the voxel-wise measurement of T_1 (60). The relation of T_1 to V/Q presented in (60, 118) would be a valuable application for fluorinated gas imaging, but it is not clear how reliable mapping may be if it relies on imaging with 30% C_3F_8 gas saturation considering the low SNR. Furthermore, considering the large variation in T_1 here it is clear that there are other factors affecting the variation of T_1 throughout the lungs. In future, the application of T_1 mapping with volunteers that have different disease pathologies may demonstrate specific differences relative to healthy volunteers even when the gas fully is fully saturated in the lungs. The method in reference (60) assumed the signal decays only according to washout and changing T_1, but there is also a possible change in T_2^* during washout due to the corresponding change in T_2 and ADC with partial pressure that would need to be compensated for. Nonetheless, as a global measure the proposed method of mapping T_1 during washout may be relatable to V/Q and provide important information.

The only previously published data reporting in-vivo measurement of ADC of C_3F_8 used a t=1ms and b=1.33 s/cm^2, so with the reported mean ADC of 0.023 cm^2/s only a 3% decrease in signal would be expected from equation (2-85) (372). The work presented here shows measured ADC values more commensurate to what is expected physiologically (ADC<0.03 cm^2/s) with high image SNR. In this work, calculated ADC values were found to be consistently lower than the free diffusion coefficient of C_3F_8, demonstrating acinar diffusion

restriction. In addition, clear changes in ADC between FRC and TLC were observed as well as regional differences due to the gravitational gradient. There is a strong indication from this work that ^{19}F C$_3$F$_8$ ADC mapping will be able to detect changes in lung microstructure in different pathologies, since the regional changes due to posture and lung inflation are typically less than those caused by disease. However, future work will require acquiring C$_3$F$_8$ ADC in patients with respiratory diseases to fully evaluate the sensitivity of C$_3$F$_8$ to emphysematous changes in alveolar airspaces.

Direct comparison on the expected difference is difficult, as the ^{129}Xe imaging conditions place it the regime of restricted diffusion, where the length scale is larger than the external airway radii $L_{diff} > R$ and/or $L_{diff} > (S/V)^{-1}$. However, considering the longer diffusion time available to be used with longer T$_2^*$, and free diffusion coefficient D_0, the ADC of ^{129}Xe should show a greater change with variations in lung microstructure, characterized by S/V. This proportional difference was observed with the shift in the mean and median of histograms in Figure 8-9 that occurs for both ^{129}Xe and C$_3$F$_8$ in the case of FRC compared to TLC lung inflation. The shift is greater for ^{129}Xe imaging, as well as the relative difference between ADC in the anterior and posterior portions of the lungs. In future work it will be necessary to ensure consistent saturation of the fluorinated gas mixture as the partial pressure strongly influences the free diffusion coefficient (approximately D$_0$=0.23-0.77cm^2/s for 100%-0% partial pressure with O$_2$ (117)). In this study full saturation with the gas mixture at 79% PFP / 21% O$_2$ was maintained for ADC mapping (D$_0 \approx$0.027cm^2/s), which may be the most reproducible method of ADC mapping with C$_3$F$_8$.

The mean T$_2^*$ of PFP in lungs of volunteers with full saturation of the gas was found to be higher than previously reported (126), but previous measurement was likely performed as a global spectroscopic measurement rather than pixlewise and also with less than full saturation of the gas mixture. Significant variations in the mean T$_2^*$ was found between different volunteers, but the distribution of values in the lung normalized to this mean was consistent (Figure 8-6). In this study changes in the T$_2^*$ were found based on the level of gas saturation (Figure 8-11) and inflation level, but it is not known if this is enough to explain differences between measurements with different volunteers. Factors such as total lung volume, anatomical differences in susceptibility gradients and normal variations in alveolar dimensions within the population (373) may explain the variation of T$_2^*$, which for fluorinated gases is predicted to be primarily dependent on the susceptibility effects from the inhomogeneity of the tissue interfaces (differences in the bulk magnetic susceptibility (374) at the air tissue interfaces of

alveoli (375)). Therefore, it is expected that differences in age (376), or different disease pathologies like asthma (347, 377), may show correlation with changes in T_2^*. Similar mapping performed at 1.5T would ascertain definitively whether ^{19}F imaging at 1.5T is preferable to that at 3T, since as a much longer T_2^* at 1.5T, as expected based on results with HP gases (378), would demonstrate that similar SNR could be obtained with reduced SAR constraints, even using SPGR imaging rather than SSFP imaging as has been demonstrated previously (135) .

In measuring FV in this study the time to washout is shorter here than in (123) due to the different breathing manoeuvre employed. In the analysis presented here, and other studies (58, 123), it was assumed each breath is identical, which is reasonable based on the repeatability of the breathing manoeuvre employed and from previous results that matched the results of performing HP gas ventilation imaging along with pneumotachograph measurement (364). Any study involving fluorinated gas imaging in the future should include a method of FV mapping as it may prove to be the most relevant and easily reproducible and quantifiable metric obtained with fluorinated gas imaging.

8.7   Conclusion

The work presented in this chapter is preliminary work in the establishment of expected values of typical lung imaging parameters measured through MRI with C_3F_8 lung imaging: T_1, T_2^*, SNR, ADC, FV and %VV in healthy volunteers. For T_1, %VV, T_2^*, and ADC there has not previously been in-vivo regional mapping presented of comparable quality due to the higher SNR achieved with the optimization of imaging and coil design developed in this thesis. In addition, with %VV and ADC comparison to ^{129}Xe imaging explored the extent that %VV can be comparably measured with ^{19}F imaging in healthy volunteers despite the lower resolution. Also, while the percent change in ADC with lung inflation level is lower with ^{19}F changes due to variation in lung physiology are clearly detectable, indicating sensitivity to change in acinar airways dimensions.

Chapter 9: Optimization of ^{1}H and ^{19}F Imaging at 3T and Post-Processing for the Evaluation of %VV[7]

9.1 Overview

Purpose: To develop and implement a repeatable and reliable scan protocol for ^{19}F imaging of lung ventilation properties at 3T.

Methods: In the first phase of the study MRI scan protocol methods were optimized. In the second phase the reproducibility of SNR and %VV between volunteers was analysed. A single transceive birdcage coil was used for ^{19}F and ^{1}H imaging, so tests were performed to characterize the receive and transmit performance of the coil at both Larmor frequencies. Then scan parameters were varied for single breath-hold anatomical and ^{19}F ventilation scans in 14 healthy volunteers to optimize SNR and contrast. Scanning was then performed in 18 healthy volunteers to evaluate reproducibility. Methods of segmentation and image registration of anatomical and ventilation scans were evaluated and implemented.

Results: The birdcage coil used for images was found to have reasonable transmit homogeneity and matching at the ^{19}F frequency, but to be greatly mismatched with inhomogeneous transmit efficiency and receive sensitivity at the ^{1}H frequency. With the use of rapid low flip angle 3D multi-echo SPGR imaging SNRs of ~60 and ~14 for ^{1}H anatomical ($3x3x6mm^3$ resolution) and ^{19}F ventilation imaging ($10x10x10mm^3$ resolution) was found to be obtainable. An SNR of ~25 was obtained with ^{1}H 2D SPGR interleaved slice imaging ($4x4x10mm^3$ resolution), which greater visual contrast between lung cavity and the rest of body tissue. In images from healthy volunteers image registration was able to compensate for variations in lung inflation and volunteer movement during image so that the %VV was consistently >97%. For healthy volunteers measurements of %VV lower than 97% were found to be caused by regions of signal drop-off and low SNR, causing regions not easily distinguishable from defects. The mean SNR was greater than 8 in ventilation images for 13 of the 18 volunteers. The mean SNR showed high intersubject variability, but low intrasubject variability between ventilation scans.

Conclusion: The consistency of results with ^{19}F C_3F_8 ventilation imaging was established for healthy volunteers. In the future ventilation and anatomical images acquired in patients with known respiratory conditions will be compared.

---

[7] All analysis on data were carried and described in the written manuscript by AMM. For part of imaging performed in phase 1 scanning was performed by AMM. For imaging performed in the the later half of phase 1 and all of phase 2 of the LIFT imaging scanning was performed by the radiographic team at the University of Sheffield (Julia Bigley, Charlotte Oram), while Matt Austin perfomed gas administration in one scan session, AMM performed gas adminsistration in others. Manuscript revisions performed with JMW and AMM.

9.2 **Introduction**

Ventilation MRI imaging with inert gases is a valuable tool for assessing and monitoring lung disease pathology (106, 124, 353). Hyperpolarized (HP) gas imaging (with ^{3}He and ^{129}Xe) has become a well-established method for ventilation imaging, with numerous studies demonstrating the assessment of %VV for different pathologies (57, 142, 379, 380), and its correlation with common global measures of lung function through spirometry FEV_1 and FVC (142, 381)). Typically, the %VV for healthy volunteers is >97%, while for patients with COPD or other lung disease pathologies the %VV is less than 85% (142).

The regional information provided by ventilation imaging has also proven to be relevant in pathologies such as asthma. For asthmatic patients with moderate severity %VV may be nearly normal, but "patchiness" is observed and the heterogeneity of the gas distribution as measured by MR may correlate more closely with lung function (347-349, 371, 377). Also, spirometry gives no anatomical information, which is readily provided in MR imaging and spirometry alone also only provides information about global lung function that does not necessarily correlate well with patient symptoms or survival (382). In addition, the regional information from ventilation imaging can be important clinically for procedures such as lung volume reduction surgery (383), endobronchial valve placement (384) and radiation therapy planning for lungs cancer to avoid regions of functional ventilation (359).

Currently, the modality of ^{19}F ventilation imaging has not been developed/quantified to the same extent in such applications because of its inherently lower signal. However, compared to HP imaging fluorinated gas imaging does not have the same requirements of initial infrastructure investment for HP equipment, expertise and expense. Consequently, if ^{19}F ventilation imaging was demonstrated to be of sufficiently quality it may be prove valuable as a pre-screening measure at sites that have ^{19}F imaging capabilities for less numerous sites with HP gas capabilities, or even as a replacement in specific instances. Also, in ^{19}F imaging gas moves into area that are initially not ventilated since multiple breathes are taken of the gas mixture to fully saturate the lungs (collateral or delayed ventilation (344)), so ^{19}F imaging may also operate as a complementary method that provides additional functional information compared to HP gas imaging.

Therefore, establishing if the lower-resolution imaging of ^{19}F C_3F_8 imaging can reliably and reproducibly measure the %VV in healthy and diseased volunteers is the objective of the Lung magnetic resonance Imaging of Fluorocarbon Tracer gases (LIFT) study, which is a collaboration between groups at Newcastle and Sheffield University. The work presented in

this chapter is a description of the methodology and results of the LIFT study carried out at the University of Sheffield site thus far. The LIFT project is separated into three phases: MRI scan protocol development, reproducibility of ventilation measurements, and comparison of lung function measurements between patients with asthma, COPD and healthy volunteers. This chapter provides an overview of the first two phases, with the second phase currently underway.

A unique challenge for ^{19}F imaging is the relative closeness of the Larmor frequencies of ^{1}H and ^{19}F nuclei: 128 and 120 MHz at 3T, respectively. Consequently, it is an engineering challenge to develop a coil that is either sufficiently detuned during ^{1}H body coil transmission/reception, is dual-tuned without compromising sensitivity at either nuclei, or incorporates multiple single-tuned coils that are decoupled while providing both homogeneous transmission and high receive sensitivity. It is also essential for the coil to follow ethical research guidelines for safety regarding SAR and be certified by the appropriate regulatory bodies to be used. In this study a single-tuned volume transceive coil was used for both ^{19}F and ^{1}H imaging, with compromised performance at the ^{1}H frequency. As a result, quantification of the coils transmit/receive properties was an important first step prior to imaging parameter. In addition, imaging parameters were limited due to the SAR properties of the coil at 3T, and the resulting effect on sequence optimization are detailed.

Optimization of ^{1}H anatomical imaging was carried out with the objectives of 1) maximizing SNR, 2) use of robust scan parameters insensitive to motion, FA inhomogeneity and artefacts, and 3) providing clearly defined lung/tissue/defect boundaries for easy registration and segmentation. For the ability to accurately and repeatable segment lung images SNR and resolution are important and related factors. The FA was varied in in-vivo 3D imaging to determine the optimal mean considering the inhomogeneity present in the coils transmit field. A multi-echo 3D imaging sequence was tested and predicted to provide some benefits over single echo imaging in terms of maximizing signal-to-noise (SNR) of lower T_2^* tissues, while increasing the contrast between lung and non-lung regions. Also, 2D interleaved slice select imaging was also tested to provide better/different contrast between tissue interfaces.

In ^{19}F imaging, the B_1/B_0 inhomogeneity and SAR was found limit the parameters and sequence choice to just SPGR/GRE imaging with a lower than optimal choice of prescribed FA for the T_1 of C_3F_8. However, for regions where the prescribed FA and actual FA match the SNR compared to optimum should be $\approx$ 90%. Multi-echo imaging was tested for ventilation imaging as a strategy to maximize the acquisition time for each TR. T_2^* mapping derived from multi-echo imaging demonstrated that there are regions around intrapulmonary blood vessels

and near the inferior portions of the lungs that T_2^* is significantly lower than the mean (<1 ms). Since these are areas where the highest SNR is desired for segmentation the use of sum-of-squares reconstruction multi-echo images, despite the additional post-processing step.

The steps take in segmenting images for %VV calculation are shown in Figure 9-1. Registration of ventilation and anatomical data is a critical step in the calculation of %VV since acquisition of ventilation/structural images are acquired in a separate breath-hold. The inflation level and body positioning may change significantly between scans, especially over the period of a 40-minute scan session. In previous comparisons of same breath and separate breath HP and ^{1}H imaging (321) mis-registration of the separate breath images is obvious. Therefore, affine image registration using mutual information was carried out to transform anatomical images (385). Interpolation is particularly problematic with ^{19}F imaging compared to HP since the imaging resolution is significantly lower than in HP gas imaging. Subsequently, the interpolation may cause a blurring effect reducing size of defects and expanding the borders of apparent lung ventilation.
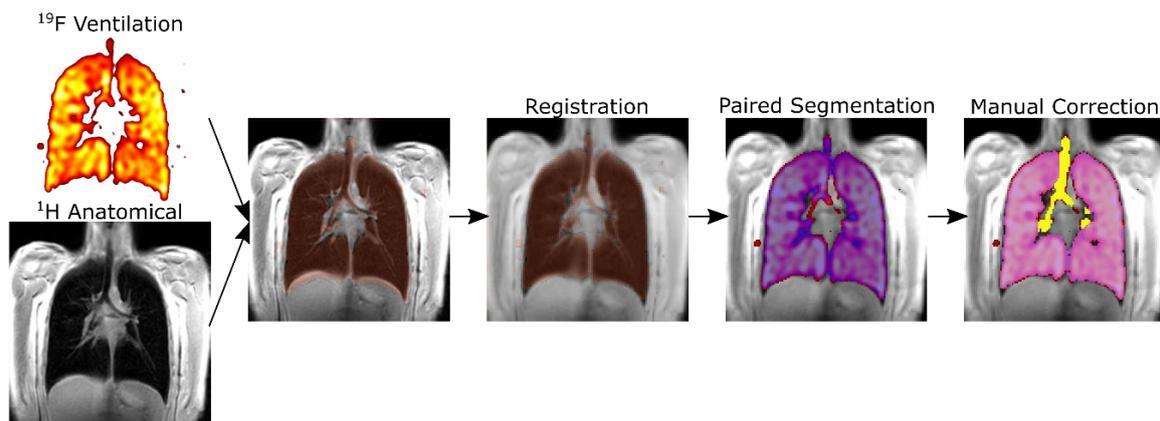
Figure 9-1: Flow chart demonstrating the process carried out for calculation of %VV from combined ventilation and anatomical imaging.

Segmentation methods can be paired or unpaired, and based on different algorithms: clustering, thresholding, region classification based methods, with additional methods of bilateral filtering (57, 61, 379, 384, 386). With this study segmentation is performed with a GUI based method developed within the POLARIS group (57). Here, %VV was >95% in healthy volunteers, except for cases where reductions in analysed %VV arose due to low SNR in the outer anterior and posterior slices and some variation between inflation level in anatomical vs. ventilation scans. It is not yet clear how analysis will be in patient data, but the analysis performed so far has shown that the %VV assessment in healthy volunteers can be reproducible with SNR histograms and inflation level measured by TLC remaining consistent, depending on volunteer compliance with breathing instructions.

9.3 Methods

9.3.1 Coil Characterization

To determine the relative sensitivity and FA homogeneity of the two coils imaging was performed with varying values of prescribed FA. The image SNR and actual FA is then fit to equation (2-50). The imaging sequence parameters followed are in Table 9-1. For in-vivo and phantom ^{1}H imaging The T_1 value used in fitting for ^{1}H imaging was assumed to be much smaller than the TR value used (1500 ms and 400 ms, respectively) and in-vivo imaging is performed while volunteer breathed as shallowly as possible. In-vivo ^{19}F imaging FA parameter variation series was performed in a single breath hold.

Table 9-1: Sequence parameters used for ^{19}F and ^{1}H FA mapping in torso phantom and in-vivo. Fitting of the resulting signal was performed pixelwise according to equation (1).

	Sequence	TE (ms)	TR (ms)	BW (Hz)	Resolution (mm^3)	FOV (cm^3)	Target FA (°)	Avg.
Phantom Imaging								
^{1}H	2D Coronal SPGR	2.6	400	1021	6x6x10	44x36.7x26	30/60/90	1
^{19}F	2D Coronal SPGR	2.9	200	500	12x12x10	44x34.2x26	22.5/45/67.5/90	10
In-vivo Imaging (MICHAL 05)								
^{1}H	2D Coronal SPGR	2.4	1500	1020	6.25x6.4x7.5	40x37.5x29	30/60/90	1
^{19}F	3D Coronal SPGR	1.8	30	250	12.5x12.5x30	40x30x24	30/60/90	1

9.3.2 Scan Protocol Development

Table 9-2 includes the sequences and imaging parameters used for in-vivo imaging experiments for the protocol development phase (labelled S1, with volunteers actually imaged with subject numbers 01,03,04,07-10,12,13,16,17) of the LIFT study at the Sheffield site, as well as the final protocol used in reproducibility analysis in the second phase (labelled S2, with volunteers actually imaged with subject numbers 02,03,05,8-20). Additional sequence optimization experiments were carried out under the ethics of another study (MICHAL) with two subjects M1 and M6 and imaging parameters listed in Table 9-3.

9.3.3 Multi-echo imaging

There are restrictions on the minimum TR that can be used due to SAR and hardware constraints, and the acquisition time is required to be short to lower TE and reduce T_2^* blurring and signal loss. However, to maximize SNR in tissues or regions of higher T_2^*, while not compromising SNR in low T_2^* tissues/regions, multi-echo imaging (where multiple read-out gradients are acquired for each TR as described in section 2.8.2) was explored. At tissue/material interfaces the variations in magnetic susceptibility is highest, which indicates that locations of ventilation defects within the lungs will have lower T_2^*. Therefore, to clearly identify these regions in %VV analysis the SNR of low T_2^* regions should be prioritized. As a demonstrative example Figure 9-2 shows the relative SNR that may be expected for different levels of T_2^*, with realistic parameters for ^{19}F imaging at 3T, using equation (2-53). The variables TR and FA remain fixed such that only TE and BW affect the final relative difference in SNR. The demonstrative example shows the benefits of multiecho-imaging for low T_2^* when FA and TR are restricted to certain values. Therefore, the use of multi-echo and single echo imaging is compared experimentally here in in-vivo imaging.

9.3.4 Anatomical ^{1}H scan

Sequences that have been employed previously in anatomical ^{1}H thorax imaging for the purpose of segmentation include SPGR, b-SSFP, Turbo FSE or UTE SPGR (263). However, due to restrictions on B_1 and B_0 homogeneity, as well as maximum power delivered to the dual ^{19}F/^{1}H birdcage, only low FA SPGR or SPGR UTE may reasonably be employed. Relevant relaxation parameters of lung parenchyma at 3T are $T_2^* \approx 0.85 \pm 0.1\ ms$ and $T_1 \approx 1002 \pm 82\ ms$ (362), which influenced the choice of imaging parameters BW, TR and FA. There is an expected $\sqrt{N_z}$ increase in SNR with 3D imaging vs. 2D SPGR imaging if each slice is acquired sequentially, but also increased motion artefacts; all other parameters remaining constant. An alternative is the use of 2D multi-slice imaging where individual slices are excited in an interleaved fashion during acquisition of k-space.

For subject S1_01, ventilation and anatomical imaging was performed at TLC and FRC+1L to determine if there were any differences in the resulting SNR with ventilation and anatomical imaging. In future subjects all imaging was performed at TLC. 3D Imaging was performed with a bandwidth that maximized the minimal TR of 4 ms, while FA was 30°. The FA was larger than the optimum for most tissues to compensate for coil inhomogeneity.
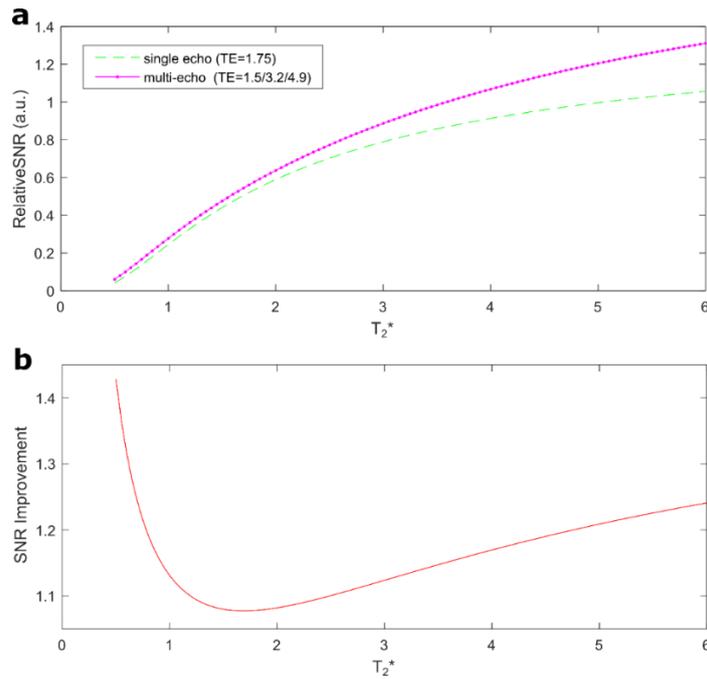
Figure 9-2: a: Predicted relative SNR for multi-echo vs single echo imaging, with $T_{aq} = 2$ ms for single echo and $T_{aq} = 1.5$ ms for 3 echos, T_{D1}=0.75ms and T_{DE}=0.2 ms. b: Predicted relative improvement using the multi-echo sequence compared to single echo.

For subject S1_03 Both 2D and 3D anatomical imaging sequences were tested and compared since they result in different contrast/SNR and have different potential artefacts of imaging associated with them.

For subjects S1_04-08 a multi-echo 3D anatomical imaging sequence was considered as an alternative to the single echo low BW sequence.

For subjects S1_09-13 a slice interleaved 2D sequence was tested since the resulting TR could be increased allowing for greater longitudinal magnetization recovery resulting in improved SNR compared to a non-interleaved 2D sequence.

In subjects S1_16-17 the slice interleaved 2D sequence was tested with increased bandwidth and also employing a partial echo to determine if susceptibility artefacts could be reduced. Additionally, a 3D sequence with reduced FA, increased BW and partial echo was tested for the same reason; the resolution was also increased to attempt to reduce effects of partial-voluming.

For the subject M6 subject three 3D sequences were compared: a multi-echo sequence, a low bandwidth high FA (30°) sequence and a 3D sequence with low FA (12°), partial echo and relatively high bandwidth.

For the subject M1 subject the low FA sequences was tested and compared to one with the same with the FA increased to (12°), and same sequence with multiple echos. In addition, the 2D slice interleaved sequence was tested and compared with an additional echo.

205

Anatomical images are compared qualitatively with comparison of slices in central, and posterior and anterior slices. Images are also compared quantitatively by selecting a central area of each slice and comparing the average SNR in anterior to posterior slices.

9.3.5 Ventilation ^{19}F Scan Protocol Development

The Relevant relaxation parameters for sequence optimization of C_3F_8 ^{19}F imaging at 3T are $T_2^* \approx 2.2\ ms$ and $T_1 \approx T_2 \approx 12.4\ ms$ (98, 126). For ^{19}F imaging a b-SSFP sequence with a short TR and high FA would result in highest SNR and best image quality. However, due to restrictions on B_1 and B_0 homogeneity, transmit efficiency and SAR by the dual ^{19}F/^{1}H birdcage only SPGR with a larger than optimal TR to FA ratio was be considered.

For subject S1_01 ventilation imaging at two different inflation levels was compared. T_2^* mapping was also performed at two different inflation levels (RV and TLC) with lower resolution imaging to compare.

For subject S1_03 three ventilation scans were attempted with two marginally different imaging parameters. For subject S1_04-12 a multi-echo (with higher imaging bandwidth) and single-echo ventilation scan was attempted with equal breath-hold times. T_2^* mapping was carried out with the multi-echo data after filtering data for sufficient SNR to fit. A comparison of the SNR from all subjects was performed with the two sequences. For subject S1_04-8 T_2^* mapping with a lower resolution imaging sequence was also carried out in the same breath-hold as the spectral central frequency measurement sequence to determine if the result matched those from the multi-echo ventilation scan.

For subjects S1_05/08 low resolution SPGR and SSFP imaging was carried out in the same breath-hold to determine if with the non-optimal FA and TR required by SAR constraints any benefit was obtainable with SSFP imaging. For subjects S1_09-11 FA mapping was attempted in the same breath-hold as the spectral centre frequency measurement and a T_1 mapping sequence was attempted in a separate breath-hold to ideally combine the data from both and allow for a better optimization of the ideal imaging parameters.

For subject S1_13 three different multi-echo sequences were tested and compared to the standard single-echo sequence. For subjects S1_16-17, S2_02-08 and M6 the same ventilation scan was performed 4 times with 3 compared to 4 averages of previous scans, while for M6 a multi-echo sequence was also carried out in the same breath-hold as the spectral centre frequency measurement.

To ensure that a direct comparison made could be made between sequences in terms of SNR without consideration of different levels of saturation of ^{19}F in lungs 4 sequences were run within the same breath-hold with the M1 subject.

Comparisons between different sequences were made quantitatively in terms of SNR histograms within the masks of the segmented lungs and also qualitatively in terms of comparison between edge definition on lung boundaries and around vessels.

9.3.6 Semi-Automated Registration and Segmentation

Registration of anatomical images to lung images was carried out by using a combination of automatic and manual segmentation in the ITK snap program (387) to obtain a lung cavity mask. Then, within MATLAB the affine transformation required to warp the masked inverse of the anatomical image to the segmented and masked ventilation image was found by maximizing the mutual information (385). The need for registration is demonstrated from the overlap of signal in the ventilation and anatomical images observed in Figure 9-1 prior to registration. Segmentation of lungs and calculation of %VV was carried out according to previously described methods using a GUI developed within the POLARIS group (57). For every group of ventilation images acquired from a single volunteer the ventilation images were also registered to the same base image and then averaged, with the same registration and segmentation process carried out on the combined image.

Table 9-2: Imaging parameters for scans performed on volunteers as part of the LIFT study for phase 1

Measurement	Sequence	TE (ms)	TR (ms)	BW (Hz)	Matrix size (pixels^3)	FOV (cm^3)	Prescribed FA (°)	Avg.
Phase 1: Sequence Optimization 1								
LIFT S1 01								
Anatomical (TLC and FRC+1L)	3D SPGR	2.1	4.1	413	110x112x43	44x44x32.3	30	1
Ventilation (TLC and FRC+1L)	3D SPGR	1.98	7.0	499	40x32x25	40x32x25	50	4
T_2^* mapping (TLC then RV)	3D SPGR	1:1:6	7.0	2894	33x29x13	40x35x29.3	26	12
LIFT S1 03								
Anatomical	3D SPGR	2.1	4.1	413	110x112x43	44x44x32.3	30	1
Anatomical	2D SPGR	2.2	4.9	500	110x112x30	45x45x30	30	1
Ventilation	3D SPGR	1.74	7.5	499	40x32x25	40x32x25	45	4
(2) Ventilation	3D SPGR	1.87	7.0	499	40x32x25	40x32x25	50	4
LIFT S1 04								
Anatomical Multi-echo	3D SPGR	1:1:3	4	1447	73x75x34	44x44x34	20	1
Anatomical[1]	3D SPGR	5.8	12	100	110x112x34	44x44x34	30	1
T_2^* mapping	3D SPGR	1:1:5	7.0	2894	33x29x13	40x35x29.3	26	4
Ventilation Multi-echo	3D SPGR	1.3:1.4:4.1	6.0	962.6	40x32x28	40x32x28	45	4
(2) Ventilation[2]	3D SPGR	1.87	6.0	484	40x32x28	40x32x28	45	4
LIFT S1 05-08[3]								
Anatomical Multi-echo	3D SPGR	1:1:3	4	1447	73x75x34	44x44x34	20	1
Anatomical	3D SPGR	1.88	4.0	485	110x112x33	44x44x33	30	1
T_2^* mapping	3D SPGR	1:1:5	7.0	2894	33x29x13	40x35x29.3	26	4
Ventilation Multi-echo	3D SPGR	1.3:1.4:4.1	6.0	962.6	40x32x28	40x32x28	45	4
Ventilation	3D SPGR	1.87	6.0	484	40x32x28	40x32x28	45	4
SPGR-SSFP Same-breath	3D SPGR or SSFP	2.7	6.0	241	40x32x14	40x32x28	40	4
LIFT S1 09-12								
Anatomical	3D SPGR	1.88	4.0	485	110x112x34	44x44x34	30	1
Anatomical 2D MS	2D MS SPGR	1.69	130	896	110x112x32	44x44x32	25	1
Ventilation Multi-echo	3D SPGR	1.3:1.4:4.1	6.0	962.6	40x32x28	40x32x28	45	4
Ventilation	3D SPGR	1.87	6.0	484	40x32x28	40x32x28	45	4
FA mapping Same breath[5]	2D MS	3.2	100	484	27x23x14	40x35x28	27/81	2
T1 mapping Same breath	3D SPGR	1.41	6.5	250	32x28x14	40x35x28	25/37.5/50	2
LIFT S1 13								
Anatomical	3D SPGR	1.88	4.0	485	110x112x34	44x44x34	30	1
Anatomical 2D MS	2D MS SPGR	1.69	130	896	110x112x32	44x44x32	25	1
Ventilation	3D SPGR	1.87	6.0	484	40x32x28	40x32x28	45	4
Ventilation Multi-echo	3D SPGR	1.0:1.1:3.2	5	1378	40x32x28	40x32x28	37.5	4
Ventilation Multi-echo 2	3D SPGR	1.3:1.3:3.9	6	963	40x32x28	40x32x28	45	4
Ventilation Multi-echo 3	3D SPGR	1.1/2.4	4	963	40x32x28	40x32x28	28	6
LIFT S1 16-17 and phase 2 LIFT subjects								
Anatomical (insp. and exp.)	3D SPGR	0.437*	4.0	2815	147x149x33	44x44x25	6	1
Anatomical 2D MS (partial echo)	2D MS SPGR	0.89*	100	1240	110x112x32	44x44x32	25	1
(4) Ventilation	3D SPGR	1.74	7.5	499	40x32x25	40x32x25	45	3
LIFT S1 16-17 exclusive								
Anatomical 2D MS	2D MS SPGR	1.22	100	1240	110x112x32	44x44x32	25	1
Anatomical	3D SPGR	1.7	4.0	498	110x112x33	44x44x25	30	1

1. TE,TR and BW tabulated and used were not the intended, leading to overly long sequence (34 second) and resulting in artefacts
2. First ventilation image resulted in no ^{19}F signal
3. Ventilation images from S1 07 had no ^{19}F signal
4. Not performed for S1 09
5. Signal in FA mapping proved to be too low for accurate results to be obtainable, likely due to too long pulse width and use of MS sequence
   * partial Fourier echo (60%)

Table 9-3: Additional protocol testing performed as part of MICHAL ethics for protocol development of optimal imaging parameters.

M6 – Test M2 protocol								
Anatomical (insp. and exp.)	3D SPGR	0.437*	4.0	2815	147x149x33	44x44x25	6	1
Anatomical 2D MS (partial echo)	2D MS SPGR	0.89*	100	1240	110x112x32	44x44x32	25	1
(4) Ventilation	3D SPGR	1.62	7.5	499	40x32x25	40x32x25	45	3
Ventilation Multi-echo	3D SPGR	1.2:1.2:3.6	7.5	1086	40x32x28	40x32x28	45	3
Anatomical	3D SPGR	2.1	4.1	413	110x112x43	44x44x32.3	30	1
Anatomical Multi-echo	3D SPGR	0.85*:1.1:3	4	1240	110x112x25	44x44x25	6	1
M1 – ^{19}F LIFT phase 2 ^{1}H additional optimization								
Anatomical	3D SPGR	0.437*	4.0	2815	147x149x33	44x44x25	6	1
Anatomical High Flip	3D SPGR	0.5*	4.0	2815	147x149x33	44x44x25	12	1
Anatomical High Flip (multiecho)	3D SPGR	0.5*/1.1/1.8	4.0	2815	147x149x33	44x44x25	12	1
Anatomical 2D MS (partial echo)	2D MS SPGR	0.89*	100	1240	110x112x32	44x44x32	25	1
Anatomical 2D MS (multi echo)	2D MS SPGR	0.89*/1.94	100	1240	110x112x32	44x44x32	25	1
M1 – LIFT phase 2 ^{19}F additional optimization								
Ventilation	3D SPGR	1.74	7.5	499	40x32x25	40x32x25	45	3
Ventilation v2 (multiecho)	3D SPGR	1.53/3.4/5.3	7.5	667	40x32x25	40x32x25	52	3
Ventilation v3 (multiecho)	3D SPGR	1.2/3.1	5.5	667	40x32x25	40x32x25	30	4
Ventilation v3 (multiecho)	3D SPGR	0.96*/2.8/4.7	7.5	667	40x32x25	40x32x25	52	3

9.4 Results

9.4.1 Coil Characterization

The scattering parameters measured at the input of the two quadrature ports of the birdcage coil are shown in Figure 9-3. At the ^{1}H frequency a high reflection coefficient for both ports was observed. The isolation between ports is also lower than ideal at the ^{19}F frequency.
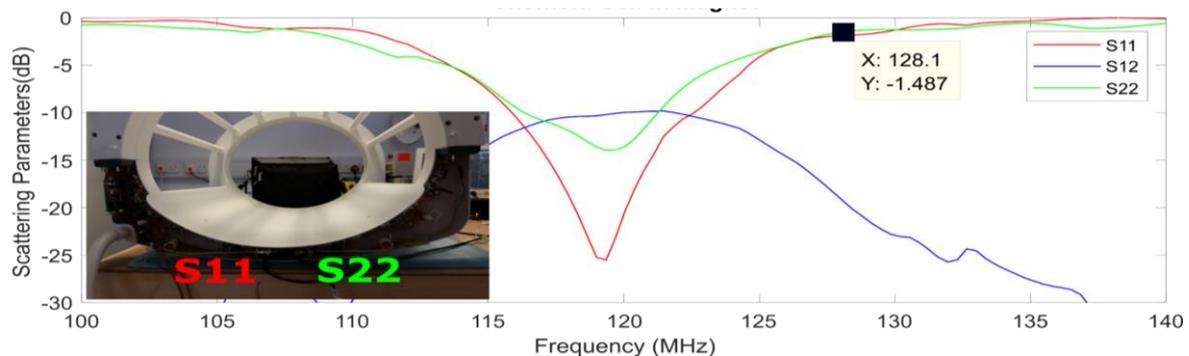
Figure 9-3: S-parameter measurements within the scanner bore of the birdcage coil with a volunteer inside.

FA maps in a human shaped thorax phantom at the ^{19}F and ^{1}H frequencies are shown in Figure 9-6 along with receive sensitivity maps according to (2-50)). The homogeneity at the ^{19}F frequency is much better than at the ^{1}H frequency. The receive sensitivity is particularly inhomogeneous with the sensitivity at the anterior being less than 20% of that in the centre.
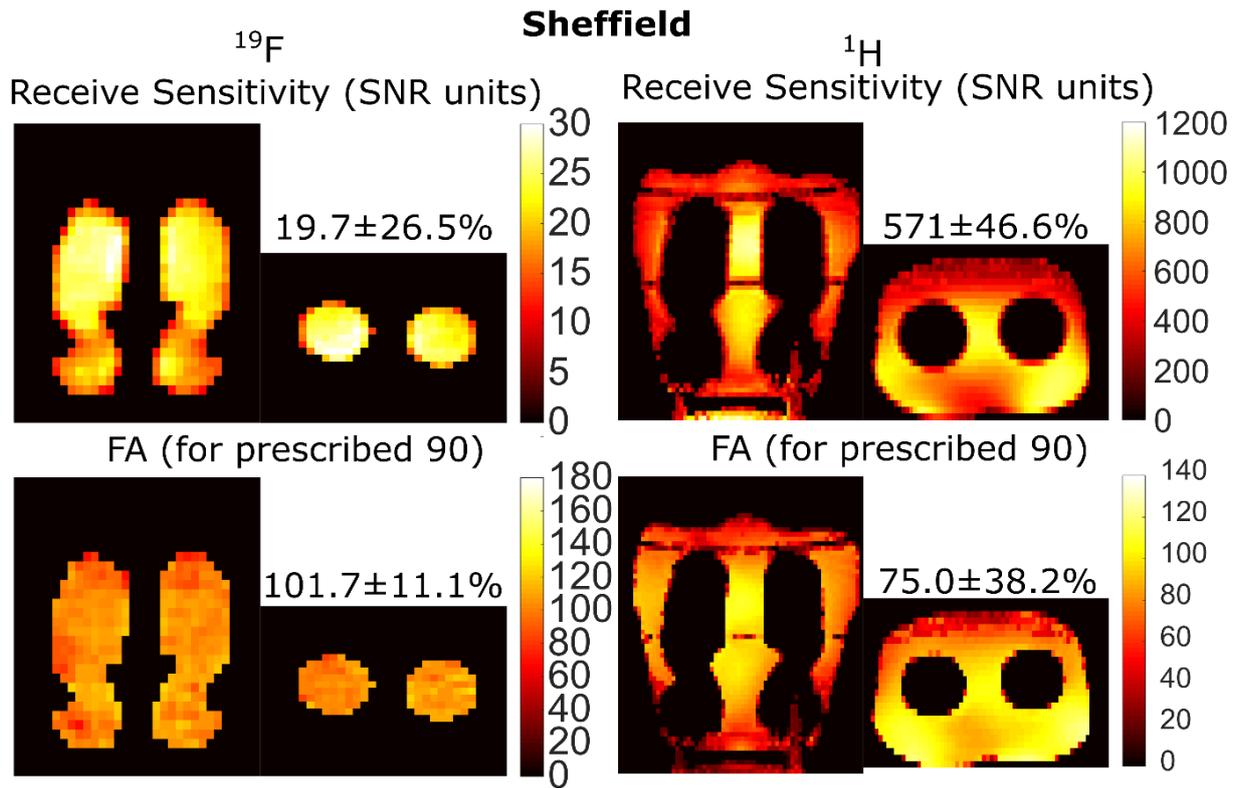
Figure 9-4: FA and receive sensitivity maps in human torso shaped multinuclear phantom for ^{1}H and ^{19}F.

In-vivo FA receive sensitivity mapping shown in Figure 9-5 demonstrate similar homogeneity differences between ^{1}H and ^{19}F frequencies as phantom imaging. In both phantom and in-vivo imaging the receive sensitivity is more inhomogeneous than the FA.
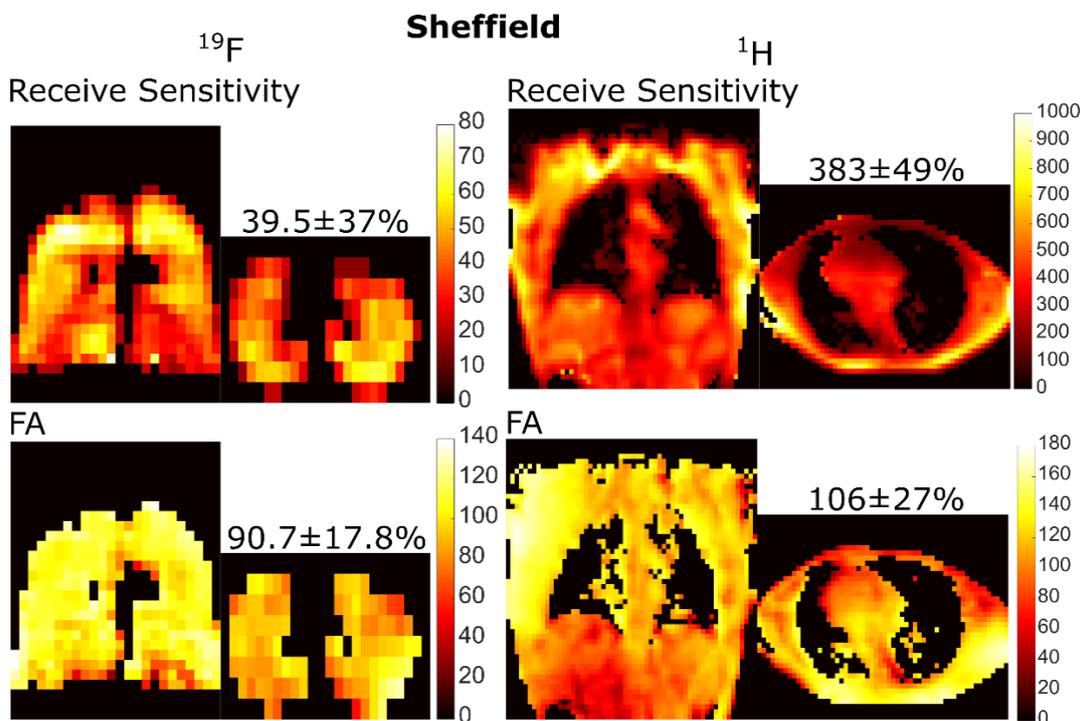
Figure 9-5: FA and receive sensitivity maps in-vivo for ^{1}H anatomical and ^{19}F ventilation imaging.

9.4.2 Semi-Automated Registration

Results of registered representative ventilation/anatomical images are shown in Figure 9-6 for different cases of phase 2 subjects. In the before registration images regions are highlighted where the ventilation images do not overlap exactly with the lung cavity in anatomical images. It is clear from these examples that registration is necessary for correction or incorrect alignment will lead to unreliable %VV and lung volume calculations. The images after registration, where the anatomical images are warped, demonstrate the improved matching with between the anatomical and ventilation images.
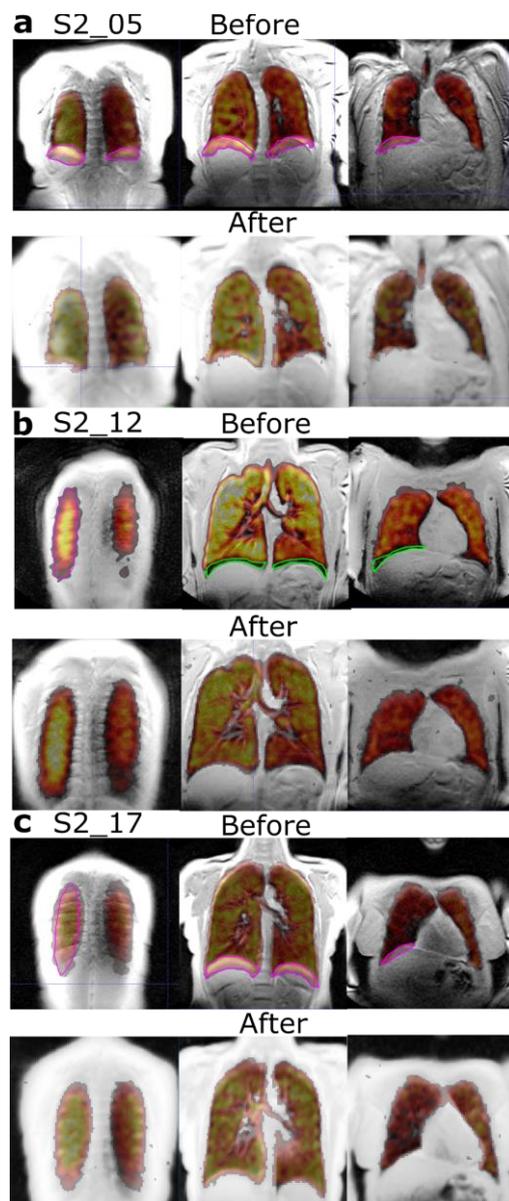
Figure 9-6: Ventilation images overlaid anatomical images before and after registration for LIFT subjects a: S2_05, b: S2_12 and c: S2_17. Purple regions encircle areas where the ventilation images extend past the lung cavity in anatomical images and green regions encircle areas where the lung cavity is apparent in anatomical images but not matched by ventilation.

9.4.3 **2D Imaging Optimization**

The comparison of central SNR between 2D MS and 3D imaging for subjects S1 09-12 is shown in Figure 9-7. With nearly identical resolutions, the MS sequence has similar SNR to the 3D images, but it is lower in the anterior. The FA for the MS sequence is nearly the optimum for lung parenchyma. However, because of the inhomogeneity in the RF field there is nearly a 7-fold difference in SNR between the central region of the body and the anterior. On the other hand, the vessels and tissue interfaces are much clearer with 2D MS imaging. Based on results in the three volunteers shown ^{1}H image SNR was repeatable between different volunteers.
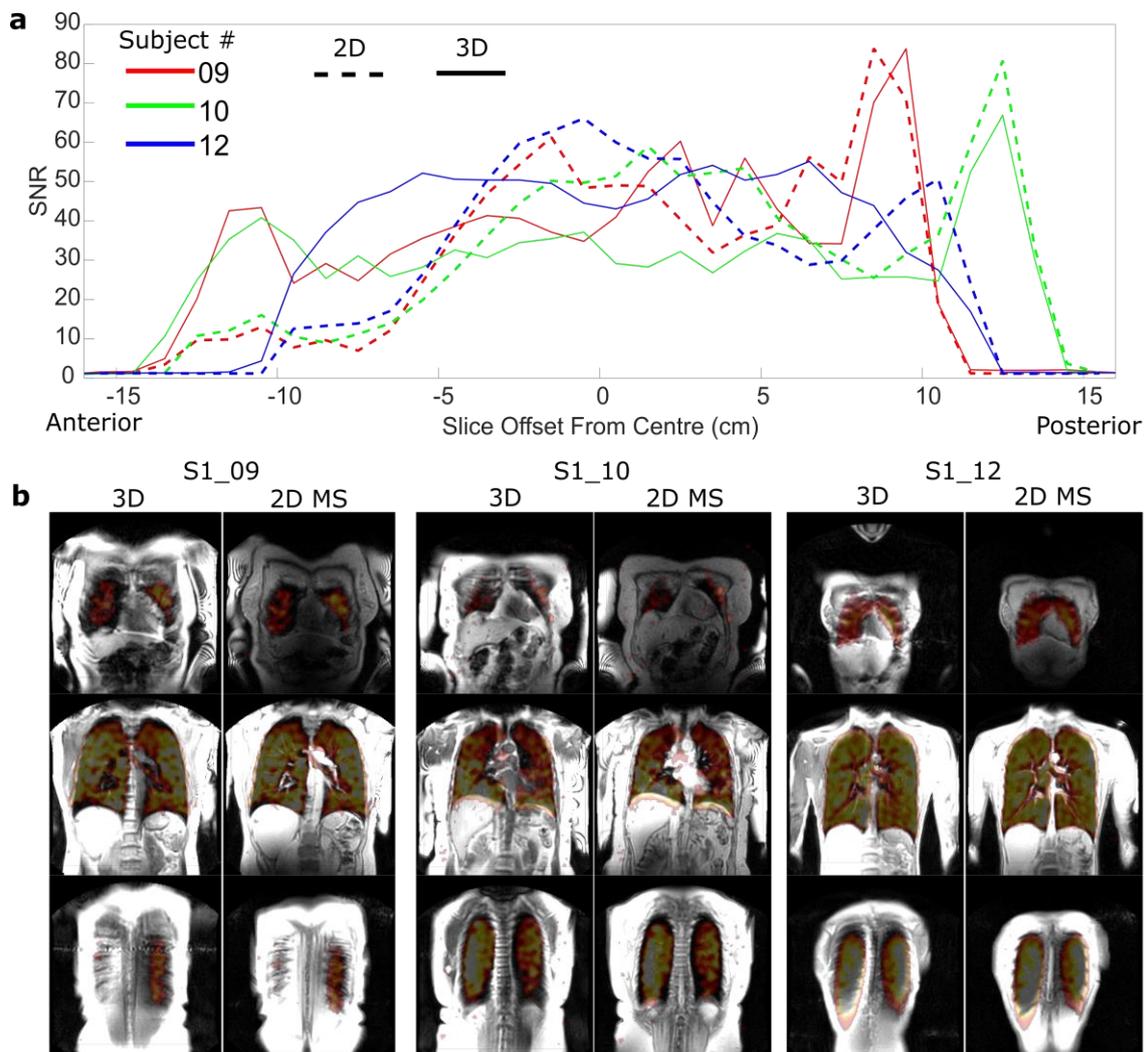
Figure 9-7: a: The SNR for 2D MS and 3D imaging in slices throughout the body. Also shown are b: SNR scaled images in anterior, posterior and central slices overlaid with ventilation images prior to registration.

The resulting SNR and images using a 2D MS sequence, with a single partial echo or with two echoes combined by sum-of-squares, is shown in Figure 9-8. Susceptibility related signal

212

nulls around the ribs and other regions were eliminated with the multi-echo combination. Additionally, SNR was nearly doubled throughout the body.
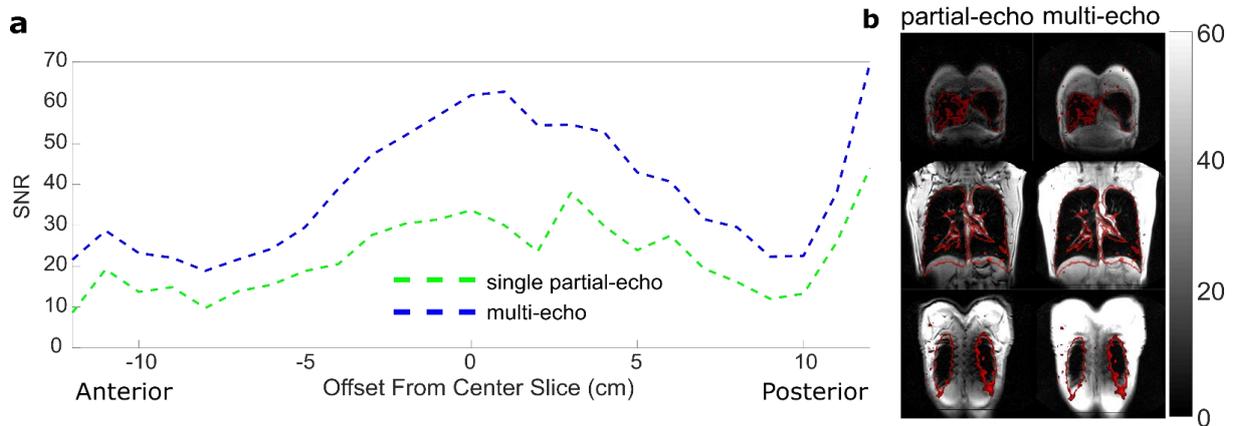
Figure 9-8: The SNR for 2D MS imaging in slices throughout the body (MICHAL 01) with or without the combination of multiple echoes. Also shown are b: SNR scaled images in anterior, posterior and central slices overlaid with ventilation images prior to registration.

9.4.4 3D Imaging Optimization

The comparison of 3D imaging with two different strategies are shown in Figure 9-9. The lower FA and partial echo imaging results increased in increased SNR in this case. Susceptibility related contrast between ribs and tissue interfaces is introduced in higher FA imaging due to longer TE as well.
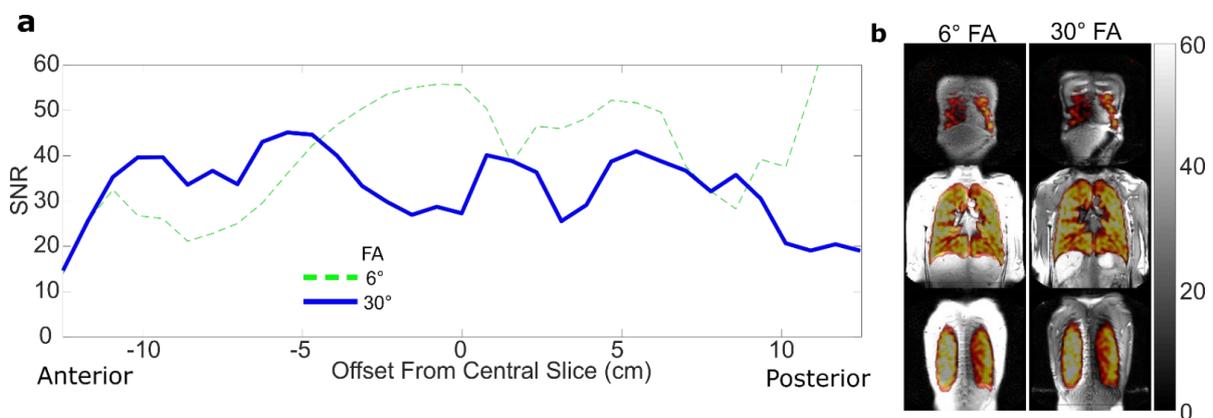
Figure 9-9: The SNR for 3D imaging in slices throughout the body (subject S1 16) with different FAs, but same resolution, and a partial echo with the lower FA. Also shown are b: SNR scaled images in anterior, posterior and central slices overlaid with ventilation images prior to registration.

A comparison of 3D imaging sequence with 12° FA (intermediate between 6° and 30°) and 6° FA, is shown in Figure 9-10. The same 12° FA sequence performed with multiple-echoes and sum of squares combination is also shown. The sum of squares combination has the benefits of the higher FA imaging, with higher overall SNR. In addition, the strong signal variation at tissue interfaces and around regions such as the ribs or spine present in the first

echo was reduced. Nearly triple the SNR was obtained with the multi-echo imaging with reduced signal nulls around the ribs and spine.
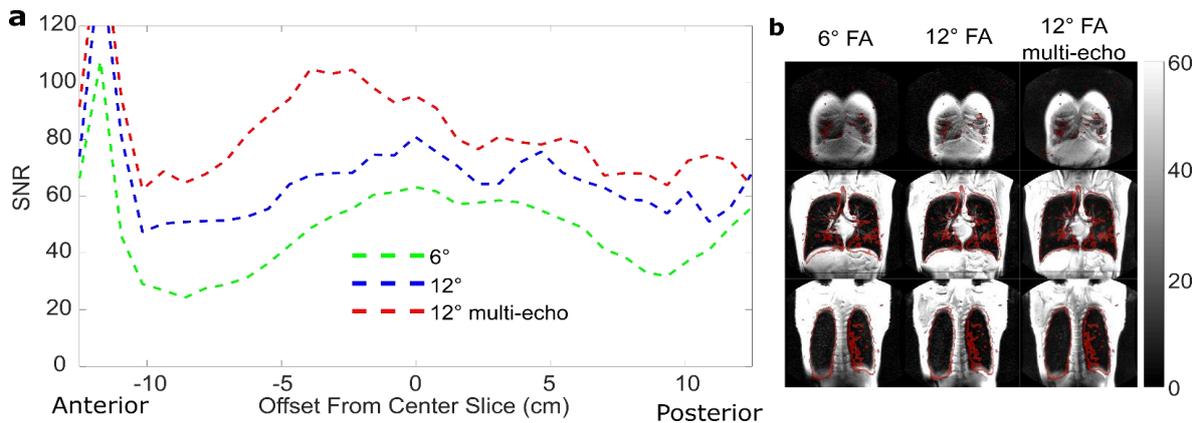
Figure 9-10: **a:** The SNR for 3D imaging in slices throughout the body (MICHAL 01) with different FAs, but same resolution, and with the combination of multiple echoes with the higher FA sequence. Also shown are **b:** SNR scaled images in anterior, posterior and central slices overlaid with ventilation images prior to registration.

9.4.5 Ventilation Scans in Protocol Development Phase

SNR histograms and representative slices from the volunteers recruited in the first phase of LIFT are shown in Figure 9-11. In single-echo images blurring may be more visible near the diaphragms and regions of signal dropout are larger around pulmonary vessels, which may be due to T_2^* dependent signal decrease and k_x filtering due to the lower BW. In two of the eight volunteers (S1_04/11) the single-echo image had greater SNR than the multi-echo, but the large intersubject variability makes any definite conclusions difficult.
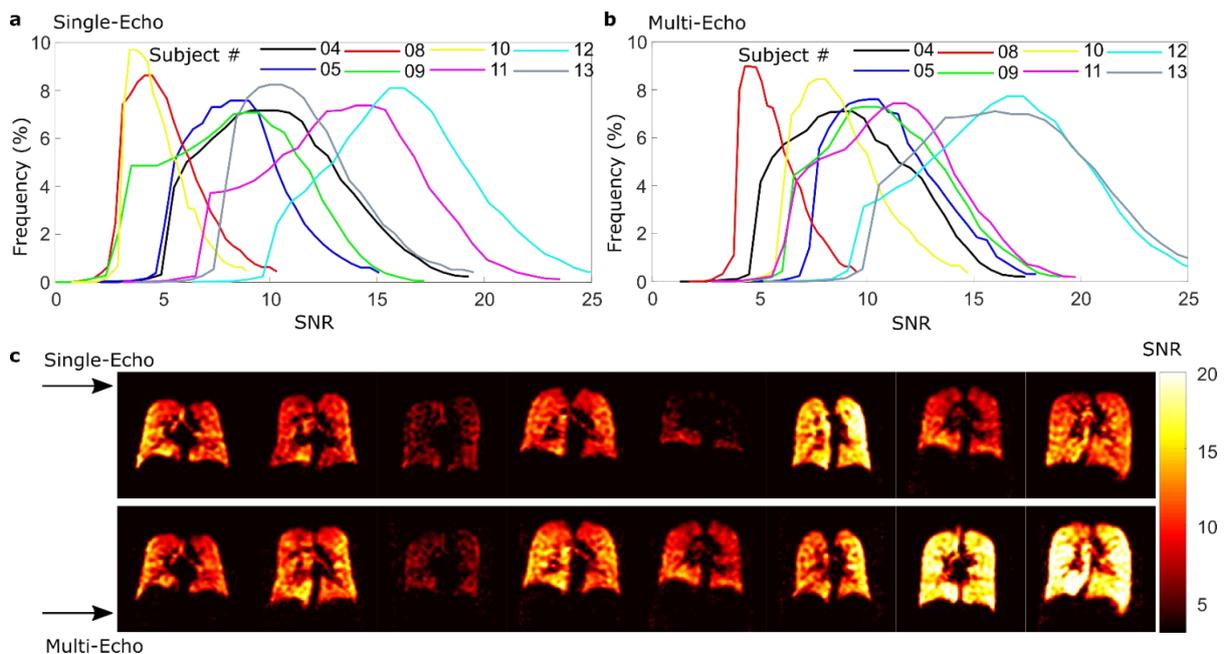
Figure 9-11: SNR histograms for ventilation images obtained from subjects S1_04-13 are shown for the a: single echo or b: multi-echo ventilation sequences employed. Also, c: a central representative slice is shown for the subjects.

214

9.4.6 T_2^* Analysis

T_2^* maps and histograms are shown in Figure 9-12. The distribution remains similar across all healthy volunteers, indicating that it may be a repeatable and reproducible metric for normal lungs. The mean varies amongst volunteers, which may be influenced by the following factors: inflation level, volunteer size, gas mixture saturation in the lungs and physiology. However, the standard deviation, expressed as a percent, remain similar, while also being large relative to the mean. The values obtained either with the higher resolution or the lower resolution imaging, in a limited number of volunteers, are consistent considering differences in inflation level. Due to the broad nature of the distribution it may be more beneficial to optimize imaging for T_2^* values at the lower end of the range.
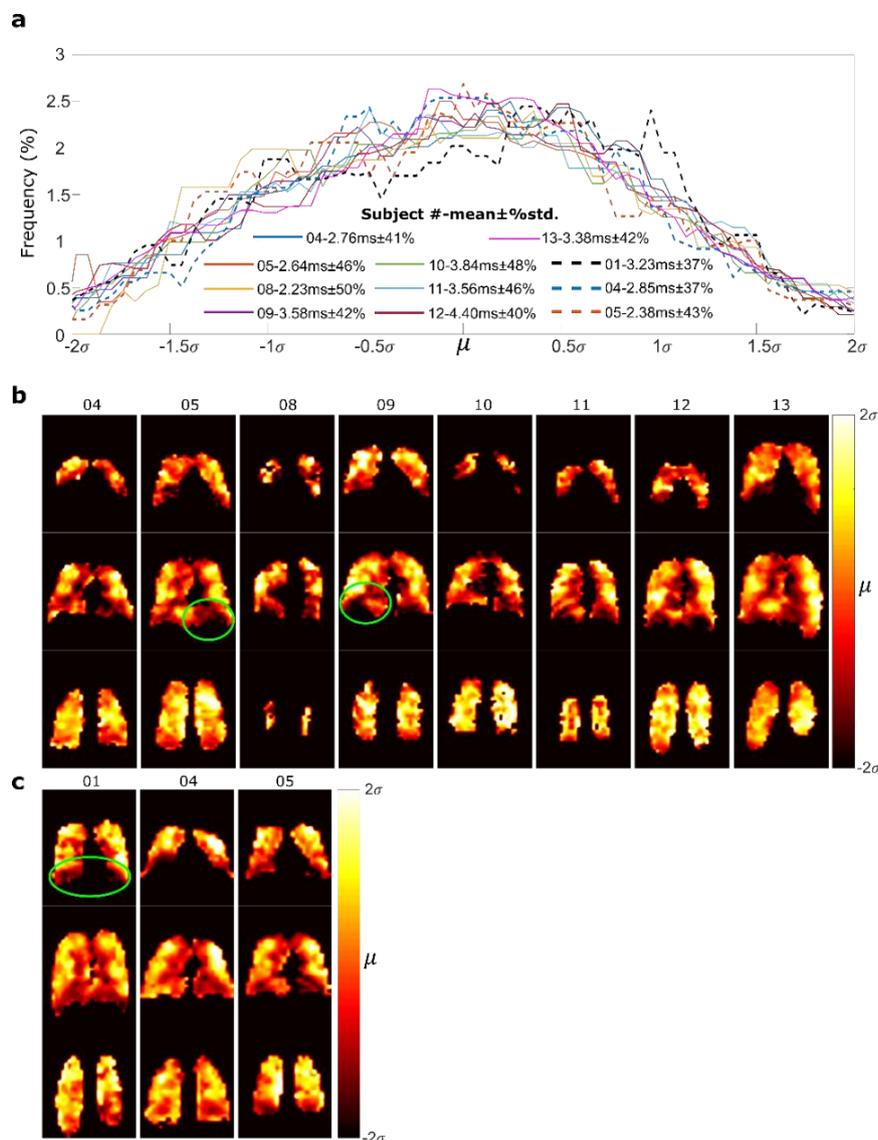
Figure 9-12: a: Histograms of the fitted T_2^* in different LIFT volunteers during phase 1 protocol development are shown normalized to the mean and standard deviation. **b:** The T_2^* maps in anterior central and posterior representative slices are shown obtained from b: the filtered multi-echo ventilation scans and c: the lower resolution with greater number of echoes.

215

The SNR histograms from three different ventilation sequences obtained in a single breath-hold (see Table 9-3) are shown in Figure 9-13. Since the imaging was performed in the same breath-hold differences in SNR and image quality can be attributed to just the sequence parameters. It is encouraging that the histograms remain similar. The single echo sequence has the lowest SNR, but it is close to that of the multi-echo v2. However, this multi-echo sequence has a lower TE and higher BW, as well as smaller FA (shorter RF excitation pulse width). Therefore, in addition to being a lower SAR sequence it is more robust to differences in the RF excitation frequency and should have a greater signal in lower T_2^* regions. The multi-echo v1 (most similar to previously used sequence in phase 1 ventilation scans) and multi-echo v3 have approximately 50% higher mean SNR than the single-echo ventilation image, with the result that the outermost anterior slice would be more easily segmentable in the region with high signal drop-off. The multi-echo v3 sequence utilizes a partial echo, which allows a much lower TE, but means the determination of T_2^* more complicated and results in blurring.
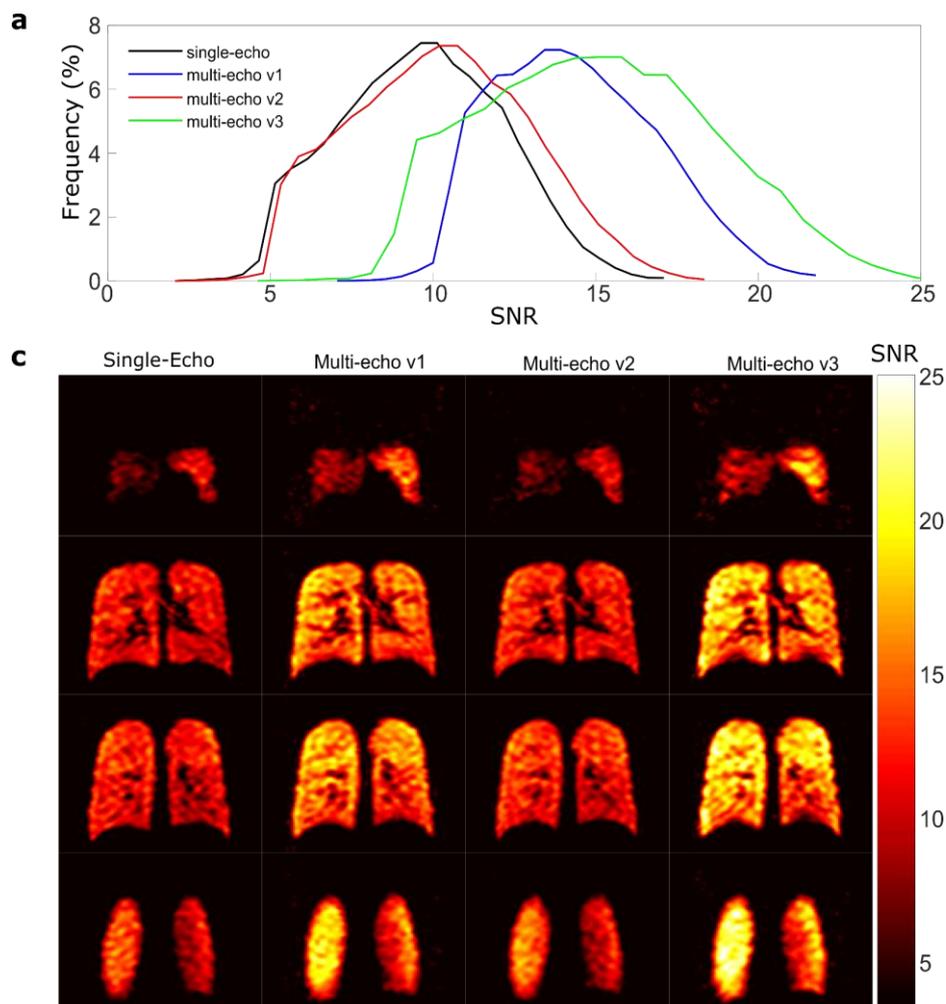
Figure 9-13: **a:** SNR histograms of the single echo sequence used in phase 2 imaging, different multi-echo ventilation scans acquired in the same breath-hold and **b:** SNR maps of representative slices.

9.4.7 %VV and SNR reproducibility

Table 9-2 summarizes the results of global %VV and TLV from segmentation of ventilation/anatomical scans in healthy volunteers for phase 1 and phase 2. The TLV can vary up to a litre within the same volunteer in different breath-holds. Also, the combined image appears to usually result in a slightly large TLV, due to increased SNR allowing more pixels to be included in the segmentation. The %VV is generally above 96% and in higher SNR ventilation scans is generally >98.5%. The %VV from the combined images is greater than individual ventilation scan due to regions of low signal being included as well as some potential blurring introduced during registration and averaging.

Figure 9-14 shows SNR histograms for the volunteers that received identical anatomical and ventilation imaging according to the phase 2 protocol. Between different ventilation scans for the same volunteers the SNR histograms remain nearly identical, except the SNR of the first ventilation scan in subjects S1_02, S2_03 and S2_08 are slightly lower than the rest in the same volunteer. This is indicative of the volunteers having greater compliance with the breathing protocol after the first ventilation scan, in some cases. Pixels with SNR less than 3 are mostly not included within the resulting segmented image mask, but since the combined images still include pixels at this level the SNR in some regions of the lungs may be too low to be detected. Figure 9-15 shows the relationship between ventilation image SNR and final %VV after segmentation. In the region indicated "Low SNR" there is a decline in the measured %VV for many scans bringing the value below the 97% line that may be considered as the threshold for healthy lungs. This demonstrates that if the median image SNR decreases below ~7.5 (with the related SNR inhomogeneity with the specific image set-up used here) regions of low signal become indistinguishable from volume defects resulting in decreased apparent %VV. As only healthy volunteers were scanned it is expected that all %VV values should be greater than 97%.
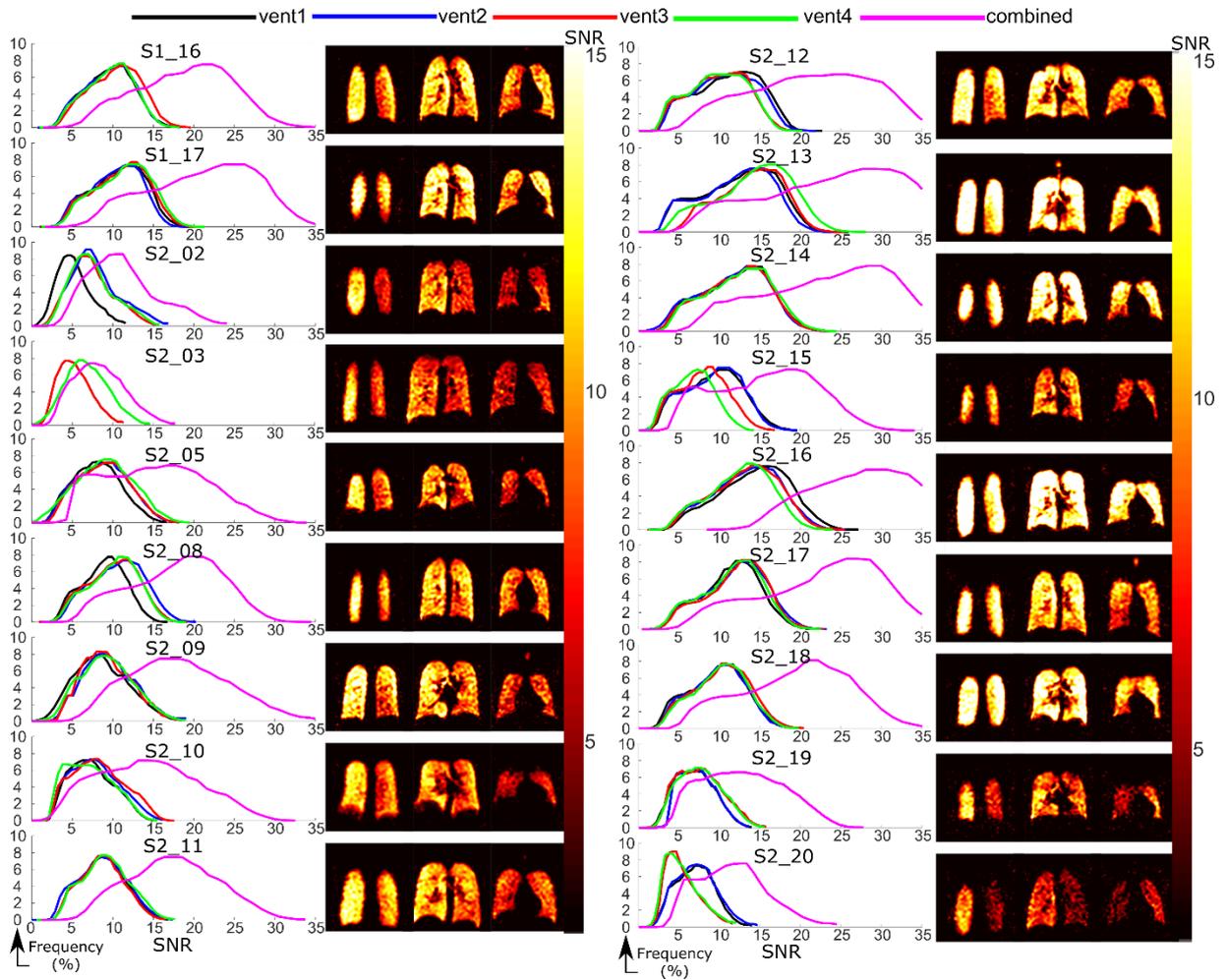
Figure 9-14: SNR histograms and representative slices for all LIFT volunteers.

Table 9-4: Global Values of %VV and TLV measured for healthy volunteers participating in the LIFT study.

Scan	%VV	TLV	Scan	%VV	TLV	SNR	Scan	%VV	TLV	SNR	Scan	%VV	TLV	SNR
LIFT S1 01			**LIFT S1 16**				**LIFT S2 10**				**LIFT S2 17**			
Vent1	97.8	6.1	**Vent1**	99.1	7.1	10.7	**Vent1**	95.0	6.5	6.4	**Vent1**	98.0	5.5	12.0
Vent2	98.9	7.6	**Vent2**	98.9	7.2	10.7	**Vent2**	98.6	6.3	7.2	**Vent2**	98.3	5.5	12.6
Combined	98.8	7.9	**Vent3**	99.0	7.1	10.9	**Vent3**	98.9	7.0	7.6	**Vent3**	98.7	5.4	12.7
			Vent4	99.3	7.2	10.8	**Vent4**	98.3	6.5	6.1	**Vent4**	98.2	5.6	13.0
			combined	99.6	7.3	21.1	**combined**	98.9	7.1	13.4	**combined**	98.7	5.6	25.6
LIFT S1 03			**LIFT S1 17**				**LIFT S2 11**				**LIFT S2 18**			
Vent1	98.4	9.1	**Vent1**	99.6	5.2	11.3	**Vent1**	99.3	8.2	8.8	**Vent1**	99.7	6.4	10.3
Vent2	99.5	9.1	**Vent2**	99.6	5.0	11.5	**Vent2**	97.7	8.4	8.1	**Vent2**	99.2	6.2	10.4
Combined	99.4	9.6	**Vent3**	99.2	5.4	12.3	**Vent3**	97.6	8.1	8.7	**Vent3**	99.6	6.3	10.2
			Vent4	99.0	5.7	11.9	**Vent4**	97.2	8.4	8.6	**Vent4**	97.6	6.4	10.7
			combined	99.7	5.8	23.7	**combined**	98.4	8.7	17.0	**combined**	99.5	6.4	20.8
LIFT S1 04			**LIFT S2 02**				**LIFT S2 12**				**LIFT S2 19**			
Vent1	95.1	4.7	**Vent1**	90.9	4.6	4.6	**Vent1**	98.8	7.0	12.6	**Vent1**	92.4	4.0	6.9
Vent2	99.0	4.5	**Vent2**	96.8	5.6	6.7	**Vent2**	99.2	6.8	11.4	**Vent2**	85.1	3.9	6.4
combined	98.3	4.6	**Vent3**	97.1	5.5	6.3	**Vent3**	99.5	6.7	12.0	**Vent3**	93.6	4.0	7.6
			Vent4	97.6	5.4	6.4	**Vent4**	99.5	6.6	9.0	**Vent4**	96.2	4.2	7.1
			combined	98.2	6.2	10.4	**combined**	99.9	6.9	24.2	**combined**	99.2	3.8	12.0
LIFT S1 05			**LIFT S2 03**				**LIFT S2 13**				**LIFT S2 20**			
Vent1	98.2	5.6	**Vent1**	95.0	6.7	4.2	**Vent1**	99.3	6.4	15.1	**Vent1**	98.6	5.5	7.0
Vent2	99.6	6.2	**Vent2**	93.6	7.2	6.1	**Vent2**	99.0	6.6	14.6	**Vent2**	99.1	5.6	7.2
combined	98.6	5.6	**combined**	98.0	7.5	7.2	**Vent3**	99.5	5.7	15.4	**Vent3**	84.0	5.9	4.2
							Vent4	99.6	6.2	16.0	**Vent4**	90.4	5.8	3.7
							combined	99.3	5.3	27.6	**combined**	98.8	6.0	12.5
LIFT S1 09			**LIFT S2 05**				**LIFT S2 14**							
Vent1	99.7	4.9	**Vent1**	97.7	4.3	8.1	**Vent1**	98.8	5.0	14.4				
Vent2	91.8	5.2	**Vent2**	98.3	4.2	9.4	**Vent2**	98.8	5.3	13.3				
combined	99.6	4.8	**Vent3**	98.1	4.1	8.9	**Vent3**	99.2	4.9	13.5				
			Vent4	97.9	4.2	9.0	**Vent4**	99.4	4.8	13.9				
			combined	98.8	4.8	16.6	**combined**	99.2	5.0	28.3				
LIFT S1 11			**LIFT S2 08**				**LIFT S2 15**							
Vent1	99.7	4.8	**Vent1**	99.5	5.8	9.4	**Vent1**	99.6	3.9	9.9				
Vent2	99.4	3.9	**Vent2**	99.4	6.0	11.2	**Vent2**	99.5	3.6	10.5				
combined	99.2	4.8	**Vent3**	99.2	5.8	11.2	**Vent3**	99.1	3.7	8.5				
			Vent4	99.6	6.0	10.7	**Vent4**	97.2	3.4	7.3				
			combined	99.5	6.3	19.0	**combined**	99.7	4.2	18.2				
LIFT S1 13			**LIFT S2 09**				**LIFT S2 16**							
Vent1	98.3	6.9	**Vent1**	97.9	7.7	8.0	**Vent1**	99.6	6.1	15.1				
Vent2	96.7	6.4	**Vent2**	96.3	7.2	8.3	**Vent2**	99.5	6.1	14.2				
Vent3	97.9	6.8	**Vent3**	94.5	7.4	8.0	**Vent3**	99.5	6.2	14.0				
Vent4	94.6	6.6	**Vent4**	98.0	7.1	8.6	**Vent4**	99.3	6.3	13.3				
			combined	98.0	7.5	17.0	**combined**	99.8	5.7	29.4				
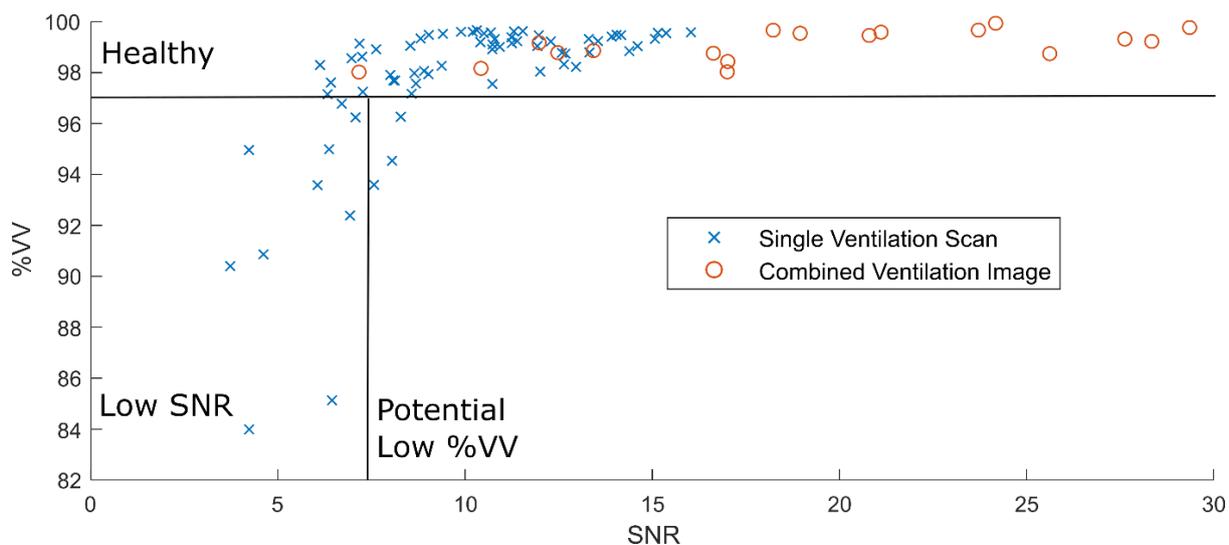
Figure 9-15: %VV with SNR for the analysis of different ventilation scans from healthy LIFT volunteers

9.5 Discussion

Through the development phase of LIFT study ^{1}H ventilation scans were optimized under the constraints of SAR and coil inhomogeneity. The worse homogeneity at the ^{1}H frequency compared to ^{19}F could be partially due to dielectric focusing effect not seen in gases. The resulting 3D ^{1}H scan employed for phase 2 has been found to be able to be segmented easily, though effects of partial-voluming and low signal/contrast in the anterior are non-ideal. Some improvements with slightly increased FA and the combination of multiple echoes have been demonstrated: triple the SNR in anterior parts of the body and reduced regions of signal null. In addition, the use of a second echo in 2D imaging was found to eliminate issues of susceptibility related signal dropout for greater contrast between tissue and the lung cavity, while also more than doubling SNR in the anterior.

For ^{19}F imaging close to optimal FA can be prescribed for 3D SPGR imaging with a TR of 7.5 ms, but due to the low T_2^* the full acquisition time cannot be utilized without introducing blurring. The use of a multi-echo sequence was shown to maximize SNR, while also allowing measurement of the T_2^*, which may be relatable to physiological difference between healthy vs. diseased lungs. It was observed that an average 50% higher SNR could be gained compared to the currently employed phase 2 single-echo ventilation sequence, while reducing the readout acquisition time of individual echoes.

Currently, except in cases where ventilation SNR is low, segmentation and measurement of %VV in healthy volunteers appears to be reproducible. It still needs to be determined if SNR

220

with volunteers that have lung disease will be lower due to lower levels of gas saturation after three breaths or changes in T_2^* from fibrosis, emphysema, or differences in lung physiology.

Measurements here are performed at TLV as it is the most reproducible lung inflation level, but since the appearance of VDP is reduced in TLV it will need to be determined if this affects the correlation of measured %VV compared to HP gas imaging that has typically be performed at different inflation levels. The variability of T_2^*, variation in FA and receive sensitivity with volunteer size and the level of saturation of the gas mixture in the lungs results in different SNR in different volunteers. However, it appears that the assessment of healthy lungs in terms of %VV remains possible. For the volunteers scanned one resulted in no ventilation scans being obtained, and two during phase 1 had low SNR resulting in no usable ventilation scans for segmentation. In phase 2 two of four ventilation scans from one volunteer were of sufficient SNR to be usable, but all others scans from volunteers were able to be used for segmentation. The resulting %VV is repeatable between the different ventilation datasets in each session providing SNR is high enough. The SNR between different volunteers appears to be highly variable, which may correlate with the high variability in the mean T_2^* found in mapping with different volunteers.

9.6 Conclusion

In a number of healthy subjects imaging has been optimized for %VV analysis with C_3F_8 gas MRI at 3T under the constraints of the study and imaging set-up. The evaluation and repeatability of performing %VV analysis in a number of healthy volunteers has been established. It remains to perform the same analysis in a cohort of volunteers with known respiratory conditions to evaluate the robustness and repeatability of C_3F_8 MRI at 3T in a clinical population.

Chapter 10: Conclusion and Future Directions

Fluorinated gas imaging (C_3F_8, C_2F_6 SF_6 etc.) has been shown to be feasible for producing lung ventilation images, but they are of lower quality than those obtained with HP gas imaging. This thesis investigated methods optimizing and improving of fluorinated gas MRI imaging. In addition, in-vivo MR parameters and image based methods of quantifying lung function with fluorinated gas imaging were characterized in healthy volunteers. The following current challenges of fluorinated gas ventilation imaging were addressed: the optimization of imaging sequence methods considering the particular MR parameters of C_3F_8, the challenges involved in grouping radio frequency (RF) detector coils capable of imaging (^1H) and fluorine (^{19}F) nuclei and the comparison of ventilation criteria obtained via ^{19}F ventilation imaging vs. HP gas imaging.

In the progress of this thesis various RF coils were developed to be wearable and target the thoracic lung region for imaging both ^{19}F and ^1H. In **Chapter 3**, a single transceive coil was described that utilized a microelectromechanical system (MEMS) switches to shift the resonance between ^{19}F and ^1H. The key figures of merit for the MEMS switch and more commonly employed PIN diode were compared: power handling capability, ESR and final impact on coil performance. It was determined that both devices operated effectively, while the PIN diode still has benefits in terms of ease of use interfacing with the system and lower ESR. At the same time, it was found that the receive sensitivity was not adversely affected by the coil being mismatched at the ^1H frequency, although transmit efficiency was decreased. Therefore, for the purpose of imaging both ^1H and ^{19}F nuclei the benefit of including dual tuning was marginal considering the additional complexity introduced, since a higher input power may often be employed. For this reason, in the additional coil designs presented in this thesis, and in future work, the use of a coil tuned to the ^{19}F frequency may reasonably be used for many applications including ^1H imaging assuming a reasonably low loaded Q-factor (and resulting wide bandwidth).

In **Chapter 4**, an 8-element transceiver coil utilizing MEMS to shift the individual elements between receive and transmit modes was designed and evaluated. In addition, this design was modified with an additional 6 receive-only loops to improve receive sensitivity. Simulation and imaging results with this array demonstrated a 2-3 fold increase in mean SNR throughout the lungs, and that in central portions of the lungs (near the heart) >75% of the uSNR was achieved. Furthermore, the transmit homogeneity was sufficient for the sequences employed throughout this thesis and those expected to be used routinely in ^{19}F lung imaging. Thus, future

222

modifications of coil design to improve image quality are restricted by theoretical considerations of the uSNR, so the quality of imaging performed will likely not exceed those presented in this thesis by any considerable amount.

A coil with identical geometry employing PIN diodes to switch LC traps resonant at the ^{19}F frequency during transmit and receive states was constructed. Due to the broadband nature of the MEMS switch a higher isolation between Tx/Rx states was achieved at the ^{1}H frequency compared to the PIN diode design, however it was found that the lower isolation did not result in any damage to the preamplifiers, or measurably affect the transmit performance. This may be attributed to the distributed nature of the power delivery for the 8-element array and the matching system employed. Thus, the PIN diode design was employed in subsequent imaging studies due to the greater ease of use. In a similar manner that the results of **Chapter 3** demonstrated that re-tuning a single transceive coil between ^{19}F and ^{1}H frequencies have limited benefits, **Chapter 4** demonstrated that appropriate transceive array designs may eliminate the need for broadband detuning, so that arrays of coils may be used for both frequencies in the future.

Improvements in receive sensitivity with improved coil design were shown to be limited in **Chapter 4**, but it was also observed that improvements in SAR performance, transmit homogeneity and volunteer comfort could be achieved. Therefore, in **Chapter 5**, a 6-element transceiver/ladder array using a novel method of resonator design for improved transmit field homogeneity and efficiency was described. In comparison to the coil array described in **Chapter 4** the transmit homogeneity was improved and SAR was reduced for an equivalent input power, while detachable arm straps and a larger volume improved the practical considerations of comfort and ease of use. However, the receive sensitivity was decreased by an amount commensurate by the reduced number of receive elements. This could be remedied by the addition of a receive only array as with the design of **Chapter 4**. The design of this coil explored an alternate method of asymmetric tuning/excitation of the ladder structure, which required a new formalism to solve the mesh equations of a ladder coil. As such, this new theoretical framework may be employed in future designs of RF resonator structures within MRI, and perhaps in other fields.

In MRI the sequence used for encoding the imaging data is essential for optimizing the SNR and contrast between tissues. Thus, in **Chapter 6** the use of "steady-state free precession" sequence for C_3F_8 imaging was optimized by both simulation and experimental validation, through both phantom and in-vivo imaging. Due to the requirement of high FA and low TR SAR constraints were a limiting factor for in-vivo imaging. In fact, for in-vivo imaging an

improvement in SNR over SPGR imaging by nearly a factor of 2 was demonstrated at 1.5T, but not at 3T, due to safety constraints of power deposition. This has important implications in determining the optimal field strength to perform ^{19}F ventilation imaging. The improvement in SNR with SSFP is close to the increase expected with the higher field strength of 3T vs. 1.5 T. Also, at 1.5T the T_2^* is higher, allowing for a further relative greater SNR at 1.5T. However, for various methods of parameter mapping that employ SPGR imaging, with higher TRs, 3T imaging still has a higher base SNR. Additionally, the use of the SSFP sequence at 1.5T introduces the potential for artefacts. Therefore, future comparisons of imaging and parameter mapping at the two field strengths are still required, with T_2^* mapping to be performed at 1.5T comparable to those presented in **Chapter 6** at 3T.

Chapter 7 details the investigation of methods of acquiring and reconstructing sparsely sampled k-space data for ^{19}F ventilation imaging. Initially, retrospective simulation was carried out with a HP ^{3}He high-resolution 3D imaging data-set obtained with a single transceive coil and comparing an established method of reconstruction to a newly developed one. The results of this simulation showed that AF should remain lower than 2-3, that there is an optimal AF and resolution associated with a given SNR and that for the range of SNR expected with ^{19}F ventilation imaging a high degree of error is expected compared to the high-resolution of HP gas imaging. However, it is difficult to apply the results generally to the ^{19}F ventilation imaging carried out within this thesis due to the different in contrast with ^{19}F vs. HP gas imaging and since receive arrays were primarily used in imaging.

This limitation in the analysis was partially overcome by first developing 3D printed lung phantoms to perform prospective experimentation with, then performing ^{19}F sparsely sampled in-vivo imaging with receiver arrays. Results obtained from prospective analysis of images with the 3D lung phantoms corroborated those of the retrospective simulations. Also, the sparsely sampled in-vivo data appeared to be visually superior to low-resolution images obtained with equivalent imaging times, but there was no way to obtain an objective measure without a baseline fully sampled image to compare to.

To overcome the limitations of the research presented in **Chapter 7** four significant improvements to the methodology should be done in future work.

- High resolution HP gas images should be obtained using an array with comparable element count to that used with ^{19}F imaging for retrospective simulation.
- ^{19}F imaging should be performed with an improved and more realistic lung phantom using an array of receivers for prospective analysis.

- The two reconstruction methods already proposed in **Chapter 7** should be compared to the more recent variations of SPIRiT.

- In-vivo sparse imaging should be performed with HP gas imaging to compare to the fully-sampled data by the same reconstruction methods, which will contribute to the validation of the sparsely sampled ^{19}F in-vivo data.

Although the proposed improvements would greatly improve the reliability of the results, and provide greater insight into the optimal reconstruction method for an array of coils, some of the key results may be applied to future ^{19}F ventilation imaging. Specifically, sparse sampling does result in some improvement in image quality over simple Cartesian lower-resolution imaging, AF should be restricted to <2-3, and different reconstruction strategies result in comparable image quality.

The preliminary results of two research studies exploring ventilation metrics obtained by ^{19}F ventilation imaging are also described in this thesis.

Presented in **Chapter 8**, healthy volunteer participants of a study were scanned with C_3F_8 ^{19}F and HP ^{129}Xe and measured metrics of ventilation and diffusion were compared. The results presented in this chapter were achievable largely as a result of the progress presented in the previous chapters. The use of SSFP imaging, in addition to the use of coil arrays, allowed ventilation imaging with $10x10x10mm^3$ resolution to be obtained at 1.5T with SNRs higher than that obtained at 3T. This allowed segmentation and %VV analysis to be carried out with a number of volunteers, demonstrating consistent results that were comparable to %VV obtained with HP ^{129}Xe ventilation scanning. In addition, the improvement in SNR obtained with the coil arrays permitted the mapping of ADC in healthy individuals, which would not have been possible with the resolution used otherwise, since the SNR obtained was near the border of the range acceptable for accurate analysis regions of the lung. The ^{19}F ADC mapping was also found to be comparable to ^{129}Xe ADC mapping, but with reduced sensitivity to changes in lung physiology due to lung inflation, attributed to the lower diffusion coefficient. Furthermore, the mapping of T_1 at the resolution used would not have been achievable without the improved SNR, since the accuracy of the variable flip angle method is highly SNR and FA dependent.

In **Chapter 9**, imaging parameters with ^{19}F at 3T were optimized, and a cohort of healthy volunteers were scanned and %VV analysed. This study was performed in collaboration with Newcastle University, but results presented and analysed here are those obtained at the University of Sheffield. The first phase of the study involved sequence optimization and a

number of easily implementable proposed improvements over the initial tested sequence parameters were derived. Since the TR is restricted for proton imaging, and a low TE is desired to reduce susceptibility artefacts and improve the SNR of lung parenchyma, the use of multi-echo imaging is recommended to improve the SNR and segmentability of images for single breath-hold images. Furthermore, the use of multi-echo imaging was also found to improve the SNR of ^{19}F ventilation imaging by 50% by optimizing the dead-time required by constrained TR length and lowering the echo time of the first echo, while allowing for T_2^* mapping as a valuable source of physiologically related data to be analysed. The use of higher than optimal mean FA for lung parenchyma was deemed to be beneficial for final image quality due to the inhomogeneity of the coil, and in combination with multi-echo imaging resulted in nearly triple the SNR in regions critical for successful segmentation. These proposed improvements were not implemented in the final protocol, but may be beneficial in future studies. As a result of the methods developed in **Chapter 8,** changes to the protocol where continual imaging is employed as the volunteer breathes from the bag would allow for FV to be obtained along-side T_2^* maps and ventilation scans with improved SNR.

The second phase of the study detailed in **Chapter 9** involved testing the repeatability of ventilation imaging in terms of SNR and inter-operator based calculation of %VV from multiple scans in the same session with healthy volunteers. Based on the analysis presented the SNR remains consistent across the multiple scans for each volunteers, but there is high variability between individuals. For healthy individuals the %VV calculated is >97%, but some reduction in %VV is noted in multiple volunteers in the anterior portion of the lungs due to low SNR. This is remedied when the images from multiple scans are registered and averaged together, which is post-processing step that may be useful for future ^{19}F imaging because of the ease of performing multiple breath-hold scans. Overall, the result of high %VV in healthy individual is not unexpected, and the most interesting results are expected to come from comparison to imaging performed on volunteers with known respiratory conditions. This will be done in future work in phase 3 of the study and comparison to previous studies with HP gas imaging may also be made.

The results presented in **Chapter 8** and **Chapter 9** are very encouraging for future ^{19}F gas lung research. It was established that consistent values of ventilation and parameter mapping are obtained in healthy volunteers, and that many scans may be performed efficiently in the same imaging session. As such, the work presented here will promote fluorinated gas MRI as a viable method of ventilation imaging that is complementary to HP gas MRI. Furthermore, the advantage of ^{19}F imaging is that these results may be obtained in a reduced scan time, and

with reduced cost compared to HP gas imaging, due to the immediate availability of TP gas. However, the clear downside with ^{19}F imaging is reduced sensitivity compared to HP gas imaging. The results presented in this thesis are at the boundaries of what may be achieved with ^{19}F imaging, since the coil design and sequence optimization performed were shown to be approaching theoretical limits. Therefore, future work will focus on establishing what the sensitivity of the fully optimized ^{19}F ventilation imaging and parameter mapping (T_2^*, T_1, ADC and FV) is to observable differences in diseased lungs, and determining whether the sensitivity is enough to be useful either clinically or as a research tool.

List of Publications

Journal Articles

- **Maunder A**, Rao M, Robb F, Wild JM. "Comparison of MEMS switches and PIN diodes for switched dual tuned RF coils. " Magn Reson Med. 2018; 80(4):1746-1753. doi: 10.1002/mrm.27156.

- **Maunder A**, Rao M, Robb F, Wild JM. "Optimization of Steady-State Free Precession MRI for Lung Ventilation Imaging with ^{19}F C_3F_8 at 1.5 T and 3T. " Magn Reson Med. 2019; 81(2):1130:1142. doi: 10.1002/mrm.27479

- **Maunder A**, Rao M, Robb F, Wild JM. "Linear Ladder Resonators for Improved Transmit Efficiency of Individual Elements in Transceive Arrays: Application for a Thorax Transceive Array for ^{19}F and ^{1}H Lung MRI" to be submitted to IEEE transactions on Medical Imaging

- **Maunder A**, Rao M, Robb F, Wild JM. "An 8-element Tx/Rx Array Utilizing MEMS Detuning Combined with 6 Rx Loops for ^{19}F and ^{1}H Lung Imaging at 1.5 T." submitted to Mag. Reson. Med.

Conference Proceedings

- Chan H-F, **Maunder A**, Wild J. "Comparison of apparent diffusion coefficient mapping in the lungs of healthy volunteers with ^{19}F C_3F_8 and hyperpolarized ^{129}Xe gas MRI," Proc. Intl. Soc. Mag. Reson. Med. 2019;27

- **Maunder A**, Robb F, Rao M, Wild J. "Triple Tuned 6-element Asymmetric Mode Ladder-Resonator/Transceive-Array for Thoracic Imaging of ^{19}F/^{1}H at 1.5T and ^{129}Xe/^{19}F at 3T," Proc Intl Soc Mag Reson Med. 2019;27:4945

- Pippard B, Neal M, **Maunder A**, Forrest I, Sabroe I, Lawson R, et al. Assessing regional lung ventilation with ^{19}F-MRI of inhaled perfluoropropane. European Respiratory Journal. 2018;52(suppl 62):OA3799

- **Maunder A**, Hughes P, Norquay G, Robb F, Rao M, Wild J. Comparison of inhaled 19F C_3F_8 and hyperpolarized ^{129}Xe lung ventilation MRI. European Respiratory Journal. 2018;52(suppl 62):OA5177

- **Maunder A**, Robb F, Rao M, Wild J. A 3D printed lung phantom for exploration of the limits of ^{19}F-C_3F_8 ventilation imaging resolution and SNR," Proc Intl Soc Mag Reson Med. 2018;26:1729

- **Maunder A**, Collier G Robb F, Rao M, Wild J. "Evaluation of Sparse Sampling for Improved Image Quality of ^{19}F Fluorinated Gas Lung Ventilation MRI Proc Intl Soc Mag Reson Med. 2018;26:3538

- **Maunder A**, Robb F, Rao M, Wild J. Application of Asymmetric Mode Ladder Resonators for Improved Efficiency of Individual Elements in Transceive Arrays. Proc Intl Soc Mag Reson Med. 2018;26:4273

- **Maunder A**, Rao M, Wild J. Optimization of Steady-state Free Precession with ^{19}F Perfluoropropane for Increased Signal-to-Noise for Human Lung Ventilation Imaging at 3 T. Proc Intl Soc Mag Reson Med. 2018;26:2470

- **Maunder A**, Hughes PJC, Chan H-F, Norquay G, Collier G, Rodgers O, et al. Comparing ^{19}F C$_3$F$_8$ Lung Ventilation Imaging with Hyperpolarized ^{129}Xe: Similarities and Limitations. Proc Intl Soc Mag Reson Med. 2018;26:1085

- Chacon-Caldera, J, **Maunder A**, Rao M, Norquay G, Rodgers O, Clemence M, Puddu C, Schad L, Wild J, "Dynamic MRI of Hyperpolarized Xenon-129 Uptake in the Human Kidney Using a Dedicated Transmission-Only-Reception-Only Array at 3 Tesla," Proc Intl Soc Mag Reson Med. 2018;26:4470

- **Maunder A**, Norquay G, Rao M, Wild J, "Compact NMR Spectrometer for ^{129}Xe Polarization Monitoring with Java Based Signal Processing and User Interface," Proc. Intl. Soc. Mag. Reson. Med. 2017;25:4438

- **Maunder A**, Stewart NJ, Rao M, Robb F, Wild J "Steady-state Free Precession for Improved Signal to Noise in Lung Ventilation Imaging with ^{19}F Perfluoropropane at 1.5T." Proc. Intl. Soc. Mag. Reson. Med. 2017;25;3318

- **Maunder A**, Rao M, Robb FJL, Wild JM. Combined Transmit Array and 8-Channel Receive Coil Array for ^{19}F/^{1}H for Human Lung Imaging at 1.5 T Utilizing MEMS Transmit-Receive Detuning. Proc Intl Soc Mag Reson Med. 2017;25:1052

- **Maunder A**, Rao M, Robb F, Wild J. RF coil design for multi-nuclear lung MRI of ^{19}F fluorinated gases and ^{1}H using MEMS. Proc Intl Soc Mag Reson Med. 2016;24:3504

References

1.   Bloch F, Hansen WW, Packard M. The Nuclear Induction Experiment. Physical Review. 1946;70(7-8):474-85.
2.   Purcell EM, Torrey HC, Pound RV. Resonance Absorption by Nuclear Magnetic Moments in a Solid. Physical Review. 1946;69(1-2):37-8.
3.   Lauterbur PC. Image Formation by Induced Local Interactions: Examples Employing Nuclear Magnetic Resonance. 1973;242(5394):190-1.
4.   Mansfield P. Multi-planar image formation using NMR spin echoes. Journal of Physics C: Solid State Physics. 1977;10(3):L55.
5.   Hudson TM, Hamlin DJ, Enneking WF, Pettersson H. Magnetic resonance imaging of bone and soft tissue tumors: Early experience in 31 patients compared with computed tomography. Skeletal Radiology. 1985;13(2):134-46.
6.   Weekes RG, Berquist TH, McLeod RA, Zimmer WD. Magnetic resonance imaging of soft-tissue tumors: comparison with computed tomography. Magn Reson Imaging. 1985;3(4):345-52.
7.   Nishimura DG. Principles of Magnetic Resonance Imaging: Stanford University; 1996.
8.   Liang Z, Lauterbur P. Principles of Magnetic Resonance Imaging: A Signal Processing Perspective: Wiley-IEEE Press; 2000.
9.   Abragam A. Principles of Nuclear Magnetism: Oxford University Press; 1961.
10.   Bransden PBH, Joachain PCJ. Quantum Mechanics. 2nd ed. Essex: Pearson Education Limited; 2000.
11.   Krane KS. Introductory Nuclear Physics. 2nd ed: John Wiley and Sons, Inc.; 1988.
12.   Santiago-Gonzalez D, Auranen K, Avila ML, Ayangeakaa AD, Back BB, Bottoni S, et al. Probing the Single-Particle Character of Rotational States in ^{19}F Using a Short-Lived Isomeric Beam. Physical Review Letters. 2018;120(12):122503.
13.   Wildenthal BH, Chung W. Collapse of the conventional shell-model ordering in the very-neutron-rich isotopes of Na and Mg. Physical Review C. 1980;22(5):2260-2.
14.   Harris RK, Becker ED, Cabral de Menezes SM, Goodfellow R, Granger P. NMR nomenclature: nuclear spin properties and conventions for chemical shifts. IUPAC Recommendations 2001. International Union of Pure and Applied Chemistry. Physical Chemistry Division. Commission on Molecular Structure and Spectroscopy. Magnetic Resonance in Chemistry. 2002;40(7):489-505.
15.   Bowley R, Sanchez M. Introductory Statistical Mechanics. Oxford: Claredon Press; 2000.
16.   Bottomley PA. The Basics. eMagRes: John Wiley & Sons, Ltd; 2007.
17.   Hoult DI. The principle of reciprocity in signal strength calculations—A mathematical guide. Concepts in Magnetic Resonance. 2000;12(4):173-87.
18.   Solomon I. Relaxation Processes in a System of Two Spins. Physical Review. 1955;99(2):559-65.
19.   Bloembergen N, Purcell EM, Pound RV. Relaxation Effects in Nuclear Magnetic Resonance Absorption. Physical Review. 1948;73(7):679-712.
20.   Jameson CJ, Jameson AK, Hwang JK. Nuclear spin relaxation by intermolecular magnetic dipole coupling in the gas phase. 129Xe in oxygen. The Journal of Chemical Physics. 1988;89(7):4074-81.
21.   Wright SM. Receiver Loop Arrays. eMagRes. 2011.
22.   Ocali O, Atalar E. Ultimate intrinsic signal-to-noise ratio in MRI. Magnetic Resonance in Medicine. 1998;39(3):462-73.
23.   Jian-Ming J. Electromagnetics in magnetic resonance imaging. IEEE Antennas and Propagation Magazine. 1998;40(6):7-22.

24.   Hidalgo-Tobon SS. Theory of gradient coil design methods for magnetic resonance imaging. Concepts in Magnetic Resonance Part A. 2010;36A(4):223-42.

25.   Pauly J, Le Roux P, Nishimura D, Macovski A. Parameter relations for the Shinnar-Le Roux selective excitation pulse design algorithm [NMR imaging]. IEEE transactions on medical imaging. 1991;10(1):53-65.

26.   Edelstein WA, Glover GH, Hardy CJ, Redington RW. The intrinsic signal-to-noise ratio in NMR imaging. Magnetic Resonance in Medicine. 1986;3(4):604-18.

27.   Parker DL, Gullberg GT. Signal-to-noise efficiency in magnetic resonance imaging. Medical physics. 1990;17(2):250-7.

28.   Reeder SB, McVeigh ER. The Effect of High Performance Gradients on Fast Gradient Echo Imaging. Magnetic Resonance in Medicine. 1994;32(5):612-21.

29.   Ernst RR, Anderson WA. Application of Fourier Transform Spectroscopy to Magnetic Resonance. Review of Scientific Instruments. 1966;37(1):93-102.

30.   Hargreaves BA, Vasanawala SS, Pauly JM, Nishimura DG. Characterization and reduction of the transient response in steady-state MR imaging. Magn Reson Med. 2001;46(1):149-58.

31.   Scheffler K, Hennig J. Is TrueFISP a gradient-echo or a spin-echo sequence? Magn Reson Med. 2003;49(2):395-7.

32.   Scheffler K, Lehnhardt S. Principles and applications of balanced SSFP techniques. European radiology. 2003;13(11):2409-18.

33.   Ajraoui S, Lee KJ, Deppe MH, Parnell SR, Parra-Robles J, Wild JM. Compressed sensing in hyperpolarized 3He Lung MRI. Magnetic Resonance in Medicine. 2010;63(4):1059-69.

34.   Wild JM, Teh K, Woodhouse N, Paley MNJ, Fichele S, de Zanche N, et al. Steady-state free precession with hyperpolarized 3He: Experiments and theory. Journal of Magnetic Resonance. 2006;183(1):13-24.

35.   Stewart NJ, Norquay G, Griffiths PD, Wild JM. Feasibility of human lung ventilation imaging using highly polarized naturally abundant xenon and optimized three-dimensional steady-state free precession. Magnetic Resonance in Medicine. 2015;74(2):346-52.

36.   Deppe MH, Wild JM. Simulations of the hyperpolarized 129Xe SSFP and SPGR pulse sequence signal response. Proc Intl Soc Mag Reson Med. 2008;16:2681.

37.   Chilla GS, Tan CH, Xu C, Poh CL. Diffusion weighted magnetic resonance imaging and its recent trend-a survey. Quantitative imaging in medicine and surgery. 2015;5(3):407-22.

38.   Yablonskiy DA, Sukstanskii AL, Leawoods JC, Gierada DS, Bretthorst GL, Lefrak SS, et al. Quantitative in vivo assessment of lung microstructure at the alveolar level with hyperpolarized 3He diffusion MRI. Proceedings of the National Academy of Sciences. 2002;99(5):3111-6.

39.   Chen XJ, Möller HE, Chawla MS, Cofer GP, Driehuys B, Hedlund LW, et al. Spatially resolved measurements of hyperpolarized gas properties in the lung in vivo. Part I: Diffusion coefficient. Magnetic Resonance in Medicine. 1999;42(4):721-8.

40.   Rahmer J, Bornert P, Groen J, Bos C. Three-dimensional radial ultrashort echo-time imaging with T2 adapted sampling. Magn Reson Med. 2006;55(5):1075-82.

41.   Kemper VG, De Martino F, Vu AT, Poser BA, Feinberg DA, Goebel R, et al. Sub-millimeter T(2) weighted fMRI at 7 T: comparison of 3D-GRASE and 2D SE-EPI. Frontiers in Neuroscience. 2015;9:163.

42.   Pruessmann KP, Weiger M, Scheidegger MB, Boesiger P. SENSE: Sensitivity encoding for fast MRI. Magnetic Resonance in Medicine. 1999;42(5):952-62.

43.   Sodickson DK, Manning WJ. Simultaneous acquisition of spatial harmonics (SMASH): fast imaging with radiofrequency coil arrays. Magnetic resonance in medicine. 1997;38(4):591-603.

44. Blaimer M, Breuer F, Mueller M, Heidemann RM, Griswold MA, Jakob PM. SMASH, SENSE, PILS, GRAPPA: how to choose the optimal method. Topics in magnetic resonance imaging : TMRI. 2004;15(4):223-36.

45. Griswold MA, Jakob PM, Heidemann RM, Nittka M, Jellus V, Wang J, et al. Generalized autocalibrating partially parallel acquisitions (GRAPPA). Magnetic Resonance in Medicine. 2002;47(6):1202-10.

46. Larkman DJ, Nunes RG. Parallel magnetic resonance imaging. Phys Med Biol. 2007;52(7):R15-55.

47. Breuer FA, Kannengiesser SA, Blaimer M, Seiberlich N, Jakob PM, Griswold MA. General formulation for quantitative G-factor calculation in GRAPPA reconstructions. Magn Reson Med. 2009;62(3):739-46.

48. Lustig M, Donoho D, Pauly JM. Sparse MRI: The application of compressed sensing for rapid MR imaging. Magnetic Resonance in Medicine. 2007;58(6):1182-95.

49. Lustig M, Pauly JM. SPIRiT: Iterative self-consistent parallel imaging reconstruction from arbitrary k-space. Magnetic Resonance in Medicine. 2010;64(2):457-71.

50. Murphy M, Alley M, Demmel J, Keutzer K, Vasanawala S, Lustig M. Fast ℓ_1-SPIRiT Compressed Sensing Parallel Imaging MRI: Scalable Parallel Implementation and Clinically Feasible Runtime. IEEE transactions on medical imaging. 2012;31(6):1250-62.

51. Hollingsworth KG. Reducing acquisition time in clinical MRI by data undersampling and compressed sensing reconstruction. Phys Med Biol. 2015;60(21):R297-322.

52. Henderson AC, Sá RC, Theilmann RJ, Buxton RB, Prisk GK, Hopkins SR. The gravitational distribution of ventilation-perfusion ratio is more uniform in prone than supine posture in the normal human lung. Journal of Applied Physiology. 2013;115(3):313-24.

53. Verbanck S, Thompson BR, Schuermans D, Kalsi H, Biddiscombe M, Stuart-Andrews C, et al. Ventilation heterogeneity in the acinar and conductive zones of the normal ageing lung. Thorax. 2012;67(9):789-95.

54. Dempsey TM, Scanlon PD. Pulmonary Function Tests for the Generalist: A Brief Review. Mayo Clinic proceedings. 2018;93(6):763-71.

55. Berthezène Y, Vexler V, Clément O, Mühler A, Moseley ME, Brasch RC. Contrast-enhanced MR imaging of the lung: assessments of ventilation and perfusion. Radiology. 1992;183(3):667-72.

56. Biederer J, Mirsadraee S, Beer M, Molinari F, Hintze C, Bauman G, et al. MRI of the lung (3/3)-current applications and future perspectives. Insights into imaging. 2012;3(4):373-86.

57. Hughes PJC, Horn FC, Collier GJ, Biancardi A, Marshall H, Wild JM. Spatial fuzzy c-means thresholding for semiautomated calculation of percentage lung ventilated volume from hyperpolarized gas and 1 H MRI. Journal of magnetic resonance imaging : JMRI. 2017.

58. Couch MJ, Fox MS, Viel C, Gajawada G, Li T, Ouriadov AV, et al. Fractional ventilation mapping using inert fluorinated gas MRI in rat models of inflammation and fibrosis. NMR in Biomedicine. 2016;29(5):545-52.

59. Horn FC, Deppe MH, Marshall H, Parra-Robles J, Wild JM. Quantification of regional fractional ventilation in human subjects by measurement of hyperpolarized [3]He washout with 2D and 3D MRI. Journal of Applied Physiology. 2014;116(2):129-39.

60. Obert A, Gutberlet M, Rotärmel A, Wacker F, Vogel-Claussen J. Mapping of Ventilation/Perfusion Ratios in the human lung using ^{19}F MRI of Perfluoropropane. Proc Intl Soc Mag Reson Med. 2018;26:2473.

61. Kohlmann P, Strehlow J, Jobst B, Krass S, Kuhnigk JM, Anjorin A, et al. Automatic lung segmentation method for MRI-based lung perfusion studies of patients with chronic

obstructive pulmonary disease. International journal of computer assisted radiology and surgery. 2015;10(4):403-17.

62.   Cleveland ZI, Cofer GP, Metz G, Beaver D, Nouls J, Kaushik SS, et al. Hyperpolarized 129Xe MR Imaging of Alveolar Gas Uptake in Humans. PLOS ONE. 2010;5(8):e12192.

63.   Paris OfEC-oaD. Organisation for Economic Co-operation and Development. OECD Health Data 2005: statistics and indicators for 30 countries. 2005.

64.   Organization WH. The Global Burden of Disease Report. 2004.

65.   Brody AS, Klein JS, Molina PL, Quan J, Bean JA, Wilmott RW. High-resolution computed tomography in young patients with cystic fibrosis: distribution of abnormalities and correlation with pulmonary function tests. The Journal of pediatrics. 2004;145(1):32-8.

66.   Gustafsson PM, Aurora P, Lindblad A. Evaluation of ventilation maldistribution as an early indicator of lung disease in children with cystic fibrosis. The European respiratory journal. 2003;22(6):972-9.

67.   Lopez AD, Shibuya K, Rao C, Mathers CD, Hansell AL, Held LS, et al. Chronic obstructive pulmonary disease: current burden and future projections. The European respiratory journal. 2006;27(2):397-412.

68.   Jacobs JE, van de Lisdonk EH, Smeele I, van Weel C, Grol R. Management of patients with asthma and COPD: monitoring quality of life and the relationship to subsequent GP interventions. Family Practice. 2001;18(6):574-80.

69.   Middleton H, Black RD, Saam B, Cates GD, Cofer GP, Guenther R, et al. MR Imaging with Hyperpolarized 3He Gas. Magnetic Resonance in Medicine. 1995;33(2):271-5.

70.   Kastler A. Quelques suggestions concernant la production optique et la détection optique d'une inégalité de population des niveaux de quantifigation spatiale des atomes. Application à l'expérience de Stern et Gerlach et à la résonance magnétique. J Phys Radium. 1950;11(6):255-65.

71.   Albert MS, Cates GD, Driehuys B, Happer W, Saam B, Springer CS, et al. Biological magnetic resonance imaging using laser-polarized ^{129}Xe. Nature. 1994;370(6486):199-201.

72.   Lange Ed, Brookemand J, III JM, Daniel T, Driehuys B, Cates G, et al. Proc RSNA, 82nd Annual Meeting. 1996.

73.   Albert MS, Balamore D. Development of hyperpolarized noble gas MRI. Nuclear instruments & methods in physics research Section A, Accelerators, spectrometers, detectors and associated equipment. 1998;402:441-53.

74.   Happer W, Miron E, Schaefer S, Schreiber D, van Wijngaarden WA, Zeng X. Polarization of the nuclear spins of noble-gas atoms by spin exchange with optically pumped alkali-metal atoms. Physical Review A. 1984;29(6):3092-110.

75.   Driehuys B, Cates GD, Happer W. Surface Relaxation Mechanisms of Laser-Polarized 129Xe. Physical Review Letters. 1995;74(24):4943-6.

76.   Shao W, Wang G, Hughes EW. Measurement of spin-exchange rate constants between 129Xe and alkali metals. Physical Review A. 2005;72(2):022713.

77.   Happer W. Optical Pumping. Reviews of Modern Physics. 1972;44(2):169-249.

78.   Romalis MV, Miron E, Cates GD. Pressure broadening of Rb D1 and D2 lines by (3)He, (4)He, N2, and Xe: Line cores and near wings. Physical Review A. 1997;56(6):4569-78.

79.   Happer W, Van Wijngaarden WA. An optical pumping primer. Hyperfine Interact. 1987;38(1-4):435-70.

80.   Driehuys B, Cates GD, Miron E, Sauer K, Walter DK, Happer W. High-volume production of laser-polarized 129Xe. Applied Physics Letters. 1996;69(12):1668-70.

81.   Kaushik SS, Cleveland ZI, Cofer GP, Metz G, Beaver D, Nouls J, et al. Diffusion-weighted hyperpolarized 129Xe MRI in healthy volunteers and subjects with chronic obstructive pulmonary disease. Magnetic Resonance in Medicine. 2011;65(4):1154-65.

82.	Emami K, Stephen M, Kadlecek S, Cadman RV, Ishii M, Rizi RR. Quantitative Assessment of Lung Using Hyperpolarized Magnetic Resonance Imaging. Proceedings of the American Thoracic Society. 2009;6(5):431-8.

83.	Stoltz E, Meyerhoff M, Bigelow N, Leduc M, Nacher PJ, Tastevin G. High nuclear polarization in3He and3He-4He gas mixtures by optical pumping with a laser diode. Appl Phys B. 1996;63(6):629-33.

84.	Stewart NJ, Norquay G, Marshall H, Wild JM. Feasibility of high quality lung MRI with naturally-abundant hyperpolarised 129Xe. European Respiratory Journal. 2014;44(Suppl 58).

85.	Chan HF, Stewart NJ, Norquay G, Collier GJ, Wild JM. 3D diffusion-weighted (129)Xe MRI for whole lung morphometry. Magnetic Resonance in Medicine. 2018;79(6):2986-95.

86.	Conradi MS, Yablonskiy DA, Woods JC, Gierada DS, Jacob RE, Chang YV, et al. 3He Diffusion MRI of the Lung1. Academic Radiology. 2005;12(11):1406-13.

87.	Ajraoui S, Parra-Robles J, Marshall H, Deppe MH, Clemence M, Wild JM. Acquisition of 3He ventilation images, ADC, T2* and B1 maps in a single scan with compressed sensing. NMR in Biomedicine. 2012;25(1):44-51.

88.	Kauczor HU, Hanke A, Van Beek EJ. Assessment of lung ventilation by MR imaging: current status and future perspectives. European radiology. 2002;12(8):1962-70.

89.	Månsson S, Wolber J, Driehuys B, Wollmer P, Golman K. Characterization of diffusing capacity and perfusion of the rat lung in a lipopolysaccharide disease model using hyperpolarized 129Xe. Magnetic Resonance in Medicine. 2003;50(6):1170-9.

90.	Kaushik SS, Freeman MS, Yoon SW, Liljeroth MG, Stiles JV, Roos JE, et al. Measuring diffusion limitation with a perfusion-limited gas—Hyperpolarized 129Xe gas-transfer spectroscopy in patients with idiopathic pulmonary fibrosis. Journal of Applied Physiology. 2014;117(6):577-85.

91.	Weatherley ND, Stewart NJ, Chan H-F, Austin M, Smith LJ, Collier G, et al. Hyperpolarised xenon magnetic resonance spectroscopy for the longitudinal assessment of changes in gas diffusion in IPF. Thorax. 2018.

92.	Smith LJ, Collier GJ, Marshall H, Hughes PJC, Biancardi AM, Wildman M, et al. Patterns of regional lung physiology in cystic fibrosis using ventilation magnetic resonance imaging and multiple-breath washout. European Respiratory Journal. 2018;52(5).

93.	Marshall H, Collier GJ, Johns CS, Chan H-F, Norquay G, Lawson RA, et al. Imaging Collateral Ventilation in Patients With Advanced Chronic Obstructive Pulmonary Disease: Relative Sensitivity of 3He and 129Xe MRI. Journal of Magnetic Resonance Imaging.0(0).

94.	Hughes PJC, Smith L, Chan H-F, Tahir BA, Norquay G, Collier GJ, et al. Assessment of the influence of lung inflation state on the quantitative parameters derived from hyperpolarized gas lung ventilation MRI in healthy volunteers. Journal of Applied Physiology.0(0):null.

95.	Halaweish AF, Hoffman EA, Thedens DR, Fuld MK, Sieren JP, van Beek EJR. Effect of Lung Inflation Level on Hyperpolarized (3)He Apparent Diffusion Coefficient Measurements in Never-Smokers. Radiology. 2013;268(2):572-80.

96.	Holland GN, Bottomley PA, Hinshaw WS. 19F magnetic resonance imaging. Journal of Magnetic Resonance. 1977;28(1):133-6.

97.	Jacob RE, Chang YV, Choong CK, Bierhals A, Zheng Hu D, Zheng J, et al. ^{19}F MR imaging of ventilation and diffusion in excised lungs. Magnetic Resonance in Medicine. 2005;54(3):577-85.

98.	Couch MJ, Ball IK, Li T, Fox MS, Littlefield SL, Biman B, et al. Pulmonary ultrashort echo time 19F MR imaging with inhaled fluorinated gas mixtures in healthy volunteers: feasibility. Radiology. 2013;269(3):903-9.

99. Kauczor H, Surkau R, Roberts T. MRI using hyperpolarized noble gases. European radiology. 1998;8(5):820-7.

100. Mohanty S, Bernstein HJ. Fluorine Relaxation by NMR Absorption in Gaseous CF4, SiF4, and SF6. The Journal of Chemical Physics. 1970;53(1):461-2.

101. Huang MQ, Ye Q, Williams DS, Ho C. MRI of lungs using partial liquid ventilation with water-in-perfluorocarbon emulsions. Magnetic Resonance in Medicine. 2002;48(3):487-92.

102. Thomas SR, Gradon L, Pratsinis SE, Pratt RG, Fotou GP, McGoron AJ, et al. Perfluorocarbon Compound Aerosols for Delivery to the Lung as Potential 19F Magnetic Resonance Reporters of Regional Pulmonary pO_2. Investigative Radiology. 1997;32(1):29-38.

103. Rinck PA, Petersen SB, Lauterbur PC. NMR-Imaging von fluorhaltigen Substanzen. Fortschr Röntgenstr. 1984;140(03):239-43.

104. Nelson TR, Newman FD, Schiffer LM, Reith JD, Cameron SL. Fluorine nuclear magnetic resonance: Calibration and system optimization. Magnetic Resonance Imaging. 1985;3(3):267-73.

105. Lizak MJ, Conradi MS, Fry CG. NMR imaging of gas imbibed into porous ceramic. Journal of Magnetic Resonance (1969). 1991;95(3):548-57.

106. Kuethe DO, Caprihan A, Fukushima E, Waggoner RA. Imaging lungs using inert fluorinated gases. Magnetic Resonance in Medicine. 1998;39(1):85-8.

107. Eger MDEdmond I, Lundgren MDC, Miller MDStanley L, Stevens MDWendell C. Anesthetic Potencies of Sulfur Hexafluoride, Carbon Tetrafluoride, Chloroform and Ethrane in DogsCorrelation with the Hydrate and Lipid Theories of Anesthetic Action. Anesthesiology. 1969;30(2):127-34.

108. Schreiber WG, Eberle B, Laukemper-Ostendorf S, Markstaller K, Weiler N, Scholz A, et al. Dynamic 19F-MRI of pulmonary ventilation using sulfur hexafluoride (SF6) gas. Magnetic Resonance in Medicine. 2001;45(4):605-13.

109. Kuethe DO, Caprihan A, Gach HM, Lowe IJ, Fukushima E. Imaging obstructed ventilation with NMR using inert fluorinated gases. Journal of applied physiology (Bethesda, Md : 1985). 2000;88(6):2279-86.

110. Kuethe DO, Behr VC, Begay S. Volume of rat lungs measured throughout the respiratory cycle using 19F NMR of the inert gas SF6. Magn Reson Med. 2002;48(3):547-9.

111. Canfield RE, Rahn H. Arterial-Alveolar N2 Gas Pressure Differences Due to Ventilation-Perfusion Variations. Journal of Applied Physiology. 1957;10(2):165-72.

112. Kober F, Koenigsberg B, Belle V, Viallon M, Leviel JL, Delon A, et al. NMR Imaging of Thermally Polarized Helium-3 Gas. Journal of Magnetic Resonance. 1999;138(2):308-12.

113. Zhao L, Mulkern R, Venkatesh A, Gudbjartsson H, Jolesz F, Albert M. Hyperpolarized Xe-129 T2 and diffusion measurements for fast spinecho
MRI. Proc 6th Annual Meeting ISMRM. 1998.

114. Pérez-Sánchez JM, de Alejo RP, Rodríguez I, Cortijo M, Peces-Barba G, Ruiz-Cabello J. In vivo diffusion weighted ^{19}F MRI using SF_6. Magnetic Resonance in Medicine. 2005;54(2):460-3.

115. Ruiz-Cabello J, Pérez-Sánchez JM, Pérez de Alejo R, Rodríguez I, González-Mangado N, Peces-Barba G, et al. Diffusion-weighted ^{19}F-MRI of lung periphery: Influence of pressure and air–SF_6 composition on apparent diffusion coefficients. Respiratory Physiology & Neurobiology. 2005;148(1–2):43-56.

116. Kuethe DO, Pietraß T, Behr VC. Inert fluorinated gas T1 calculator. Journal of Magnetic Resonance. 2005;177(2):212-20.

117. Chang YV, Conradi MS. Relaxation and diffusion of perfluorocarbon gas mixtures with oxygen for lung MRI. Journal of Magnetic Resonance. 2006;181(2):191-8.

118.   Adolphi NL, Kuethe DO. Quantitative mapping of ventilation-perfusion ratios in lungs by 19F MR imaging of T1 of inert fluorinated gases. Magn Reson Med. 2008;59(4):739-46.
119.   Wolf U, Scholz A, Heussel CP, Markstaller K, Schreiber WG. Subsecond fluorine-19 MRI of the lung. Magnetic Resonance in Medicine. 2006;55(4):948-51.
120.   Wolf U, Scholz A, Terekhov M, Muennemann K, Kreitner K, Werner C, et al. Fluorine-19 MRI of the lung: first human experiment Proc Intl Soc Mag Reson Med. 2008;16:3207.
121.   Halaweish AF, Moon RE, Foster WM, Soher BJ, McAdams HP, MacFall JR, et al. Perfluoropropane gas as a magnetic resonance lung imaging contrast agent in humans. Chest. 2013;144(4):1300-10.
122.   Ball IK, Li T, Fox MS, Biman B, Albert MS. Can Inert Fluorinated Gas MRI Provide Meaningful Functional Lung Information Similar to Hyperpolarized 3He MRI? State of play in Respiratory Structure and Function: Seeing is Believing. p. A3931-A.
123.   Gutberlet M, Kaireit TF, Voskrebenzev A, Lasch F, Freise J, Welte T, et al. Free-breathing Dynamic 19F Gas MR Imaging for Mapping of Regional Lung Ventilation in Patients with COPD. Radiology. 2017:170591.
124.   Couch M, Blasiak B, Tomanek B, Ouriadov A, Fox M, Dowhos K, et al. Hyperpolarized and Inert Gas MRI: The Future. Mol Imaging Biol. 2015;17(2):149-62.
125.   Kruger SJ, Nagle SK, Couch MJ, Ohno Y, Albert M, Fain SB. Functional imaging of the lungs with gas agents. Journal of Magnetic Resonance Imaging. 2015:295-315.
126.   Couch MJ, Ball IK, Li T, Fox MS, Ouriadov AV, Biman B, et al. Inert fluorinated gas MRI: a new pulmonary imaging modality. NMR in Biomedicine. 2014;27(12):1525-34.
127.   Couch MJ, Ball IK, Li T, Fox MS, Biman B, Albert MS. 19F MRI of the Lungs Using Inert Fluorinated Gases: Challenges and New Developments. Journal of Magnetic Resonance Imaging.0(0).
128.   Wild JM, Marshall H, Xu X, Norquay G, Parnell SR, Clemence M, et al. Simultaneous Imaging of Lung Structure and Function with Triple-Nuclear Hybrid MR Imaging. Radiology. 2013;267(1):251-5.
129.   Chen XJ, Möller HE, Chawla MS, Cofer GP, Driehuys B, Hedlund LW, et al. Spatially resolved measurements of hyperpolarized gas properties in the lung in vivo. Part II: T∗2. Magnetic Resonance in Medicine. 1999;42(4):729-37.
130.   Saam B, Yablonskiy DA, Gierada DS, Conradi MS. Rapid imaging of hyperpolarized gas using EPI. Magnetic Resonance in Medicine. 1999;42(3):507-14.
131.   Ouriadov AV, Fox MS, Couch MJ, Li T, Ball IK, Albert MS. In vivo regional ventilation mapping using fluorinated gas MRI with an x-centric FGRE method. Magnetic Resonance in Medicine. 2015;74(2):550-7.
132.   Moller HE, Chen XJ, Saam B, Hagspiel KD, Johnson GA, Altes TA, et al. MRI of the lungs using hyperpolarized noble gases. Magn Reson Med. 2002;47(6):1029-51.
133.   Maunder A, Rao M, Robb F, Wild JM. Optimization of Steady-State Free Precession MRI for Lung Ventilation Imaging with 19F C3F8 at 1.5 T and 3T. Magnetic Resonance in Medicine. 2018.
134.   Deppe MH, Wild JM. Variable flip angle schedules in bSSFP imaging of hyperpolarized noble gases. Magn Reson Med. 2012;67(6):1656-64.
135.   Maunder A, Rao M, Robb F, Wild JM. Optimization of steady-state free precession MRI for lung ventilation imaging with (19) F C3 F8 at 1.5T and 3T. Magn Reson Med. 2018.
136.   Sukstanskii AL, Yablonskiy DA. In vivo lung morphometry with hyperpolarized 3He diffusion MRI: Theoretical background. Journal of Magnetic Resonance. 2008;190(2):200-10.
137.   Karlicek RF, Lowe IJ. A modified pulsed gradient technique for measuring diffusion in the presence of large background gradients. Journal of Magnetic Resonance (1969). 1980;37(1):75-91.

138. Chan H-F, Collier GJ, Weatherley ND, Wild JM. Comparison of in vivo lung morphometry models from 3D multiple b-value 3He and 129Xe diffusion-weighted MRI. Magnetic Resonance in Medicine. 2018;0(0).

139. Chan H-F, Stewart NJ, Parra-Robles J, Collier GJ, Wild JM. Whole lung morphometry with 3D multiple b-value hyperpolarized gas MRI and compressed sensing. Magnetic Resonance in Medicine. 2017;77(5):1916-25.

140. Mitra PP, Sen PN, Schwartz LM. Short-time behavior of the diffusion coefficient as a geometrical probe of porous media. Physical Review B. 1993;47(14):8565-74.

141. Yablonskiy DA, Sukstanskii AL, Quirk JD. Diffusion lung imaging with hyperpolarized gas MRI. NMR Biomed. 2017;30(3).

142. J. SN, Ho-Fung C, J.C. HP, C. HF, Graham N, Madhwesha R, et al. Comparison of 3He and 129Xe MRI for evaluation of lung microstructure and ventilation at 1.5T. Journal of Magnetic Resonance Imaging. 2018;48(3):632-42.

143. Evans A, McCormack D, Ouriadov A, Etemad-Rezai R, Santyr G, Parraga G. Anatomical distribution of 3He apparent diffusion coefficients in severe chronic obstructive pulmonary disease. Journal of magnetic resonance imaging : JMRI. 2007;26(6):1537-47.

144. Fichele S, Woodhouse N, Swift AJ, Said Z, Paley MN, Kasuboski L, et al. MRI of helium-3 gas in healthy lungs: posture related variations of alveolar size. Journal of magnetic resonance imaging : JMRI. 2004;20(2):331-5.

145. Albert RK, Hubmayr RD. The prone position eliminates compression of the lungs by the heart. Am J Respir Crit Care Med. 2000;161(5):1660-5.

146. Commission IE. International Stamdard Medical Equipment-part 2: particular requirements for the safety of magnetic resonance equipment for medical diagnosis, 2nd revision. 2002.

147. 60601-2-33 I. Particular requirements for the basic safety and essential performance of magnetic resonance equipment for medical diagnosis. Medical electrical equipment - Part 2-332015.

148. Roemer PB, Edelstein WA, Hayes CE, Souza SP, Mueller OM. The NMR phased array. Magnetic Resonance in Medicine. 1990;16(2):192-225.

149. Jensen MA, editor A history of MIMO wireless communications. IEEE International Symposium on Antennas and Propagation; 2016 26 June-1 July.

150. Jianmin W, Reykowski A, Dickas J. Calculation of the signal-to-noise ratio for simple surface coils and arrays of coils [magnetic resonance imaging]. Biomedical Engineering, IEEE Transactions on. 1995;42(9):908-17.

151. Mellor P, Checkley D. Active coil isolation in NMR imaging and spectroscopy using PIN diodes and tuned transmission line: a practical approach. Magn Reson Mater Phy. 1995;3(1):35-40.

152. Reykowski A, Wright SM, Porter JR. Design of Matching Networks for Low Noise Preamplifiers. Magnetic Resonance in Medicine. 1995;33(6):848-52.

153. Hayes CE, Roemer PB. Noise correlations in data simultaneously acquired from multiple surface coil arrays. Magnetic Resonance in Medicine. 1990;16(2):181-91.

154. Redpath TW. Signal-to-noise ratio in MRI. The British journal of radiology. 1998;71(847):704-7.

155. Hayes CE, Axel L. Noise performance of surface coils for magnetic resonance imaging at 1.5 T. Medical physics. 1985;12(5):604-7.

156. Morris ML, Jensen MA. Network model for MIMO systems with coupled antennas and noisy amplifiers. IEEE Transactions on Antennas and Propagation. 2005;53(1):545-52.

157. Warnick KF, editor Noise theory of multiport networks and applications to phased array feeds, MRI coil arrays, and MIMO communications. International Conference on Electromagnetics in Advanced Applications; 2012 2-7 Sept.

158.   Warnick KF, Woestenburg B, Belostotski L, Russer P. Minimizing the Noise Penalty Due to Mutual Coupling for a Receiving Array. IEEE Transactions on Antennas and Propagation. 2009;57(6):1634-44.

159.   Warnick KF, Jensen MA, editors. Optimal noise matching condition for mutually-coupled antenna arrays. IEEE Antennas and Propagation Society International Symposium; 2007 9-15 June.

160.   Findeklee C. Array Noise Matching—Generalization, Proof and Analogy to Power Matching. IEEE Transactions on Antennas and Propagation. 2011;59(2):452-9.

161.   Meys RP. A Wave Approach to the Noise Properties of Linear Microwave Devices. IEEE Transactions on Microwave Theory and Techniques. 1978;26(1):34-7.

162.   Wedge SW, Rutledge DB. Noise waves and passive linear multiports. IEEE Microwave and Guided Wave Letters. 1991;1(5):117-9.

163.   Pozar DM. Microwave Engineering. 4th ed: John Wiley and Sons, Inc.; 2012.

164.   Pronic O, Markovic V, editors. Wave approach to S-parameter and noise parameter prediction of FET devices. ICMMT 2000 2000 2nd International Conference on Microwave and Millimeter Wave Technology Proceedings (Cat No00EX364); 2000 14-16 Sept. 2000.

165.   Vaidya MV, Sodickson DK, Lattanzi R. Approaching ultimate intrinsic SNR in a uniform spherical sample with finite arrays of loop coils. Concepts in Magnetic Resonance Part B: Magnetic Resonance Engineering. 2014;44(3):53-65.

166.   Ohliger MA, Ledden P, McKenzie CA, Sodickson DK. Effects of inductive coupling on parallel MR image reconstructions. Magn Reson Med. 2004;52(3):628-39.

167.   Reykowski A, Saylor C, Duensing GR. Do We Need Preamplifier Decoupling? Proc Intl Soc Mag Reson Med. 2011;19:3883.

168.   Kumar A, Bottomley PA. Optimizing the intrinsic signal-to-noise ratio of MRI strip detectors. Magnetic Resonance in Medicine. 2006;56(1):157-66.

169.   Celik H, Eryaman Y, Altintas A, Abdel-Hafez IA, Atalar E. Evaluation of internal MRI coils using ultimate intrinsic SNR. Magn Reson Med. 2004;52(3):640-9.

170.   Soher BJ, Dale BM, Merkle EM. A review of MR physics: 3T versus 1.5T. Magnetic resonance imaging clinics of North America. 2007;15(3):277-90, v.

171.   Kwok WE, You Z. In vivo MRI using liquid nitrogen cooled phased array coil at 3.0 T. Magn Reson Imaging. 2006;24(6):819-23.

172.   Zanche ND, Maunder AM, Charlton T, Wachowicz K, Fallone BG. A Unified Framework for SNR Comparisons of Four Array Image Combination Methods. Proc Intl Soc Mag Reson Med. 2011;19:4659.

173.   Wright SM. Full-wave analysis of planar radiofrequency coils and coil arrays with assumed current distribution. Concepts in Magnetic Resonance. 2002;15(1):2-14.

174.   Hand JW. Modelling the interaction of electromagnetic fields (10 MHz-10 GHz) with the human body: methods and applications. Phys Med Biol. 2008;53(16):R243-86.

175.   Akgun CE. Radiofrequency Fields and SAR for Transverse Electromagnetic (TEM) Surface Coils. eMagRes: John Wiley & Sons, Ltd; 2007.

176.   Moyer ET, Schroeder EA. Finite element formulations of Maxwell's equations-advantages and comparisons between available approaches. IEEE Transactions on Magnetics. 1991;27(5):4217-20.

177.   Sheng XQ, Song W. Essentials of Computational Electromagnetics: John Wiley & Sons Singapore Pte. Ltd.; 2012.

178.   Ho-Le K. Finite element mesh generation methods: a review and classification. Computer-Aided Design. 1988;20(1):27-38.

179.   Jo-Yu W, Lee R. The advantages of triangular and tetrahedral edge elements for electromagnetic modeling with the finite-element method. IEEE Transactions on Antennas and Propagation. 1997;45(9):1431-7.

180.   Shewchuk JR. Delaunay refinement algorithms for triangular mesh generation. Computational Geometry. 2002;22(1):21-74.

181.   Pekel Ü, Mittra R. A finite-element-method frequency-domain application of the perfectly matched layer (PML) concept. Microwave and Optical Technology Letters. 1995;9(3):117-22.

182.   Lattanz R, Grant AK, Sodickson DK. Approaching ultimate SNR and ideal current patterns with finite surface coil arrays on a dielectric cylinder. Proc Intl Soc Mag Reson Med 2008;16.

183.   Wiesinger F, Boesiger P, Pruessmann KP. Electrodynamics and ultimate SNR in parallel MR imaging. Magnetic Resonance in Medicine. 2004;52(2):376-90.

184.   Guerin B, Villena JF, Polimeridis AG, Adalsteinsson E, Daniel L, White JK, et al. The ultimate signal-to-noise ratio in realistic body models. Magn Reson Med. 2017;78(5):1969-80.

185.   Ohliger MA, Grant AK, Sodickson DK. Ultimate intrinsic signal-to-noise ratio for parallel MRI: electromagnetic field considerations. Magn Reson Med. 2003;50(5):1018-30.

186.   De Zanche N, Yahya A, Vermeulen FE, Allen PS. Analytical approach to noncircular section birdcage coil design: Verification with a Cassinian oval coil. Magnetic Resonance in Medicine. 2005;53(1):201-11.

187.   Zanche ND. Birdcage Volume Coil Design. eMagRes: John Wiley & Sons, Ltd; 2007.

188.   Leifer MC. Theory of the quadrature elliptic birdcage coil. Magnetic Resonance in Medicine. 1997;38(5):726-32.

189.   De Zanche N, Chhina N, Teh K, Randell C, Pruessmann KP, Wild JM. Asymmetric quadrature split birdcage coil for hyperpolarized 3He lung MRI at 1.5T. Magnetic Resonance in Medicine. 2008;60(2):431-8.

190.   Dregely I, Ruset IC, Wiggins G, Mareyam A, Mugler JP, Altes TA, et al. 32-channel phased-array receive with asymmetric birdcage transmit coil for hyperpolarized xenon-129 lung imaging. Magnetic Resonance in Medicine. 2013;70(2):576-83.

191.   Vaughan JT, Adriany G, Garwood M, Yacoub E, Duong T, DelaBarre L, et al. Detunable transverse electromagnetic (TEM) volume coil for high-field NMR. Magnetic Resonance in Medicine. 2002;47(5):990-1000.

192.   Hayes CE, Edelstein WA, Schenck JF, Mueller OM, Eash M. An efficient, highly homogeneous radiofrequency coil for whole-body NMR imaging at 1.5 T. Journal of Magnetic Resonance (1969). 1985;63(3):622-8.

193.   Vaughan T. TEM Body Coils. eMagRes: John Wiley & Sons, Ltd; 2007.

194.   Vaughan JT, Hetherington HP, Otu JO, Pan JW, Pohost GM. High frequency volume coils for clinical NMR imaging and spectroscopy. Magnetic Resonance in Medicine. 1994;32(2):206-18.

195.   Metzger GJ, Snyder C, Akgun C, Vaughan T, Ugurbil K, Van de Moortele P-F. Local B1+ shimming for prostate imaging with transceiver arrays at 7T based on subject-dependent transmit phase measurements. Magnetic Resonance in Medicine. 2008;59(2):396-409.

196.   Collins CM, Liu W, Wang J, Gruetter R, Vaughan JT, Ugurbil K, et al. Temperature and SAR calculations for a human head within volume and surface coils at 64 and 300 MHz. Journal of Magnetic Resonance Imaging. 2004;19(5):650-6.

197.   Wang C, Shen GX. B1 field, SAR, and SNR comparisons for birdcage, TEM, and microstrip coils at 7T. Journal of Magnetic Resonance Imaging. 2006;24(2):439-43.

198.   Froncisz W, Kneeland JB, Grist TM, Campagna NF. Parallel image acquisition from noninteracting local coils. Journal of Magnetic Resonance. 1986;70:512-7.

199.   Boskamp EB. A new Revolution in Surface Coil Technology: the Array Surface Coil. SMRM 6th Annual Meeting. 1987:405.

200.   Kumar A, Bottomley P. Optimized quadrature surface coil designs. Magn Reson Mater Phy. 2008;21(1-2):41-52.

201.   Ohliger MA, Sodickson DK. An introduction to coil array design for parallel MRI. NMR Biomed. 2006;19(3):300-15.

202.   Lee SW, Hilal SK, Cho ZH. A multinuclear magnetic resonance imaging technique-simultaneous proton and sodium imaging. Magnetic Resonance Imaging. 1986;4(4):343-50.

203.   Magill AW, Gruetter R. Nested Surface Coils for Multinuclear NMR. eMagRes: John Wiley & Sons, Ltd; 2007.

204.   Stanisz GJ, Odrobina EE, Pun J, Escaravage M, Graham SJ, Bronskill MJ, et al. T1, T2 relaxation and magnetization transfer in tissue at 3T. Magnetic Resonance in Medicine. 2005;54(3):507-12.

205.   Meyer KL, Ballon D. A 3×3 Mesh Two-Dimensional Ladder Network Resonator for MRI of the Human Head. Journal of Magnetic Resonance, Series B. 1995;107(1):19-24.

206.   Zakian KL, Koutcher JA, Ballon D. A dual-tuned resonator for proton-decoupled phosphorus-31 chemical shift imaging of the brain. Magnetic Resonance in Medicine. 1999;41(4):809-15.

207.   Kocharian A, Rossman PJ, Hulshizer TC, Felmlee JP, Riederer SJ. Determination of appropriate RF blocking impedance for MRI surface coils and arrays. Magn Reson Mater Phy. 2000;10(2):80-3.

208.   Hockett FD, Wallace KD, Schmieder AH, Caruthers SD, Pham CTN, Wickline SA, et al. Simultaneous Dual Frequency 1H and 19F Open Coil Imaging of Arthritic Rabbit Knee at 3T. Medical Imaging, IEEE Transactions on. 2011;30(1):22-7.

209.   Goette MJ, Keupp J, Rahmer J, Lanza GM, Wickline SA, Caruthers SD. Balanced UTE-SSFP for 19F MR imaging of complex spectra. Magnetic Resonance in Medicine. 2015;74(2):537-43.

210.   Rao M, Wild JM. RF instrumentation for same-breath triple nuclear lung MR imaging of 1H and hyperpolarized [3]He and [129]Xe at 1.5T. Magnetic Resonance in Medicine. 2016;75(4):1841-48.

211.   Wetterling F, Högler M, Molkenthin U, Junge S, Gallagher L, Mhairi Macrae I, et al. The design of a double-tuned two-port surface resonator and its application to in vivo Hydrogen- and Sodium-MRI. Journal of Magnetic Resonance. 2012;217:10-8.

212.   Rao M, Robb F, Wild JM. Dedicated receiver array coil for ^{1}H lung imaging with same-breath acquisition of hyperpolarized [3]He and [129]Xe gas. Magnetic Resonance in Medicine. 2015;74(1):291-99.

213.   Shen GX, Wu JF, Boada FE, Thulborn KR. Experimentally verified, theoretical design of dual-tuned, low-pass birdcage radiofrequency resonators for magnetic resonance imaging and magnetic resonance spectroscopy of human brain at 3.0 Tesla. Magnetic Resonance in Medicine. 1999;41(2):268-75.

214.   Seunghoon H, Mark JH, Orhan N, Muftuler LT. A PIN diode controlled dual-tuned MRI RF coil and phased array for multi nuclear imaging. Physics in Medicine and Biology. 2010;55(9):2589.

215.   Meyerspeer M, Roig ES, Gruetter R, Magill AW. An improved trap design for decoupling multinuclear RF coils. Magnetic Resonance in Medicine. 2014;72(2):584-90.

216.   Schnall MD, Harihara Subramanian V, Leigh JS. The application of overcoupled tank circuits to NMR probe design. Journal of Magnetic Resonance (1969). 1986;67(1):129-34.

217.   Isaac G, Schnall MD, Lenkinski RE, Vogele K. A design for a double-tuned birdcage coil for use in an integrated MRI/MRS examination. Journal of Magnetic Resonance (1969). 1990;89(1):41-50.

218.   Shen GX, Boada FE, Thulborn KR. Dual-frequency, dual-quadrature, birdcage RF coil design with identical B1 pattern for sodium and proton imaging of the human brain at 1.5 T. Magn Reson Med. 1997;38(5):717-25.

219.   Fitzsimmons JR, Brooker HR, Beck B. A comparison of double-tuned surface coils. Magnetic Resonance in Medicine. 1989;10(3):302-9.

220.   Maunder A, Fallone BG, Daneshmand M, De Zanche N. Experimental verification of SNR and parallel imaging improvements using composite arrays. NMR in Biomedicine. 2015;28(2):141-53.

221.   Choi C-H, Hutchison JMS, Lurie DJ. Design and construction of an actively frequency-switchable RF coil for field-dependent Magnetisation Transfer Contrast MRI with fast field-cycling. Journal of Magnetic Resonance. 2010;207(1):134-9.

222.   Grant PD, Denhoff MW, Mansour RR. A Comparison between RF MEMS Switches and Semiconductor Switches. Proceedings of the International Conference on MEMS, NANO and Smart Systems 2004:515-21.

223.   Fuentes M, Weber E, Wilson S, Li B, Crozier S. Micro-Electromechanical Systems (MEMS) based RF-switches in MRI – a performance study. Proc Intl Soc Mag Reson Med. 2010;18:704.

224.   Keimel C, Claydon G, Bo L, Park J, Valdes ME. Microelectromechanical-Systems-Based Switches for Power Applications. IEEE Transactions on Industry Applications. 2012;48(4):1163-9.

225.   Walraven JA, editor Failure mechanisms in mems. Test Conference, 2003 Proceedings ITC 2003 International; 2003 Sept. 30-Oct. 2, 2003.

226.   Bulumulla SB, Fiveland E, Park K, Iannotti J. MEMS Reconfigurable Coils. Proc Intl Soc Mag Reson Med. 2015;23:1797.

227.   Waiczies H, Kuehne A, Nagel AM, Schuchardt D, Lysiak D, Rieger J, et al. 8CH 19F/1H Transceiver Array for Lung Imaging at 7T (pTX). Proc Int Soc Magn Reson Med. 2016;24:3506.

228.   Lu JY, Grafendorfer T, Zhang T, Vasanawala S, Robb F, Pauly JM, et al. Depletion-Mode GaN HEMT Q-Spoil Switches for MRI Coils. IEEE transactions on medical imaging. 2016;35(12):2558-67.

229.   Bulumulla SB, Park KJ, Fiveland E, Iannotti J, Robb F. MEMS switch integrated radio frequency coils and arrays for magnetic resonance imaging. Review of Scientific Instruments. 2017;88(2):025003.

230.   Maunder A, Rao M, Robb F, Wild J. RF coil design for multi-nuclear lung MRI of ^{19}F fluorinated gases and ^{1}H using MEMS. Proc Intl Soc Mag Reson Med. 2016;24:3504.

231.   Hu L, Hockett FD, Chen J, Zhang L, Caruthers SD, Lanza GM, et al. A generalized strategy for designing 19F/1H dual-frequency MRI coil for small animal imaging at 4.7 Tesla. Journal of Magnetic Resonance Imaging. 2011;34(1):245-52.

232.   Choi C-H, Hong S-M, Ha Y, Shah NJ. Design and construction of a novel 1H/19F double-tuned coil system using PIN-diode switches at 9.4 T. Journal of Magnetic Resonance. 2017;279:11-5.

233.   Spence D, Aimi M. Custom MEMS Switch for MR Surface Coil decoupling. Proc Intl Soc Mag Reson Med. 2015;23:704.

234.   Brunner D. A high speed, high power T/R switching frontend. Proc Int Soc Magn Reson Med. 2016;23:496.

235.   Caverly RH, Doherty WE, Watkins RD, editors. Modeling high speed MRI coil switching using PIN diodes. IEEE International Microwave Symposium; 2011 5-10 June.

236.   Maunder AM, Daneshmand M, Mousavi P, Fallone BG, De Zanche N. Stray Capacitance Between Magnetic Resonance Imaging Coil Elements: Models and Application to Array Decoupling. IEEE Transactions on Microwave Theory and Techniques. 2013;61(12):4667-77.

237. Och JG, Clarke GD, Sobol WT, Rosen CW, Mun SK. Acceptance testing of magnetic resonance imaging systems: Report of AAPM Nuclear Magnetic Resonance Task Group No. 6. Medical physics. 1992;19(1):217-29.

238. Deoni SCL. High-resolution T1 mapping of the brain at 3T with driven equilibrium single pulse observation of T1 with high-speed incorporation of RF field inhomogeneities (DESPOT1-HIFI). Journal of Magnetic Resonance Imaging. 2007;26(4):1106-11.

239. NEMA. Determination of Signal-to-Noise Ratio (SNR) in Diagnostic Magnetic Resonance Imaging NEMA, MS 1-2008 (R2014). 2015.

240. Christ A, Kainz W, Hahn EG, Honegger K, Zefferer M, Neufeld E, et al. The Virtual Family - development of surface-based anatomical models of two adults and two children for dosimetric simulations. Phys Med Biol. 2010;55(N23).

241. Directive 2014/35/EU of the European Parliament and of the Council of 26 February 2014 on the harmonisation of the laws of the Member States relating to the making available on the market of electrical equipment designed for use within certain voltage limits Text with EEA relevance, (18/04/2014, 2014).

242. Avdievich NI, Bradshaw K, Kuznetsov AM, Hetherington HP. High-field actively detuneable transverse electromagnetic (TEM) coil with low-bias voltage for high-power RF transmission. Magn Reson Med. 2007;57(6):1190-5.

243. Caverly RH, Hiller G. Establishing the minimum reverse bias for a p-i-n diode in a high-power switch. IEEE Transactions on Microwave Theory and Techniques. 1990;38(12):1938-43.

244. Maunder A, Rao M, Robb FJL, Wild aJM. Combined Transmit Array and 8-channel Receive Coil Array for 19F/1H for Human Lung Imaging at 1.5 T Utilizing MEMS Transmit-receive Detuning. Proc Intl Soc Mag Reson Med. 2017;25:1052.

245. Ebner B, Behm P, Jacoby C, Burghoff S, French BA, Schrader J, et al. Early assessment of pulmonary inflammation by 19F MRI in vivo. Circ Cardiovasc Imaging. 2010;3(2):202-10.

246. Pennati F, Quirk JD, Yablonskiy DA, Castro M, Aliverti A, Woods JC. Assessment of Regional Lung Function with Multivolume (1)H MR Imaging in Health and Obstructive Lung Disease: Comparison with (3)He MR Imaging. Radiology. 2014;273(2):580-90.

247. Bauman G, Lützen U, Ullrich M, Gaass T, Dinkel J, Elke G, et al. Pulmonary Functional Imaging: Qualitative Comparison of Fourier Decomposition MR Imaging with SPECT/CT in Porcine Lung. Radiology. 2011;260(2):551-9.

248. Zapke M, Topf HG, Zenker M, Kuth R, Deimling M, Kreisler P, et al. Magnetic resonance lung function--a breakthrough for lung imaging and functional assessment? A phantom study and clinical trial. Respiratory research. 2006;7:106.

249. Kampani VV, Jones RW, Charles HC, Hussey N. Dual-Tuned RF Coil system for Parallel Imaging of Human Lungs Using Perfluorinated Gases. Proc Intl Soc Mag Reson Med. 2017;25.

250. Steensma BR, Voogt IJ, Leiner T, Luijten PR, Habets J, Klomp DWJ, et al. An 8-channel Tx/Rx dipole array combined with 16 Rx loops for high-resolution functional cardiac imaging at 7 T. Magma (New York, NY). 2018;31(1):7-18.

251. Maunder A, Stewart NJ, Rao M, Robb FJL, Wild JM. Steady-state Free Precession for Improved Signal to Noise in Lung Ventilation Imaging with 19F Perfluoropropane at 1.5 T. Proc Intl Soc Mag Reson Med. 2017;25:3318.

252. Reykowski A, Wright SM, Porter JR. Design of matching networks for low noise preamplifiers. Magn Reson Med. 1995;33(6):848-52.

253. Walsh DO, Gmitro AF, Marcellin MW. Adaptive reconstruction of phased array MR imagery. Magn Reson Med. 2000;43(5):682-90.

254. Brown R, Wang Y, Spincemaille P, Lee RF. On the noise correlation matrix for multiple radio frequency coils. Magnetic Resonance in Medicine. 2007;58(2):218-24.

255.   Nordmeyer-Massner JA, De Zanche N, Pruessmann KP. Noise figure characterization of preamplifiers at NMR frequencies. Journal of magnetic resonance (San Diego, Calif : 1997). 2011;210(1):7-15.
256.   Deoni SC. High-resolution T1 mapping of the brain at 3T with driven equilibrium single pulse observation of T1 with high-speed incorporation of RF field inhomogeneities (DESPOT1-HIFI). Journal of magnetic resonance imaging : JMRI. 2007;26(4):1106-11.
257.   Maunder A, Rao M, Robb F, Wild JM. Comparison of MEMS switches and PIN diodes for switched dual tuned RF coils. Magnetic Resonance in Medicine. 2018;80(4):1746-53.
258.   Couch MJ, Ball IK, Li T, Fox MS, Ouriadov AV, Biman B, et al. Optimized Strategies for 19F MRI of Human Lungs and Comparison of UTE and Gradient Echo Imaging. Proc Intl Soc Mag Reson Med. 2014;22:777.
259.   Byron K, Robb F, Vasanawala S, Pauly J, Scott G. Switching Impedance Matching and Primary Coil Array Using RF MEMS switches for a Wireless Power Transfer System. Proc Intl Soc Mag Reson Med. 2018;26:4424.
260.   Darnell D, Ma Y, Wang H, Robb F, Song AW, Truong T-K. Adaptive integrated parallel reception, excitation, and shimming (iPRES-A) with microelectromechanical systems switches. Magnetic Resonance in Medicine. 2018;80(1):371-9.
261.   Colotti R, Delacoste J, Ginami G, Pellegrin M, Kober T, Natsuaki Y, et al. A Comparison between the UTE and PETRA Pulse Sequences for Fluorine-19 MRI at 3 Tesla. Proc Int Soc Magn Reson Med. 2016;24:3714.
262.   Weiger M, Pruessmann KP. MRI with Zero Echo Time. eMagRes: John Wiley & Sons, Ltd; 2007.
263.   Wild JM, Marshall H, Bock M, Schad LR, Jakob PM, Puderbach M, et al. MRI of the lung (1/3): methods. Insights into imaging. 2012;3(4):345-53.
264.   Raki H, Saniour I, Robb F, Koon KT, Souchay H, Lambert SA, et al. Comparison of single-loop endoluminal receiver coils based on serial or parallel active decoupling circuits using controllable MEMS switches. Proc Intl Soc Mag Reson Med. 2018;26:4286.
265.   Rietsch SHG, Orzada S, Maderwald S, Brunheim S, Philips BWJ, Scheenen TWJ, et al. 7T ultra-high field body MR imaging with an 8-channel transmit/32-channel receive radiofrequency coil array. Med Phys. 2018;45(7):2978-90.
266.   Pfaffenrot V, Brunheim S, Rietsch SHG, Koopmans PJ, Ernst TM, Kraff O, et al. An 8/15-channel Tx/Rx head neck RF coil combination with region-specific B1 + shimming for whole-brain MRI focused on the cerebellum at 7T. Magn Reson Med. 2018;80(3):1252-65.
267.   Rietsch SHG, Pfaffenrot V, Bitz AK, Orzada S, Brunheim S, Lazik-Palm A, et al. An 8-channel transceiver 7-channel receive RF coil setup for high SNR ultrahigh-field MRI of the shoulder at 7T. Medical Physics. 2017;44(12):6195-208.
268.   Deppe MH, Parra-Robles J, Marshall H, Lanz T, Wild JM. A flexible 32-channel receive array combined with a homogeneous transmit coil for human lung imaging with hyperpolarized 3He at 1.5 T. Magnetic Resonance in Medicine. 2011;66(6):1788-97.
269.   Damen FC, Cai K. B1(-) non-uniformity correction of phased-array coils without measuring coil sensitivity. Magn Reson Imaging. 2018;51:20-8.
270.   Vovk U, Pernus F, Likar B. A Review of Methods for Correction of Intensity Inhomogeneity in MRI. IEEE Transactions on Medical Imaging. 2007;26(3):405-21.
271.   Yan X, Xue R, Zhang X. A monopole/loop dual-tuned RF coil for ultrahigh field MRI. Quantitative Imaging in Medicine and Surgery. 2014;4(4):225-31.
272.   Gilbert KM, Curtis AT, Gati JS, Martyn Klassen L, Villemaire LE, Menon RS. Transmit/receive radiofrequency coil with individually shielded elements. Magnetic Resonance in Medicine. 2010;64(6):1640-51.

273.   Adriany G, Auerbach EJ, Snyder CJ, Gözübüyük A, Moeller S, Ritter J, et al. A 32-Channel Lattice Transmission Line Array for Parallel Transmit and Receive MRI at 7 Tesla. Magnetic Resonance in Medicine. 2010;63(6):1478-85.

274.   Doty FD, Entzminger Jr G, Hauck CD, Staab JP. Practical Aspects of Birdcage Coils. Journal of Magnetic Resonance. 1999;138(1):144-54.

275.   Alagappan V, Nistler J, Adalsteinsson E, Setsompop K, Fontius U, Zelinski A, et al. Degenerate mode band-pass birdcage coil for accelerated parallel excitation. Magn Reson Med. 2007;57(6):1148-58.

276.   Guérin B, Gebhardt M, Serano P, Adalsteinsson E, Hamm M, Pfeuffer J, et al. Comparison of simulated parallel transmit body arrays at 3 T using excitation uniformity, global SAR, local SAR, and power efficiency metrics. Magnetic Resonance in Medicine. 2015;73(3):1137-50.

277.   Ballon D, Graham MC, Miodownik S, Koutcher JA. A 64 MHz half-birdcage resonator for clinical imaging. Journal of Magnetic Resonance (1969). 1990;90(1):131-40.

278.   Atiyah Y, Nicola DZ, S. AP. A dual-tuned transceive resonator for 13C{1H} MRS: two open coils in one. NMR in Biomedicine. 2013;26(5):533-41.

279.   Noury F, Mispelter J, Szeremeta F, Même S, Doan B-T, Beloeil J-C. MRI methodological development of intervertebral disc degeneration: a rabbit in vivo study at 9.4 T. Magnetic Resonance Imaging. 2008;26(10):1421-32.

280.   Hudson AM, Kockenberger W, Bowtell RW. Open access birdcage coils for microscopic imaging of plants at 11.7 T. Magma (New York, NY). 2000;10(2):69-74.

281.   Gasson J, Summers IR, Fry ME, Vennart W. Modified birdcage coils for targeted imaging. Magn Reson Imaging. 1995;13(7):1003-12.

282.   Yahya A, De Zanche N, Allen PS. A dual-tuned transceive resonator for 13C{1H} MRS: two open coils in one. NMR in Biomedicine. 2013;26(5):533-41.

283.   Lawrence BG, Crozier S, Cowin G, Yau DD. An inverse design of an open, head/neck RF coil for MRI. IEEE Transactions on Biomedical Engineering. 2002;49(9):1024-30.

284.   Abraham CB, Loree-Spacek J, Drainville RA, Pichardo S, Curiel L. Development of custom RF coils for use in a small animal platform for magnetic resonance-guided focused ultrasound hyperthermia compatible with a clinical MRI scanner. International journal of hyperthermia : the official journal of European Society for Hyperthermic Oncology, North American Hyperthermia Group. 2018:1-13.

285.   Fan X, Markiewicz EJ, Zamora M, Karczmar GS, Roman BB. Comparison and evaluation of mouse cardiac MRI acquired with open birdcage, single loop surface and volume birdcage coils. Phys Med Biol. 2006;51(24):N451-9.

286.   Peshkovsky AS, Kennan RP, Fabry ME, Avdievich NI. Open half-volume quadrature transverse electromagnetic coil for high-field magnetic resonance imaging. Magn Reson Med. 2005;53(4):937-43.

287.   Adriany G, Gruetter R. A Half-Volume Coil for Efficient Proton Decoupling in Humans at 4 Tesla. Journal of Magnetic Resonance. 1997;125(1):178-84.

288.   Avdievich NI, Bradshaw K, Lee J-H, Kuznetsov AM, Hetherington HP. 4T split TEM volume head and knee coils for improved sensitivity and patient accessibility. Journal of magnetic resonance. 2007;187(2):234-41.

289.   Sengupta S, Adriany G, Kempe V, Zimmermann J, Goebel R. An Open 4ch. Transmit/16 Ch. Receive Coil for High Resolution Occipital and Temporal Visual Cortex Imaging at 7T. Proc Intl Soc Mag Reson Med. 2015;23:1777.

290.   JT V. The head cradle: an open faced, high performance TEM coil. . Proc Intl Soc Mag Reson Med. 2001;9:15.

291.   G A, E Y, I T, P A, H M, JT V. Shielded surface coils and halfvolume cavity resonators for imaging and spectroscopy applications at 7 T. Proc Intl Soc Mag Reson Med. 2000;8:563.

292.   De Zanche N, Pruessmann KP. Algebraic method to synthesize specified modal currents in ladder resonators: Application to noncircular birdcage coils. Magnetic Resonance in Medicine. 2015;74(5):1470-81.

293.   Leifer MC. Resonant Modes of the Birdcage Coil. Journal of Magnetic Resonance. 1997;124(1):51-60.

294.   Stephen Boyd, Vandenberghe L. Introduction to Applied Linear Algebra: Vectors, Matrices, and Least Squares: Cambridge University Press; 2018.

295.   Maunder A, Robb F, Rao M, Wild J. Application of Asymmetric Mode Ladder Resonators for Improved Efficiency of Individual Elements in Transceive Arrays. Proc Intl Soc Mag Reson Med. 2018;26:4273.

296.   Voss HU, Ballon DJ. High-Pass Two-Dimensional Ladder Network Resonators for Magnetic Resonance Imaging. IEEE Transactions on Biomedical Engineering. 2006;53(12):2590-3.

297.   Heuermann H, editor GSOLT: the calibration procedure for all multi-port vector network analyzers. IEEE International Microwave Symposium Digest; 2003 8-13 June.

298.   Chen C, Hoult D. Biomedical Magnetic Resonance Technology. Bristol: Hilger; 1989.

299.   Weinberger O, Winter L, Dieringer MA, Els A, Oezerdem C, Rieger J, et al. Local Multi-Channel RF Surface Coil versus Body RF Coil Transmission for Cardiac Magnetic Resonance at 3 Tesla: Which Configuration Is Winning the Game? PLOS ONE. 2016;11(9):e0161863.

300.   Adriany G, Van de Moortele PF, Wiesinger F, Moeller S, Strupp JP, Andersen P, et al. Transmit and receive transmission line arrays for 7 Tesla parallel imaging. Magn Reson Med. 2005;53(2):434-45.

301.   Yahya A, De Zanche N, Allen Peter S. A dual-tuned transceive resonator for ^{13}C^{1}H MRS: two open coils in one. NMR in Biomedicine. 2013;26(5):533-41.

302.   Koh D, Felder J, Shah NJ. A novel analytical description of periodic volume coil geometries in MRI. Journal of Magnetic Resonance. 2018;288:37-42.

303.   Corea JR, Flynn AM, Lechêne B, Scott G, Reed GD, Shin PJ, et al. Screen-printed flexible MRI receive coils. Nature Communications. 2016;7:10839.

304.   Gutberlet M, Kaireit T, Voskrebenzev A, Freise J, Welte T, Wacker F, et al. Real-time dynamic fluorinated gas MRI in free breathing for mapping of regional lung ventilation in patients with COPD and healthy volunteers using a 16 channel receive coil at 1.5T. Proc Int Soc Magn Reson Med. 2016;24:1140.

305.   Fleysher L, Fleysher R, Liu S, Zaaraoui W, Gonen O. Optimizing the precision-per-unit-time of quantitative MR metrics: examples for T1, T2, and DTI. Magn Reson Med. 2007;57(2):380-7.

306.   Jean-David J, Keith W, Guillaume G, Nicola DZ. SNR efficiency of combined bipolar gradient echoes: Comparison of three-dimensional FLASH, MPRAGE, and multiparameter mapping with VFA-FLASH and MP2RAGE. Magnetic Resonance in Medicine. 2017;77(6):2186-202.

307.   Courtney JA, Armstrong RL. A Nuclear Spin Relaxation Study of the Spin–Rotation Interaction in Spherical Top Molecules. Canadian Journal of Physics. 1972;50(12):1252-61.

308.   F. KT, Marcel G, Andreas V, Julia F, Tobias W, M. HJ, et al. Comparison of quantitative regional ventilation-weighted fourier decomposition MRI with dynamic fluorinated gas washout MRI and lung function testing in COPD patients. Journal of Magnetic Resonance Imaging.0(0).

309.   Reeder SB, Herzka DA, McVeigh ER. Signal-to-Noise Ratio Behavior of Steady-State Free Precession. Magnetic resonance in medicine. 2004;52(1):123-30.

310.   Hargreaves BA, Vasanawala SS, Pauly JM, Nishimura DG. Characterization and reduction of the transient response in steady-state MR imaging. Magnetic Resonance in Medicine. 2001;46(1):149-58.

311.   van Heeswijk RB, Colotti R, Darçot E, Delacoste J, Pellegrin M, Piccini D, et al. Chemical shift encoding (CSE) for sensitive fluorine-19 MRI of perfluorocarbons with complex spectra. Magnetic Resonance in Medicine.79(5):2724-30.

312.   Colotti R, Bastiaansen JAM, Wilson A, Flögel U, Gonzales C, Schwitter J, et al. Characterization of perfluorocarbon relaxation times and their influence on the optimization of fluorine-19 MRI at 3 tesla. Magnetic Resonance in Medicine. 2017;77(6):2263-71.

313.   Wild JM, Paley MNJ, Viallon M, Schreiber WG, van Beek EJR, Griffiths PD. k-Space filtering in 2D gradient-echo breath-hold hyperpolarized 3He MRI: Spatial resolution and signal-to-noise ratio considerations. Magnetic Resonance in Medicine. 2002;47(4):687-95.

314.   Wang HZ, Riederer SJ. A spoiling sequence for suppression of residual transverse magnetization. Magnetic Resonance in Medicine. 1990;15(2):175-91.

315.   Goette MJ, Lanza GM, Caruthers SD, Wickline SA. Improved Quantitative (19)F MR Molecular Imaging With Flip Angle Calibration and B(1)-Mapping Compensation. Journal of magnetic resonance imaging : JMRI. 2015;42(2):488-94.

316.   Balezeau F, Eliat P-A, Cayamo AB, Saint-Jalmes H. Mapping of low flip angles in magnetic resonance. Physics in Medicine and Biology. 2011;56(20):6635-47.

317.   Cheng HL, Wright GA. Rapid high-resolution T(1) mapping by variable flip angles: accurate and precise measurements in the presence of radiofrequency field inhomogeneity. Magn Reson Med. 2006;55(3):566-74.

318.   Terekhov MV, Wolf UA, Scholz AW, Schreiber WG. Rapid In-vivo MRI Measurement of Fluorinated Gas Concentration in Lungs Using T1- mapping. Proc Intl Soc Mag Reson Med.15:1336.

319.   Rochefort Ld, Vignaud A, Maitre X, Guillot G, Darasse L, Bittoun J, et al. Influence of lung filling on T_2^* values in human at 1.5 T with hyperpolarised ^{3}He Proc Intl Soc Mag Reson Med. 2004;11:2724.

320.   Deppe MH, Parra-Robles J, Ajraoui S, Parnell SR, Clemence M, Schulte RF, et al. Susceptibility effects in hyperpolarized 3He lung MRI at 1.5T and 3T. Journal of Magnetic Resonance Imaging. 2009;30(2):418-23.

321.   Wild JM, Ajraoui S, Deppe MH, Parnell SR, Marshall H, Parra-Robles J, et al. Synchronous acquisition of hyperpolarised 3He and 1H MR images of the lungs – maximising mutual anatomical and functional information. NMR in Biomedicine. 2011;24(2):130-4.

322.   Collier GJ, Wild JM. In vivo measurement of gas flow in human airways with hyperpolarized gas MRI and compressed sensing. Magnetic Resonance in Medicine. 2015;73(6):2255-61.

323.   Qing K, Altes TA, Tustison NJ, Feng X, Chen X, Mata JF, et al. Rapid acquisition of helium-3 and proton three-dimensional image sets of the human lung in a single breath-hold using compressed sensing. Magnetic Resonance in Medicine. 2015;74(4):1110-5.

324.   Vasanawala SS, Alley MT, Hargreaves BA, Barth RA, Pauly JM, Lustig M. Improved pediatric MR imaging with compressed sensing. Radiology. 2010;256(2):607-16.

325.   Neal M, Pippard B, Hollingsworth K, Thelwall P. Accelerated 19F-MR Imaging of Inhaled Perfluoropropane for Assessment of Pulmonary Ventilation. Proc Intl Soc Mag Reson Med. 2018;26:2474.

326.   Tsao J, Boesiger P, Pruessmann KP. k-t BLAST and k-t SENSE: Dynamic MRI with high frame rate exploiting spatiotemporal correlations. Magnetic Resonance in Medicine. 2003;50(5):1031-42.

327.   Chen X, Salerno M, Yang Y, Epstein FH. Motion-compensated compressed sensing for dynamic contrast-enhanced MRI using regional spatiotemporal sparsity and region tracking:

block low-rank sparsity with motion-guidance (BLOSM). Magn Reson Med. 2014;72(4):1028-38.

328. Zhou R, Huang W, Yang Y, Chen X, Weller DS, Kramer CM, et al. Simple motion correction strategy reduces respiratory-induced motion artifacts for k-t accelerated and compressed-sensing cardiovascular magnetic resonance perfusion imaging. Journal of cardiovascular magnetic resonance : official journal of the Society for Cardiovascular Magnetic Resonance. 2018;20(1):6.

329. Usman M, Atkinson D, Odille F, Kolbitsch C, Vaillant G, Schaeffter T, et al. Motion corrected compressed sensing for free-breathing dynamic cardiac MRI. Magn Reson Med. 2013;70(2):504-16.

330. Dietrich O. General Advantages of Parallel Imaging. In: Schoenberg SO, Dietrich O, Reiser MF, editors. Parallel Imaging in Clinical MR Applications. Berlin, Heidelberg: Springer Berlin Heidelberg; 2007. p. 173-6.

331. Khare K, Hardy CJ, King KF, Turski PA, Marinelli L. Accelerated MR imaging using compressive sensing with no free parameters. Magnetic Resonance in Medicine. 2012;68(5):1450-7.

332. Donoho DL, Tsaig Y, Drori I, Starck J. Sparse Solution of Underdetermined Systems of Linear Equations by Stagewise Orthogonal Matching Pursuit. IEEE Transactions on Information Theory. 2012;58(2):1094-121.

333. Uecker M, Lai P, Murphy MJ, Virtue P, Elad M, Pauly JM, et al. ESPIRiT—an eigenvalue approach to autocalibrating parallel MRI: Where SENSE meets GRAPPA. Magnetic Resonance in Medicine. 2014;71(3):990-1001.

334. Aelterman J, Naeyaert M, Gutierrez S, Luong H, Goossens B, Pižurica A, et al. Automatic High-Bandwidth Calibration and Reconstruction of Arbitrarily Sampled Parallel MRI. PLoS ONE. 2014;9(6):e98937.

335. Yu Y, Hong M, Liu F, Wang H, Crozier S. Comparison and analysis of nonlinear algorithms for compressed sensing in MRI. Conference proceedings : Annual International Conference of the IEEE Engineering in Medicine and Biology Society IEEE Engineering in Medicine and Biology Society Annual Conference. 2010;2010:5661-4.

336. Daducci A, Canales-Rodriguez EJ, Descoteaux M, Garyfallidis E, Gur Y, Lin YC, et al. Quantitative comparison of reconstruction methods for intra-voxel fiber recovery from diffusion MRI. IEEE transactions on medical imaging. 2014;33(2):384-99.

337. Jaspan ON, Fleysher R, Lipton ML. Compressed sensing MRI: a review of the clinical literature. The British journal of radiology. 2015;88(1056):20150487.

338. Mann LW, Higgins DM, Peters CN, Cassidy S, Hodson KK, Coombs A, et al. Accelerating MR Imaging Liver Steatosis Measurement Using Combined Compressed Sensing and Parallel Imaging: A Quantitative Evaluation. Radiology. 2016;278(1):247-56.

339. Oh H, Lee S. Visually weighted reconstruction of compressive sensing MRI. Magnetic Resonance Imaging. 2014;32(3):270-80.

340. Ajraoui S, Parra-Robles J, Wild JM. Incorporation of prior knowledge in compressed sensing for faster acquisition of hyperpolarized gas images. Magnetic Resonance in Medicine. 2013;69(2):360-9.

341. Giesel FL, Mehndiratta A, von Tengg-Kobligk H, Schaeffer A, Teh K, Hoffman EA, et al. Rapid Prototyping Raw Models on the Basis of High Resolution Computed Tomography Lung Data for Respiratory Flow Dynamics. Academic Radiology. 2009;16(4):495-8.

342. Chikop SA, Konar AS, Reddy NSL, Vajuvalli N, Keelara DS, Kumnoor A, et al. A Cost-effective 3D Printed Cardiac MR Phantom. Proc Int Soc Magn Reson Med. 2017;25:2765.

343. Gopalan K, Tamir JI, Arias AC, Lustig M. Toward 3D Printed, Anatomy-Mimicking, Quantitative MRI Phantoms. Proc Intl Soc Mag Reson Med. 2017;25:3733.

344.	Marshall H, Deppe MH, Parra-Robles J, Hillis S, Billings C, Miller SR, et al. S118 Direct visualisation of collateral ventilation in COPD with hyperpolarised Gas MRI. Thorax. 2011;66(Suppl 4):A54-A5.

345.	Bernstein MA, King KF, Zhou XJ. Introduction to Data Acquisition, K-Space Sampling, and Image Reconstruction. In: Bernstein MA, King KF, Zhou XJ, editors. Handbook of MRI Pulse Sequences. Burlington: Academic Press; 2004. p. 363-6.

346.	Lisboa JC, Guarini M, Irarrazaval P. A correction algorithm for undersampled images using dynamic segmentation and entropy based focus criterion. Magnetic Resonance Imaging. 2002;20(9):659-66.

347.	Tzeng YS, Lutchen K, Albert M. The difference in ventilation heterogeneity between asthmatic and healthy subjects quantified using hyperpolarized 3He MRI. Journal of applied physiology (Bethesda, Md : 1985). 2009;106(3):813-22.

348.	Altes TA, Powers PL, Knight-Scott J, Rakes G, Platts-Mills TA, de Lange EE, et al. Hyperpolarized 3He MR lung ventilation imaging in asthmatics: preliminary findings. Journal of magnetic resonance imaging : JMRI. 2001;13(3):378-84.

349.	He M, Driehuys B, Que LG, Huang YT. Using Hyperpolarized (129)Xe MRI to Quantify the Pulmonary Ventilation Distribution. Acad Radiol. 2016;23(12):1521-31.

350.	Sano K, Matsushita R, Tanaka T. Trade-off in compressed sensing with noisy measurements. IEEE International Symposium on Information Theory2014. p. 1316-20.

351.	Qu X, Guo D, Ning B, Hou Y, Lin Y, Cai S, et al. Undersampled MRI reconstruction with patch-based directional wavelets. Magnetic Resonance Imaging. 2012;30(7):964-77.

352.	Norquay G, Leung G, Stewart NJ, Tozer GM, Wolber J, Wild JM. Relaxation and exchange dynamics of hyperpolarized 129Xe in human blood. Magn Reson Med. 2015;74(2):303-11.

353.	Kauczor H-U, Ebert M, Kreitner K-F, Nilgens H, Surkau R, Heil W, et al. Imaging of the lungs using 3he MRI: Preliminary clinical experience in 18 patients with and without lung disease. Journal of Magnetic Resonance Imaging. 1997;7(3):538-43.

354.	Xu X, Norquay G, Parnell SR, Deppe MH, Ajraoui S, Hashoian R, et al. Hyperpolarized 129Xe gas lung MRI-SNR and T2* comparisons at 1.5 T and 3 T. Magn Reson Med. 2012;68(6):1900-4.

355.	Moller HE, Hedlund LW, Chen XJ, Carey MR, Chawla MS, Wheeler CT, et al. Measurements of hyperpolarized gas properties in the lung. Part III: (3)He T(1). Magn Reson Med. 2001;45(3):421-30.

356.	Diaz S, Casselbrant I, Piitulainen E, Pettersson G, Magnusson P, Peterson B, et al. Hyperpolarized 3He apparent diffusion coefficient MRI of the lung: reproducibility and volume dependency in healthy volunteers and patients with emphysema. Journal of magnetic resonance imaging : JMRI. 2008;27(4):763-70.

357.	Ouriadov A, Farag A, Kirby M, McCormack DG, Parraga G, Santyr GE. Lung morphometry using hyperpolarized (129) Xe apparent diffusion coefficient anisotropy in chronic obstructive pulmonary disease. Magn Reson Med. 2013;70(6):1699-706.

358.	O'Halloran RL, Holmes JH, Altes TA, Salerno M, Fain SB. The effects of SNR on ADC measurements in diffusion-weighted hyperpolarized He-3 MRI. Journal of magnetic resonance (San Diego, Calif : 1997). 2007;185(1):42-9.

359.	Ireland RH, Bragg CM, McJury M, Woodhouse N, Fichele S, van Beek EJR, et al. Feasibility of Image Registration and Intensity-Modulated Radiotherapy Planning With Hyperpolarized Helium-3 Magnetic Resonance Imaging for Non–Small-Cell Lung Cancer. International Journal of Radiation Oncology, Biology, Physics. 2007;68(1):273-81.

360.	Lee Y, Akinnagbe-Zusterzeel E, Goralski J, Donaldson S, An H, Charles HC, et al. [19]F Ventilation Imaging of Cystic Fibrosis Patients. Proc Int Soc Magn Reson Med. 2016;24:1607.

361.   Weiskopf N, Suckling J, Williams G, Correia M, Inkster B, Tait R, et al. Quantitative multi-parameter mapping of R1, PD*, MT, and R2* at 3T: a multi-center validation. Frontiers in Neuroscience. 2013;7(95).

362.   Gai ND, Malayeri AA, Bluemke DA. Three-dimensional T1 and T2* mapping of human lung parenchyma using interleaved saturation recovery with dual echo ultrashort echo time imaging (ITSR-DUTE). Journal of magnetic resonance imaging : JMRI. 2017;45(4):1097-104.

363.   Siemonsen S, Finsterbusch J, Matschke J, Lorenzen A, Ding XQ, Fiehler J. Age-dependent normal values of T2* and T2' in brain parenchyma. AJNR American journal of neuroradiology. 2008;29(5):950-5.

364.   Horn FC, Rao M, Stewart NJ, Wild JM. Multiple breath washout of hyperpolarized (129) Xe and (3) He in human lungs with three-dimensional balanced steady-state free-precession imaging. Magn Reson Med. 2017;77(6):2288-95.

365.   Maunder A, Rao M, Robb F, Wild JM. Combined Transmit Array and 8-channel Receive Coil Array for 19F/1H for Human Lung Imaging at 1.5 T Utilizing MEMS Transmit-receive Detuning. Proc Intl Soc Mag Reson Med. 2017;25:1052.

366.   Norquay G, Collier GJ, Rao M, Stewart NJ, Wild JM. ^{129}Xe-Rb Spin-Exchange Optical Pumping with High Photon Efficiency. Physical Review Letters. 2018;121(15):153201.

367.   Ouriadov A, Farag A, Kirby M, McCormack DG, Parraga G, Santyr GE. Lung morphometry using hyperpolarized 129Xe apparent diffusion coefficient anisotropy in chronic obstructive pulmonary disease. Magnetic Resonance in Medicine. 2013;70(6):1699-706.

368.   Halaweish AF, Hoffman EA, Thedens DR, Fuld MK, Sieren JP, van Beek EJ. Effect of lung inflation level on hyperpolarized 3He apparent diffusion coefficient measurements in never-smokers. Radiology. 2013;268(2):572-80.

369.   Kaushik SS, Cleveland ZI, Cofer GP, Metz G, Beaver D, Nouls J, et al. Diffusion-weighted hyperpolarized 129Xe MRI in healthy volunteers and subjects with chronic obstructive pulmonary disease. Magn Reson Med. 2011;65(4):1154-65.

370.   Hopkins SR, Henderson AC, Levin DL, Yamada K, Arai T, Buxton RB, et al. Vertical gradients in regional lung density and perfusion in the supine human lung: the Slinky effect. Journal of applied physiology (Bethesda, Md : 1985). 2007;103(1):240-8.

371.   Hughes PJC, Smith L, Horn F, Biancardi AM, Stewart N, Norquay G, et al. Assessment of ventilation heterogeneity using hyperpolarized gas MRI histogram analysis. Proc Intl Soc Mag Reson Med. 2018;26:2476.

372.   Ball IK, Couch MJ, Li T, Fox MS, Lovis JA, Hashoian R, et al. 19F Apparent Diffusion Coefficient MRI of Inert Fluorinated Gases in Human Lungs. Proc Intl Soc Mag Reson Med. 2013;21:1483.

373.   Ochs M, Nyengaard JR, Jung A, Knudsen L, Voigt M, Wahlers T, et al. The number of alveoli in the human lung. Am J Respir Crit Care Med. 2004;169(1):120-4.

374.   Yablonskiy DA, Haacke EM. Theory of NMR signal behavior in magnetically inhomogeneous tissues: The static dephasing regime. Magnetic Resonance in Medicine. 1994;32(6):749-63.

375.   Durney CH, Bertolina J, Ailion DC, Christman R, Cutillo AG, Morris AH, et al. Calculation and interpretation of inhomogeneous line broadening in models of lungs and other heterogeneous structures. Journal of Magnetic Resonance. 1989;85(3):554-70.

376.   Hyde DM, Tyler NK, Putney LF, Singh P, Gundersen HJ. Total number and mean size of alveoli in mammalian lung estimated using fractionator sampling and unbiased estimates of the Euler characteristic of alveolar openings. The anatomical record Part A, Discoveries in molecular, cellular, and evolutionary biology. 2004;277(1):216-26.

377.	Svenningsen S, Kirby M, Starr D, Leary D, Wheatley A, Maksym GN, et al. Hyperpolarized ^{3}He and ^{129}Xe MRI: differences in asthma before bronchodilation. Journal of magnetic resonance imaging : JMRI. 2013;38(6):1521-30.

378.	Wong GP, Tseng CH, Pomeroy VR, Mair RW, Hinton DP, Hoffmann D, et al. A system for low field imaging of laser-polarized noble gas. Journal of magnetic resonance (San Diego, Calif : 1997). 1999;141(2):217-27.

379.	Kirby M, Heydarian M, Svenningsen S, Wheatley A, McCormack DG, Etemad-Rezai R, et al. Hyperpolarized 3He magnetic resonance functional imaging semiautomated segmentation. Acad Radiol. 2012;19(2):141-52.

380.	Pike D, Kirby M, Eddy RL, Guo F, Capaldi DP, Ouriadov A, et al. Regional Heterogeneity of Chronic Obstructive Pulmonary Disease Phenotypes: Pulmonary (3)He Magnetic Resonance Imaging and Computed Tomography. Copd. 2016;13(5):601-9.

381.	Smith L, Marshall H, Aldag I, Horn F, Collier G, Hughes D, et al. Longitudinal Assessment of Children with Mild Cystic Fibrosis Using Hyperpolarized Gas Lung Magnetic Resonance Imaging and Lung Clearance Index. American Journal of Respiratory and Critical Care Medicine. 2018;197(3):397-400.

382.	Celli BR, Cote CG, Marin JM, Casanova C, Montes de Oca M, Mendez RA, et al. The Body-Mass Index, Airflow Obstruction, Dyspnea, and Exercise Capacity Index in Chronic Obstructive Pulmonary Disease. New England Journal of Medicine. 2004;350(10):1005-12.

383.	Martini K, Caviezel C, Schneiter D, Milanese G, Opitz I, Weder W, et al. Dynamic magnetic resonance imaging as an outcome predictor for lung-volume reduction surgery in patients with severe emphysema. European journal of cardio-thoracic surgery : official journal of the European Association for Cardio-thoracic Surgery. 2018.

384.	Matin TN, Rahman N, Nickol AH, Chen M, Xu X, Stewart NJ, et al. Chronic Obstructive Pulmonary Disease: Lobar Analysis with Hyperpolarized 129Xe MR Imaging. Radiology. 2017;282(3):857-68.

385.	Maes F, Vandermeulen D, Suetens P. Medical image registration using mutual information. Proceedings of the IEEE. 2003;91(10):1699-722.

386.	Doel T, Matin TN, Gleeson FV, Gavaghan DJ, Grau V, editors. Pulmonary lobe segmentation from CT images using fissureness, airways, vessels and multilevel B-splines. IEEE International Symposium on Biomedical Imaging 2012 2-5 May

387.	Yoo TS, Ackerman MJ, Lorensen WE, Schroeder W, Chalana V, Aylward S, et al. Engineering and algorithm design for an image processing Api: a technical report on ITK--the Insight Toolkit. Studies in health technology and informatics. 2002;85:586-92.

;l